Mechanisms of Mild Cellular Stress Response

Inaugural-Dissertation
to obtain the academic degree
Doctor rerum naturalium (Dr. rer. nat.)

submitted to the Department of Biology, Chemistry and Pharmacy
of Freie Universität Berlin

by Annabell Plauth (M. Sc.)

from Erfurt

May 2016

Die Dissertation wurde in der Zeit von Dezember 2011 bis Mai 2016 im Max-Planck-Institut für molekulare Genetik in Berlin in der Arbeitsgruppe Nutrigenomics and Gene Regulation unter der Leitung von Dr. Sascha Sauer angefertigt.

1. Gutachter: Dr. Sascha Sauer
(Max-Planck-Institut für molekulare Genetik, Universität Würzburg)

2. Gutachter: Prof. Dr. Sigmar Stricker
(Freie Universität Berlin)

Disputation am: 11.10.2016

To my beloved husband.

Acknowledgements

I am grateful to my advisor Dr. Sascha Sauer for giving me the opportunity to freely develop my research study on resveratrol, for supporting me with guidance and discussions, and for reviewing this thesis. Additionally, I thank Prof. Dr. Sigmar Stricker for reviewing this work.

I would like to express my gratitude to my colleagues for their technical support, scientific discussions and daily encouragements. My special thanks are to Luise Fuhr, Morten Rousseau, Sophia Bauch, Dr. Christopher Weidner and Dr. Susanne Cichon. I also thank all the other members of the Nutrigenomics and Gene Regulation group for their help and the good working atmosphere.

I am further grateful to Dr. Radmila Feldmann, Dr. David Meierhofer, Anja Freiwald, Silvina Lotito, Linda J. Wainwright for fruitful discussions. Moreover, I wish to acknowledge Sylvia Wowro, Linda Liedgens, and Anne Geikowski.

My special thanks are to my dear husband Max, to my family and friends (especially Aylin) for their encouragement, sympathy, and love. Furthermore, I would like to thank the Operating Systems and Middleware Group at Hasso Plattner Institute.

This work was supported by Unilever and the Max Planck Society.

Contents

1 Introduction

Contents

1.1 The human skin

Covering an area of $1.6 - 1.8$ m^2 (BioNumbers ID (BNID) 100578 [1]), the human skin is the largest organ of our body [2]. It protects muscles and internal organs from environmental effectors, mediating protection against pathogens and water loss. The skin is responsible for various functionalities, including heat regulation, sensation, excretion (e.g. of sweat), deposition of lipids, and production of vitamin D. Notably, our skin comprises roughly $1.1 * 10^{11}$ cells (BNID 101734) covered with approximately 10 bacteria per cell, resulting in a total of 10^{12} bacteria (BNID 105712 [1]). There are two distinct skin types, thin and thick skin, each comprising three layers called epidermis, dermis, and hypodermis (Figure 1.1).

1.1.1 Layers of the skin

The epidermis is the outermost layer of the skin (Figure 1.1) and responsible for the protection against environmental stressors such as pathogens, heat, ultraviolet (UV) radiation, and water loss. As an avascular tissue, the epidermis is sustained solely by diffused oxygen [3]. The epidermis can be divided into five sublayers (bottom to top): stratum basale, spinosum, granulosum, licidum and stratum corneum. Notably, 95% of epidermal cells are keratinocytes (BNID 103639 [1]).

During differentiation, keratinocytes produce increased amounts of keratin resulting in a process called keratinization. Consequently, a differentiation gradient with the youngest cells at the bottom (stratum basale) and the oldest, cornified keratinocytes (stratum corneum) at the top is formed. In humans, this keratinocyte turnover takes between 26 and 27 days (BNID 109215 [1]). In total, $1.76 * 10^{11}$ cells [4] make up the epidermis, including keratinocytes, melanocytes (causing skin pigmentation), antigen-presenting immune cells, and “touch” cells.

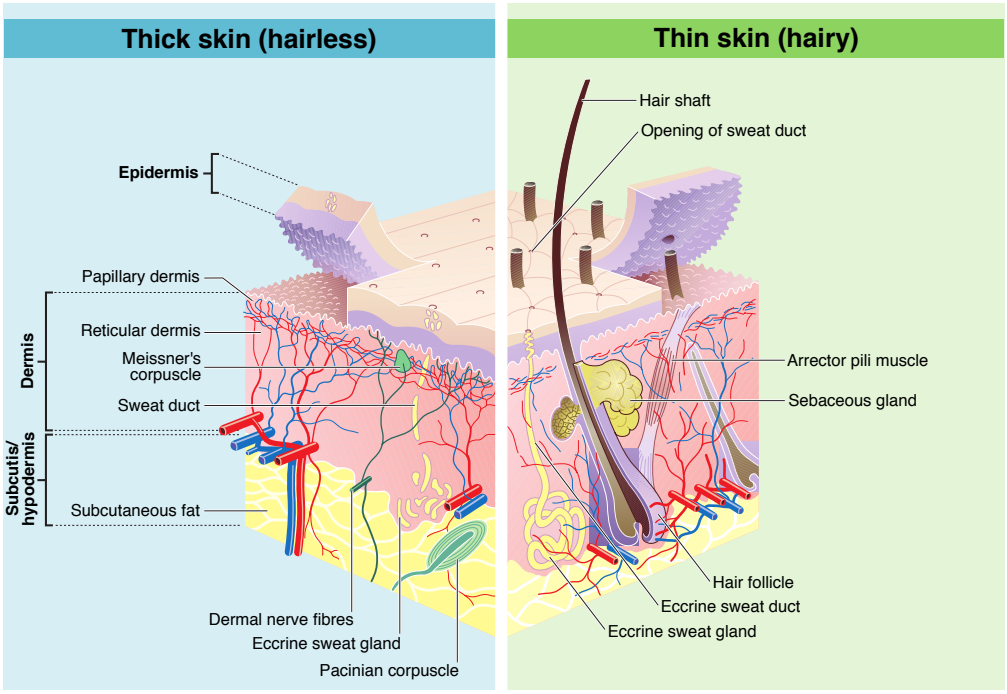

Figure 1.1: Layers of the skin. The human skin contains two skin types, namely thick and thin skin, each containing three layers called epidermis, dermis, and hypodermis. Adapted from [5].

The dermis is the second layer of the skin (Figure 1.1) consisting of connective tissue and providing touch (Meissner's corpuscle) and heat sensation through about $4 * 10^6$ free nerve endings (BNID 101736 [1]). The dermis is segregated into two sublayers called papillary and reticular region. The latter is characterized by a dense network of matrix components, e.g. collagen, elastin and an extrafibrillar matrix, providing strength and elasticity. This layer contains mainly fibroblasts, macrophages, and adipocytes, as well as hair follicles, sweat and sebaceous glands, and diverse blood vessels (Figure 1.1).

The hypodermis is the third skin layer (Figure 1.1) connecting the skin to bones and muscles. It consists of connective tissue, elastin, and subcutaneous fat and contains fibroblasts, macrophages and adipocytes which sum up to a total number of $1.85 * 10^{12}$ dermal cells [4].

1.1.2 Skin aging

Aging is a complex phenomenon caused by intrinsic and extrinsic factors. Aged skin is characterized by increased wrinkling, irregular pigmentation and increased laxity [6, 7].

Aging is associated with reduced metabolic activity, accumulation of oxidative damage and inflammatory processes. During aging, the skin decreases in volume and elasticity, becomes thinner, and has reduced self-healing properties. Consequently, anti-aging supplements were developed and used frequently to combat aging of the skin.

The intrinsic skin aging describes a deterioration of tissue function and as such is comparable to the aging of internal organs. Although the outermost epidermis layer (stratum corneum) remains comparatively stable, both epidermis and dermis change metabolically and structurally. This process is characterized by decreased proliferation of keratinocytes, fibroblasts and melanocytes, as well as reduced matrix synthesis and elevated expression of collagen matrix disintegrating enzymes [6].

The primary reason for extrinsic aging is UV light exposure [8]. In general, photoaging describes the aging of skin due to continuous and long-term exposure to UV radiation [9–11]. Photoaged skin can be identified histopathologically by a substantial accumulation of extracellular matrix (ECM) components in the dermis and increased expression of so-called matrix metalloproteinases [6]. The relations between photoaging, UV radiation and matrix metalloproteinases are reviewed in [7, 12, 13].

1.2 Polyphenols

Polyphenols are natural organic substances, historically known as “vegetable tannins” [14], which are characterized by multiple phenolic structures. In 2011, Quideau et al. revised the White-Bate-Smith-Swain-Haslam (WBSSH) definition [15] of plant polyphenols (Figure 1.2) [14]. The authors suggested defining polyphenols as plant secondary metabolites derived from distinct pathways featuring at least two phenolic rings while lacking a nitrogen-based functional group in their basic structure [14]. The biological role of plant polyphenols is diverse, as these natural products regulate growth, provide coloration, protect against solar radiation, and antagonize microbial pathogens and animal herbivores [14].

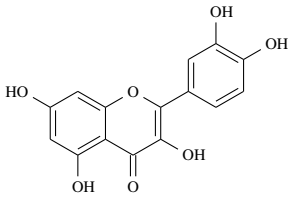

(a) Quercetin

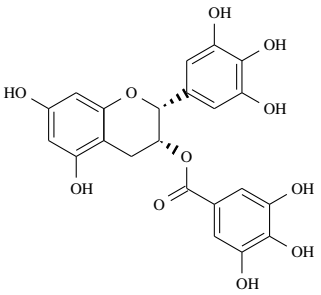

(b) Epigallocatechin gallate (EGCG)

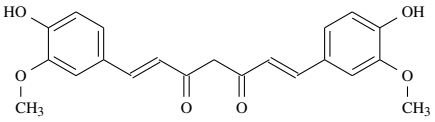

(c) Curcumin

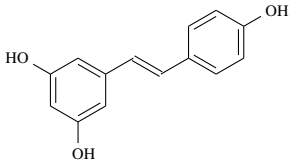

(d) *Trans*-Resveratrol (RSV)

Figure 1.2: Representatives of plant polyphenols. According to Quideau et al. (2011), plant polyphenols are defined as plant secondary metabolites derived from distinct pathways featuring at least two phenolic rings while lacking a nitrogen-based functional group in their basic structure [14]. Representatives include the flavonols quercetin (a) and epigallocatechin gallate (EGCG) (b) as well as the phenylpropanoid-derived pigment curcumin (c) and the hydroxystilbene *trans*-resveratrol (RSV) (d).

Traditional medicines have been using polyphenol-rich extracts for thousands of years and their molecular and supposedly health beneficial effects were studied in the past decades. Consequently, the number of scientific publications on "polyphenols" increased almost exponentially over the last 20 years (Figure 1.3). The "French paradox" drew major attention towards plant polyphenols in the late 1980s. Despite consuming a high fat diet, the French population has a low incidence of coronary heart diseases. In 1992, Renaud and De Lorgeril published their scientific data on the "French paradox" [16].

Trans-resveratrol (RSV) (Figure 1.2d) was identified as a major polyphenolic component of red wine [17, 18] and received considerable attention in subsequent research (Figure 1.3). This scientific focus was even intensified, when Jang et al. reported striking chemo-preventive properties of RSV [19].

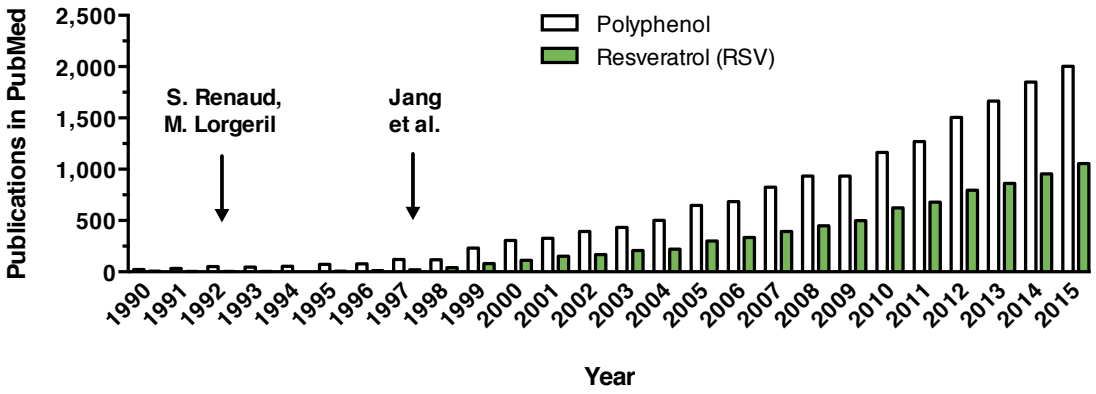

Figure 1.3: Publications in PubMed concerning "Polyphenol" and "Resveratrol". The "French paradox" in the late 1980s and a corresponding scientific study presented by Renaud and De Lorgeril in 1992 [16] as well as evidence of a chemo-preventive action of RSV in 1997 [19] boosted polyphenol research. Publications from 01.01.1990 until 31.12.2015 were considered (data from PubMed database [20]).

From early on, polyphenols were thought to have antioxidant properties and to nonspecifically interact with diverse proteins [21, 22]. The increasing number of studies on plant polyphenols enabled a more detailed insight into the mechanism of action, molecular targets, and regulated pathways. Nowadays, many polyphenolic compounds are known to interact more or less directly with their target(s), thereby inducing inhibition of key enzymes or modulation of receptors and transcription factors. Thus, polyphenols can broadly influence cellular functions such as proliferation, inflammation, apoptosis and metastasis [23–25].

Nevertheless, bioavailability studies on plant polyphenols have delivered rather disappointing results, so far [26]. In general, dietary plant polyphenols are ineffectively absorbed and immediately metabolized, which disqualifies them as potential pharmaceutical drugs. However, these characteristics could be beneficial, when considering long-term treatments to prevent slowly developing diseases [27]. The development and design of novel polyphenol-inspired drugs could have an important impact on future research [28, 29]. When consumed on a regular basis, polyphenols are present in modest but continuous doses owing to weak absorption and rapid metabolization.

1.3 Resveratrol

Trans-resveratrol (RSV) (Figure 1.2d) was originally isolated in 1939 from roots of *Veratrum grandiflorum O. Loes* [30] and is naturally occurring in at least 72 plant species [19], including Japanese knotweed [31], grapevines [32], red wine [17, 18], mulberries and peanuts [33]. These plants synthesize RSV as protection against microbial infections and environmental stressors such as UV light [32]. Notably, grape skin contains between 50 and 100 μg RSV per gram wet weight [34].

Since the "French paradox" and the identification of RSV as a major ingredient of red wine, RSV has become the object of numerous studies and publications (Figure 1.3). Moreover RSV incited research, whether regular wine consumption could be beneficial for human health. Nowadays, RSV is widely known, however, most of its suggested health benefits have yet to be verified *in vitro* and *in vivo*.

1.3.1 Chemical properties and stability

The stability of RSV and its chemical properties are influenced by diverse factors, which are still a matter of debate (Figure 1.4). Nevertheless, these factors need to be kept in mind when considering the use of RSV in biological assays or cell culture.

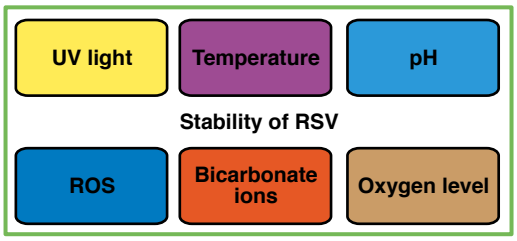

Figure 1.4: Determinants of RSV stability. Under experimental conditions several factors influence the stability of RSV. These factors include temperature [35], pH value [35–37], the presence of reactive oxygen species [38–40] and bicarbonate ions [41, 42], the oxygen level [43], and UV irradiation [36, 44].

One of the well-known characteristics of RSV is its photosensitivity. If exposed to UV or visible light, RSV converts from a *trans*- to a *cis*-isomer (Figure 1.5). This process is called photoisomerisation [36, 44]. Although the pharmacology of *trans*-resveratrol was intensively studied, only little is known about *cis*-resveratrol [45, 46]. Considering its characteristic absorption maximum at 308 nm [36], the amount of photoisomerisation or metabolization of RSV can be monitored and quantified [35, 44].

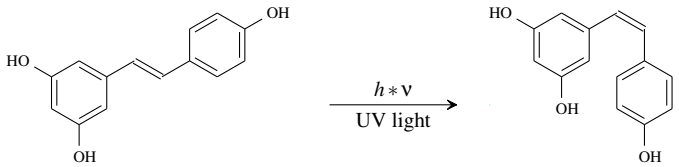

Trans-resveratrol *Cis*-resveratrol

Figure 1.5: Isomeric conversion of RSV. After exposure to light ($h*\nu$) or UV light, *trans*-resveratrol isomerizes rapidly into its *cis*-isomer [45, 46].

There is growing evidence that polyphenols, including RSV, degrade rapidly at alkaline pH values, while they are stable at acidic pH [35–37]. Moreover, high temperature was recently reported to decrease the stability of RSV [35].

Our organism continuously generates reactive oxygen species (ROS, see Section 1.4) as a side product of metabolism and as second messengers. Notably, RSV can scavenge ROS and function as an antioxidant. During the scavenging process, RSV is rapidly oxidized and generates more or less stable radical adducts [38–40].

In biological systems the majority of ROS generated are superoxide ($O_2^{\bullet -}$) and hydrogen peroxide (H_2O_2). Spontaneous or enzymatic dismutation of $O_2^{\bullet -}$ results in H_2O_2 production, which can readily react with transition metal ions to generate hydroxyl radical ($HO^{\bullet}$) (Figure 1.10a).

Several studies identified hydroxyl radical as major species acting on RSV [38–40]. Recently, Li et al (2012) investigated the kinetics of the reaction of RSV with $HO^{\bullet}$ [40] (Figure 1.6). The reaction of RSV with $HO^{\bullet}$ generates a relatively short-lived C2 or C6 hydroxyl radical adduct (absorbance maximum 420 nm; lowest transition energy for C2 adduct [40]). Afterwards, a relatively long-lived 4′-phenoxyl radical (absorbance maximum 390 nm) is formed (Figure 1.6).

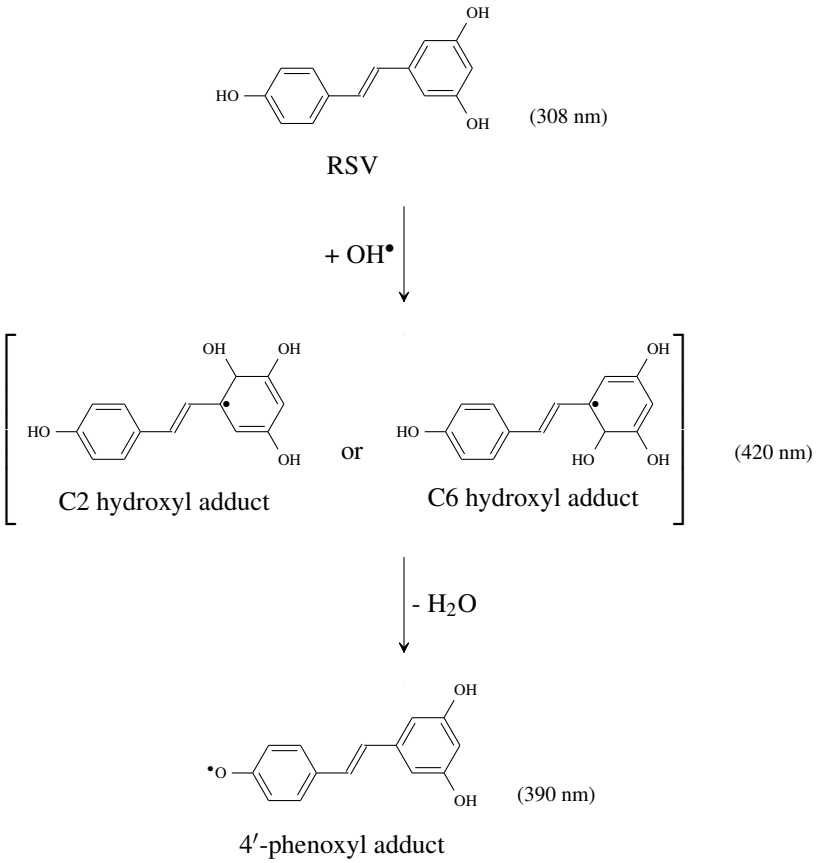

Figure 1.6: Reaction products of RSV and HO• according to Li et al. (2012) [40]. Absorbance maximum is given in brackets. Adapted from [40].

Although often ignored, it is known for several years that polyphenols, including RSV, are rapidly oxidized in cell culture media to generate significant amounts of H_2O_2 [41, 42, 47]. Notably, the degradation process and subsequent H_2O_2 generation is accelerated in the presence of bicarbonate ions [**?**, 41, 42]. In cell culture media, pyruvate was identified as an important scavenger of H_2O_2 [**?**, 48, 49].

Oxygen is essential for the survival of organs and tissues, but depending on the physiological context it can be a potent stressor as well. The oxygen partial pressure (pO_2) is a measure for the oxygen concentration [50]. The earth's atmosphere comprises 20.9460% O_2, equalling 160 mmHg [51]. Although the oxygen level is supposed to influence the oxidation of RSV, this hypothesis remains to be further investigated [43, 52]. So far most *in vitro* studies have been performed at 150 mmHg (95% air), a fact that is often referred to as "artifact of cell culture" [41, 42]. Due to the limited diffusion distance

of oxygen (physioxia range between 11% and 1% O_2) physiological oxygen amounts (e.g. in liver or kidney cells) tend to be much lower. Notably, the pO_2 in a tumor is even lower compared to normal tissue [50, 53].

Factors that determine the integrity of RSV i.e. pH, temperature, cell culture medium containing $NaHCO_3$, and supposedly pO_2, must be kept in mind to correctly interpret experimental results [41,42]. Even though a plethora of *in vitro* studies have been showing beneficial effects of RSV, those results are rarely seen *in vivo*. The low bioavailability of RSV might be one reason of this divergence [26, 54–59]). Differential conditions that influence chemical properties of RSV can be another still often neglected reason.

1.3.2 Molecular targets

The mechanism of action of RSV is largely elusive and controversially discussed, in addition, a direct molecular target remains to be identified. Currently, direct enzymatic, allosteric or indirect activation are proposed [60–63]. Notably, the reported interaction of RSV with target molecules is often low (in mid micromolar range) and most likely unspecific [63–66].

Although numerous studies have been conducted with RSV, the observed results are diverse and the induced effects seem to be highly dependent on cell type, concentration, treatment conditions, and duration [67]. An overview of RSV targets is given in Figure 1.7 [68–73].

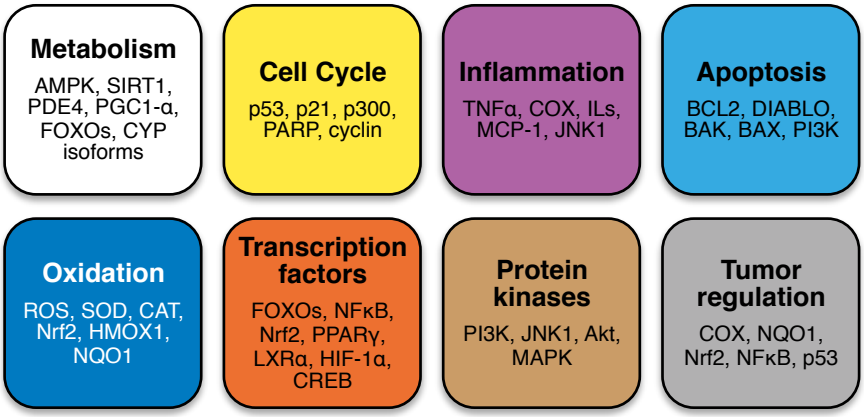

Figure 1.7: Molecular targets of RSV. In consideration of its comparatively simple structure, RSV influences an tremendous range of function and pathways resulting in multiple biological activities [68–73]. Protein kinase B (Akt), 5′adenosine monophosphate (AMP)-activated protein kinase (AMPK), B-cell lymphoma 2 (BCL2)-antagonist/killer (BAK), BCL2-associated X protein (BAX), B-cell lymphoma 2 (BCL2), catalase (CAT), cyclooxygenase (COX), cAMP-response element-binding protein (CREB), cytochrome p450 monooxygenase (CYP), direct inhibitor of apoptosis protein (IAP) binding protein with low pI (DIABLO), forkhead box proteins (FOXOs), hypoxia-inducible factor 1-alpha (HIF-1α), heme oxygenase 1 (HMOX1), interleucins (ILs), c-Jun N-terminal kinase 1 (JNK1), liver X receptor alpha (LXRα), mitogen-activated protein kinase (MAPK), monocyte chemoattractant protein 1 (MCP-1), nuclear factor kappa-light-chain-enhancer of activated B cells (NFκB), NAD(P)H dehydrogenase (quinone 1) (NQO1), nuclear factor (erythroid-derived 2)-like 2 (Nrf2), cyclin-dependent kinase (CDK) inhibitor 1A (p21), adenovirus early region 1A (E1A) binding protein p300 (p300), tumor protein p53 (p53), poly(ADP-ribose) polymerase (PARP), cyclic adenosine monophosphate (cAMP)-specific 3′,5′-cyclic phosphodiesterase 4 (PDE4), peroxisome proliferator-activated receptor (PPAR) gamma (PPARγ) coactivator 1-beta (PGC1-α), phosphatidylinositol-4,5-bisphosphate 3-kinase (PI3K), PPARγ, reactive oxygen species (ROS), superoxide dismutase (SOD), sirtuin 1 (SIRT1), tumor necrosis factor α (TNFα).

Sirtuins

Sirtuins were originally discovered as NAD-dependent type III histone deacetylase (HDAC) in *Saccharomyces cerevisiae*, where silent information regulator 2 (SIR2) (orthologue of SIRT1) silenced specific genomic loci by deacetylation [74]. The mammalian family of sirtuins can be divided into four classes (I-IV) comprising seven members (SIRT1-SIRT7) in total, each with characteristic tissue specificity, subcellular localization, enzyme activity and target proteins [75, 76].

At first, RSV was identified to extend lifespan by direct interaction with the histone deacetylase sirtuin 1 (SIRT1) [65]. However, several reports indicated that fluorescent labels produced activation artifacts and the unlabeled peptide did not activate SIRT1 at all [60, 61, 77]. Still a potential direct enzymatic, allosteric or indirect activation have

been discussed [60–63]. Sirtuins have been suggested as a mediator of beneficial effects of calorie restriction (CR) on health and longevity [65, 78–81].

Regulation of SIRT1. SIRT1 is regulated by different kinases, modifiers and diverse regulatory mechanisms [82–86], thus connecting various metabolic pathways [87] (Figure S1). To catalyze the deacetylation of target proteins, SIRT1 requires nicotinamide adenine dinucleotide phosphate (NAD^+) cofactor [88]. Therefore, this cofactor is a potent regulator of SIRT1 activity [86, 89, 90]. In contrast, the reaction product nicotinamide (NAM) functions as inhibitor [91]. Notably, the deoxyribonucleic acid (DNA) repair enzyme PARP also requires NAD^+ for the repair of DNA strand breaks and chromatin remodeling. Consequently, PARP and SIRT1 seem to be connected via a negative feedback loop as both enzymes compete for NAD^+ [92–94].

During oxidative stress, JNK1 phosphorylates SIRT1 at three distinct sites, increasing its activity and linking SIRT1 to inflammatory processes and ROS signaling [95]. Interestingly, the level and activity of SIRT1 is regulated by the intracellular thiols [96, 97]. Post-translational modifications such as phosphorylation of SIRT1 by cell cycle kinases have been shown to increase enzyme activity and additionally link SIRT1 to proliferation and cell cycle progression [98]. For a detailed review of the regulation of SIRT1 and other members of this family please see [75, 76] and Figure S1.

Molecular targets of SIRT1. The genome integrity depends on the chromatin structure and DNA repair mechanisms, which in turn depends on the (de-)acetylation status of histones and general chromatin-associated factors [99–103]. In addition, deacetylation of SIRT1 target proteins often results in epigenetic silencing of genes including the interaction with p300 [104–106]. Apart from histones, SIRT1 has several non-histone targets such as transcription factors, cell signaling components, DNA repair modulators and metabolic regulators [75, 76, 107–113] (Figure S1). However, the identification of signaling targets remains incomplete. Notably, the acetylation status of a target protein might influence its cellular localization [99] and stability [114]. For a detailed review of SIRT1 target molecules please see [75, 76, 112, 115, 116].

1.3.3 Hormesis

Hormesis describes a biphasic dose-response phenomenon characterized by low-dose stimulation and high-dose inhibition [117]. Although the importance and relevance is vigorously discussed [118, 119], hormesis has become an appropriate model in toxicology and risk assessment [120, 121]. Meanwhile, the concept of hormesis is applied to various fields including xenohormesis [122], neurohormesis [123] and mitohormesis [124, 125]. Moreover, hormesis might in fact represent a superior model for low-dose assessment of drugs, as low treatment doses might activate repair mechanisms, thus preventing future damage. [119, 126].

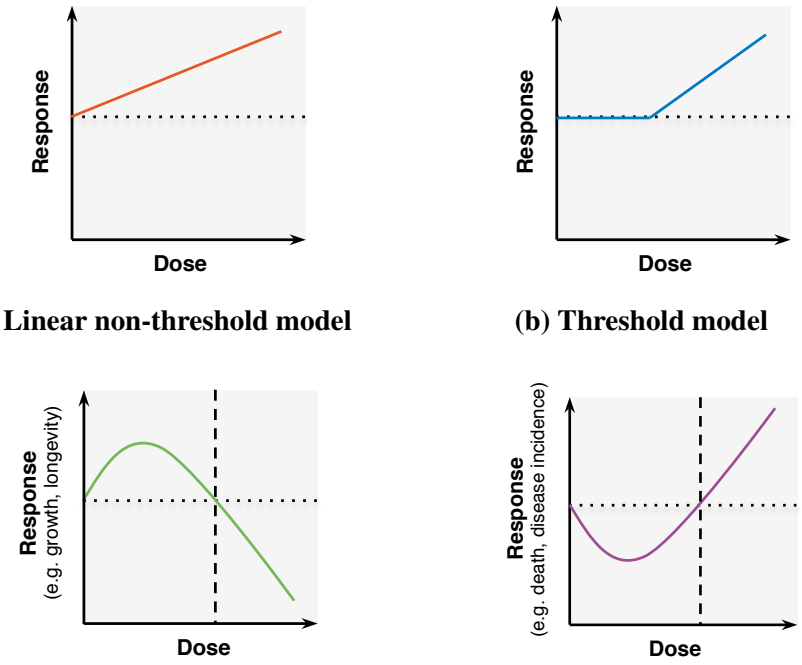

(a) Linear non-threshold model **(b) Threshold model**

(c) Inverted U-shaped model **(d) J-shaped model**

Figure 1.8: Dose-response models used in toxicology and risk assessment. The linear non-threshold model (a) is used to estimate cancer risks, whilst the threshold model (b) is used in toxicology and pharmacology. (c and d) Typical hormetic models show either a U- or J-shaped dose-response relationship depending on the type of response. The control level is indicated by a dotted line. Adapted from [127].

In general, the linear non-threshold model (Figure 1.8a) is used to assess the health risks of chemical carcinogens and radiation, whilst for non-carcinogens and drugs the threshold model (Figure 1.8b) is applied [127]. However, both linear models overlook the

fact that organisms might have developed mechanisms to respond to noxious substances and radiation. When considering hormetic models for risk assessment either an inverted U-shaped or a J-shaped model can be applied, depending on the endpoint of measurement (Figures 1.8c and 1.8d) [127].

In fact, the reported health benefits of diverse phytochemicals seem to be based on hormetic mechanisms, as phytochemicals activate adaptive stress response signaling [123]. These pathways are commonly associated with activation of kinases and transcriptions factors, leading to increased levels of cytoprotective phase 2 and antioxidant enzymes, heat-shock proteins, growth factors and energy metabolism regulators [123, 128].

Resveratrol and other phytochemicals

The biological role of phytochemicals is to protect the plant against microorganisms and insects [129]. However, in humans consumption of low doses of phytochemicals might induce a mild cellular stress response. Hormetic effects have been described for several polyphenols and phytochemicals including curcumin [130], quercetin [131], RSV [132, 133] and sulforaphane (SFN) [129]. According to Calabrese et al. (2009) the antioxidant potential of polyphenols results from up-regulation of so called "vitagenes" including heat shock proteins (HSPs) and sirtuins (SIRTs) as well as the thioredoxin (TXN) system [134].

Curcumin. The phenolic compound curcumin (Figure 1.2c) can be isolated from the roots of Turmeric (*Curcuma longa*) and is known to induce hormetic effects [130]. Activation of nuclear factor (erythroid-derived 2)-like 2 (Nrf2) signaling (see Section 1.5) induces expression of heme oxygenase 1 (HMOX1) and results in cellular protection against further stressors [135–137].

Resveratrol. Hormetic effects of RSV have been described in several publications [132, 133]. RSV activates various hormetic pathways including the expression of phase 2 enzymes and antioxidant enzymes (catalase (CAT) and glutathione *S*-transferase (GST)) [138], Nrf2 signaling and the expression of the antioxidant enzyme HMOX1 [139].

Sulforaphane. The isocyanate sulforaphane (SFN) (Figure 1.15a) can be found in broccoli sprouts, kale, radish, mustard and many more [140]. It is known to activate Nrf2-dependent expression of antioxidant enzymes [141], increase glutathione (GSH) and thioredoxin (TXN) levels as well as NAD(P)H dehydrogenase (quinone 1) (NQO1) expression [142, 143].

Potential and limitations

In general, hormetic effects resemble mild stress conditions causing only moderate and not striking effects, thus making it difficult to justify the biological significance of hormesis. However, even if the initial hormetic effects might be small and difficult to detect biochemically, the biological outcome might be larger leading to improved stress-tolerance and longevity, respectively. Hormesis might represent an adaptive amplification principle to improve overall cellular robustness and performance [137, 143–148].

1.4 Reactive oxygen species

The term reactive oxygen species (ROS) describes oxygen-derived reactive molecules. This definition includes the two major reactive species superoxide ($O_2^{\bullet -}$) and hydroxyl radical ($HO^{\bullet}$) [149] as well as hydrogen peroxide (H_2O_2) and nitric oxide (NO). ROS are omnipresent and hazardous, however, they are also important second messengers and regulators of transcription factor activity [150–153].

During oxidative stress the cell is attacked by ROS which decreases the cellular antioxidant capacity. ROS interact with biomolecules causing oxidation of nucleic acids, lipid peroxidation and protein denaturation. Notably, ROS-mediated oxidative stress is involved in carcinogenesis [154], neurodegeneration [155], diabetes [156] and aging [157].

1.4.1 Origins

ROS are either exogenously or endogenously produced, in addition, ROS are formed by Fenton and Haber-Weiss reaction (Figures 1.9 and 1.10) [158, 159]. The majority of endogenous ROS are produced in the mitochondria during generation of adenosine

triphosphate (ATP) generation [160–162]. Approximately 1% of the total rate of the mitochondrial oxygen consumption are ROS [163]. Considering the average rate of oxygen consumption per cell ($2.5 * 10^{-18}$ mol s^{-1} [51]), roughly 1.3 billion ($1.3 * 10^{9}$) ROS are generated daily per cell. Considering only the epidermis with its $1.76 * 10^{11}$ cells [4], the "physiological" ROS flux would be roughly 229 sextillion ($2.29 * 10^{20}$) molecules per day.

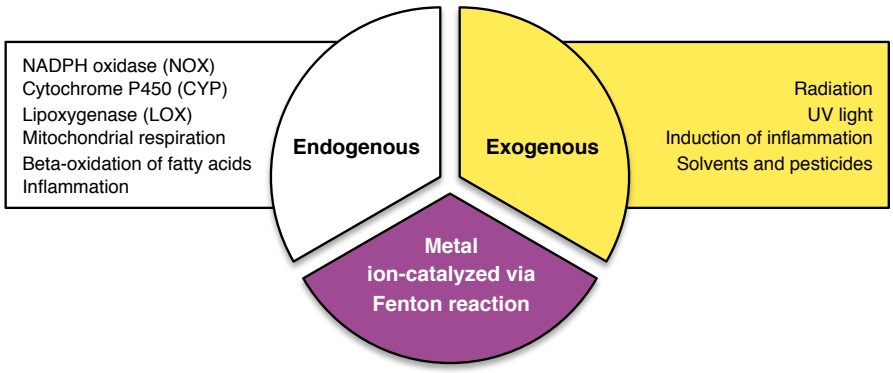

Figure 1.9: Origins of ROS. ROS are either exogenously, endogenously or metal ion-catalyzed via Fenton reaction (adapted from [164]).

Regardless of being a ROS, superoxide ($O_2^{\bullet -}$) is not highly reactive (half-life time [s] at 37°C: $1 * 10^{-6}$ [165]), as it is unable to penetrate lipid membranes and is therefore "trapped" in the compartment where it was initially generated. Superoxide is endogenously produced by several enzymes including lipoxygenases (LOXs), NADPH oxidases (NOXs) and cyclooxygenases (COXs) [151, 164]. Enzymatic detoxification of superoxide is conducted by superoxide dismutases (SODs) [166].

Hydrogen peroxide (H_2O_2) is often generated as intermediate reaction product in the generation of additional reactive oxygen species [159, 167] (Figure 1.10a) and an important intracellular signaling molecule and second messenger [150, 168]. The removal of H_2O_2 is conducted by catalases (CATs), glutathione peroxidases (GPXs) and peroxiredoxins (PRXs).

$$H_2O_2 + M_n \longrightarrow OH^{\bullet} + OH^{-} + M_{n+1}$$

(a) Fenton reaction

$$H_2O_2 + O_2^{\bullet -} \longrightarrow O_2 + OH^{-} + OH^{\bullet}$$

(b) Haber-Weiss reaction

Figure 1.10: Physiological ROS generation by Fenton and Haber-Weiss reaction. (a) Transition metal ions (M) such as iron (Fe(II)), copper (Cu(I)), chromium (Cr(III-V)), cobalt (Co(I)) and vanadium (V(III)) are prone to engage in these reactions [158, 164, 169]. Notably, standard cell culture media provide an ideal environment for Fenton reactions. (b) An alternative way to generate hydroxyl radical ($HO^{\bullet}$) via H_2O_2 and $O_2^{\bullet -}$ [159].

The hydroxyl radical ($HO^{\bullet}$), generated via Fenton [158] or Haber-Weiss reaction [159, 167] (Figure 1.10), is highly reactive and thus comparatively short-lived (half-life time [s]: $1 * 10^{-9}$ at 37°C) [165]. Due to its reactivity $HO^{\bullet}$ is often bound to proteins and biomolecules.

Physiologically ROS are used against infections, e.g. by activated phagocytes as they produce ROS when attacking bacteria [170]. Moreover, ROS affect the conformation of thiol-containing molecules, which is an important mechanism known as redox-regulated signaling. Similarly, ROS are able to influence several transcription factors [171–174].

1.4.2 Defense mechanisms

The cellular antioxidant defense mechanisms can be divided into non-enzymatic (Figure 1.11) and enzymatic strategies (Figure 1.12). Increasing the antioxidant capacity is an essential concept when facing oxidative stress and accomplishing protection against oxidative damage. Accordingly, the defense system is strongly regulated and highly coordinated [151, 165]. The epidermis possesses an extremely high antioxidant capacity which is supposed to be superior to the capacity of most tissues of our organism [175].

Non-enzymatic defense

Non-enzymatic ROS defense consists mainly of intracellular scavengers such as glutathione (GSH, Figure 1.11c) and vitamins (Figures 1.11a and 1.11b).

Vitamin C, also known as ascorbic acid (Figure 1.11a), is a hydrophilic antioxidant capable of reducing peroxides and ROS [176]. Additionally, vitamin C recycles vitamin E radicals, which are located in lipid membranes. In concert with GSH, vitamin C protects cell membranes against lipid peroxidation [177]. In contrast, vitamin E (α-tocopherol, Figure 1.11b) has lipophilic properties and is thus often associated with lipid-rich membranes in mitochondria and the endoplasmatic reticulum (ER) [165].

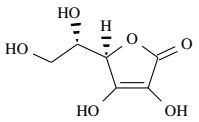

(a) Vitamin C (Ascorbic acid)

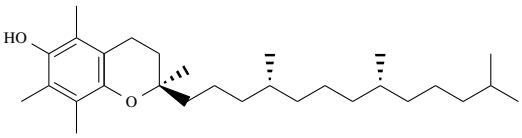

(b) Vitamin E (α-Tocopherol)

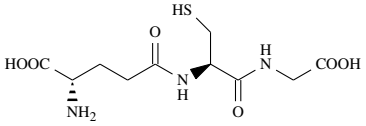

(c) Reduced glutathione (GSH)

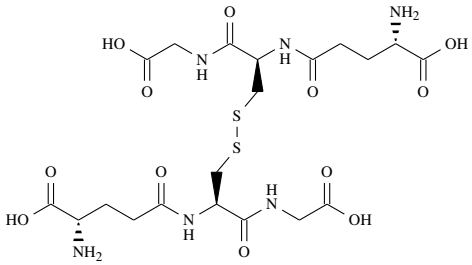

(d) Oxidized glutathione (GSSG)

Figure 1.11: Non-enzymatic defense against ROS. (a) Vitamin C is a hydrophilic antioxidant, while vitamin E has lipophilic properties (b). The thiol-based tripeptide glutathione can be found in a reduced (GSH, c) or oxidized form (GSSG, d).

The GSH system is one of the most potent cellular antioxidant systems. GSH (Figure 1.11c) is a thiol-based tripeptide (γ-glutamyl-cysteine-glycine) with intracellular concentrations in millimolar range [151]. Two GSH molecules are oxidized to form glutathione (oxidized form, GSSG) (Figure 1.11d) and enable the detoxification of ROS and xenobiotic compounds via glutathione peroxidase (GPX) and glutathione *S*-transferase, respectively. The ATP-dependent *de-novo* GSH synthesis is conducted by the glutamate-cysteine ligase (GCL) and the glutathione synthase (GSS, Figure 1.12). Notably, the GSH system is closely connected to the nicotinamide adenine dinucleotide phosphate

(NADPH) metabolism (e.g. via glucose-6-phosphate dehydrogenase (G6PD)) as both biomolecules are responsible for maintaining the cellular redox balance (Figure 1.12).

Intriguingly, recent studies revealed the importance of GSH for cellular proliferation [178]. The substitution of GSH with its precursor N-acetyl-cysteine (NAC) did not promote proliferation, thus indicating a more complex purpose of GSH than "just" the equilibration of redox homeostasis [179].

Enzymatic defense

Antioxidant enzymes play a major role in reducing ROS levels and represent the second layer of the cellular defense system. In general, the cell can increase its antioxidant capacity through expression of NADPH producing enzymes (e.g. G6PD) and ROS metabolizing enzymes including superoxide dismutases (SODs), catalases (CATs), glutathione peroxidases (GPXs) and thioredoxins (TXNs) (Figure 1.12).

SODs catalyze the transformation of superoxide ($O_2^{\bullet -}$) into hydrogen peroxide (H_2O_2) [166] (Figure 1.12). In humans, three isoenzymes have been found: Mn-SOD (SOD2) localized in the mitochondria and two Cu/Zn-SODs (cytosolic SOD1 and extracellular SOD3). Notably, the dismutation of $O_2^{\bullet -}$ by SOD is roughly 10^4 times faster than the spontaneous dismutation of $O_2^{\bullet -}$ [180].

Catalase (CAT) is localized in mammalian peroxisomes and catalyzes the detoxification of H_2O_2 [181, 182], phenols and alcohols [151] (Figure 1.12). Its ability to bind NADPH protects the enzyme from inactivation and increases its efficiency [183]. While low H_2O_2 concentrations are handled by peroxidases, CAT is responsible for the metabolization of higher concentrations [165]. By limiting the amount of hydrogen peroxide catalase prevents the formation of hydroxyl radicals ($HO^{\bullet}$).

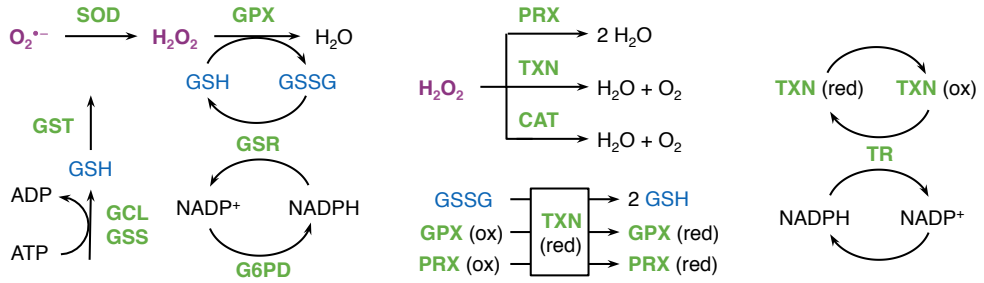

Figure 1.12: Enzymatic antioxidant defense. The second level of ROS detoxification is mediated by several highly interconnected enzymes. Superoxide dismutase (SOD) neutralizes superoxide ($O_2^{\bullet -}$), whereas catalase (CAT) metabolizes hydrogen peroxide (H_2O_2). The glutathione (GSH and GSSG, blue) and thioredoxin (TXN) system increase the antioxidant capacity and facilitate the link to the nicotinamide adenine dinucleotide phosphate (reduced form, NADPH) metabolism. Enzymes are depicted in bold green font and reactive oxygen species in magenta. Adenosine diphosphate (ADP), adenosine triphosphate (ATP), glucose-6-phosphate dehydrogenase (G6PD), glutamate-cysteine ligase (GCL), glutathione peroxidase (GPX), reduced glutathione (GSH), glutathione reductase (GSR), glutathione synthase (GSS), oxidized glutathione (GSSG), glutathione *S*-transferase (GST), nicotinamide adenine dinucleotide phosphate ($NADP^+$), peroxiredoxin (PRX), thioredoxin reductase (TR), thioredoxin (TXN), oxidized (ox), reduced (red). Adapted from [184].

Glutathione peroxidases (GPXs) use GSH to detoxify H_2O_2; in mammals four isoenzymes are known including the ubiquitously expressed GPX1 and GPX4 both localized in the cytosol. The glutathione reductase (GSR) recycles GSSG to refill the glutathione pool (Figure 1.12).

In addition to the GSH system, the so called thioredoxin (TXN) system is in place to cope with ROS (Figure 1.12). Thioredoxins are ubiquitously expressed and characterized by a wide substrate specificity [151]. In general, thioredoxin targets comprise specific proteins, transcription factors and enzymes from the antioxidant defense [185, 186]. Thioredoxin reductase (TR) catalyzes recycling of oxidized TXN in a NADPH-dependent manner [151]. Finally, peroxiredoxin (PRX) reduce peroxides including H_2O_2 and are recycled through the TXN system [185–187] (Figure 1.12).

1.4.3 Oxidative damage and cellular signaling

Due to their highly reactive character, oxygen species can cause tremendous damage to biomolecules including DNA, lipids and proteins. Alterations such as DNA cleavage, crosslinking to proteins and oxidation of purines are caused by the interaction with ROS [151]. These DNA damages are recognized by repair enzymes such as ataxia

telangiectasia mutated (ATM) and ataxia telangiectasia and Rad3-related protein (ATR) [188–191].

Moreover, ROS efficiently target the double bonds of polyunsaturated fatty acids thus leading to lipid peroxidation. When targeting amino acid residues, ROS attacks can generate modified enzymes and proteins with less or completely diminished activity, denaturation and malfunction [192].

ROS and cancer

The role of ROS in cancer is controversially discussed and complex. Most cancer cells favor aerobic glycolysis, which is commonly referred to as "Warburg effect". Despite utilizing glucose for ATP and lactate generation, most cancer cells re-route glucose to pentose phosphate pathway (PPP) to generate NADPH, which in turn is needed for the recycling of glutathione (reduced form, GSH). The path of glucose is influenced by the pyruvate kinase (PKM) activity [193]. Additionally, ROS interlink cancer metabolism to autophagy [194], senescence [195] and apoptosis [196].

Mechanisms of ROS signaling

ROS are able to directly interfere with various cellular signaling pathways by utilizing cysteine (Cys) and methionine (Met) residues as redox-dependent switches. The process is similar to the de-/phosphorylation of serine (Ser) and threonine (Thr) residues, a rapid and reversible regulatory mechanism. Interestingly, many kinases and transcription factors are regulated in a redox-sensitive manner including mitogen-activated protein kinases (MAPKs) and PI3K [152, 197] as well as NFκB [171, 198, 199], activating protein 1 (AP-1), FOXO [174] and Nrf2 [172, 173].

1.5 Nuclear factor (erythroid-derived 2)-like 2

The transcription factor nuclear factor (erythroid-derived 2)-like 2 (Nrf2) was first described by Moi et al. (1994) [200] and comprises seven domains, called Nrf2-ECH homology (Neh) domain 1-7 [201]. The most important is the Neh1 domain as it enables dimerization with small musculoaponeurotic fibrosarcoma (Maf) proteins [202] and

facilitates the binding to DNA containing an antioxidant response element (ARE) or electrophile response element (EpRE) [203–205].

Although the biological relevance of Nrf2 remained elusive at first [206], it is now regarded as key mediator of oxidative stress response [202]. Currently, about 200 target genes linking Nrf2 to cytoprotection, lipid metabolism, NADPH regeneration, xenobiotic metabolism and oxidative stress response are known [207].

1.5.1 Regulatory mechanisms of Nrf2

Due to the central role of Nrf2 in metabolism, its activity is tightly regulated. Most important is the regulation by kelch-like ECH-associated protein 1 (Keap1) that sequesters Nrf2 to the cytosol. In cooperation with the actin cytoskeleton Keap1 prevents Nrf2 from translocation and thus limits its basal activity [208]. In addition to several Keap1 dependent mechanisms, the activity of Nrf2 can be regulated independently from Keap1 [209] (Figure 1.13).

Keap1-independent regulation

In addition to the regulation of Nrf2 by Keap1, there is growing evidence of regulatory mechanisms independent of Keap1. The expression and function of a protein can be influenced transcriptionally, post-transcriptionally and by the availability of binding partners and ARE-inducing compounds (Figure 1.13). However, the Keap1-independent regulation of Nrf2 is complex and highly regulated as various factors are involved [209].

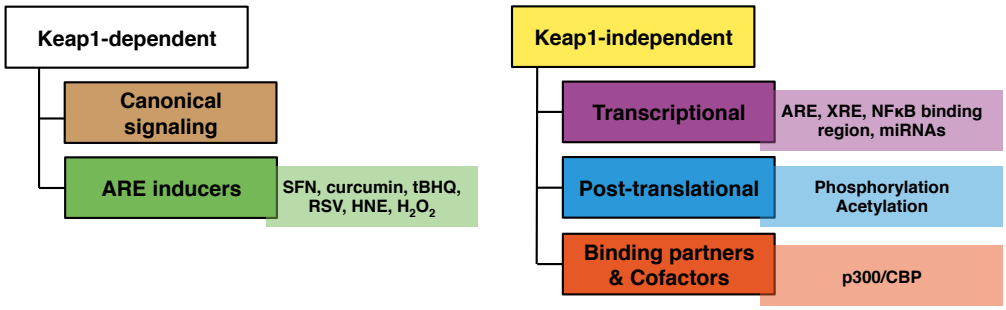

Figure 1.13: Regulation of Nrf2 signaling. Regulation of Nrf2 can be either dependent or independent of kelch-like ECH-associated protein 1 (Keap1). The canonical signaling Nrf2 (Figure 1.14) is Keap1-dependent. In general, the Keap1-independent regulation of Nrf2 is quite complex and highly regulated as various factors are involved. On a transcriptional level different DNA binding sequences enable auto-regulation of Nrf2 [210, 211]. In addition, micro RNAs (miRNAs) have been recently identified as Nrf2 regulators. Post-translational modification is a well established mechanism of regulation e.g. considering cellular localization and interaction with binding factors. Moreover, antioxidant response element (ARE)-inducing agents are known to regulate the activity of Nrf2. 4-hydroxynonenal (HNE), nuclear factor kappa-light-chain-enhancer of activated B cells (NFκB), *tert*-butylhydroquinone (tBHQ), xenobiotic response element (XRE).

Transcriptional regulation. The promotor region of many cellular defense genes comprises an antioxidant response element (ARE) or xenobiotic response element (XRE) sequence. Nrf2 can bind to ARE sequences, while the transcription factor aryl hydrocarbon receptor (AhR) binds to XRE to induce the expression of phase I enzymes including cytochrome p450 monooxygenases (CYPs) [212]. Interestingly, the Nrf2 promotor itself contains XRE elements and an ARE sequence, thus establishing a feedback loop and enabling autoregulation of Nrf2 [210, 211]. However, when analyzing the Nrf2 interactome, Papp et al. (2012) discovered that roughly 20% of the identified Nrf2 interacting proteins have a regulatory feedback connection with Nrf2 [209].

MiRNAs are short, single-stranded non-coding ribonucleic acids (RNAs) which are exported after transcription and bind their target messenger RNA (mRNA) to cause mRNA degradation, inhibition of protein translation, and inhibition of protein expression [213]. Up to now several miRNAs have been identified to regulate Nrf2 [214] (Figure 1.13).

Post-translational regulation. Comprising many serine (Ser), threonine (Thr) and tyrosine (Tyr) residues, Nrf2 provides various sides for phosphorylation (Figure 1.13). Several kinase pathways have been identified as regulators including MAPK cascades

[215–218], PI3K and Akt pathway [217–219], protein kinase C (PKC) [220, 221] and glycogen synthase kinase 3 beta (GSK3β) pathway [222–225]. Only recently, Nrf2 has been shown to be regulated by acetylation [226–228].

Binding Partners and co-factors. Next to ubiquitination and phosphorylation, acetylation plays a major role in the regulation of Nrf2. Once translocated into the nucleus, Nrf2 is able to recruit additional transcriptional machinery. Transcriptional co-activators such as p300/CREB binding protein protein (CBP) are known to acetylate histones and reported to associate with Nrf2 [226–228] (Figure 1.13).

Keap1-dependent regulation

In 1999, Itoh et al. identified Keap1 as negative regulator of Nrf2 [203]. Notably, the Keap1 protein contains twice the amount of cysteine residues (roughly 4.3%) than the average protein [229]. In general, cysteine residues are redox-responsive to their environment and can be found in functional protein domains and enable Keap1 to act as redox sensor [230, 231].

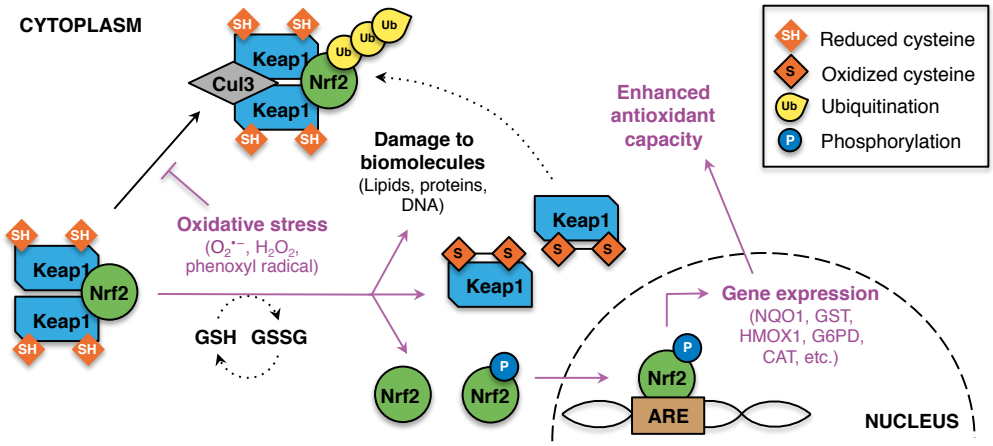

Figure 1.14: Canonical nuclear factor (erythroid-derived 2)-like 2 (Nrf2) signaling. Under physiological conditions Nrf2 resides in the cytoplasm and is bound to its inhibitor kelch-like ECH-associated protein 1 (Keap1) [203], which facilitates ubiquitination via cullin 3-based ubiquitin E3 ligase (Cul3) [232–235]. Oxidative stimuli trigger the formation of bisulfide bonds of Keap1 cysteine residues. The resulting conformational change causes the release of Nrf2, subsequent translocation into the nucleus and expression of target genes [202, 207, 211, 236]. Antioxidant response element (ARE), catalase (CAT), glucose-6-phosphate dehydrogenase (G6PD), reduced glutathione (GSH), oxidized glutathione (GSSG), glutathione *S*-transferase (GST), heme oxygenase 1 (HMOX1), NAD(P)H dehydrogenase (quinone 1) (NQO1).

Under physiological, non-stressed conditions, the majority of Nrf2 resides in the cytoplasm (Figure 1.14) whilst each Nrf2 molecule is sequestered by a Keap1 homodimer [203,237,238]. In addition to its inhibitory functionality on Nrf2, Keap1 serves as adaptor for the cullin 3-based ubiquitin E3 ligase (Cul3) [232–234], facilitating ubiquitination and proteasomal degradation of the complex [234, 235]. Thus, Keap1 causes the high turnover and short half life of Nrf2 of roughly 10-20 min [239, 240].

Keap1 comprises multiple highly reactive and redox sensitive cysteine residues (Cys), which are accessible for oxidation by ROS or electrophiles [236, 241]. Specifically, modification of Cys151, Cys273 and Cys288 is suggested to affect the conformation of Keap1 [173]. Upon oxidation of Keap1 cysteines, Nrf2 is freed and translocates into the nucleus (Figure 1.14). Notably, there is still an ongoing discussion concerning the relief of Nrf2 [242–245]. In the nucleus, Nrf2 forms a heterodimer with small musculoaponeurotic fibrosarcoma (Maf) proteins, which promote binding to the ARE and subsequent expression of target genes (Figure 1.14).

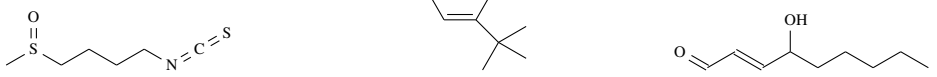

(a) Sulforaphane (SFN) **(b) *tert*-Butylhydroquinone (tBHQ)** **(c) 4-Hydroxynonenal (HNE)**

Figure 1.15: Representative examples of ARE-inducing agents. Both compounds induce Nrf2 signaling [135, 246, 247]. (a) The isothiocyanate sulforaphane (SFN) can be found in broccoli and other cruciferous vegetables such as kohlrabi, mustard and radish. (b) 4-hydroxynonenal (HNE) was first characterized by Esterbauer et al. (1991) [248] and is endogenously generated by the oxidation of lipids. (c) The hydroquinone derivative *tert*-butylhydroquinone (tBHQ) is a potent antioxidant and used as food additive (E number: E319).

ARE inducers. Small molecule electrophiles are known to modify cysteine residues of Keap1 thus rendering it inactive [236, 249] and simultaneously increasing the half-life of Nrf2 (roughly 7.5-15 min) depending on the electrophile and cell line used [210, 219, 250, 251]. Several pharmacological compounds and natural agents have been shown to activate Nrf2 signaling including sulforaphane (SFN, found in broccoli, Figure 1.15a [246]), curcumin (found in tumeric, Figure 1.2c, [135, 247]), *tert*-butylhydroquinone (tBHQ, Figure 1.15b, [217, 219, 252]), resveratrol (RSV, Figure 1.2d, [139, 146]), 4-hydroxynonenal (HNE, Figure 1.15c, [253]) and hydrogen peroxide (H_2O_2) [254].

1.5.2 Nrf2-Keap1 signaling: Nexus of metabolic pathways

Up to now more than 200 target genes of Nrf2 are known [207, 209]. These target genes are involved in gene transcription, detoxification, cytoprotection, lipid metabolism, glutathione synthesis and ROS homeostasis [207, 209, 255–257]. At present, it appears that proteasomal degradation of Nrf2 and transcription factor half-life are dependent on the redox state of the cell and mediated by the redox sensor Keap1 [258].

NADPH regeneration

The important metabolite and cofactor nicotinamide adenine dinucleotide phosphate (NADPH) is used for reductive biosynthesis (e.g. fatty acids, aromatic amino acids) and contributes to the maintenance of the cellular redox state. Notably, NADPH is used to recycle GSH and thus replenishes the cellular GSH pool via glutathione reductase (glutathione reductase) (Figure 1.12). Nrf2 regulates the expression of various NADPH generating enzymes including glucose-6-phosphate dehydrogenase (G6PD), phosphogluconate dehydrogenase (PGD), isocitrate dehydrogenase 1 (IDH1) and malic enzyme 1 (ME1) [255, 259–262] (Figure 1.17). The regulation of the NADPH links Nrf2 to cancer cell metabolism and increased cell proliferation [263, 264].

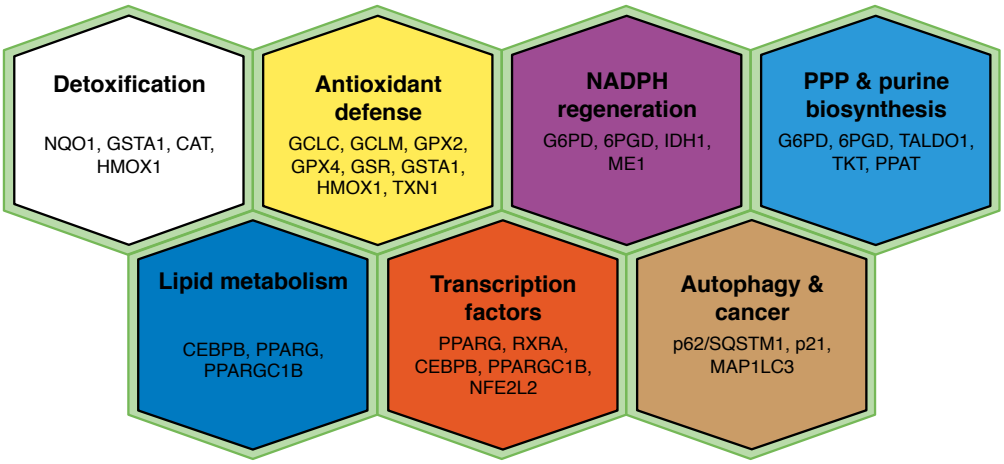

Figure 1.16: Nrf2 target genes. Nrf2 is the nexus of various metabolic pathways thus inducing the expression of a plethora of genes [205, 256, 257, 265, 266]. Phosphogluconate dehydrogenase (6PGD), catalase (CAT), CCAAT/enhancer-binding protein beta (CEBPB), glucose-6-phosphate dehydrogenase (G6PD), glutamate-cysteine ligase (catalytic subunit, GCLC), glutamate-cysteine ligase (modifier subunit, GCLM), glutathione peroxidase 2 (GPX2), GPX4, glutathione reductase (GSR), glutathione *S*-transferase alpha 1 (GSTA1), heme oxygenase 1 (HMOX1), isocitrate dehydrogenase 1 (IDH1), microtubule-associated protein 1 light chain 3 (MAP1LC3), malic enzyme 1 (ME1), NFE2L2 (Nrf2), NAD(P)H dehydrogenase (quinone 1) (NQO1), CDK inhibitor 1A (p21), sequestosome-1 (p62), PPAR gamma (PPARG), PPARγ coactivator 1-beta (PPARGC1B), phosphoribosyl pyrophosphate amidotransferase (PPAT), retinoid X receptor alpha (RXRA), transaldolase 1 (TALDO1), transketolase (TKT), thioredoxin 1 (TXN1).

Transcription factors

Nrf2 binds to the PPARγ promotor and stimulates its transcription [267]. Furthermore, PPARγ and Nrf2 are linked via a mutual feedback loop [268]. As direct interaction between the two transcription factors is possible as well, the inter-regulatory mechanisms appear to be more complex and require further investigation. Moreover, interaction of Nrf2 with retinoid X receptor alpha (RXRα) and PPARγ coactivator 1-beta (PGC1-β) [257] as well as CCAAT/enhancer-binding protein beta (C/EBPβ) [269] has been reported in mice.

Pentose phosphate pathway and purine synthesis

Recently, Mitsuishi et al. showed that Nrf2 can promote a metabolic switch by re-routing glucose and glutamine into pentose phosphate pathway (PPP) [261]. The two key functionalities of the PPP are i) to generate ribose 5-phosphate (R5P) for nucleotide synthesis and ii) to provide NADPH as reduction equivalent [261].

Oxidative arm. The oxidative PPP is irreversible and solely responsible for the NADPH generation. Glucose 6-phosphate (G6P) marks the start of the PPP and contemporaneously the conjunction to glycolysis (Figure 1.17). In a highly regulated, irreversible and rate-limiting step, G6PD catalyses the regeneration of NADPH [270, 271]. More than 400 million people suffer from a G6PD deficiency. Notably, this deficiency has major implications for DNA repair, lipogenesis and antioxidant defenses [271]. Recently, a link to DNA repair and oxidative defense was established, as SIRT2 was identified as a post-translational regulator of G6PD [271, 272]. In addition to G6PD, Nrf2 regulates the expression of phosphogluconate dehydrogenase (PGD), another $NADP^+$-dependent enzyme of the oxidative arm (Figure 1.17).

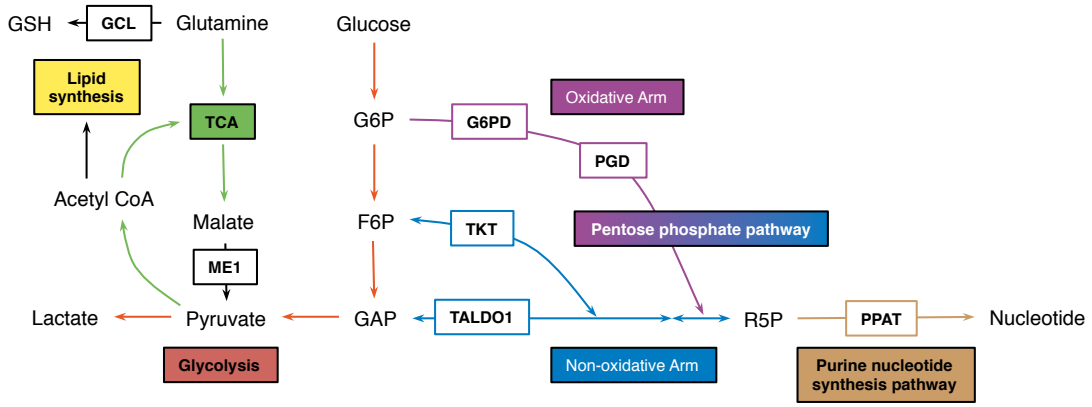

Figure 1.17: Nrf2 is at the nexus of cellular metabolism. The enzymes regulated by Nrf2 are indicated with white, framed boxes and corresponding metabolic pathways are marked with colored double-framed boxes. Fructose 6-phosphate (F6P), glucose 6-phosphate (G6P), glucose-6-phosphate dehydrogenase (G6PD), glyceraldehyde 3-phosphate (GAP), glutamate-cysteine ligase (GCL), glutathione (GSH), malic enzyme 1 (ME1), phosphogluconate dehydrogenase (PGD), phosphoribosyl pyrophosphate amidotransferase (PPAT), ribose 5-phosphate (R5P), transaldolase 1 (TALDO1), tricarboxylic acid (TCA), transketolase (TKT). Adapted from [263].

Non-oxidative arm. The requirement for NADPH drives the non-oxidative PPP, whilst the balance between NADPH and ribose 5-phosphate (R5P) determines its direction [273]. Pentose phosphates generated in the oxidative arm can be converted back to glycolytic intermediates, when NADPH is required. In contrast, both the oxidative and the non-oxidative arm can concur to R5P and nucleotide synthesis [274] (Figure 1.17). Nrf2 controls two enzymes of the non-oxidative arm: transketolase (TKT) and transaldolase 1 (TALDO1). The latter is a key enzyme of the non-oxidative arm and contributing R5P for

nucleotide synthesis as well as NADPH. Transketolase is a thiamine-dependent enzyme establishing a link between the PPP and glycolysis (Figure 1.17).

Glutamine and pyruvate metabolism. The expression of glutamate-cysteine ligase (GCL) with its catalytic (GCLC) and modifier subunit (GCLM) is driven by Nrf2 [141], thus redirecting glutamine towards GSH synthesis. The intracellular GSH level is maintained via Nrf2-dependent regulation of GPX2, GPX4 (both generating GSSG, Figure 1.12) and glutathione reductase (GSR) (regenerating GSH, Figure 1.12). Additionally, Nrf2 facilitates the decarboxylation of malate via malic enzyme 1 (ME1). Subsequently, pyruvate is introduced to TCA cycle [261] (Figure 1.17).

Purine nucleotide synthesis. Ribose 5-phosphate (R5P) generated by the PPP is the starting point for the synthesis of nucleotides, with phosphoribosyl pyrophosphate amidotransferase (PPAT) catalyzing the rate-limiting step of the *de-novo* synthesis of purines. In addition, PPAT is regulated by Nrf2 [261] (Figure 1.17).

1.5.2.1 Repair, death, and cancer

Increased levels of Nrf2 have been found in cancer tissues [275]. Consequently, Nrf2 might actually contribute to an increased cancer cell metabolism and proliferation [263, 264].

Senescence. The term senescence describes an arrest in G_1 phase of the cells cycle in deliberately proliferating cells [6, 276]. In general, senescent cells exhibit a flattened and enlarged morphology [277]. Among many factors, telomere shortening, DNA damage and oxidative stress can cause senescence [276]. Moreover, the accumulation of damaged material within a cell might result in a diminished proliferative capacity [277]. Senescence biomarker include CDK inhibitor 2A (CDKN2A), galactosidase β 1 (GLB1) [278], insulin-like growth factor-binding protein 3 (IGFBP3) [279], regucalcin (RGN) [280] and β-catenin β (CTNNB1) [281].

Autophagy. The term autophagy describes the regulated disassembly of unnecessary or dysfunctional cellular components and their subsequent recycling. There are three main types of autophagy: i) macroautophagy (often referred to as autophagy) involving the

formation of a double-membrane autophagosome; ii) microautophagy involving recycling via lysosomes and iii) chaperone-mediated autophagy [282]. Various signaling pathways induce autophagy, including amino acid signaling (via leucine and glutamine), glucose signaling (via 5′AMP-activated protein kinase (AMPK)), oxidative stress [283, 284], oxidative damage and redox signaling [285] via reactive cysteine residues acting as "molecular switches" (for a detailed review see [282]).

In general, ubiquitinylated proteins are recognized by sequestosome-1 (p62) und subsequently subjected to proteasomal or lysosomal (autophagic) degradation. Using its microtubule-associated protein 1 light chain 3 (LC3) interacting region, p62 bridges autophagy-targeted components to autophagosomes bearing LC3 on their surface [282]. Notably, p62 is regulated by Nrf2 [286, 287]; p62 binds to Keap1 [288], thus subjecting Keap1 to degradation via autophagy and enabling translocation of Nrf2 [289, 290]. Once the DNA has been damaged by ROS, repair mechanisms such as DNA damage repair (DDR) are activated. Interestingly, Poly(ADP-ribose) polymerase (PARP) establishes the link between autophagy and DDR, thus connecting it with NAD^+ and ATP metabolism as well as AMPK signaling [291–293]. On this basis, it seems likely that oxidative stress response and autophagy work hand in hand to reduce ROS levels and inhibit damage to biomolecules and cellular components (recently reviewed in [294]).

Apoptosis. While autophagy is more or less a "self-eating" mechanism, apoptosis describes a programmed cell death and thus a "self-killing" mechanism. Apoptosis involves the activation of proteases, which rapidly degrade cellular structures within the intact plasma membrane. Hallmarks of apoptosis include condensation of chromatin, nuclear fragmentation, cellular shrinkage and plasma membrane blebbing [295]. Initiation of apoptosis can be either intrinsic via mitochondria or extrinsic via activation of death receptor signaling. At the mitochondrial side, apoptosis is tightly regulated by proteins of the B-cell lymphoma 2 (BCL2) family. The three groups are i) multidomain members with anti-apoptotic functionalities (BCL2), ii) multidomain members with pro-apoptotic functionalities (BAX, BAK1) and iii) further pro-apoptotic proteins (e.g. BCL2-associated death promoter (BAD)) [277].

Cancer. The ability to directly influence the expression of genes involved in detoxification and oxidative defense makes Nrf2 a promising target for cancer prevention.

However, this ability has been proven to be a double-edged sword, as cancer cells facilitate this Nrf2 "protective mechanism" to fasten their growth and promote a drug and/or radiation resistance [296]. Indeed, increased Nrf2 levels are a frequent feature of human cancers [275, 297–300]. Mechanisms how cancer cells increase Nrf2 activity include somatic mutations in Keap1 or Nrf2, DNA hypermethylation at the Keap1 promotor, accumulation of inhibitors of Keap1-Nrf2 interaction and the modification of Keap1 itself [263].

1.5.3 Protection of the skin

The skin is frequently challenged with ultraviolet (UV) light, mechanical insults, irritants, allergens, and pathogens. Thus a robust mechanism for reactive oxygen species (ROS) detoxification is vital. Nrf2 is expressed in all cell types of the skin. Notably, in the murine epidermis an expression gradient of Nrf2 has been observed. Remarkably, highest Nrf2 levels were found in the differentiated, suprabasal keratinocytes [301, 302] (Figure 1.18). Accordingly, basal keratinocytes tend to undergo apoptosis in response to UVB irradiation to maintain skin integrity and to dispose damaged or even mutated stem cells [301]. Interestingly, Nrf2 is suggested to promote keratinocyte differentiation [302].

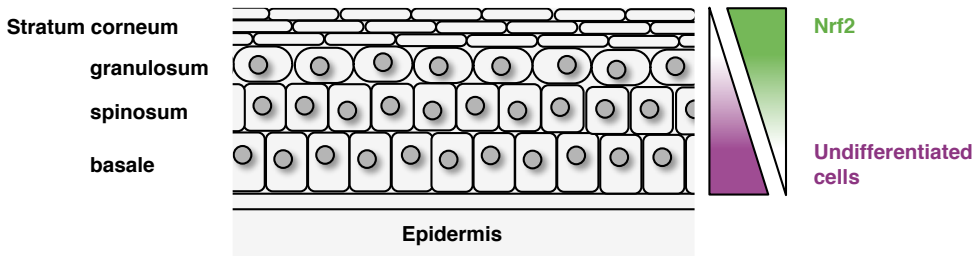

Figure 1.18: Epidermal distribution of Nrf2 expression. The expression of Nrf2 correlates with the differentiation of keratinocytes. The suprabasal keratinocytes are superiorly protected against reactive oxygen species (ROS) damage compared to basal cells. Adapted from [303].

Owing to their Nrf2-activating properties, several natural extracts have been tested for protection against UV light. Topical application of sulforaphane (SFN, Figure 1.15a) protected mice skin against UVB-induced damage and inflammation [145]. Similar protective effects were confirmed for human skin [148]. Although these results seem promising, the concern remains that long-term activation of Nrf2 might promote tu-

morgenesis. Various tumors were shown to highjack Nrf2 signaling for metabolic reprogramming, promotion of anabolic pathways and increased proliferation [261].

1.6 Redox state and redox environment

Redox processes are the fundament of almost every biological process. The cellular redox environment is a crucial parameter for biochemical pathways, networks, and organism health. The homeostasis of ROS, oxidants and antioxidants is substantial for the functioning of cells and tissues. To understand the complex dynamics of intra- and intercellular signaling mechanisms, a global and systemic approach is needed. Consequently, knowledge of the redoxome, meaning quantification of redox active compounds and information on redox enzymes and proteins is essential to generate valid models of biochemical pathways and networks [304–306].

To survive, cells and tissues sustain a reductive environment to ensure an electrochemical gradient essential for electron flow. In 1958, Bücher and Klingenberg were the first to estimate the reduction potentials of NADH/NAD^+ and NADPH/$NADP^+$ [307].

It is important to clearly discriminate redox state and environment [304]. The redox state considers only one specific redox couple (Figure 1.19a and Equation (1.8)). Moreover, it is defined by the reduction potential ($E^{\circ'}$) of one redox couple and characterized by the concentration of the reduced species. For the majority of redox couples, the ratio of oxidized to reduced form is sufficient to calculate the redox state. However, knowledge of absolute concentrations is mandatory for some redox couples including GSH/GSSG (see Equations (3.1) and (3.2)).

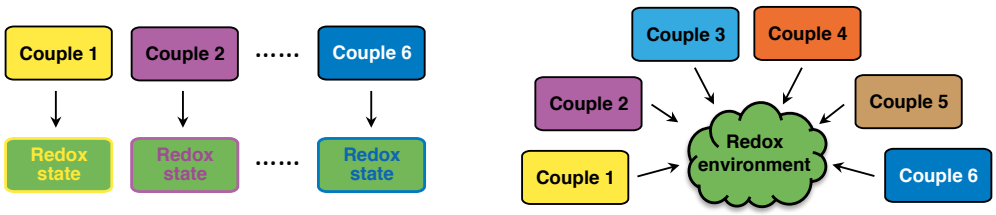

(a) Redox State **(b) Redox environment**

Figure 1.19: Redox state and redox environment. The redox state (a) considers only one specific redox couple. In contrast, the redox environment considers a set of linked redox couples (b). [304].

The redox environment (Figure 1.19b and Equation (1.9)) takes into account a set of redox couples, thus enabling a more global evaluation of the cellular redox state. Using the Gibbs energy change (ΔG, Equations (1.1) and (1.2)) the voltage of an electrochemical cell (ΔE) can be calculated according to the Nernst equation (Equation (1.3)).

$$\Delta G^{\circ} = -nF\Delta E^{\circ} \tag{1.1}$$

$$\Delta G = \Delta G^{\circ} + RT * \ln \mathrm{Q} \tag{1.2}$$

$$\Delta E = \Delta E^{\circ} - \frac{RT}{nF} * \ln \mathrm{Q} \tag{1.3}$$

with
- ΔG: Gibbs energy change
- $^{\circ}$: Standard conditions (1 M solution, $T = 298\ K$ (25°C), pH = 0)
- n: Number of exchanged electrons
- F: Faraday constant ($9.6485 * 10^4\ C\ mol^{-1}$)
- ΔE: Standard reduction potential
- R: Gas constant ($8.314\ J\ K^{-1}\ mol^{-1}$)
- T: Temperature (Kelvin)
- Q: Mass action expression

Interestingly, a physiological (cellular) system is per se not in equilibrium and often on purpose maintains a non-equilibrium steady state for structural and functional reasons. Nevertheless, the Nernst equation (Equation (1.3)) can be applied as the concentrations of the redox couples are constant at least over short periods of time [304]. Additionally, the Nernst equation (Equation (1.3)) can be adapted to fit experimental parameters in cell culture, e.g. temperature (Equation (1.4)) and pH value (Equation (1.7)).

$$\Delta E = \Delta E^{\circ} - \frac{61.5\ \mathrm{mV}}{n} * \log \mathrm{Q} \tag{1.4}$$

with
- T: Temperature ($310\ K = 37$°C)
- ln to log: Conversion factor 2.303

It is important to consider shifts in pH, as these either result in changes in redox couple concentrations or are immediately counterbalanced by certain redox couples such as

lactate/pyruvate. The half-cell reduction potential (E_{hc}, see Equation (1.5)) at a certain pH ($E_{hc,\mathrm{pH}}$) can be calculated by adjusting the standard reduction potential at pH 7 ($E^{\circ'}$, see Table 1.1) to the pH of interest (Equations (1.5) to (1.7)). Notably, $\frac{\Delta E}{\Delta \mathrm{pH}}$ depends on the number of electrons and protons involved [304].

$$E_{hc} = E^{\circ} - \frac{61.5\ \mathrm{mV}}{n} * \log \mathrm{Q} \tag{1.5}$$

$$E^{\circ}_{\mathrm{pH}} = E^{\circ'} + \left[(\mathrm{pH} - 7.0) * \frac{\Delta E}{\Delta \mathrm{pH}} \right] \tag{1.6}$$

$$E_{hc,\mathrm{pH}} = E^{\circ'} + \left[(\mathrm{pH} - 7.0) * \frac{\Delta E}{\Delta \mathrm{pH}} \right] - \frac{61.5\ \mathrm{mV}}{n} * \log \mathrm{Q} \tag{1.7}$$

with
- E_{hc}: Half-cell reduction potential at pH 7
- $'$: Experimental conditions at pH 7
- E°_{pH}: pH adjusted standard reduction potential ($E^{\circ'}$)
- $\frac{\Delta E}{\Delta \mathrm{pH}}$: Change in E, if pH is increased by 1 unit
- $E_{hc,\mathrm{pH}}$: pH adjusted half-cell reduction potential

In a biological context, most redox reactions are $2e^{-}$-processes in order to avoid the generation of reactive intermediates. Nevertheless, some redox reactions (e.g. of $O_2^{\bullet -}$) are $1e^{-}$-processes. Independently of the number of electrons involved, there is a thermodynamic hierarchy or "pecking order" (Table 1.1) for redox reactions [176, 308].

Table 1.1: Standard reduction potentials at pH 7 and 37°C, with *n* being the number of electrons transferred. Adapted from [176, 305, 308].

Oxidant	Reductant	n	$E^{\circ'}$ in mV
O_2	$O_2^{\bullet-}$	1	−330
NAD^+, H^+	NADH	2	−316
$NADP^+$, H^+	NADPH	2	−315
GSSG, $2H^+$	2GSH (Glutathione)	2	−240
TXN-SS, $2H^+$	TXN(SH_2) (Thioredoxin)	2	−240
Cys-S-S-Cys, $2H^+$	2Cys-SH (Cystiene)	2	−230
FAD, $2H^+$	$FADH_2$	2	−219
Acetaldehyde, $2H^+$	Ethanol	2	−195
Pyruvate, $2H^+$	Lactate	2	−183
Fe^{+3}	Fe^{+2}	1	770
O_2, $2H^+$	H_2O_2	2	300
H_2O_2, H^+	H_2O, $HO^\bullet$	1	320
T-$O^\bullet$, H^+	TOH (Trolox)	1	480
H_2O_2, $2H^+$	$2H_2O$	2	1320

Redox state

The redox state (Figure 1.19a and Equation (1.8)) is defined by the reduction potential ($E^{\circ'}$) of one redox couple and characterized by the concentration of the reduced species.

$$\text{Redox state} = E^{\circ'} + \left[(\text{pH} - 7.0) * \frac{\Delta E}{\Delta \text{pH}}\right] - \frac{61.5\ \text{mV}}{n} * \log \frac{[\text{Reduced species}]}{[\text{Oxidized species}]} \quad (1.8)$$

with [Reduced species]: Concentration of the reduced species of redox couple
[Oxidized species]: Concentration of the oxidized species of redox couple

Redox environment

Although the redox environment (Figure 1.19b and Equation (1.9)) considers a set of redox couples, in practice it is impossible to quantify the entirety of redox couples of a biological system. Hence, an indicator couple can be used to estimate changes in the redox environment. The glutathione couple (GSH/GSSG) provides by far the largest pool of reducing equivalents and is considered to be the major cellular redox buffer. Consequently, the glutathione couple is a suitable indicator for the cellular redox environment [304, 309].

$$\text{Redox environment} = \sum_{i=1}^{n(\text{Couple})} E_i * [\text{Reduced species}]_i \tag{1.9}$$

with E_i: Half-cell reduction potential of redox pair i
$[\text{Reduced species}]_i$: Concentration of the reduced species of redox pair i

The cellular redox environment influences cell cycle, signal transduction, synthesis of DNA, RNA and protein and enzyme activation [152, 304, 310, 311]. Moreover, many transcription factors are regulated by the cellular reduction potential including p53, NFκB and Nrf2 [310]. Consequently, cellular life is driven by the reduction potential of diverse redox couples. Schafer et al. (2001) suggested thiols and disulfides as nano-switches responsible for the movement through cellular stages (Figure 1.20) and proposed GSH as master regulator [304].

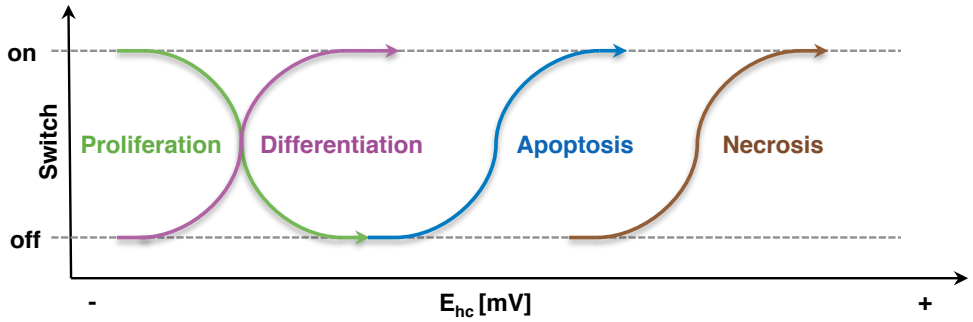

Figure 1.20: Changes in reduction potential drive the cellular life cycle. Under normal conditions, the half-cell reduction potential (E_{hc}) is highly negative and cells proliferate normally. With increasing E_{hc} (becomes more positive) fewer cells proliferate and start differentiating instead. If the reduction potential increases even further, death signaling pathways are activated and cells undergo apoptosis or even necrosis. Adapted from [304].

The metabolic activity of proliferating cells is different from that of quiescent cells. The latter invest most of their energy in maintaining functional and morphological integrity for protection against putative insults such as oxidative stress. In contrast, proliferating cell direct nutrients into anabolic pathways to promote proliferation. Consequently, a quiescent cell can be pushed into proliferation when its metabolic activities are shifted [261]. Under physiological conditions, cells proliferate normally and switches

for differentiation, apoptosis and necrosis are off (Figure 1.20 in green). A shift of the half-cell reduction potential (E_{hc}) towards a more positive value inflicts thiol groups of proteins and enzymes resulting in the initiation of differentiation. When E_{hc} becomes even more positive, the number of differentiating cells increases further, while fewer cells proliferate until the proliferation switch is completely turned off (Figure 1.20 in purple). If the reduction potential increases further, death switches are activated pushing cells into apoptosis and necrosis (Figure 1.20 in blue and brown). Consequently, proliferating cells can be pushed directly into necrosis if the oxidative stimulus is only high enough [304].

1.7 Aims of this thesis

Trans-resveratrol (RSV) has gained tremendous interest in applied, biochemical, biomedical and clinical research due to multiple reported health-beneficial effects. However, the underlying mechanism of action remained largely elusive and controversially discussed. Considering this controversy, new insights connecting the available pieces are required. Despite the promising effects observed *in vitro*, RSV failed to endorse these abilities *in vivo*.

The objective of this work is to identify the mechanism of action of RSV. Firstly, we hypothesize that RSV is unstable under physiologically relevant conditions. Thus, we determined the stability of the compound under different biochemical conditions.

Secondly, we propose that the decay of RSV results in the generation of various reactive oxygen species (ROS). Consequently, we investigated the RSV-dependent generation of ROS in a cell-free and intracellular context. On the basis of these hypotheses, a topological application of RSV seems to be a relevant approach, as already a number of dermatological products based on RSV are available. Thus, this study is focused on the potential protection of the human epidermis and primary human keratinocytes were used. Notably, these cells are frequently used for physiological testing in dermatological research as keratinocytes form the outer layer of the skin. Hence, these cells are a prime target for RSV-based lotions and emollients.

Thirdly, we anticipate that RSV-driven generation of ROS induces a mild oxidative stress resulting in a hormetic, bi-phasic dose-response relationship. Hence, “low” concentrations would result in beneficial and high concentrations in adverse effects.

Fourthly, assuming a rather broad mechanism of action and the induction of mild

oxidative stress, we propose that RSV influences the intracellular concentration of key redox biomolecules subsequently shifting the redox state of redox couples. Therefore, we determine central metabolic parameters and the intracellular concentrations of diverse metabolites. Interconvertible metabolites form redox couples, which are utilized to calculate the metabolite-specific redox state.

For a more global assessment of the cellular redox status, we calculate the redox environment of the system. Supposedly, a shift of the redox environment to a more reduced value would render the cells more robust against oxidative challenges. In contrast, a more oxidized redox environment would contribute to an increased susceptibility against oxidative challenges. The final aim is to provide a conceptually comprehensive mechanistic understanding to evaluate a potential preventive or therapeutic application of RSV.

2 Methods and Materials

Contents

2.1 Compounds and natural products

Compounds were purchased from the following sources: *Trans*-resveratrol (RSV), 4-hydroxynonenal (HNE), (Cayman Chemicals, Biomol, Hamburg, Germany), glutathione (GSH, GSSG) and N-acetyl-cysteine (NAC) (all Sigma-Aldrich, Taufkirchen, Germany).

2.2 Decay of resveratrol

The time-dependent decay of RSV in diverse solvents was analyzed with the POLARstar Omega (BMG LABTECH, Ortenberg, Germany) at 37°C. Samples (100 μl/well) were transferred into an UV-Star 96-well plate (# 655801, Greiner Bio-one, Frickenhausen, Germany) for kinetic and spectral measurement (between 220 and 720 nm, $\Delta\lambda$ 2 nm). Data was smoothed using GraphPad Prism 5.0 with four neighbors to average and 2nd order of smoothing polynomial.

pH-dependent oxidation of RSV

The time-dependent oxidation of 50 μM RSV in ddH_2O with or without 44 mM sodium bicarbonate ($NaHCO_3$, Merck GmbH, Darmstadt, Germany) was analyzed using the POLARstar Omega (BMG LABTECH) at 37°C. Samples were transferred (150 μl/well) into an UV-Star 96-well plate (# 655801, Greiner Bio-one) for kinetic and spectral measurement (between 230 and 550 nm, $\Delta\lambda$ 2 nm). The pH was adjusted from 1 to 12 using HCl and NaOH (both Merck). Putative oxidation products of RSV [40], a hydroxyl radical adduct (characteristic absorbance maximum at 420 nm) and a relatively stable 4′-phenoxyl radical adduct (characteristic absorbance maximum at 390 nm), were monitored.

For data analyses, signals were normalized to the zero value and the vehicle control. Data were fitted (dashed line) using GraphPad Prism 5.0 according to a second order polynomial (pH 3 and 5; absorbance at 420 nm all pH values) or Equation (2.1) with a Hill slope set to -1 (pH 7 and 8 except absorbance at 420 nm). The fitting model was chosen to gain maximal correlation.

$$Y = \text{Bottom} + \frac{\text{Top} - \text{Bottom}}{1 + 10^{(X - \log \text{IC}_{50})}} \tag{2.1}$$

Time- and pH-dependent oxidation of RSV were visualized as surface-contour plots using Matplotlib (Figure S4) [312].

Oxygen partial pressure-dependent oxidation of RSV

96-well plates prepared for the determination of the pH-dependent oxidation of RSV (see Section 2.2) were incubated at atmospheric oxygen levels (21% O_2), slightly reduced oxygen partial pressure (10% O_2) mimicking conditions in the blood vessels, or highly reduced oxygen levels (1% O_2) resembling tissue or tumor micro-environment. For experiments with reduced oxygen partial pressure, plates were incubated at 37°C at corresponding oxygen levels using a CO_2 Incubator Model CB 60 (Binder, Tuttlingen, Germany). For spectral measurements, plates were quickly analyzed ($<$ 2 minutes) using the POLARstar Omega (BMG LABTECH) at 37°C. Afterwards, the plates were further incubated at indicated conditions.

Putative oxidation products of RSV [40] were monitored. For data analyses signals were normalized to the zero value and the vehicle control. Data were fitted (dashed line) using GraphPad Prism 5.0 with Hill slope set to -1 according to Equation (2.1).

2.3 Cell culture

NHEK cells

Neonatal normal human epidermal keratinocyte (NHEK) cells (# CC-2503, Lonza, Basel, Swiss) were isolated from a black, newborn male and maintained in keratinocyte growth medium (KGM) containing keratinocyte basal medium (KBM) (# CC-3101, Lonza) supplemented with KGM SingleQuot Kit Suppl. & Growth Factors (# CC-4131, Lonza). Cells in passage 1 (P1) were used.

NHDF cells

Neonatal normal human dermal fibroblast (NHDF) cells (# CC-2509, Lonza) were isolated from a caucasian, newborn male and were maintained in Dulbecco′s modified

Eagle′s medium (DMEM) (# 31966, Gibco, Thermo Fisher Scientific, Karlsruhe, Germany) supplemented with 10% fetal bovine serum (FBS) (Biochrom, Berlin, Germany). NHDFs from passages 2-5 (P2-P5) were used.

HaCaT cells

Human adult low calcium high temperature keratinocyte (HaCaT) cells were kindly provided by Unilever (Sharnbrook, UK) and were cultured in the following growth medium: DMEM (# 21068-028, Gibco, Thermo Fisher Scientific), 1% FBS (Biochrom), 2 mM L-glutamine (Biochrom), 1 mM sodium pyruvate (# 11360-039, Thermo Fisher Scientific), 70 μM calcium chloride ($CaCl_2$, Merck), 100 U/ml penicillin (Biochrom) 100 μg/ml streptomycin RSV. Cells from passage 47 (P47) were treated for 16 hours with either 50 μM or 100 μM RSV or dimethyl sulfoxide (DMSO), respectively.

ARE clone 7 HaCaT cells were kindly provided by Unilever (Sharnbrook, UK) and were revived in DMEM (# 31966, Gibco, Thermo Fisher Scientific) supplemented with 10% FBS (Biochrom). The following day, the medium was changed to ARE clone 7 HaCaT selective medium (DMEM, 10% FBS (Biochrom), 400 μg/ml Hygromicin B (# 10687-010, Thermo Fisher Scientific). Cells from passage 7 (P7) were treated for 16 hours with either 50 μM or 100 μM RSV or DMSO, respectively.

HepG2 cells

Human liver carcinoma (HepG2) cells (ATCC, LGC Standards GmbH, Wesel, Germany) were cultured in DMEM (# 31966, Gibco, Thermo Fisher Scientific) supplemented with 10% FBS (Biochrom), 100 U/ml penicillin (Biochrom) and 100 μg/ml streptomycin (Biochrom). HepG2 cells from passage 9 (P9) were seeded into 12-well plates (# 3513, Corning, Thermo Fisher Scientific, Schwerte, Germany) and treated for 16 hours with either 50 μM or 100 μM RSV or DMSO, respectively.

HEK293 cells

Human embryonic kidney (HEK293T) cells (ATCC, LGC Standards GmbH) were cultured in DMEM (# 31966, Gibco, Thermo Fisher Scientific) supplemented with 10% FBS (Biochrom), 100 U/ml penicillin (Biochrom) and 100 μg/ml streptomycin

(Biochrom). HEK293T cells from passage 23 (P23) were seeded into 12-well plates (Corning, Thermo Fisher Scientific) and treated for 16 hours with either 50 μM or 100 μM RSV or DMSO, respectively.

HeLa cells

Human cervical cancer (HeLa) cells (ATCC, LGC Standards GmbH) were cultured in DMEM (# 31966, Gibco, Thermo Fisher Scientific) supplemented with 10% FBS (Biochrom), 100 U/ml penicillin (Biochrom) and 100 μg/ml streptomycin (Biochrom). Cells were seeded into 12-well plates (Corning, Thermo Fisher Scientific) and treated for 16 hours with either 50 μM or 100 μM RSV or DMSO, respectively.

HT-29 cells

Human colon cancer (HT-29) cells (# ACC-299, DSMZ, Braunschweig, Germany) were cultured in DMEM Nutrient Mixture F-12 (DMEM/F-12) (# 11330-057, Gibco, Thermo Fisher Scientific) supplemented with 5% FBS (Biochrom), 100 U/ml penicillin (Biochrom) and 100 μg/ml streptomycin (Biochrom). HT-29 cells from passage 27 (P27) were seeded into 12-well plates (Corning, Thermo Fisher Scientific) and treated for 16 hours with either 50 μM or 100 μM RSV or DMSO, respectively.

THP-1 cells

Human monocytic (THP-1) cells (# ACC-16, DSMZ) were cultivated in Roswell Park Memorial Institute medium (RPMI) (Biochrom) supplemented with 10% FBS (Biochrom) and 100 μg/ml streptomycin (Biochrom). Cells were seeded into 12-well plates (Corning, Thermo Fisher Scientific) and treated for 16 hours with either 50 μM or 100 μM RSV or DMSO, respectively.

All cell lines were maintained at 37°C in a humidified 5% CO_2 atmosphere and treated after reaching 60% confluence.

2.4 Hematoxylin and eosin staining

NHEK cells were seeded into 12-well plates (# 83.3922 Sarstedt, Nürnbrecht, Germany) and treated with RSV and DMSO for 16 hours at 37°C. Cells were washed twice with phosphate buffered saline (PBS) and fixed with 4% formaldehyde (both Sigma-Aldrich) for 5 minutes at room temperature. Afterwards, cells were washed twice with PBS and once with water prior to staining with Mayer′s Hematoxylin Solution (# MHS32, Sigma-Aldrich) staining for 1 to 2 minutes. All wells were rinsed in tap water for 1 minute and afterwards stained with Eosin Y solution (# HT110232, Sigma-Aldrich) for 10 to 30 seconds. Finally, an ethanol series containing 70%, 96% and 100% ethanol was performed before wells were air-dried.

2.5 Knockdown of Nrf2 and SIRT1

Knockdown of Nrf2 or SIRT1 with small interfering RNAs was done in NHEK cells seeded into 6-well plates (Corning). Cells were transfected with 30nM Silencer Pre-designed siRNA Nrf2 (# 16708), Silencer Pre-designed siRNA SIRT1 (# 136457) or Silencer Select negative control siRNA (# 4390844, all Ambion, Thermo Fisher Scientific) using Lipofectamine 2000 transfection reagent (# 11668019, Life Technologies, Thermo Fisher Scientific). Transfection was carried out in 1ml for 48 hours in KGM, whereby 0.5ml KGM were added after 24 hours. The medium was then renewed and cells were treated with 50 μM RSV or DMSO for 16 hours prior to harvest of RNA and protein. Data were analyzed using GraphPad Prism 5.0.

2.6 RNA purification, cDNA synthesis, and qPCR

RNeasy Plus Mini Kit (QIAGEN, Hilden, Germany) was used to isolate total RNA according to the manufacturer′s instructions. For cell lysis 10 μl/ml β-mercaptoethanol (Sigma-Aldrich) were added to RLT buffer (QIAGEN). Genomic DNA was digested on a column using the RNase-free DNase set (# 79254, QIAGEN). The concentration of extracted RNA was measured using the Nanodrop ND-2000 Spectrophotometer (Thermo Fisher Scientific).

RNA was reversely transcribed into cDNA applying the High Capacity cDNA Reverse Transcription Kit (# 4368814, Thermo Fisher Scientific) with random primers. Quantitative polymerase chain reaction (PCR) (qPCR) was carried out on the 7900 HT Fast Real-Time PCR System (Applied Biosystems, Thermo Fisher Scientific) using the Power SYBR Green PCR Master Mix (# 4367659, Thermo Fisher Scientific) to investigate the effects on target gene expression. After an initial denaturation (at 95°C) for 10 minutes, the cDNA was amplified by 40 cycles of PCR (95°C, 15 seconds; 60°C, 60 seconds).

Primers used for qPCR are summarized in Table 2.1. The relative gene expression levels were normalized using β-Actin gene (ACTB) and quantified by the $2^{-\Delta\Delta Ct}$ method [313]. Primers were designed with the Primer3 software [314] following specificity check with NCBI BLAST search [315]. All real-time PCR primer were purchased from Sigma-Aldrich.

Table 2.1: Primers and their sequences used in qPCR.

Symbol	Forward primer	Reverse primer
ACLY	TGCCATGCCACAAGATTCAGTCCC	ACAATGGCCTTGGTGTGGCGG
ACTB	CAGCCATGTACGTTGCTATCCAGG	AGGTCCAGACGCAGGATGGCATG
BAD	TCCTTTAAGAAGGGACTTCCTCG	CAAGTTCCGATCCCACCAGG
BAK1	TGATTCAGCCAAATGCAGGG	GGTGAGGGGATTGCACAGTTT
BAX	CTTCTGGAGCAGGTCACAGT	GCAGGGTAGATGAATCGGGG
BCL2	GCGGCCTCTGTTTGATTTCTC	GTTGACTTCACTTGTGGCCC
BIRC5	TGAGAACGAGCCAGACTTGG	TGTTCCTCTATGGGGTCGTCA
CAT	GCTTCAGGGCCGCCTTTTTGC	AGTTGGCCACTCGAGCACGG
CDKN2A	GTGGACCTGGCTGAGGAG	CTTTCAATCGGGGATGTCTG
CTNNB1	ACGGAGGAAGGTCTGAGGAG	TCAAATACCCTCAGGGGAACAG
CXCL8	CTGATTTCTGCAGCTCTGTG	GGGTGGAAAGGTTTGGAGTATG
DAPK1	GCAGCAGTTTGTGTACGACG	ATGTTGATCTCGCCTGTGCT
DIABLO	CCACGCGGAGGTTGTAATTG	GTGTATTCTGCGATCTCGGC
FOXO3	CTACGAGTGGATGGTGCGTT	TGTGCCGGATGGAGTTCTTC
G6PD	GCCTCTTCTACCTGGCCTTG	GATGCGGTTCCAGCCTATCT
GCLC	GAGGTCAAACCCAACCCAGT	TGTTAAGGTACTGAAGCGAGGG
GLB1	CCGTGGGTCCTTAGTCAAGT	CAACAGAGGGAGGATGCGAA
GPX1	TGTTGCTCGTAGCTGCTGAA	TGAGTCACCGGGATTTTGCC
GPX3	CTGCTTTCCCTGCTCCTGG	ACCATGGCAGTCCATCTTCG
GSR	GAGGTGCTGAAGTTCTCCCAGGTCA	CCGGGAACTGCAGTAACCATGCTG
GSTA4	AGCTCCACTATCCCAACGGA	TTCATCAAACTCGACTCCGGC
GSTZ1	CCTGATTCGTCGAGTCTCACT	ATAGAGGATGGGCTTCCCCG
IGFBP3	CGCGCCAGGAAATGCTAGTG	AATGGAGGGGGTGGAACTTG
JUN	TTGCACTGAGTGTGGCTGAA	GACTATACTGCCGACCTGGC
KEAP1	CGACAACCAAGACCCCGCA	GATAAGCAACACCACCACCTCT
KRT14	CAGAGATGTGACCTCCTCCAG	CTCAGTTCTTGGTGCGAAGG
MAP1LC3A	CCATGTGGAAAAGCAGCTGTG	CACCCTTGTAGCGCTCGAT
MAP1LC3B	CCGCCTTTTTGGGTAGAAGT	AACTGTGATGGCAAATGCGT

Symbol	Forward primer	Reverse primer
MAPK8	AGCTCCACCACCAAAGATCC	GCTGCACCTGTGCTAAAGGA
NFE2L2	CCCAACACACGGTCCACAGCTC	AATCCATGTCCTGCTGGGACGGG
NFKBIA	CTTCGAGTGACTGACCCCAG	TCACCCCACATCACTGAACG
NQO1	GAAAGGCTGGTTTGAGCGAG	CCTTCTTACTCCGGAAGGGT
PPAT	GCTTACGCAGGAAAGTGTGG	TGGCTGAATGAAGGTTCTCCC
RGN	GCCCTGTACTCCCTCTTTCC	GTGGTCTAGCGACCAATCCA
SIRT1	TGCAACAGCATCTTGCCTG	AGGACATCGAGGAACTACCTGATT

2.7 Genome-wide gene expression analyses

Genome-wide gene expression analyses were done by ATLAS Biolabs GmbH (Berlin, Germany) using HumanHT-12 Expression BeadChips (Illumina, Eindhoven, The Netherlands). A basic expression data analysis was carried out using GenomeStudio V2011.1 (Illumina). In brief, raw data were background-subtracted and normalized (cubic spline algorithm). Processed data were filtered (detection p value ≤ 0.01) and analysis of differential expression vs. DMSO was done according to the Illumina t-test error model and corrected according to the Benjamini-Hochberg procedure (p value ≤ 0.05).

Gene set enrichment analysis (GSEA) [316] was performed using the following parameters: 1,000 gene set permutations, weighted enrichment statistic and signal-to-noise metric. Microarray data were analyzed using the curated C2 KEGG pathways gene sets (version 4.0, 186 gene sets). Gene expression data were submitted to the Gene Expression Omnibus database (GSE72119).

Gene expression profiles were further subjected to analyses using the Connectivity Map database [317] (Connectivity Map build August 2012).

2.8 Viability assay

Cell viability was analyzed using the CellTiter-Fluor Cell Viability Assay (# G6081, Promega, Mannheim, Germany) according to the manufacturer′s instructions. Notably, a fluorescent-based viability assay was used, as RSV is known to inhibit luciferase and thus causes artifacts in luminescence-based assays [318, 319]. The probe enters live cells and is cleaved by live-cell proteases to generate a fluorescent signal correlating to the number of live cells. However, loss of membrane integrity results in inactivation of the

substrate. NHEK cells were seeded in a black 96-well plate (# 353219, BD Biosciences, Heidelberg, Germany) with a density of 10,000 cells/well and a final volume of 200 μl/well. The following day, the medium was renewed and cells were then treated for 16 hours with the indicated compound concentrations and a final volume of 100 μl/well.

Fluorescence intensity was measured (410/520 nm) with the POLARstar Omega (BMG LABTECH) and transformed to the relative number of cells. Data were fitted (dashed line) according to Equation (2.2) with variable Hill slope and Bottom constrained to 0. The maximal observed induction of cell death after treatment relative to non-treated cells (set to 0%) is termed efficiency. The concentration required for a 50% inhibition is called IC_{50}. For a better comparison between different cell lines the concentration required for 70% (IC_{70}) inhibition was calculated (Equation (2.3)).

$$Y = \text{Bottom} + \frac{\text{Top} - \text{Bottom}}{1 + 10^{(\log \text{IC}_{50} - X) \cdot \text{Hill Slope}}} \tag{2.2}$$

$$\log \text{IC}_{70} = \log \text{IC}_{50} + \frac{1}{\text{Hill Slope}} * \log \frac{70}{100 - 70} \tag{2.3}$$

2.9 Measurement of reactive oxygen species

Cell-free ROS generation

The CellROX Green dye (# C10444, Thermo Fisher Scientific) was used to quantify the formation of ROS. Upon oxidation by ROS the probe exhibits green photostable fluorescence and binds to DNA. The probe is compatible with cell culture medium and requires no cellular processing, the CellROX Green dye was used for measuring ROS generation in a cell-free environment. Notably, the CellROX Green dye detects particularly $HO^{\bullet}$ and $O_2^{\bullet -}$.

The dye was diluted to 10 μM in KGM in presence of 1 μg/ml lambda DNA (Thermo Fisher Scientific). Subsequently, the compounds were added as indicated. Measurement was performed in a final volume of 150 μl/well in black 96-well plates (# 655090, Greiner Bio-One). The dye was protected against atmospheric oxygen by adding a sealing layer of 100 μl/well HS mineral oil (Luxcel Biosciences, Cork, Ireland). Fluorescence intensity (485/520 nm) was recorded for 16 hours (at 37°C) in the POLARstar Omega (BMG

LABTECH). For data analyses in GraphPad Prism 5.0 fluorescence values at time zero and background signals were subtracted.

Intracellular generation of ROS

The intracellular formation of ROS was quantified using the 5-(and-6)-chloromethyl-2′,7′-dichlorodihydrofluorescein diacetate, acetyl ester (CM-H_2DCFDA) dye (# C6827, Thermo Fisher Scientific). NHEK cells were seeded in a 96-well plate (TPP, Biochrom) with a density of 10,000 cells/well. The following day, cells were washed once with pre-warmed PBS (Sigma-Aldrich) and loaded with 50 μM dye diluted in PBS (Sigma-Aldrich). For successful incorporation and activation of CM-H_2DCFDA, cells were incubated for 30 minutes at 37°C. Afterwards, free dye was removed by washing with pre-warmed PBS (Sigma-Aldrich). KGM (100 μl/well) was added and cells were once more incubated at 37°C for 60 minutes. Compounds were added as indicated and fluorescence (485/530 nm) was measured for 16 hours (at 37°C) using the POLARstar Omega (BMG LABTECH).

For the quantification of ROS generation in RSV or DMSO pre-treated NHEKs, cells were seeded in a 96-well plate (TPP, Biochrom) with a density of 10,000 cells/well. Cells were pre-treated with 50 μM RSV or DMSO for 16 hours. Afterwards, the samples were treated as already described to measure intracellular ROS generation. Putative protection of NHEKs against oxidative stress by RSV pre-treatment was tested by adding ethanol (0.781%) or the thiol-scavenger 4-hydroxynonenal (HNE) at indicated concentrations (dissolved in 0.781% ethanol) [248]. Fluorescence (485/530 nm) was measured for 16 hours (at 37°C) of treatment with the POLARstar Omega (BMG LABTECH). Data were analyzed using GraphPad Prism 5.0 and fluorescence values at time zero were subtracted.

Superoxide generation

Superoxide ($O_2^{\bullet -}$) generation was quantified using the MitoSOX Red Mitochondrial Superoxide Indicator (# M36008, Life Technologies, Thermo Fisher Scientific). $O_2^{\bullet -}$ specifically oxidizes the dye, which subsequently exhibits a red fluorescence signal after binding to nucleic acids. In combination with lambda DNA (Life Technologies, Thermo Fisher Scientific), the dye was used for measuring the amount of $O_2^{\bullet -}$ generation in a

cell-free environment. The dye (10 μM/well) was added to 200 ng/well lambda DNA prior to addition of compounds. Measurement was performed in a final volume of 150 μl/well in a black 96-well plate (# 655090, Greiner Bio-One). To protect the dye from atmospheric oxygen, a sealing layer of 100 μl/well mineral oil (Luxcel Biosciences) was added. Fluorescence intensity (485/530 nm) was recorded at 37°C for 16 hours using the POLARstar Omega (BMG LABTECH). The fluorescence signals were background-subtracted and normalized to vehicle control before they were plotted using a second order 4 neighbors smoothing in GraphPad Prism 5.0.

Quenching the effects of RSV

NHEK cells were seeded in 150 cm^2 cell culture flasks (Corning, Thermo Fisher Scientific) and treated at 60% confluence for 16 hours with: 25 mM GSH, 25 mM NAC, DMSO, 50 μM RSV, DMSO + 25 mM GSH or 25 mM NAC, 50 μM RSV + 25 mM GSH or 25 mM NAC, respectively. Trypsinized cells (Subculture Reagent Pack, # CC-5034, Lonza) were subjected to qPCR and analyses of phosphatidylserine externalization (Accuri C6 flow cytometer, BD Biosciences). Data were analyzed using GraphPad Prism 5.0 and FlowJo 7.6 (Tree Star, Ashland, USA).

2.10 Antioxidant capacity

The total antioxidant capacity of a sample equals the sum of all endogenous and food-derived antioxidants. The Antioxidant Assay Kit (# 709001, Cayman Chemicals, Biomol) measures the ability of antioxidants to inhibit the metmyoglobin-catalyzed oxidation of 2,2′-azino-di-[3-ethylbenzthiazoline sulphonate] (ABTS) to $ABTS^{\bullet+}$ (absorbance maximum at 405 nm). The amount of antioxidant is negatively correlated to the absorbance at 405 nm in a concentration-dependent manner [320–322]. Subsequently, the capacity of the antioxidant to prevent the oxidation of ABTS was compared with that of Trolox (Figure 2.1), an analog of vitamin E (Figure 1.11b).

The assay was conducted according to the manufacturer′s instructions and miniaturized to a final volume of 60 μl/well. All samples, including Trolox standards, were mixed with metmyoglobin and chromogen (both Cayman Chemicals). The reaction was initiated by adding hydrogen peroxide (H_2O_2, Cayman Chemicals) prior to a 5 minute

incubation at room temperature on a shaker. Finally, the absorbance was determined at 405 nm using the POLARstar Omega (BMG LABTECH). Data were analyzed and fitted according to a linear regression model using GraphPad Prism 5.0.

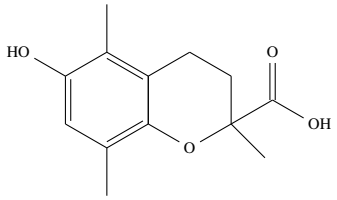

Figure 2.1: The vitamin E (Figure 1.11b) analog Trolox has potent anti-oxidative properties and is used as reference to estimate the antioxidant capacity of RSV.

2.11 Metabolic parameter measurements

For the calculation of the cellular redox state and redox environment, key metabolites were quantified.

Analyses of intracellular glucose

Intracellular glucose concentration was determined using the PicoProbe Glucose Fluorometric Assay Kit (# K688-100, Biovision, BioCat, Heidelberg, Germany). NHEK cells were seeded into 25 cm^2 cell culture flasks (Corning, Thermo Fisher Scientific) and treated at 60% confluence for 16 hours with 50 μM RSV or DMSO. Samples were processed according to the manufacturer′s instruction and deproteinized using the Deproteinizing Sample Preparation Kit (# K808-200, Biovision, BioCat).

The assay was miniaturized to 10% of the initial volume and conducted in a clear 384-well plate (# 784101, Greiner Bio-one). Fluorescence (535/587 nm) was measured after 45 minutes using the POLARstar Omega (BMG LABTECH). Samples were normalized to protein content and data analysis was conducted using GraphPad Prism 5.0.

Intracellular pyruvate quantification

Intracellular pyruvate concentration in NHEKs was determined using the Pyruvate Assay Kit (# 700470, Cayman Chemicals, Biomol). Cells were seeded in 150 cm^2 cell culture

flasks (Corning, Thermo Fisher Scientific) and treated at 60% confluence for 16 hours with 50 μM RSV or DMSO. Sample preparation was done according to the manufacturer′s instruction. Fluorescence (530/585 nm) was measured after 20 minutes (at 37°C) with the POLARstar Omega (BMG LABTECH). Samples were normalized to protein content. Data were analyzed using GraphPad Prism 5.0.

Pyruvate content in NHDFs was determined using the Pyruvate Colorimetric/Fluorometric Assay Kit (# K609-100, Biovision, BioCat). Cells were seeded in 150 cm^2 cell culture flasks (TPP, Biochrom) and treated at 60% confluence for 16 hours with 100 μM RSV or DMSO. Samples were diluted 1:5 and prepared according to the manufacturer′s instruction. OD was measured at 570 nm (background OD measured at 670 nm) after 20 minutes with the POLARstar Omega (BMG LABTECH). Samples were normalized to protein content; data were analyzed using GraphPad Prism 5.0.

Intracellular lactate quantification

Lactate content was quantified with the Lactate Assay Kit (# 700510, Cayman Chemicals, Biomol). NHEK cells were seeded in a 150 cm^2 (Corning, Thermo Fisher Scientific) and treated at 60% confluence with 50 μM RSV or DMSO for 16 hours. Sample preparation was done according to the manufacturer′s instructions. Fluorescence (530/585 nm) was measured with the POLARstar Omega (BMG LABTECH) at 37°C. Samples were normalized to protein content and data analysis was done using GraphPad Prism 5.0.

Intracellular lactate concentration in NHDFs was determined using the Lactate Colorimetric/Fluorometric Assay Kit (# K607-100, Biovision, BioCat). Cells were seeded in 150 cm^2 cell culture flasks (TPP, Biochrom) and treated at 60% confluence for 16 hours with 100 μM RSV or DMSO. Samples were diluted 1:40 and prepared according to the manufacturer′s instruction. OD was measured at 570 nm (background OD measured at 670 nm) after 20 minutes with the POLARstar Omega (BMG LABTECH). Samples were normalized to protein content; data were analyzed using GraphPad Prism 5.0.

Intracellular ADP and ATP quantification

The ADP Colorimetric/Fluorometric Assay Kit (# K355-100, Biovision, BioCat) and ATP Colorimetric/Fluorometric Assay Kit (# K354-100, Biovision, BioCat) were used to

quantify intracellular ADP and ATP content. NHEK cells were seeded into 150 cm^2 cell culture flasks (Corning, Thermo Fisher Scientific) and treated at a confluence of 60% for 16 hours with 50 μM RSV or DMSO. Flasks were washed once with ice-cold PBS (Sigma-Aldrich) prior to harvest using a dispenser (TPP, Biochrom). Cell suspensions were centrifuged at 1,000g for 5 minutes (at 4°C) and resuspended in ice-cold extraction buffer (Biovision, BioCat), aliquoted and stored at -20°C until usage.

The assay was miniaturized to 10% of the initial volume and conducted in a clear 384-well plate (# 784101, Greiner Bio-one) according to the manufacturer′s protocol. Optical density was measured after 45 minutes at 570 nm using the POLARstar Omega (BMG LABTECH). Samples were normalized to protein content. Data were analyzed using GraphPad Prism 5.0.

Intracellular NAD^+ and NADH quantification

Intracellular NAD^+ and NADH content was analyzed using the colorimetric NAD^+/NADH Quantitation Kit (# K337-100, Biovision, BioCat) according to the manufacturer′s instructions. NHEK cells were seeded into 150 cm^2 cell culture flasks (Corning, Thermo Fisher Scientific) and treated at 60% confluence for 16 hours with either 50 μM RSV or DMSO. NHDF cells were seeded into a 150 cm^2 cell culture flask (TPP, Biochrom) and treated at 60% confluence for 16 hours with either 100 μM RSV or DMSO.

Flasks were washed once with ice-cold PBS (Sigma-Aldrich) prior to harvest using a dispenser (TPP, Biochrom). Cell suspensions were centrifuged at 1,000g for 5 minutes (at 4°C) and resuspended in ice-cold extraction buffer (Biovision, BioCat). Afterwards, cells were lysed by two freeze-thaw-cycles, followed by intensive vortexing and centrifugation at 20,800g 15 minutes (at 4°C). Part of the cell lysate was incubated at 60°C for 30 minutes to generate NAD^+.

Cycling buffer, enzyme mix and developer (all Biovision, BioCat) was added and the optical density was measured after 30 minutes at 660 nm using the POLARstar Omega (BMG LABTECH). Samples were normalized to protein content and data analysis was done using GraphPad Prism 5.0.

Intracellular $NADP^+$ and NADPH quantification

The $NADP^+$/NADPH-Glo Assay Kit (# G9081, Promega, Mannheim, Germany) was used to quantify the intracellular $NADP^+$ and NADPH content in NHEKs. Cells were seeded into a 12-well plate (Corning, Thermo Fisher Scientific) and treated at 60% confluence for 16 hours with either 50 μM RSV or DMSO. The following day, cells were washed once in PBS (Sigma-Aldrich), 60 μl PBS/well were added and cells were lysed in 60 μl 0.2 M NaOH (Merck) supplemented with 1% dodecyltrimethylammonium bromide (DTAB) (# D8638, Sigma-Aldrich).

Afterwards, 50 μl lysate were transferred into a 96-well plate (TPP, Biochrom) to measure $NADP^+$ and NADPH individually according to the manufacturer′s protocol. Finally, 30 μl sample were transferred to a white 384-well plate (# 781098, Greiner Bio-one) and 30 μl of $NADP^+$/NADPH-Glo Detection Reagent (Promega) were added. Luminescence was measured after 30 minutes with the POLARstar Omega (BMG LABTECH). Samples were normalized to protein content and data analysis was done using GraphPad Prism 5.0.

The NADP/NADPH Quantitation Colorimetric Kit (# K347-100, Biovision, BioCat) was used to quantify the intracellular $NADP^+$ and NADPH content in NHDFs. Cells were seeded into a 75 cm^2 cell culture flask (TPP, Biochrom) and treated at 60% confluence for 16 hours with either 100 μM RSV or DMSO. The following day, cells were washed once in PBS (Sigma-Aldrich) and 200 μl NADP/NADPH Extraction Buffer were added followed by two freeze/thaw cycles (20 min on dry-ice, then 10 min at RT). The assay was conducted according to the manufacturer′s instructions. Finally, the OD was read at 450 nm with the POLARstar Omega (BMG LABTECH). Samples were normalized to protein content and data analysis was done using GraphPad Prism 5.0.

Analyses of intracellular reduced and oxidized glutathione

Intracellular reduced (GSH) and oxidized (GSSG) glutathione were quantified using the GSH/GSSG-Glo Assay Kit (# V6611, Promega). NHEK cells were seeded in a 96-well plate (TPP, Biochrom) with a density of 30,000 cells/well. The following day, cells were treated for 16 hours with either 50 μM RSV or DMSO. The assay was miniaturized to 25% of the initial volume and conducted according to the manufacturer′s protocol.

Cell culture medium was removed, 12.5 μl/well Total Glutathione Lysis Reagent or

Oxidized Glutathione Lysis Reagent (both Promega) were added and incubated for 5 minutes at room temperature while shaking. Afterwards, 12.5 μl/well Luciferin Generation Reagent (Promega) were added and incubated at room temperature for 30 minutes. Samples and standards were transferred to a white 96-well plate (# 655083, Greiner Bio-one) and 25 μl Luciferin Detection Reagent (Promega) were added. Luminescence was measured after 15 minutes with the POLARstar Omega (BMG LABTECH). Samples were normalized to protein content and data analysis was done using GraphPad Prism 5.0.

Extracellular acidification rate

Extracellular acidification rate (ECAR) is reflecting lactate production and thus glycolytic activity [323]. The pH-sensitive probe pH Xtra (Luxcel Biosciences) was used determine ECAR using time-resolved fluorescence. Notably, the fluorescence lifetime of the probe is anti-correlated to the pH. NHEK cells were seeded in a 96-well plate (TPP, Biochrom) with a density of 25,000 cells/well. The day after, cells were treated for 16 hours under CO_2-free conditions (at 37°C) with either 50 μM RSV or DMSO. For subsequent measurements, low-buffering aspiration buffer was used according to the manufacturers instructions: 1 mM PBS (pH 7.4), 20 mM glucose (Sigma-Aldrich), 75 mM NaCl (Sigma-Aldrich), 54 mM KCl (Sigma-Aldrich), 2.4 mM $CaCl_2$ (Merck), and 0.8 mM $MgSO_4$ (Merck).

The following day, cells were washed twice with 200 μl of aspiration buffer and incubated with 140 μl of pre-warmed probe diluted in aspiration buffer. Cells were incubated at 37°C for 20 minutes. Wells were sealed with mineral oil (Luxcel Biosciences) to prevent trapping of CO_2. Time-resolved fluorescence was measured in the POLARstar Omega (BMG Labtech) with the following settings: temperature = 37°C; TRF optic Z height 6 mm; excitation 380/20 nm; emission 615/50 nm; window 1 (w1): 100 μs delay, 30 μs integration time; window 2 (w2): 300 μs delay, 30 μs integration time; interval time 60 s; measurement time 360 min. Background fluorescence was measured in wells with medium without cells.

For data analysis, background fluorescence was subtracted for each well. Fluorescence lifetime (τ) was calculated for each sample (Equation (2.4)) and transformed to absolute pH values (Equation (2.5)) [323]. The pH values were plotted over time. The

ECAR was determined between 50 and 250 min. Data were analyzed using GraphPad Prism 5.0.

$$\tau = \frac{200}{\ln \frac{w1}{w2}} \tag{2.4}$$

$$pH = \frac{1687.2 - \tau}{199.12} \tag{2.5}$$

Analyses of oxygen consumption

Oxygen Consumption was analyzed using the cell impermeable, oxygen-sensing fluorophore MitoXpress Xtra and MitoXpress Xtra Oxygen Consumption assay (HS Method) (Luxcel Biosciences). NHEK cells were seeded in a 96-well plate (TPP, Biochrom) with a density of 25,000 cells/well. The day after, cells were incubated for 20 minutes under CO_2-free conditions at 37°C. After aspirating cell culture medium, 62.5 nM/well MitoXpress Xtra diluted in KGM (Lonza) was added. The plate was incubated for 10 minutes under CO_2-free conditions at 37°C. Compounds were added as indicated and each well was sealed with 100 μl pre-warmed HS mineral oil (Luxcel Biosciences) to limit diffusion of ambient oxygen.

Time-resolved fluorescence was measured in the POLARstar Omega (BMG Labtech) with the following settings: temperature 37°C; TRF optic Z height 6 mm; excitation 380/20 nm; emission 655/50 nm; window 1 (w1): 30 μs delay, 30 μs integration time; window 2 (w2): 70 μs delay, 30 μs integration time; interval time 90 s; measurement time 16 h. Background fluorescence was measured in wells with medium and oil but without cells and probe.

For data analysis, background fluorescence was subtracted for each well. Fluorescence lifetime (τ) was calculated (Equation (2.6)) and plotted over treatment time. For comparing oxygen consumption between treatments, the rate of probe fluorescence lifetime was determined between 1 and 4 hours and expressed relative to untreated cells. Data were analyzed using GraphPad Prism 5.0.

$$\tau = \frac{40}{\ln \frac{w1}{w2}} \tag{2.6}$$

Cell cycle analysis

Analyses of cell cycle regulation were performed in NHEK cells treated with the indicated compounds for 16 hours. Trypsinized (Subculture Reagent Pack, Lonza) cells were fixed in 70% ethanol (Merck) and incubated on ice for 15 minutes. Fixed cells were then resuspended in propidium iodide (PI)/RNase staining solution (# 4087, Cell Signaling Technology, Merck), incubated for 15 minutes at room temperature and stored at -20°C until use. Finally, cells were measured in the Accuri C6 flow cytometer (BD Biosciences). Data analyses were performed using the Watson pragmatic model in FlowJo 7.6 (Tree Star).

Analyses of phosphatidylserine externalization

To quantify the apoptosis, the externalization of phosphatidylserine [324] was determined in NHEK cells by staining with annexin-V-FLUOS (annexin) and PI using the Annexin-V-FLUOS Staining Kit (Roche, Mannheim, Germany). NHEK cells were seeded in 150 cm^2 cell culture flasks (Corning, Thermo Fisher Scientific) and treated at 60% confluence for 16 hours with 50 μM RSV, 25 mM GSH, or DMSO. In addition, RSV/DMSO and GSH were combined into one treatment to analyze quenching effects. Trypsinized cells (Subculture Reagent Pack, Lonza) were analyzed by flow cytometry (Accuri C6, BD Biosciences) according to the manufacturer′s instructions. Analyses were performed using FlowJo 7.6 (Tree Star).

Cells stained annexin positive/PI negative were defined as early apoptotic, whereas late apoptotic cells were defined as annexin positive/PI positive. Annexin negative/PI positively stained cells were defined as dead or necrotic.

2.12 Immunoblotting

Isolation of protein extracts

For the extraction of whole cell lysate, cell culture samples were washed with PBS (Sigma-Aldrich), scraped (TPP, Biochrom) in ice-cold PBS (Sigma-Aldrich) containing cOmplete ULTRA Tablets (protease inhibitor cocktail tablets, # 05892970001, Roche)

and Phosphatase Inhibitor Cocktail 2 (# P5726, Sigma-Aldrich). Samples were centrifuged at 3,200g for 5 minutes (4°C). The cell pellet was washed once more with ice-cold PBS (Sigma-Aldrich) containing cOmplete ULTRA Tablets (Roche) and Phosphatase Inhibitor Cocktail 2 (Sigma-Aldrich). Nuclear and cytoplasmic protein extracts were isolated and prepared using the NE-PER Nuclear & CytoplasmicExtraction Kit (# 78833, Thermo Fisher Scientific) according to the manufacturer′s protocol.

Protein samples were lysed in buffer containing: 50 mM Tris-HCl (pH 8.0, Merck), 10 mM ethylenediaminetetraacetic acid (EDTA) (Merck), 1% sodium dodecyl sulfate (SDS) (Sigma-Aldrich), cOmplete ULTRA Tablets (Roche) and Phosphatase Inhibitor Cocktail 2 (Sigma-Aldrich). Afterwards, samples were sonicated (Bandelin electronic, Berlin, Germany), centrifuged for 10 minutes at 10,000g (4°C) and the supernatants were stored at -80°C until use. The protein content of the isolated extracts was quantified using ionic detergent compatibility reagent (IDCR) (# 22663) and the colorimetric Protein Assay Reagent (# 22660, both Thermo Fisher Scientific). Protein concentration dependent absorbance changes were quantified at 660 nm using the POLARstar Omega (BMG Labtech). The total protein content was calculated using a bovine serum albumin (BSA) (Sigma-Aldrich) standard curve (0-1.5 mg/ml).

SDS Page and Western Blot

Protein lysates (10-20 μg) were denatured by adding 1x NuPAGE LDS Sample Buffer (Invitrogen, Thermo Fisher Scientific) and 50 mM dithiothreitol (DTT) (Sigma-Aldrich) prior to incubation at 70°C for 10 minutes. Denatured samples were separated using a NuPAGE Novex 4-12% Bis-Tris Gel (# NP0321BOX, Thermo Fisher Scientific) and blotted onto Hybond ECL nitrocellulose membranes (GE Healthcare, München, Germany) using a wet blotting system (EasyPhor PAGE WetBlotter Mini System, Biozym, Hessisch-Oldendorf, Germany) and transfer buffer (25M Trizma (Sigma-Aldrich), 186 mM glycine (Carl Roth, Karlsruhe, Germany)). Membranes were blocked for 1 hour at room temperature according to the manufacturer′s protocol and washed in diluted 10x tris(hydroxymethyl)aminomethane (Tris)-buffered saline (TBS) (0.2 M Trizma (Sigma-Aldrich), 1.37 M NaCl (Sigma-Aldrich), adjusted to pH 7.6) containing 0.1% Tween 20 (Sigma-Aldrich).

Primary antibodies (Table 2.2) were diluted in TBS-T (0.1%) with milk powder and BSA (both Sigma-Aldrich), respectively, according to the manufacturer′s protocols. Membranes were shaken at 4°C overnight, washed with TBS-T (0.1%) and subsequently incubated with anti-rabbit IgG-HRP (# sc-2004, Santa Cruz, Heidelberg, Germany) and anti-mouse IgG-HRP (# sc-2005, Santa Cruz), respectively, according to the manufacturer′s protocols. Detection was carried out with Western Lightning ECL solution (Perkin Elmer, Rodgau, Germany). Membranes were stripped with Restore Plus Western Blot Stripping Buffer (# 46430, Thermo Fisher Scientific) for 5-7 minutes. Densitometry was performed with FUSION-SL Advance 4.2 MP (Peqlab, Erlangen, Germany).

Table 2.2: Primary antibodies used for immunoblotting.

Antibody	Provider
β-Actin Antibody (C4) (# sc-47778)	Santa Cruz (Heidelberg, Germany)
Caspase-7 Antibody (# 9492)	Cell Signaling Technology (Merck, Darmstadt, Germany)
Caspase-9 Antibody (Human Specific) (# 9502)	Cell Signaling Technology (Merck, Darmstadt, Germany)
Cleaved Caspase-7 (Asp198) (D6H1) Rabbit mA (# 8438)	Cell Signaling Technology (Merck, Darmstadt, Germany)
Cleaved Caspase-9 (Asp330) (D2D4) Rabbit mAb (# 7237)	Cell Signaling Technology (Merck, Darmstadt, Germany)
Cleaved PARP (Asp214) (D64E10) XP Rabbit mAb (# 5625)	Cell Signaling Technology (Merck, Darmstadt, Germany)
CDK2 (78B2) Rabbit mAb (# 2546)	Cell Signaling Technology (Merck, Darmstadt, Germany)
CDK4 (DCS156) Mouse mAb (# 2906)	Cell Signaling Technology (Merck, Darmstadt, Germany)
Cyclin A2 (BF683) Mouse mAb (# 4656)	Cell Signaling Technology (Merck, Darmstadt, Germany)
Cyclin D1 (DCS6) Mouse mAb (# 2926)	Cell Signaling Technology (Merck, Darmstadt, Germany)
Cyclin E2 Antibody (# 4132)	Cell Signaling Technology (Merck, Darmstadt, Germany)
Glutathione reductase Antibody (B-12) (# sc-133159)	Santa Cruz (Heidelberg, Germany)
Keap1 Antibody (G-2) (# sc-365626)	Santa Cruz (Heidelberg, Germany)
Anti-NF-κB p65 (acetyl K310) antibody - ChIP Grade (# ab52175, K310)	Abcam (Cambridge, UK)
NFκB p65 (L8F6) Mouse mAb (# 6956)	Cell Signaling Technology (Merck, Darmstadt, Germany)
Anti-NQO1 antibody [A180] (# ab28947)	Abcam (Cambridge, UK)
Anti-Nrf2 (phospho S40) antibody [EP1809Y] (# ab76026, Ser40)	Abcam (Cambridge, UK)
Nrf2 Antibody (H-300) (# sc-13032)	Santa Cruz (Heidelberg, Germany)
p21 Waf1/Cip1 (12D1) Rabbit mAb (# 2947)	Cell Signaling Technology (Merck, Darmstadt, Germany)
PARP Antibody (# 9542)	Cell Signaling Technology (Merck, Darmstadt, Germany)
Anti-Pyruvate Dehydrogenase E1-α subunit antibody (# ab67592)	Abcam (Cambridge, UK)
Anti-Pyruvate Dehydrogenase E1-α subunit (phospho S293) antibody (# ab92696, Ser293)	Abcam (Cambridge, UK)
SirT1 monoclonal antibody - Pioneer (# MAb-063-050)	Diagenode (Seraing, Belgium)
Phospho-SirT1 (Ser47) Antibody (# 2314)	Cell Signaling Technology (Merck, Darmstadt, Germany)

2.13 Detection of lipid peroxidation

Click-iT Lipid Peroxidation Imaging Kit-Alexa Fluor 488 (# C10446, Thermo Fisher Scientific) was used to determine lipid peroxidation. Increasing fluorescence intensities correspond to enhanced lipid peroxidation. NHEKs were seeded in 25 cm^2 cell culture flasks (Corning, Thermo Fisher Scientific) and treated at 60% confluence for 16 hours with 50 μM RSV or DMSO in presence of 50 μM linoleamide alkyne (LAA).

Trypsinized (Subculture Reagent Pack, Lonza) cells were washed with PBS (Sigma-Aldrich) and fixed in 3.7% formaldehyde (Sigma-Aldrich) for 15 minutes at room temperature. Cells were washed in PBS (Sigma-Aldrich) again, permeabilized by use of 0.5% Triton X-100 (Sigma-Aldrich) in PBS for 10 minutes at room temperature and subsequently blocked by adding 1% BSA (Sigma-Aldrich) for 30 minutes at room temperature. The remaining BSA (Sigma-Aldrich) was removed by rigorously washing the cells with PBS (Sigma-Aldrich).

The pelleted cells were then incubated with 500 μl Click iT reaction cocktail (Thermo Fisher Scientific) for 30 minutes at room temperature according to the manufacturer′s protocol. The “Click” reaction was stopped by adding 1% BSA/PBS. The cells were again washed and resuspended with PBS (Sigma-Aldrich). Flow cytometry was performed on the Accuri C6 (BD Biosciences). Data were analyzed using FlowJo 7.6 (Tree Star) and GraphPad Prism 5.0.

2.14 Fluorescence microscopy

NHEK cells were seeded in x-well tissue culture chambers (# 94.6140.80, Sarstedt) at a density of 20,000 cells/well. The following day cells were treated for 16 hours with 50 μM RSV or DMSO, respectively. Visualization of MAP1LC3, Actin, Nrf2, Keap1, GCLC and GSR was done as recently described in [325].

Cells were treated for 16 hours with the indicated compounds, washed with PBS (Sigma-Aldrich) and fixed in 4% formaldehyde/PBS (both Sigma-Aldrich) for 15 minutes at room temperature. Cells were washed with PBS (Sigma-Aldrich), permeabilized in 0.3% Triton X-100/PBS (PBS-Tx, both Sigma-Aldrich) for 10 minutes at room temperature, washed with PBS (Sigma-Aldrich) and afterwards blocked in 5% goat serum (Sigma-Aldrich) in PBS-Tx for 60 minutes at room temperature. Afterwards, cells

were incubated with primary antibodies overnight at 4°C.

Primary antibodies and dilutions were as follows: MAP1LC3 (# AP1801d-ev-AB, Biovision, BioCat; 1:100), Nrf2 (# sc-13032X, Santa Cruz; 1:100), Keap1 (# sc-365626, Santa Cruz; 1:100), GCLC (# ab41463, Abcam; 1:100) and GSR (# sc-133159, Santa Cruz; 1:100). Subsequently, cells were washed with PBS-Tx and stained with anti-mouse IgG (H+L) F(ab′)2 fragment Alexa Fluor 555 Conjugate (# 4409, Cell Signaling Technology) and anti-rabbit IgG (H+L), F(ab′)2 fragment Alexa Fluor 488 Conjugate (# 4412, Cell Signaling Technology) diluted (1:1,000) in 1% BSA/PBS-Tx for 1 hour at room temperature in the dark. Subsequently, cells were washed with PBS (Sigma-Aldrich) for 5 minutes, and the MAP1LC3 stained cells were counterstained with Texas Red-X Phalloidin (# T7471, Thermo Fisher Scientific; 1:100) for 20 minutes at room temperature in the dark.

Cells were washed with PBS, the chamber was removed from the slide, samples were counterstained with ProLong Gold Antifade Mountant with 4',6-diamidino-2-phenylindole (DAPI) (# P-36931, Thermo Fisher Scientific), and a cover slip was applied (# 235503704, Duran Group). Afterwards, samples were incubated at room temperature for 24 hours. Fluorescence microscope imaging was performed using the LSM700 microscope (Zeiss, Jena, Germany); data were analyzed with ImageJ [326, 327].

2.15 Statistical analyses

Experimental data are presented as mean ± standard error of the mean (SEM), if not denoted otherwise. Data were analyzed using GraphPad Prism 5.0. Statistical significance was determined as follows: for single comparisons by unpaired two-tailed student's t-test and for multiple comparisons by one-way analysis of variance (ANOVA) with Dunnett′s post test. A p value ≤ 0.05 was defined as statistically significant.

2.16 Equipment and reagents

Reagents The reagents used in this study are listed in Table 2.3.

Table 2.3: Reagents.

Reagent	Manufacturer/Provider
β-Mercaptoethanol	Sigma-Aldrich (Taufkirchen, Germany)
Adenosine diphosphate (ADP)	Sigma-Aldrich (Taufkirchen, Germany)
ADP Colorimetric/Fluorometric Assay Kit	Biovision (BioCat, Heidelberg, Germany)
Annexin-V-FLUOS Staining Kit	Roche (Mannheim, Germany)
Anti-GCLC Antibody	Abcam (Cambridge, UK)
Anti-mouse IgG (H+L) F(ab′)2 Fragment Alexa Fluor 555 Conjugate	Cell Signaling Technology (Merck, Darmstadt, Germany)
Antioxidant Assay Kit	Cayman Chemicals (Biomol, Hamburg, Germany)
Anti-rabbit IgG (H+L), F(ab′)2 Fragment Alexa Fluor 488 Conjugate	Cell Signaling Technology (Merck, Darmstadt, Germany)
Adenosine triphosphate (ATP)	Sigma-Aldrich (Taufkirchen, Germany)
ATP Colorimetric/Fluorometric Assay Kit	Biovision (BioCat, Heidelberg, Germany)
Bovine serum albumin (BSA)	Sigma-Aldrich (Taufkirchen, Germany)
CellROX Green dye	Thermo Fisher Scientific (Karlsruhe, Germany)
Calcium chloride ($CaCl_2$)	Merck GmbH (Darmstadt, Germany)
CellTiter-Fluor Cell Viability Assay	Promega (Mannheim, Germany)
5-(and-6)-chloromethyl-2′,7′-dichlorodihydrofluorescein diacetate, acetyl ester (CM-H_2DCFDA)	Thermo Fisher Scientific (Karlsruhe, Germany)
Click-iT Lipid Peroxidation Imaging Kit-Alexa Fluor 488	Thermo Fisher Scientific (Karlsruhe, Germany)
cOmplete ULTRA Tablets	Roche (Mannheim, Germany)
Deproteinizing Sample Preparation Kit	Biovision (BioCat, Heidelberg, Germany)
Dimethyl sulfoxide (DMSO)	AppliChem (Darmstadt, Germany)
Dulbecco′s modified Eagle′s medium (DMEM) (# 31966)	Gibco (Thermo Fisher Scientific, Karlsruhe, Germany)
DMEM (# 21068-008)	Gibco (Thermo Fisher Scientific, Karlsruhe, Germany)
DMEM Nutrient Mixture F-12 (DMEM/F-12)	Thermo Fisher Scientific (Karlsruhe, Germany)
Dodecyltrimethylammonium bromide (DTAB)	Sigma-Aldrich (Taufkirchen, Germany)
Dithiothreitol (DTT)	Sigma-Aldrich (Taufkirchen, Germany)
Ethylenediaminetetraacetic acid (EDTA)	Merck KGaA (Darmstadt, Germany)
Eosin Y solution	Sigma-Aldrich (Taufkirchen, Germany)
Ethanol	Merck (Darmstadt, Germany)
FBS Superior	Biochrom (Berlin, Germany)
Formaldehyde (37%)	Sigma-Aldrich (Taufkirchen, Germany)
Glucose	Sigma-Aldrich (Taufkirchen, Germany)
Glutathione Reductase Antibody	Santa Cruz (Heidelberg, Germany)
Glycine	Carl Roth (Karlsruhe, Germany)
Glutathione (reduced form, GSH)	Sigma-Aldrich (Taufkirchen, Germany)
GSH/GSSG-Glo Assay	Promega (Mannheim, Germany)
Hematoxylin solution	Sigma-Aldrich (Taufkirchen, Germany)
High Capacity cDNA Reverse Transcription Kit	Applied Biosystems (Thermo Fisher Scientific, Karlsruhe, Germany)
Hydrochloride (HCl)	Merck (Darmstadt, Germany)
Hygromicin B	Thermo Fisher Scientific (Karlsruhe, Germany)
HS mineral oil	Luxcel Biosciences (Cork, Ireland)
Ionic detergent compatibility reagent (IDCR)	Thermo Fisher Scientific (Karlsruhe, Germany)
Keratinocyte basal medium (KBM)	Lonza (Basel, Swiss)
Keap1 Antibody	Santa Cruz (Heidelberg, Germany)
L-glutamine	Sigma-Aldrich (Taufkirchen, Germany)
Lactate Assay Kit	Cayman Chemicals (Biomol, Hamburg, Germany)
Lactate Colorimetric/Fluorometric Assay Kit	Biovision (BioCat, Heidelberg, Germany)

Reagent	Manufacturer/Provider
Lambda DNA	Thermo Fisher Scientific (Karlsruhe, Germany)
Lipofectamine 2000	Thermo Fisher Scientific (Karlsruhe, Germany)
Magnesium sulfate ($MgSO_4$)	Merck GmbH (Darmstadt, Germany)
MAP1LC3A Antibody	Biovision (BioCat, Heidelberg, Germany)
Milk powder	Sigma-Aldrich (Taufkirchen, Germany)
Mineral oil	Luxcel Biosciences (Cork, Ireland)
MitoSOX Red Mitochondrial Superoxide Indicator	Life Technologies (Thermo Fisher Scientific, Karlsruhe, Germany)
MitoXpress Xtra Oxygen Consumption Assay (HS Method)	Luxcel Biosciences (Cork, Ireland)
N-acetyl-cysteine (NAC)	Sigma-Aldrich (Taufkirchen, Germany)
NAD^+/NADH Quantitation Colorimetric Kit	Biovision (BioCat, Heidelberg, Germany)
$NADP^+$/NADPH Quantification Colorimetric Kit	Biovision (BioCat, Heidelberg, Germany)
$NADP^+$/NADPH-Glo Assay	Promega (Mannheim, Germany)
NE-PER Nuclear and Cytoplasmic Extraction Kit	Thermo Fisher Scientific (Karlsruhe, Germany)
Nrf2 Antibody	Santa Cruz (Heidelberg, Germany)
Nuclease-free water	Ambion (Thermo Fisher Scientific, Karlsruhe, Germany)
NuPAGE LDS sample buffer (4x)	Thermo Fisher Scientific (Karlsruhe, Germany)
NuPAGE MES SDS running buffer (20x)	Thermo Fisher Scientific (Karlsruhe, Germany)
Opti-MEM I medium	Thermo Fisher Scientific (Karlsruhe, Germany)
PBS	Sigma-Aldrich (Taufkirchen, Germany)
Penicillin	Biochrom (Berlin, Germany)
pH-Xtra	Lucxel Biosciences (Cork, Ireland)
Phosphatase Inhibitor Cocktail 2	Sigma-Aldrich (Taufkirchen, Germany)
PicoProbe Glucose Fluorometric Assay Kit	Biovision (BioCat, Heidelberg, Germany)
PonceauS 0.1%	AppliChem (Darmstadt, Germany)
Potassium chloride (KCl)	Sigma-Aldrich (Taufkirchen, Germany)
Power SYBR Green PCR Master Mix	Applied Biosystems (Thermo Fisher Scientific, Karlsruhe, Germany)
ProLong Gold Antifade Mountant with DAPI	Thermo Fisher Scientific (Karlsruhe, Germany)
PI/RNase Staining Solution	Cell Signaling Technology (Merck, Darmstadt, Germany)
Pyruvate Assay Kit	Cayman Chemicals (Biomol, Hamburg, Germany)
Pyruvate Colorimetric/Fluorometric Assay Kit	Biovision (BioCat, Heidelberg, Germany)
ReagentPack Subculture Reagents	Lonza (Basel, Swiss)
RPMI 1640	Biochrom (Berlin, Germany)
RNase-free DNase set	QIAGEN (Hilden, Germany)
RNeasy Plus Mini Kit	QIAGEN (Hilden, Germany)
RNase-free water	Ambion (Thermo Fisher Scientific, Karlsruhe, Germany)
Protein Assay Reagent	Thermo Fisher Scientific (Karlsruhe, Germany)
Restore Plus Western Blot Stripping Buffer	Thermo Fisher Scientific (Karlsruhe, Germany)
Silencer Pre-Designed siRNA Nrf2	Ambion (Thermo Fisher Scientific, Karlsruhe, Germany)
Silencer Pre-Designed siRNA SIRT1	Ambion (Thermo Fisher Scientific, Karlsruhe, Germany)
Silencer Select Negative Control siRNA	Ambion (Thermo Fisher Scientific, Karlsruhe, Germany)
SingleQuot Kit Suppl. & Growth Factors	Lonza (Basel, Swiss)
Sodium bicarbonate ($NaHCO_3$)	Merck GmbH (Darmstadt, Germany)
Sodium chloride (NaCl)	Sigma-Aldrich (Taufkirchen, Germany)
Sodium dodecyl sulfate (SDS)	Sigma-Aldrich (Taufkirchen, Germany)
Sodium hydroxide (NaOH)	Merck GmbH (Darmstadt, Germany)
Sodium pyruvate	Thermo Fisher Scientific (Karlsruhe, Germany)
Streptomycin	Biochrom (Berlin, Germany)
Subculture Reagent Pack	Lonza (Basel, Swiss)
Texas Red-X Phalloidin	Thermo Fisher Scientific (Karlsruhe, Germany)
Trizma	Sigma-Aldrich (Taufkirchen, Germany)

Reagent	Manufacturer/Provider
Tris hydrochloride (Tris-HCl)	Merck (Darmstadt, Germany)
Triton X-100	Sigma-Aldrich (Taufkirchen, Germany)
Tween-20	Sigma-Aldrich (Taufkirchen, Germany)
Western Lightning ECL solution	Perkin Elmer (Rodgau, Germany)

Cell lines Cellular models used in this study are listed in Table 2.4.

Table 2.4: Cell lines.

Cell line	Provider
NHDF-Neo	Lonza (Basel, Swiss)
NHEK-Neo	Lonza (Basel, Swiss)
HaCaT	Kindly provided by Unilever (Sharnbrook, UK)
HaCaT ARE Clone 7	Kindly provided by Unilever (Sharnbrook, UK)
HepG2	ATCC (LGC Standards GmbH, Wesel, Germany)
HEK293T	ATCC (LGC Standards GmbH, Wesel, Germany)
HeLa	Kindly provided by Dr. David Meierhofer (Berlin, Germany)
HT-29	DSMZ (Braunschweig, Germany)
THP-1	DSMZ (Braunschweig, Germany)

Equipment and consumables The equipment and consumables used in this study are listed in Table 2.5.

Table 2.5: Equipment and consumables.

Product	Manufacturer
0.22 μm Steritop-GP Polyethersulfon filter (SCGPT02RE)	Millipore (Schwalbach, Germany)
3MM chromatography paper	Whatman (GE Healthcare, München, Germany)
6-well cell culture plate	Corning (Thermo Fisher Scientific, Schwerte, Germany)
12-well cell culture plate	Corning (Thermo Fisher Scientific, Schwerte, Germany)
12-well cell culture plate	Sarstedt (Nürnbrecht, Germany)
96-well plate, Thermowell, PCR	Corning (Thermo Fisher Scientific, Schwerte, Germany)
96-well plate, cell culture	TPP (Biochrom, Berlin, Germany)
96-well plate, UV-Star (# 655801)	Greiner Bio-one (Frickenhausen, Germany)
96-well plate, white (# 655083)	Greiner Bio-One (Frickenhausen, Germany)
96-well plate, black (# 353219)	BD Biosciences (Heidelberg, Germany)
96-well plates, black (# 655090)	Greiner Bio-One (Frickenhausen, Germany)
384-well plate, white (# 781098)	Greiner Bio-One (Frickenhausen, Germany)
384-well plate, clear (# 784101)	Greiner Bio-One (Frickenhausen, Germany)
384-well plate, black (# 784076)	Greiner Bio-One (Frickenhausen, Germany)
x-well tissue culture chambers	Sarstedt (Nürnbrecht, Germany)
7900 HT Fast Real-Time PCR System	Applied Biosystems (Thermo Fisher Scientific, Karlsruhe, Germany)
Accuri C6 flow cytometer	BD Biosciences (Heidelberg, Germany)
CO_2-Incubator Model CB 60	Binder (Tuttlingen, Germany)
CO_2-Incubator BBD 6220	Thermo Fisher Scientific (Karlsruhe, Germany)

Product	Manufacturer
C-Chip counting chamber	Biochrom (Berlin, Germany)
Cell culture flask	TPP (Biochrom, Berlin, Germany)
Cell culture flask	Corning (Thermo Fisher Scientific, Schwerte, Germany)
Collection Microtube Caps	QIAGEN GmbH (Hilden, Germany)
Collection Microtubes	QIAGEN GmbH (Hilden, Germany)
Cover slip	DURAN (Wertheim/Main, Germany)
Dispenser	TPP (Biochrom, Berlin, Germany)
EasyPhor PAGE WetBlotter Mini System	Biozym (Hessisch Oldendorf, Germany)
fluorescence-activated cell sorting (FACS) tubes	BD Falcon (NJ, USA)
FUSION-SL Advance 4.2MP	Peqlab (Erlangen, Germany)
Hybond ECL nitrocellulose membranes	GE Healthcare (München, Germany)
Image Reader LAS-1000 Pro V2.61	Fujifilm (Düsseldorf, Germany)
LSM700 microscope	Zeiss (Jena, Germany)
MicroAmp optical adhesive cover	Applied Biosystems (Thermo Fisher Scientific, Karlsruhe, Germany)
MicroAmp optical 384 well plate	Applied Biosystems (Thermo Fisher Scientific, Karlsruhe, Germany)
Nanodrop ND-2000	Thermo Fisher Scientific (Karlsruhe, Germany)
Nunclon cell culture plate	Nunc (Wiesbaden, Germany)
NuPAGE Novex 4-12% Bis-Tris Gel	Thermo Fisher Scientific (Karlsruhe, Germany)
NuPAGE LDS-PAGE chamber	Invitrogen (Thermo Fisher Scientific, Karlsruhe, Germany)
POLARstar Omega	BMG Labtech (Ortenberg, Germany)
Protein LoBind Tubes	Eppendorf (Hamburg, Germany)
PTC-200 Peltier Thermal Cycler	MJ Research (Waltham, MA, USA)
Sonificator OW 2200	Bandelin electronic (Berlin, Germany)
Stericup Receiver Flask (SC00B05RE)	Millipore (Schwalbach, Germany)
Thermomixer comfort	Eppendorf (Hamburg, Germany)
UV Gel Imaging System	Ultra Lum (Claremont, USA)
Xcell SureLock Mini-Cell Electrophoresis System	Invitrogen (Thermo Fisher Scientific, Karlsruhe, Germany)

Software The software used in this study is listed in Table 2.6.

Table 2.6: Software.

Software	Manufacturer
Connectivity Map	Broad Institute (Cambridge, MA, USA)
FlowJo software	TreeStar Inc. (Ashland, USA)
FUSION-SL Advance 4.2 MP	Peqlab (Erlangen, Germany)
GelAnalyzer 2010a	GelAnalyzer
Gene Set Enrichment Analysis (GSEA)	Broad Institute (Cambridge, MA, USA)
GenomeStudio V2011.1	Illumina (Eindhoven, The Netherlands)
GraphPad Prism 5.0	GraphPad Software (La Jolla, CA, USA)
ImageJ	W.S. Rasband [326] (Bethesda, MD, USA)
Primer-BLAST	National Center for Biotechnology Information (NCBI)
SDS 2.2	Applied Biosystems (Thermo Fisher Scientific, Karlsruhe, Germany)

3 Results

Contents

3.1 Chemical properties of resveratrol

The majority of studies tends to assume the integrity of RSV throughout treatments and presume a specific RSV-target molecule mechanism. However, several recent publications challenge this presumption [35–44]. To examine the stability of RSV a simple setup was chosen to avoid unpredictable disturbances [42]. With cell culture-oriented applications of RSV in mind, the $NaHCO_3$ concentration was set to a value matching most generic cell culture media (44 mM $NaHCO_3$). In addition, a mid micromolar range concentration of 50 μM RSV, which is often used in the literature [59, 133, 328, 329], was used for the experiments.

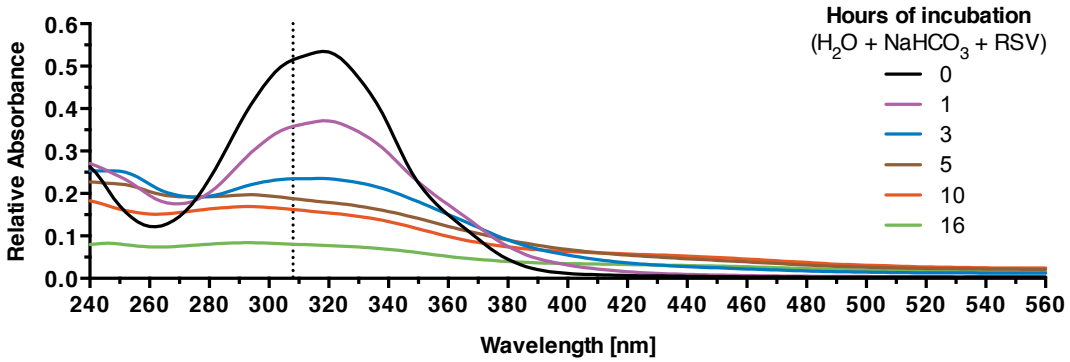

Figure 3.1: Effect of $NaHCO_3$ on RSV. Kinetic wavelength scan of water containing 44 mM $NaHCO_3$ and 50 μM RSV after indicated incubation periods at 37°C. Absorbance was recorded between 240 and 560 nm (Δ 2 nm) and data were smoothed. The dotted line marks RSV absorbance maximum at 308 nm. Data are expressed as mean (n = 3) relative to DMSO. See also Figure S2.

RSV was incubated for different time periods at 37°C in water without (Figure S2) or with 44 mM $NaHCO_3$ (Figure 3.1) while a wavelength scan between 240 and 560 nm (Δ 2 nm) was performed. Whereas the principal shape of the curve did not change when RSV was incubated in water (Figure S2), the presence of 44 mM $NaHCO_3$ dramatically changed the curve shape in a time-dependent manner (Figure 3.1). An effect that is also observed at the specific absorbance maximum of RSV at 308 nm (dotted line in Figures 3.1 and S2, [36]), where the absorbance was decreased roughly 30% after 1 hour of incubation. After 16 hours of incubation, there is almost no measurable absorbance at 308 nm in the presence of $NaHCO_3$ (Figure 3.1).

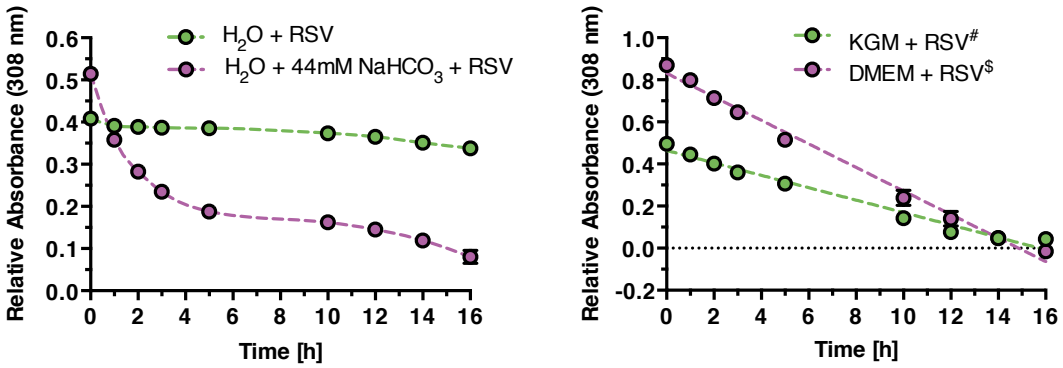

(a) Water **(b) Cell culture media**

Figure 3.2: Time-dependent decay of RSV. Decay of the RSV-specific absorbance maximum at 308 nm after incubation in water with and without 44 mM $NaHCO_3$ (a) and cell culture media (b) at 37°C. Absorbance was measured kinetically and values are expressed as mean (n = 3) relative to corresponding DMSO controls. Data were fitted (dashed line) using cubic spline fit (a) and linear regression model (b). # 50 μM RSV; $ 100 μM RSV. See also Figure S3 and Table S1.

A detailed view on time-dependent changes of the absorbance at 308 nm is depicted in Figure 3.2a. Whereas the absorbance remained stable in water over 16 hours, a multiphase decrease was observed in presence of 44 mM $NaHCO_3$. In preparation of cell culture-based applications, RSV was incubated in DMEM (100 μM) and KGM (50 μM) while the absorbance at 308 nm was monitored. Interestingly, the decay of RSV-specific absorbance in cell culture media was linear (Figure 3.2b) and not multi-phased as observed in $NaHCO_3$ containing water (Figure 3.2a magenta). According to the linear regression fit, the decay of RSV-specific absorbance was almost equally fast in both cell culture media tested (Table S1).

Based on the time-dependent decrease in RSV-specific absorbance (Figure 3.1), we hypothesized that RSV did decompose in response to 44 mM $NaHCO_3$ [42]. Hence, the wavelength scan data (Figure 3.1) was scanned for putative breakdown products of RSV, as their time-dependent increase in absorbance should correspond to the decrease of RSV absorbance. Remarkably, the wavelength scan data (Figure 3.1) revealed a time-dependent absorbance increase around 390 nm and 420 nm, if RSV was incubated in the presence of 44 mM $NaHCO_3$ (Figure S3).

Li et. al. (2012) determined two major reaction products of the reaction of RSV and $HO^{\bullet}$ (Figure 1.6) [40]. At first, a rather short-lived hydroxyl radical of RSV was

formed (absorbance maximum: 420 nm) and second a long-lived 4‘-phenoxyl radical adduct (absorbance maximum: 390 nm) (Figure 1.6) [40]. For both oxidation products, the absorbance increased in a time-dependent manner, thus these findings endorse the results published by Li et al. (2012) [40].

3.1.1 Effect of pH

pH has been identified as another factor that influences RSV stability [35–37]. Continuing to focus on preferably simple solvents, a pH gradient was applied to determine the effect of pH on the stability of RSV in water without (Figure 3.3a) and with 44 mM $NaHCO_3$ (Figure 3.3b) after 16 hours of incubation at 37°C. The RSV-specific absorbance at 308 nm was decreased at alkaline pH levels below 8 (Figure 3.3a). The presence of 44 mM $NaHCO_3$ dramatically shifted the starting point of absorbance decrease to lower pH levels ($pH < 4$, Figure 3.3b). Notably, the absorbance of RSV did not converge to 0% but only to roughly 40% of the initial value independent of the presence of $NaHCO_3$ (Figure 3.3).

Although widely ignored, it has been known for several years now that polyphenols including RSV are rapidly oxidized in cell culture media and generate significant amounts of H_2O_2 [41, 42, 47]. The H_2O_2 generation is accelerated in the presence of bicarbonate ions [41, 42]. Incidentally, the majority of cell culture and physiological media contain minerals including iron, thus enabling the generation of $HO^{\bullet}$ through the Fenton reaction (Figure 1.10) [158].

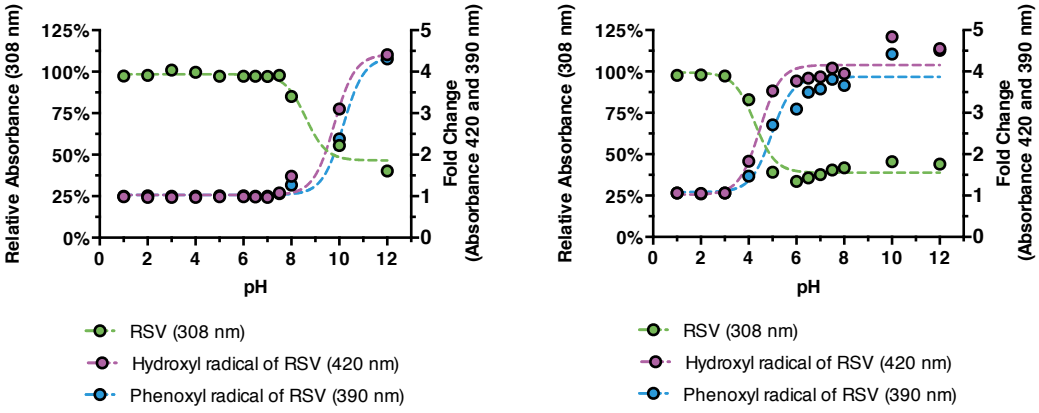

Figure 3.3: Effect of pH on the oxidation of RSV. RSV (50 μM) was incubated for 16 hours in water (a) and in presence of 44 mM $NaHCO_3$ (b) at 37°C. Absorbance of RSV was measured at 308 nm, whilst the absorbance of corresponding oxidation products was measured at 420 nm (hydroxyl radical adduct) and 390 nm (phenoxyl radical adduct), respectively. pH values were adjusted using HCl and NaOH. Values are expressed as mean (n = 3) relative to corresponding DMSO controls. Data were fitted (dashed line) according to equation Equation (2.1).

The generation of putative oxidation products of RSV according to [40] was monitored in pH titration experiments in the absence (Figure 3.3a magenta and blue) and presence of 44 mM $NaHCO_3$ (Figure 3.3b magenta and blue). In water the absorbance of both oxidation products started to increase at pH 8 (Figure 3.3a), whereas in presence of 44 mM $NaHCO_3$ an increase was already observed at pH around 4 (Figure 3.3b). Notably, the curve shape of RSV absorbance mirrored the curve of RSV oxidation products (Figure 3.3a).

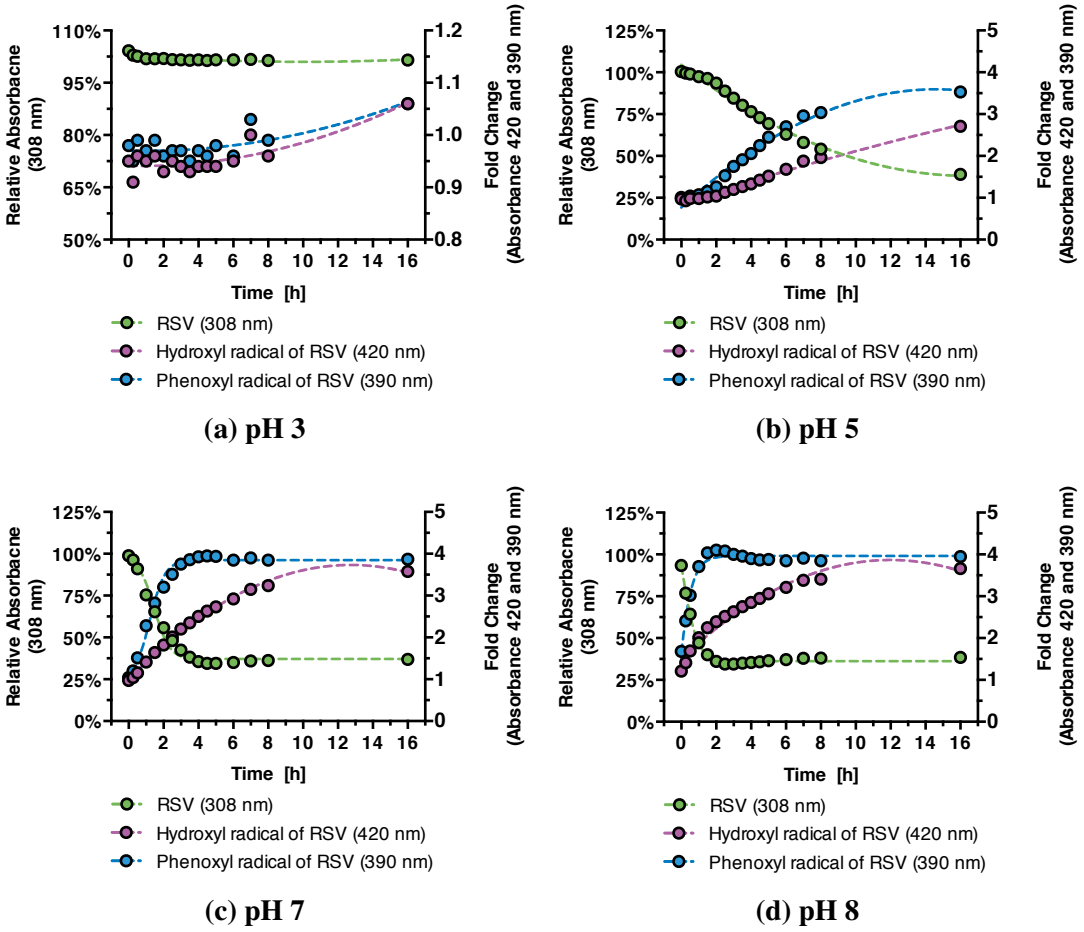

Figure 3.4: Kinetic view on the pH-dependent oxidation of RSV. RSV (50 μM) was incubated in water containing 44 mM $NaHCO_3$ at pH 3 (a), pH 5 (b), pH 7 (c) and pH 8 (d) at 37°C. Absorbance of RSV was measured at 308 nm, whilst the absorbance of corresponding oxidation products was measured at 420 nm (hydroxyl radical adduct) and 390 nm (phenoxyl radical adduct), respectively. pH values were adjusted using HCl and NaOH. Values are expressed as mean (n = 3) relative to corresponding DMSO controls. Data were fitted (dashed line) according to second order polynomial (pH 3 and 5; absorbance at 420 nm all pH values) or equation Equation (2.1) (pH 7 and 8 except absorbance at 420 nm). See also Figure S4.

A more detailed view on the kinetics of pH-dependent oxidation of RSV is given in Figures 3.4 and S4. At acid pH (Figure 3.4a), absorbance of RSV remained quite stable and corresponded to the fold change of the putative oxidation products. Nevertheless, at a pH of 5 oxidation of RSV started already after 2 hours of incubation, while the amount of both radical adducts of RSV increased correspondingly (Figure 3.4b). Notably, at pH above 7 (pH $\geq$ 7) the oxidation of RSV started within the first hour of incubation and

reached a plateau after roughly 4 hours (Figures 3.4c and 3.4d).

The fold change of the hydroxyl radical adduct of RSV (magenta) steadily increased whereas the phenoxyl radical adduct (blue) did not reach a plateau (Figures 3.4c and 3.4d). The kinetics of the oxidation of RSV changes in a pH-dependent manner. Hence, different fitting models were used to obtain optimal correlation coefficients (see Section 2.2).

3.1.2 Effect of oxygen

According to the mechanism proposed by Li et al. [40] it seemed likely that the oxygen level might influence the oxidation of RSV [43, 52], a hypothesis referred to as "cell culture artifact" [41, 47]. Therefore, the RSV oxidation experiments in water and in presence of 44 mM $NaHCO_3$ were conducted under reduced oxygen conditions at 10% oxygen (Figures 3.5a and S5a) and 1% oxygen (Figures 3.5b and S5b), respectively.

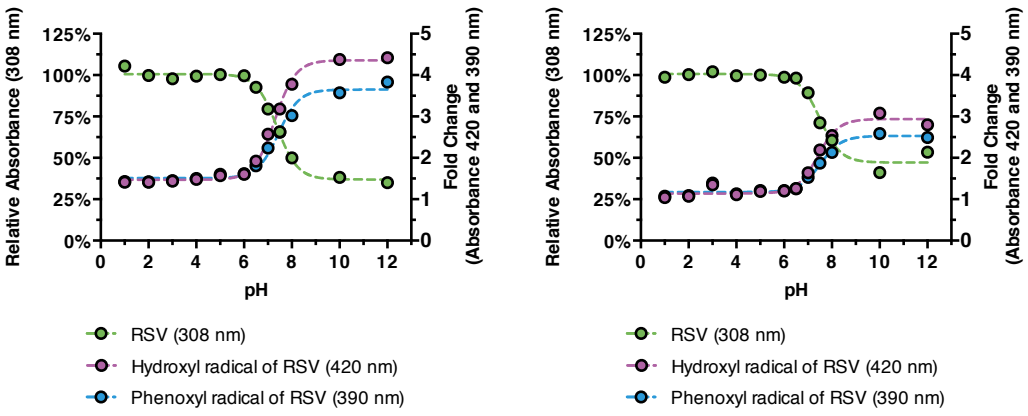

(a) 10% Oxygen **(b) 1% Oxygen**

Figure 3.5: Effects of oxygen level and pH on the oxidation of RSV. RSV (50 μM) was incubated at 37°C for 16 hours in water containing 44 mM $NaHCO_3$ and in presence of 10% oxygen (a) and 1% oxygen (b), respectively. Absorbance of RSV was measured at 308 nm, whilst the absorbance of corresponding oxidation products was measured at 420 nm (hydroxyl radical adduct) and 390 nm (phenoxyl radical adduct), respectively. pH values were adjusted using HCl and NaOH. Values are expressed as mean (n = 3) relative to corresponding DMSO controls. Data were fitted (dashed line) according to equation Equation (2.1).

A reduction of oxygen to 10% (Figure S5a) considerably shifted the starting point of oxidation of RSV in water to higher pH values (pH $>$ 10). Notably, a more significant reduction of oxygen to 1% did not shift the oxidation process any further (Figure S5b).

In presence of 44 mM $NaHCO_3$, the efficiency of RSV oxidation was dependent on the amount of oxygen available (Figure 3.5). At 10% oxygen a markable oxidation of RSV was observed at pH 6 (Figure 3.5a), however, at 1% oxygen the starting point was slightly shifted to a pH of 7 (Figure 3.5b).

3.2 Generation of reactive oxygen species

In view of the oxidation products caused by the interaction of RSV with $HO^{\bullet}$ [40] (see Figures 3.3 to 3.5, S4 and S5), the generation of $HO^{\bullet}$, $O_2^{\bullet -}$ and other ROS was monitored in a cell-free and intracellular environment (Figures 3.6a, 3.6b and S6).

3.2.1 Hydroxyl radical and superoxide generation

RSV incubated in water did not generate ROS (Figures S6a and S6b in green), whereas the presence of 44 mM $NaHCO_3$ resulted in a 1.75-fold increase of ROS (Figure S6b in magenta) compared to DMSO. A kinetic analysis revealed that generation of ROS increased in the first hours of incubation before it reached a stable plateau after 4 hours (Figure S6a in magenta).

In a next step, 50 μM RSV was incubated at 37°C in KGM cell culture medium, which is used for NHEK cells (Figure 3.6a). After 16 hours the levels of ROS increased significantly by 1.16-fold (Figure 3.6a in green) when RSV was incubated in KGM compared to DMSO. Notably, comparable effects were also observed for the generation of $O_2^{\bullet -}$ (Figure S7a).

The ongoing generation of $O_2^{\bullet -}$ in KGM (Figure S7a green) can be explained by Fenton reaction-favoring conditions prevalent in cell culture medium. In contrast, in water containing 44 mM $NaHCO_3$ the $O_2^{\bullet -}$ generation declined (Figure S7a magenta), after reaching a maximum after roughly 2 hours, and amounted a similar level as the DMSO control.

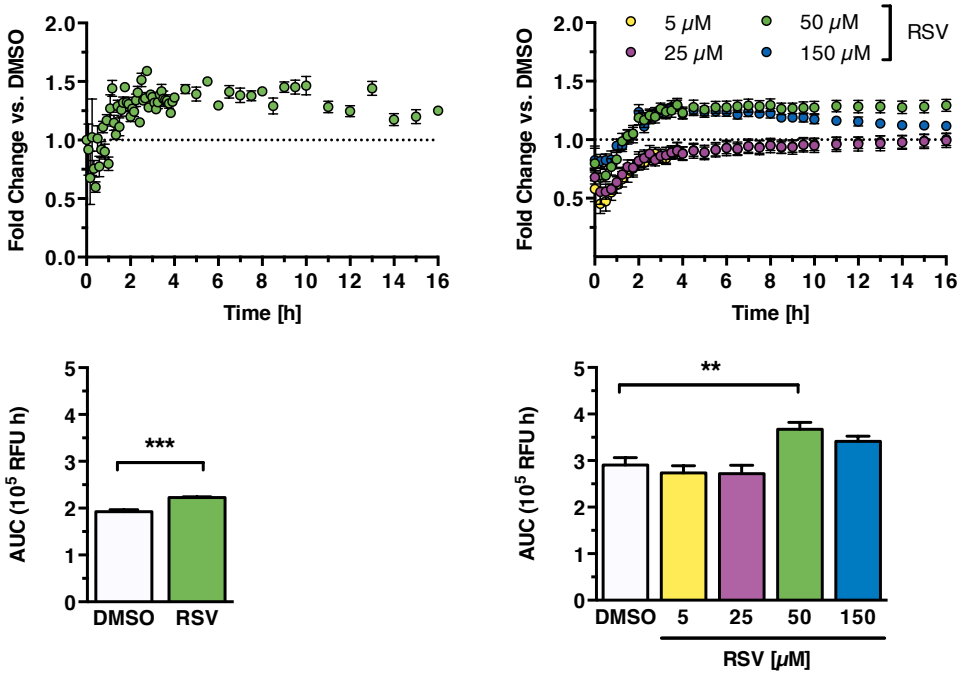

(a) Cell-free environment **(b) Intracellular (NHEK cells)**

Figure 3.6: RSV-driven generation of ROS. Kinetic (upper panel) and summed (lower panel) generation of ROS during 16 hours of incubation of RSV at 37°C. (a) Experiment was conducted in a cell-free environment using 50 μM RSV. Values are expressed as mean ± SEM (n = 6) relative to DMSO (dotted line) and statistical analysis was done using two tailed Student′s t-test: $***p \leq 0.001$ versus DMSO. (b) Intracellular generation of ROS during treatment NHEK cells with RSV. Values are expressed as mean ± SEM (n = 6) relative to DMSO (dotted line) and statistical analysis was done using one-way ANOVA with Dunnett′s post test for multiple comparisons: $**p < 0.01$ versus DMSO. See also Figure S6 for kinetic/summed ROS generation in water and Figure S7a for $O_2^{\bullet-}$ generation in KGM (both: cell-free environment).

The use of RSV in a skin context is a cutting-edge topic [329] as epidermal keratinocytes are a prime target for RSV-based lotions and emollients. In this work, neonatal normal human epidermal keratinocyte (NHEK) cells were chosen as primary cellular model for the study of the mechanism of action of RSV. The treatment of NHEKs with 50 μM RSV for 16 hours at 37°C resulted in a significant 1.26-fold increase of ROS compared to DMSO (Figure 3.6b). Interestingly, for lower RSV concentrations (< 50 μM) increased intracellular ROS levels could not be detected. However, higher RSV concentrations (150 μM, 1.17-fold) increased ROS levels (Figure 3.6b lower panel).

ROS can interact with various biomolecules including DNA, proteins and lipids. When targeting amino acid residues, ROS attacks can generate modified enzymes and proteins with less or completely diminished activity, denaturation and malfunction [192]. Moreover, ROS efficiently target the double bonds of polyunsaturated fatty acids thus leading to lipid peroxidation. The protection of cell membranes against lipid peroxidation is facilitated e.g. by GSH (Figure 1.11c), vitamin C (Figure 1.11a) and vitamin E (Figure 1.11b) [165, 177].

We hypothesized that an increased generation of diverse ROS driven by oxidation of RSV could cause lipid peroxidation in NHEK cells. Consequently, we analyzed NHEK cells treated with 50 μM RSV for 16 hours for intracellular lipid peroxidation (Figure S7b). Indeed, RSV significantly increased the lipid peroxidation in treated NHEK cells, thus endorsing our hypothesis.

3.2.2 Antioxidant capacity

From early on, polyphenols including RSV have been thought to possess antioxidant properties accounting to their ability to scavenge ROS [22, 38–40, 330]. The here applied assay measures the ability of antioxidants to inhibit the metmyoglobin-catalyzed oxidation of ABTS to $ABTS^{\bullet+}$. The amount of antioxidant is negatively correlated to the absorbance at 405 nm in a concentration-dependent manner [320–322]. Subsequently, the capacity of the antioxidant to prevent oxidation of ABTS (Figure 3.7a and Table S2a) is compared with that of Trolox (Figures 2.1 and 3.7b and Table S2b).

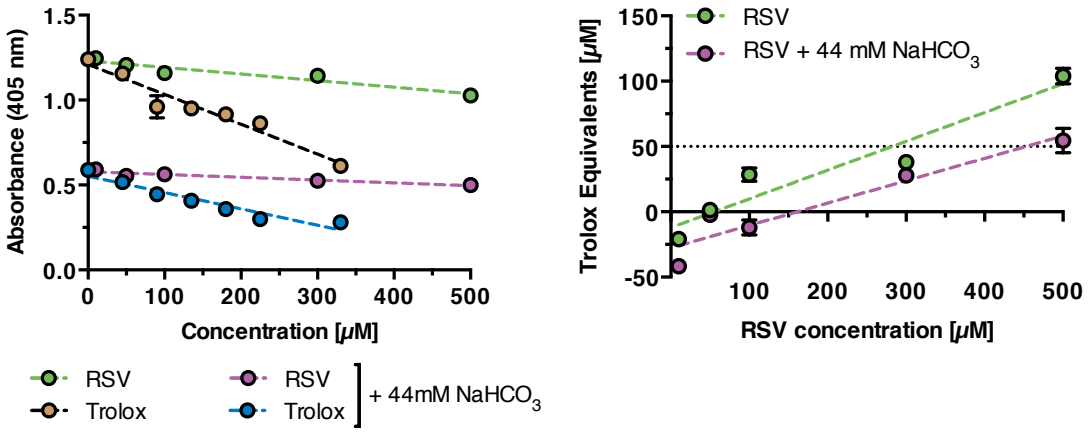

(a) Inhibition of ABTS oxidation **(b) Antioxidant capacity of RSV**

Figure 3.7: Antioxidant capacity of RSV and Trolox. (a) Trolox and RSV inhibit the oxidation of ABTS. (b) Antioxidant capacity of RSV was expressed as Trolox equivalents. Values are expressed as mean ± SEM (n = 3). Data were fitted (dashed line) using linear regression model. See also Table S2 and Figure 2.1.

The anti-oxidative capacity of RSV was roughly 6-fold smaller than that of Trolox, as an absorbance reduction to 0.1 OD was reached in presence of approximately 40 μM Trolox, whereas about 240 μM RSV were needed for the same effect (Figure 3.7a and Table S2a). Notably, the presence of 44 mM $NaHCO_3$ tremendously decreased the antioxidant capacity of RSV, whereas it did not affect Trolox (Figure 3.7a and Table S2a) [331].

The impact of 44 mM $NaHCO_3$ on RSV became obvious, when the antioxidant capacity of RSV was expressed as Trolox equivalents (Figure 3.7b and Table S2b). While about 280 μM RSV had an anti-oxidative capacity equal to 50 μM Trolox, 450 μM RSV were needed in the presence of 44 mM $NaHCO_3$ (dotted line in Figure 3.7b and Table S2b).

3.2.3 Antioxidants as scavengers

The ability of the potent antioxidants GSH and NAC to quench the RSV-driven generation of ROS was determined in cell-free environment as well as intracellularly using NHEKs.

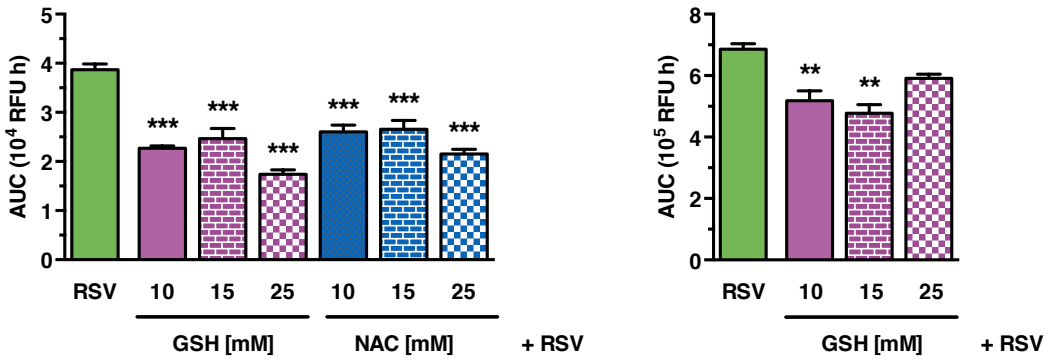

(a) Cell-free environment **(b) Intracellular (NHEK cells)**

Figure 3.8: Effects of GSH and NAC on RSV-driven generation of ROS. (a) Summed ROS generation after 16 hours of incubation in KGM. Either 50 μM RSV (green) or a combination of 50 μM RSV and GSH (magenta) or NAC (blue) were incubated at 37°C. Values are expressed as mean $\pm$ SEM (n = 4). (b) Summed intracellular ROS generation in NHEK cells after 16 hours treatment with RSV or a combination of RSV (green) and GSH (magenta). Values are expressed as mean $\pm$ SEM (n = 2-5). One-way ANOVA with Dunnett's post test for multiple comparisons: $**p < 0.01$, $***p \leq 0.001$ versus DMSO.

GSH and NAC significantly reduced the generation of ROS caused by the incubation of 50 μM RSV in KGM for 16 hours at 37°C (Figure 3.8a). Interestingly, the generation of ROS was reduced largely independent of the concentration of antioxidant. In a cellular context, GSH but not NAC (10−25 mM) efficiently quenched intracellular ROS generation (Figure 3.8b, data for NAC data not shown).

3.3 Cytotoxic effects

Under physiological conditions keratinocytes (including NHEKs) form a tight cell-layer (Figure 3.9) suitable as epidermal graft [329]. Notably, treatment with higher RSV concentrations for 16 hours changed the macroscopical appearance of NHEK cells tremendously to a more cobble-stone-like shape (Figure 3.9, 150 μM RSV). At 300 μM RSV holes appeared in the NHEK layer, the overall cell shape appeared to be more fringy and membrane blebbing was increased [67, 328].

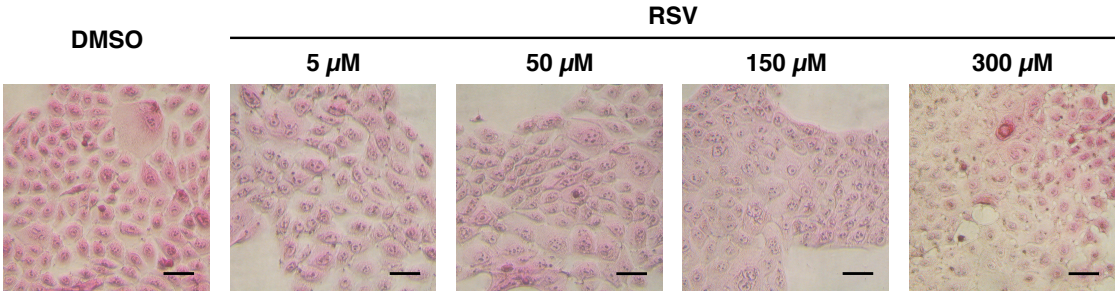

Figure 3.9: NHEK cells after 16 hours of treatment with RSV. Cells were stained with hematoxylin and eosin. Scale bar indicating 50 μm.

Keeping in mind the pro-oxidative and potentially cytotoxic effects of RSV [67, 328], the cytotoxicity of RSV was measured in diverse cellular models including skin and liver cells as well as macrophages (Figures 3.10 and S8). The majority of viability assays are luminescent-based and utilize luciferase as a reporter. However, luciferase is known to be inhibited by RSV [318]. Thus, a fluorescent-based viability assay was used measuring live-cell protease activity.

In NHEK cells treated with RSV for 16 hours at 37°C the amount of viable cells decreased with increasing RSV concentrations (Figure 3.10a green). However, at low doses an increase of viability was observed. In a control experiment, RSV treatment was conducted in presence of 25 mM GSH to quench ROS derived from RSV oxidation. Strikingly, there were almost no measurable effects on the viability of NHEKs (Figure 3.10a magenta). GSH tremendously truncated the cytotoxic effects of RSV on NHEK cells. When the IC_{50} and IC_{70} as well as the efficiency of RSV in NHEK cells was analyzed, the presence of 25 mM GSH resulted in a roughly 20-fold decreased IC_{70} value and a 75% reduced efficiency compared to RSV only treatment (Table S3). Importantly, the beneficial effects of lower RSV doses were also truncated in presence of GSH (Figure 3.10a magenta).

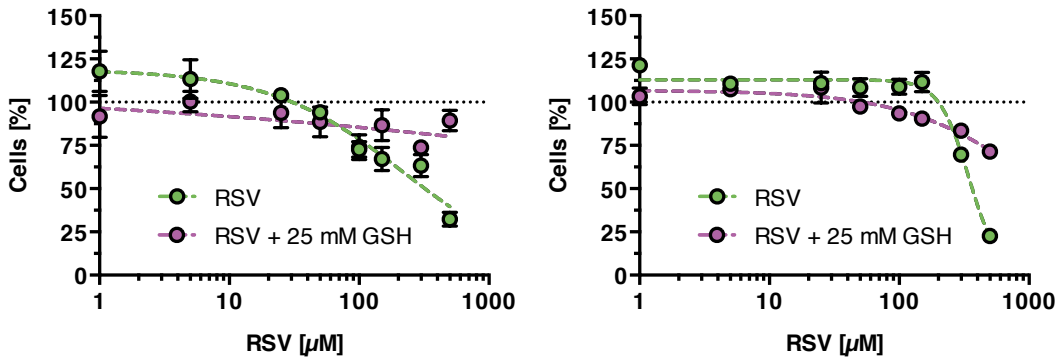

(a) NHEK cells **(b) NHDF cells**

Figure 3.10: Effects on viability of skin cells. NHEK (n = 3) (a) and NHDF cells (n = 6) (b) were treated for 16 hours with either RSV (green) or a combination of RSV and 25 mM GSH (magenta). Data were fitted (dashed line) according to equation Equation (2.3). Values are expressed as mean ± SEM. See also Figure S8 and Table S3.

In addition to epidermal keratinocytes, the cytotoxicity of RSV was assessed in NHDF cells, which were in summary less susceptible to RSV (Figure 3.10b). While lower doses of RSV (< 150 μM) exhibited beneficial effects on NHDF cells, higher concentrations resulted in a reduction of cellular viability (Figure 3.10b green). Similar to the effects observed in NHEK cells, the addition of 25 mM GSH resulted in a decreased IC_{70} value (roughly 1.6-fold) and a 63% reduced efficiency compared to RSV only treatment (Table S3). Quenching of ROS truncated not only the adverse but also the beneficial effects of RSV on cell viability (Figure 3.10b magenta).

Notably, the effects of RSV and quenching abilities of GSH were similar in HepG2 cells (Figure S8a) and THP-1 cells (Figure S8b), although the quenching effects of 25 mM GSH were smaller (Table S3) in these cell lines compared to skin cells (Figure 3.10).

3.4 Changes in whole-genome gene expression

To further analyze global expression changes induced by RSV, NHEK, and NHDF cells were subjected to genome-wide gene expression analysis. Experimental array data were validated with data obtained by qPCR. Accordingly, several target genes were chosen from qPCR-derived expression values and correlated to the array data (Figure S9).

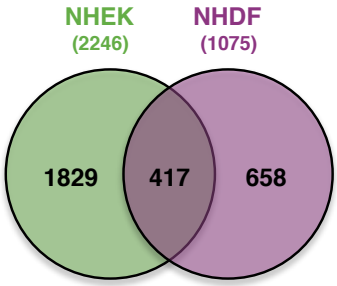

Figure 3.11: Venn diagram of differentially expressed genes after treatment of NHEK cells with 50 μM RSV (green) and NHDF cells with 100 μM RSV (magenta). Numbers in circles indicate up- and down-regulated genes, numbers in parentheses represent a total of regulated genes.

Whole-genome gene expression analysis of NHEK cells treated with 50 μM RSV and NHDF cells treated with 100 μM RSV revealed striking expression patterns (Figure 3.11). In treated NHEKs, 2,246 genes were significantly regulated (Figure 3.11 green), whereas in NHDFs RSV treatment resulted in 1,075 significantly regulated genes (Figure 3.11 magenta).

Gene set enrichment analysis (GSEA) was performed on the NHEK expression data to gain insights on major regulated gene pathways. The gene sets comprised curated KEGG pathways. Gene sets that were highly significantly changed (false discovery rate (FDR) ≤ 0.05) by RSV are shown in Figure 3.12 (See also Table S4). Gene sets were manually clustered; the most enriched pathways for RSV included oxidative stress, energy metabolism, inflammatory and PPAR signaling (all up-regulated) as well as down-regulated proliferation pathways (Figure 3.12 and Table S4).

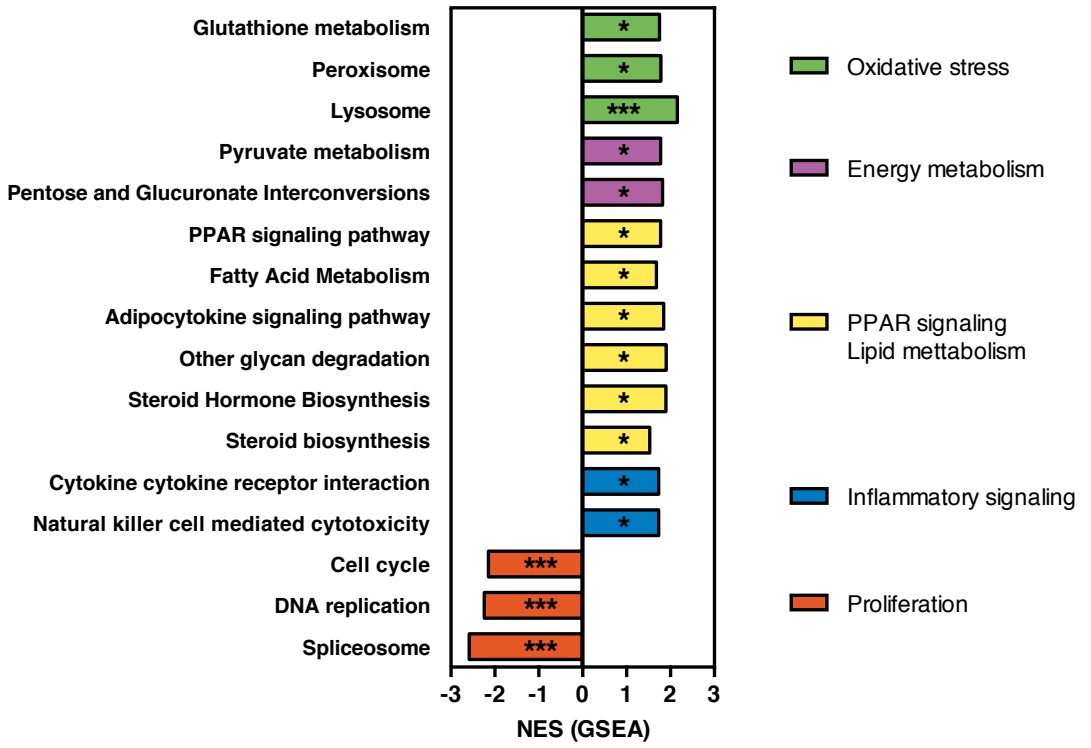

Figure 3.12: Enriched KEGG pathways after RSV treatment. NHEKs treated with 50 μM RSV for 16 hours were subjected to GSEA and the most highly enriched KEGG pathways (FDR ≤ 0.05) were selected. Values are NES (DMSO: n = 4; RSV: n = 3). Statistical analysis was done as described in Section 2.7: $*p < 0.05$, $**p < 0.01$, $***p \leq 0.001$ versus DMSO. See also Table S4. False discovery rate (FDR), normalized enrichment score (NES).

The Connectivity Map tool [317] was applied to the NHEK data to connect small molecules sharing a mechanism of action by comparison with stored data that were obtained from other research groups. Notably, a rather broad mechanism was revealed as in total 37 gene expression profiles of cells treated with diverse small molecules correlated highly significantly with a p value below 0.001 (data not shown).

Using the Connectivity Map implemented Anatomical Therapeutic Chemical (ATC) classification reduced the number of connections to 16 ($p \leq 0.001$, Table S5). ATC classifications included amongst many others anti-nematodal, anti-psychotic, immunosuppressant, anti-depressant, anti-cestodal, and anti-fungal agents. These results again emphasized a rather broad mode of action of RSV at least in NHEK cells.

3.5 Identification of marker genes

The whole-genome gene expression analysis highlighted several significantly regulated pathways. To elucidate the mechanism of action of RSV targeted experiments were conducted to explore the relationship of RSV to inflammatory signaling, proliferation, oxidative stress and energy metabolism in NHEKs.

3.5.1 Inflammation

As affirmed by whole-genome gene expression analysis (Figure 3.12), several pathways associated with inflammatory signaling were significantly up-regulated. The transcription factor NFκB is a key mediator of the inflammatory response and involved in diverse cellular pathways including apoptosis and development. Upon phosphorylation of its inhibitor nuclear factor of kappa light polypeptide gene enhancer in B-cells inhibitor (IκB), NFκB translocates into the nucleus to induce transcription of target genes [332, 333]. Recently, NFκB signaling has been linked to Nrf2 as both transcription factors appear to be redox-regulated [334–337]. However, the interaction of these two important factors requires further study.

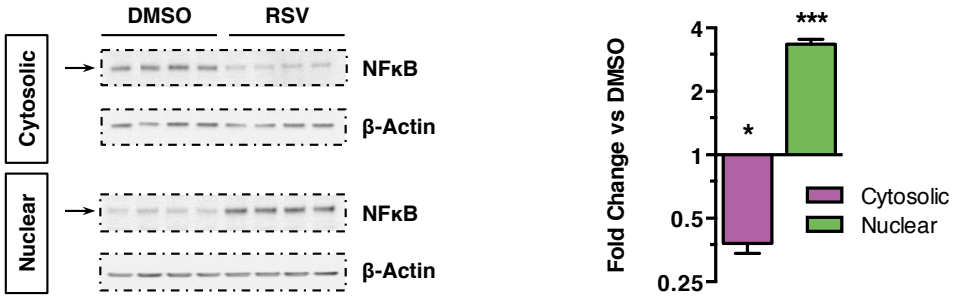

Figure 3.13: Effects of RSV on the expression of NFκB in NHEKs. Cells were treated with 50 μM RSV for 16 hours at 37°C. Expression of NFκB was detected by Western blot (left) and analyzed densitometrically (right) relative to β-Actin. Values are expressed as mean ± SEM (n = 4). Statistical analyses were done using two tailed Student′s t-test: $*p < 0.05$, $***p \leq 0.001$ versus DMSO.

The expression of NFκB in the nuclear fraction of NHEK cells treated with 50 μM RSV for 16 hours was investigated using Western blot (Figure 3.13). The amount of NFκB was highly significantly increased in the nuclear fraction of treated NHEK cells. Simultaneously, the amount of NFκB was highly significantly decreased in the cytosolic

fraction (Figure 3.13). These findings indicate a RSV-induced translocation of NFκB into the nucleus.

To further elucidate the mechanism of action of RSV in a concentration- and time-dependent manner, genes associated with inflammatory signaling were selected and analyzed by qPCR. CXCL8 gene encodes the chemokine interleukin 8 (IL-8), which can be produced by numerous cell types including macrophages and keratinocytes [338]. As a so-called neutrophil chemotactic factor, IL-8 is able to induce chemotaxis as well as phagocytosis. Nuclear factor of kappa light polypeptide gene enhancer in B-cells inhibitor alpha (NFκBIA) encodes nuclear factor of kappa light polypeptide gene enhancer in B-cells inhibitor alpha (IκB α), which inhibits the translocation of NFκB by blocking its translocation signal and ability to bind to DNA [332, 333].

JUN gene encodes the transcription factor c-Jun, which is known to interact with Nrf2 and CBP [339, 340]. JNK1 is encoded by mitogen-activated protein kinase 8 (MAPK8) gene and involved in proliferation, differentiation and regulation of transcription factors. In addition, it is known to interact with c-Jun [341], SIRT1 [95] and Nrf2 [342].

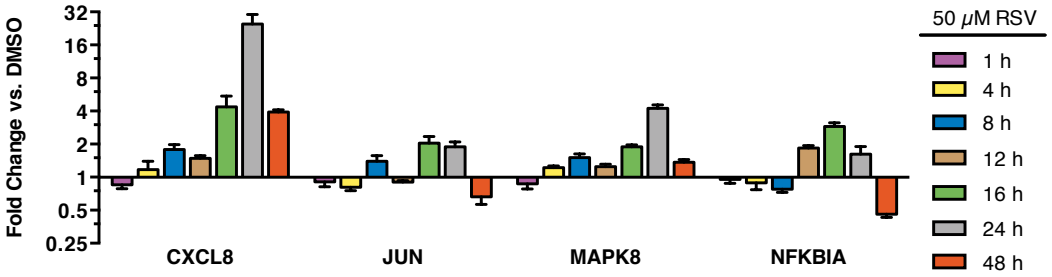

(a) Time-dependent gene expression

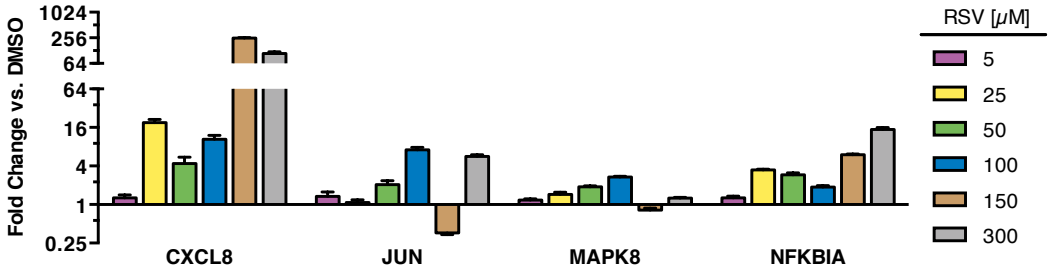

(b) Concentration-dependent gene expression

Figure 3.14: Effects of RSV on expression of inflammatory marker genes in NHEKs. Cells were treated at 37°C. Expression of marker genes was determined in response to different treatment times (a) and concentrations of RSV (b) relative to β-Actin. Values are expressed as mean ± SEM (n = 4).

As depicted in Figure 3.14a, the induction of inflammatory markers was dependent on the duration of treatment with 50 μM RSV. Notably, distinct increases were observed after 12 to 24 hours (Figure 3.14a) of treatment. Remarkably, the concentration of RSV had only a minor influence on the gene expression after 16 hours of treatment (Figure 3.14b). Starting from 25 μM, the increases in expression were comparable between the biomarkers up to 300 μM RSV. In addition, CXCL8 expression was increased considerably at RSV concentrations above 100 μM [343].

Notably, the induction of inflammatory marker genes by RSV was not only restricted to NHEKs cells, as similar effects were observed in diverse cellular model systems (Figure S10). These findings suggest at least a mild induction of inflammation in RSV treated NHEKs as well as in other cell lines.

3.5.2 Proliferation and Autophagy

As revealed by whole-genome gene expression analysis several pathways associated with proliferation, including cell cycle, DNA replication, and spliceosome, were highly significantly down-regulated (Figure 3.12). Thus, cell cycle phase distribution and the expression of several proliferation marker genes were analyzed in RSV-treated NHEKs.

Cell cycle phase distribution

The cell cycle is defined by several highly controlled phases. The G_1 phase is the entrance phase of the cell cycle where cells prepare for DNA duplication in S phase. Afterwards, cells enter G_2 phase where preparations are made for the subsequent M phase. Finally, cells can re-enter cell cycle through G_1 phase or go into the quiescent phase (G_0).

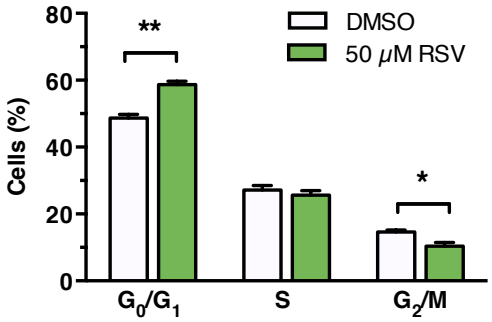

Figure 3.15: Effects of RSV on the cell cycle phase distribution. NHEK cells were treated for 16 hours with 50 μM RSV or DMSO. A Watson pragmatic fitting model was applied using FlowJo software. Values are shown as mean $\pm$ SEM (n = 4). Statistical analysis was done using two tailed Student′s t-test: $*p < 0.05$, $**p < 0.01$ versus DMSO.

To analyze the cell cycle phase distribution, NHEK cells were treated with 50 μM RSV for 16 hours at 37°C, stained by propidium iodide (PI) and subjected to flow cytometric analysis (Figure 3.15). The percentage of cells in S phase was not altered, in contrast to G_0/G_1 and G_2/M phase, which were both influenced by RSV. The number of cells in G_0/G_1 phase was significantly increased (+ 10%) by RSV, whereas the percentage of cells in the G_2 phase was significantly decreased ($-$ 4%) after RSV treatment (Figure 3.15). These findings corroborate the results revealed by whole-genome gene expression analysis (Figure 3.12).

In a next step several cell cycle progression proteins were analyzed, to determine whether a RSV-induced cell cycle arrest might be involved in the cell cycle phase distribution (Figure 3.15). Thus, several cyclins, cyclin-dependent kinases (CDKs) and cell cycle regulators were detected by Western blot.

During G_1 phase cyclin D1 forms a complex with CDK4 to enable cell cycle progression [344]. Moreover, CDK2 is known to form complexes with cyclin E2 in G_1 phase [345] and cyclins A2 in S phase [346]. Several other cyclin-CDK complexes are required to complete the cell cycle including cyclin A/CDK1 in G_2 and cyclin B/CDK1 in S phase. p21 binds to cyclin-CDK complexes and regulates cell cycle progression by inhibiting complexes of CDK1 and CDK2 at G_1 and S phase. Correspondingly, p21 is associated with cell cycle arrest, apoptosis and protection against oxidative stress [347,348].

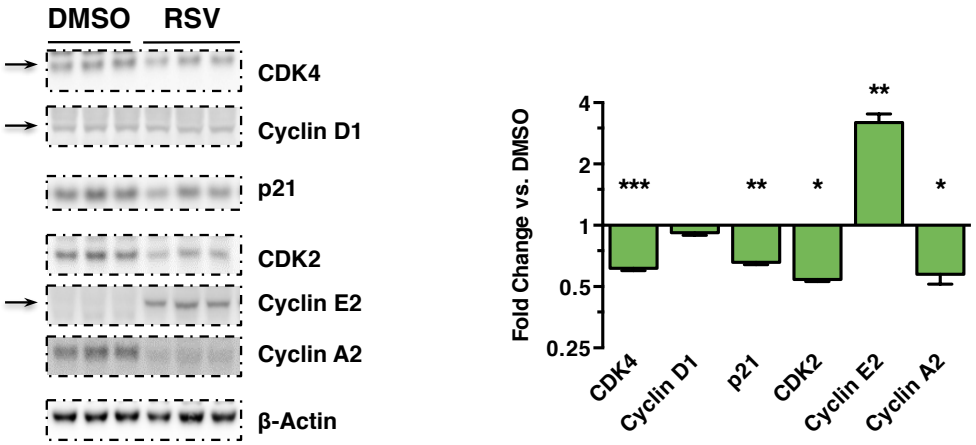

Figure 3.16: Effects of RSV on protein expression of cell cycle markers in NHEKs. Cells were treated for 16 hours at 37°C with 50 μM RSV. Expression of marker proteins was detected by Western blot (left) and analyzed densitometrically (right) relative to β-Actin. Values are expressed as mean ± SEM (n = 3). Statistical analysis was done using two tailed Student′s t-test: $*p < 0.05$, $**p < 0.01$, $***p \leq 0.001$ versus DMSO.

After 16 hours of treatment with 50 μM RSV, the protein levels of almost all cell cycle markers were highly significantly decreased in treated NHEK cells (Figure 3.16). The only exception was cyclin E2, which was up-regulated 3-fold (Figure 3.16). The accumulation of cyclin E2 and the simultaneous decrease of CDK4 and CDK2 suggested a cell cycle arrest in G_1 phase, thus supporting the results presented in Figure 3.15.

Apoptosis

The link between cell cycle arrest and apoptosis has been well established [349, 350]. Apoptosis describes a form of programmed cell death and involves active proteases, which degrade cellular structures within the intact plasma membrane. Initiation of apoptosis can be either intrinsic (via mitochondrial signaling) or extrinsic (via death receptor signaling). To investigate the role of RSV in the putative induction of apoptosis, several marker genes associated with (mitochondrial regulated) programmed cell death were analyzed by qPCR (Figure 3.17a). Furthermore, the externalization of phosphatidylserine was investigated by flow cytometric analysis (Figure 3.17b) and several protein markers for apoptosis were monitored (Figure 3.18).

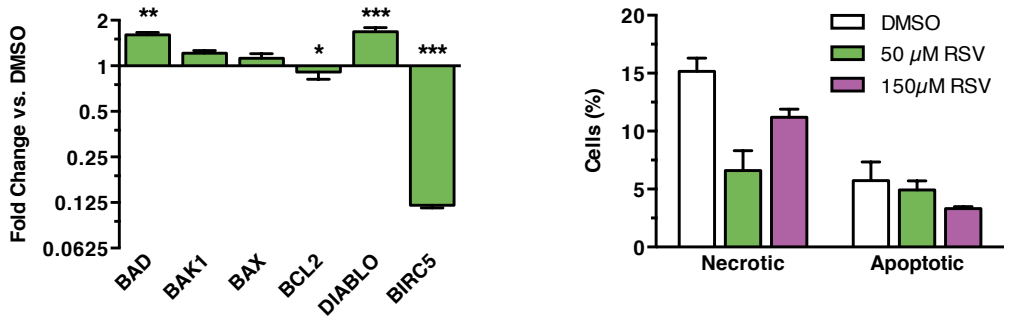

(a) Apoptosis marker genes **(b) Apoptotic cell proportion**

Figure 3.17: Effect of RSV on apoptosis. (a) Expression of apoptosis marker genes in NHEKs after treatment with 50 μM RSV for 16 hours. Values are expressed as mean $\pm$ SEM (n = 4). Statistical analysis was done using two tailed Student′s t-test: $*p < 0.05$, $**p < 0.01$, $***p \leq 0.001$ versus DMSO. (b) Effect of RSV on the externalization of propidium iodide (PI) in NHEKs treated with RSV for 16 hours analyzed by flow cytometric FACS. Values are expressed as mean $\pm$ SEM (n = 2).

The proteins of the B-cell lymphoma 2 (BCL2) family tightly regulate intrinsic apoptotic signaling. Members of this family are the anti-apoptotic BCL2, as well as pro-apoptotic BCL2-associated X protein (BAX), BCL2-antagonist/killer1 (BAK1) and BCL2-associated death promoter (BAD). For a detailed review of specific functionalities please see [351, 352]. In NHEK cells treated with 50 μM RSV for 16 hours at 37°C, the expression of most apoptosis marker genes was not significantly changed. A mild induction of apoptosis is nevertheless suggested by the increased expression of pro-apoptotic BAD as well as decreased expression of anti-apoptotic BCL2 (Figure 3.17a).

Direct IAP binding protein with low pI (DIABLO) is required for the cytochrome-c-dependent activation of caspase cascades by binding several apoptosis inhibitors including baculoviral inhibitor of apoptosis repeat-containing 5 (BIRC5) [353]. The gene expression of both apoptosis markers was highly significantly regulated, hence further endorsing the hypothesis of a mild induction of apoptosis by RSV treatment in NHEK cells (Figure 3.17a).

Using flow cytometry the externalization propidium iodide (PI) was analyzed to further elucidate the role of apoptosis in RSV treated NHEKs. After 16 hours of treatment with RSV the proportion of necrotic cells was reduced, while the number of apoptotic cells remained unchanged (Figure 3.17b). These findings suggest a protective effect of RSV against necrosis, simultaneously there is no evidence of increased apoptosis.

Additionally, apoptosis was studied by Western blotting of relevant caspases (Figure 3.18). Caspases are cysteine-aspartic proteases and important regulators of apoptosis. Caspase signaling although hierarchical is highly inter-dependent as each caspase has an inactive pro-form and a cleaved effector form [354]. Cleavage and thus activation of caspase 9 is caused by intrinsic signaling via c-Jun N-terminal kinase (JNK) and cytochrome c. Once activated, the effector caspase 9 cleaves pro-caspase 7, which in turn cleaves PARP [354].

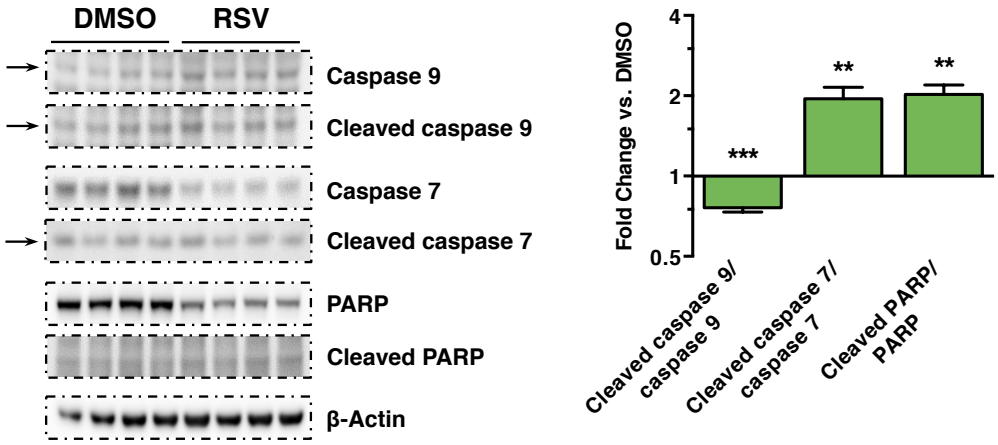

Figure 3.18: Effect of RSV on apoptotic protein markers. Protein expression in NHEK cells treated for 16 hours at 37°C with 50 μM RSV. Expression of marker proteins was detected by Western blot (left) and analyzed densitometrically (right) relative to β-Actin. Values are expressed as mean ± SEM (n = 4). Statistical analysis was done using two tailed Student′s t-test: $**p < 0.01$, $***p \leq 0.001$ versus DMSO.

In NHEKs treated with 50 μM RSV for 16 hours, the amount of the effector form of caspase 9 was significantly decreased compared to the pro-form (Figure 3.18). The significant increase of cleaved caspase 7 suggested apoptotic signaling downstream of caspase 9 [355] and cleavage of PARP indicating efficient activation of the apoptotic cascade in NHEKs (Figure 3.18).

Senescence and Autophagy

Besides apoptosis, senescence and autophagy are two additional possibilities to cope with damaged cells [277]. In general, senescence features an arrest in G_1 cell cycle phase of deliberately proliferating cells in account to stress [6,276]. As such, senescence can be a part of cell cycle arrest. Although senescence is widely regarded as a contributor to life span expansion, with age the cells accumulate in tissues diminishing their proliferative capacity [277]. In contrast, autophagy describes the regulated disassembly of unnecessary or dysfunctional elements and their subsequent recycling [277, 282].

The expression of selected senescence marker genes was analyzed in NHEK cells treated with 50 μM RSV for 16 hours (Figure S11a). While the cell cycle regulators cyclin-dependent kinase inhibitor 2A (CDKN2A) and insulin-like growth factor-binding protein 3 (IGFBP3) were significantly down-regulated, the remaining senescence markers including e.g. galactosidase β 1 (GLB1) were significantly up-regulated (Figure S11a). The observed effects indicate a slightly increased senescence, which in turn might be attributed to the cell cycle arrest in G_1 phase.

To investigate the putative induction of autophagy by RSV, treated NHEKs were stained against microtubule-associated protein 1 light chain 3 (MAP1LC3), a frequently used marker of autophagosomes [356, 357] (Figure 3.19). After RSV treatment, fluorescent MAP1LC3 signals were visible throughout the cell (Figure 3.19d) and not anymore restricted to the proximity of the nucleus (Figure 3.19c). In addition, gene expression analysis of autophagy markers showed a highly significant up-regulation of death associated protein kinase 1 (DAPK1) and MAP1LC3 (Figure S11b). These findings suggest that RSV slightly induced autophagy in NHEK cells [358].

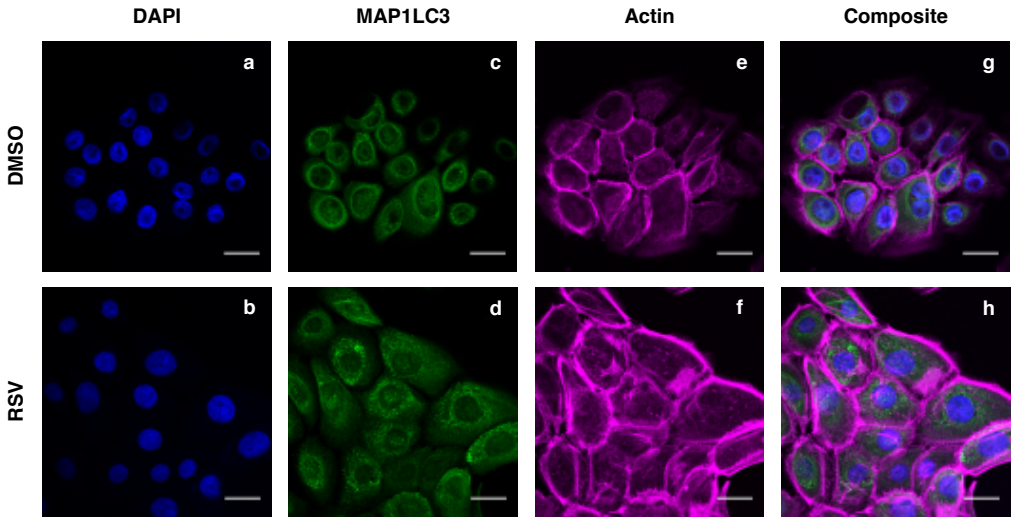

Figure 3.19: Effects of RSV on autophagosomal marker protein MAP1LC3. NHEKs were treated with 50 μM RSV and DMSO were subjected to fluorescence staining marking DAPI (blue, a and b), MAP1LC3 (green, c and) and Actin (magenta, e and f). Scale bar equals 25 μm. Pictures were processed using ImageJ [326, 327].

To further elucidate the mechanism of action of RSV, genes associated with proliferation and autophagy were selected and analyzed by qPCR. Keratin 14 (KRT14) encodes a member of the very diverse keratin family and is important for the cytoskeleton of epithelial cells and a well-known differentiation marker of keratinocytes. However, the influence of RSV on KRT14 gene expression was very minor. Whereas prolonged (12 to 24 hours) treatment with 50 μM RSV increased the expression of KRT14 (Figure 3.20a), a concentration-dependent regulation was not observed after 16 hours of treatment with RSV (Figure 3.20b).

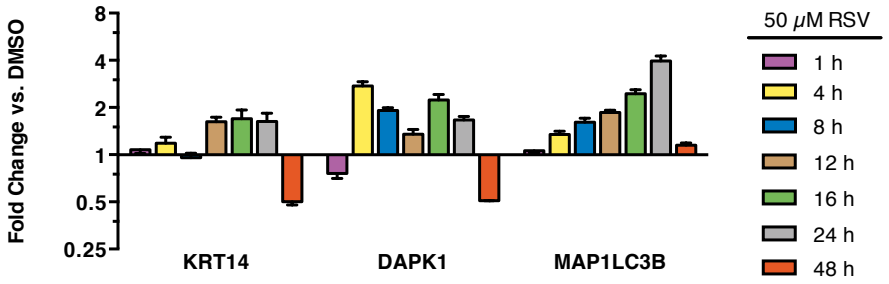

(a) Time-dependent gene expression

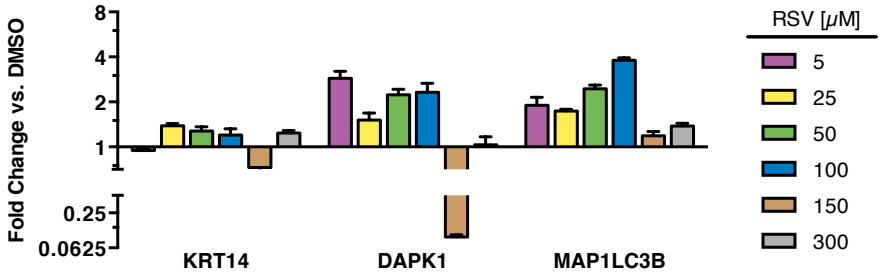

(b) Concentration-dependent gene expression

Figure 3.20: Effects of RSV on expression of proliferation marker genes. NHEK cells were treated at 37°C. Expression of marker genes was determined in response to different treatment times (a) and concentrations of RSV (b) relative to β-Actin. Values are expressed as mean ± SEM (n = 4).

Death associated protein kinase 1 (DAPK1) and microtubule-associated protein 1 light chain 3B (MAP1LC3B) are both associated with autophagy [359] and often used as autophagosomal markers [356, 357]. After treatment with 50 μM RSV, the expression of DAPK1 and MAP1LC3B was increased after 4 to 24 hours of treatment (Figure 3.20a) and after 16 hours at 5 to 100 μM RSV (Figure 3.20b). Notably, the induction of autophagy marker genes by RSV was not only restricted to NHEKs. It was observed in diverse cellular model systems (Figure S12). These findings suggest at least a mild induction of autophagy in RSV treated NHEKs [360] as well as in other cell lines.

3.5.3 Oxidative stress

Under physiologically relevant conditions the oxidation of RSV resulted in the generation of various ROS. In addition, whole-genome gene expression analysis displayed significantly increased pathways related to oxidative stress (Figure 3.12). To further

elucidate the mechanism of action of RSV, genes associated with oxidative stress were selected and analyzed by qPCR (Figure 3.21).

Catalase (CAT) is localized in mammalian peroxisomes and catalyzes the detoxification of H_2O_2 [181, 182], phenols and alcohols [151] (Figure 1.12). Nrf2 is the central regulator of oxidative stress response, as the transcription factor binds to the promotor of target genes including NAD(P)H dehydrogenase (quinone 1) (NQO1), glutamate-cysteine ligase (catalytic subunit) (GCLC) and glutathione reductase (GSR) to induce transcription (see Section 1.5). Kelch-like ECH-associated protein 1 (KEAP1) directly interacts with Nrf2 and regulates the activity of the transcription factors very tightly (see Section 1.5).

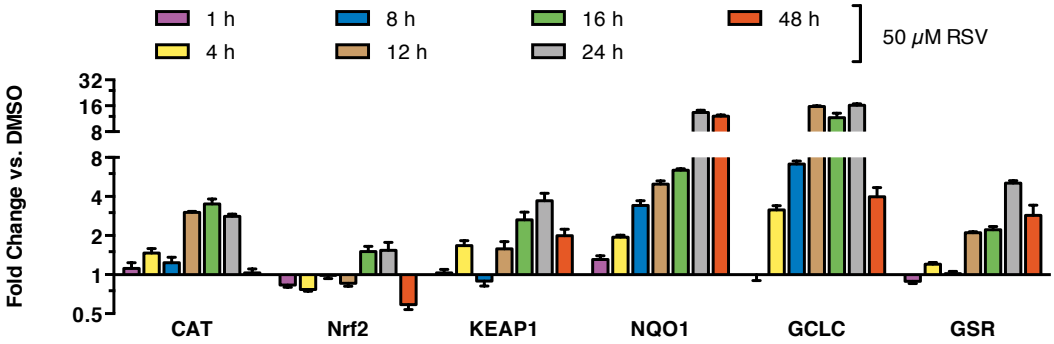

(a) Time-dependent gene expression

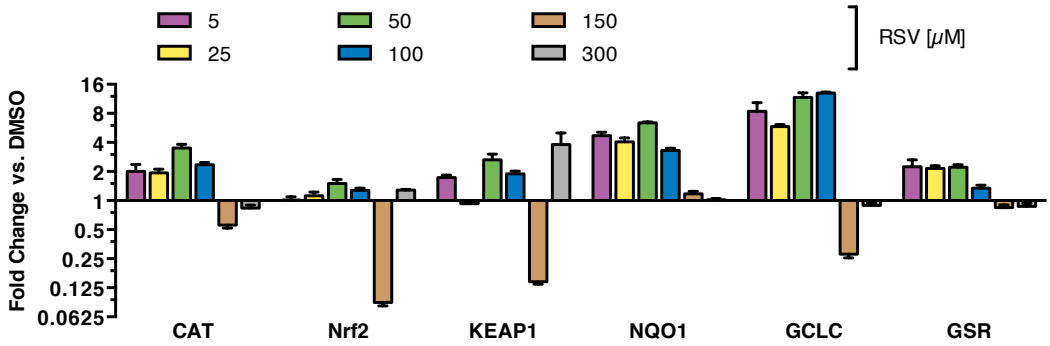

(b) Concentration-dependent gene expression

Figure 3.21: Effects of RSV on expression of oxidative stress marker genes. NHEK cells were treated at 37°C and the expression of marker genes was determined in response to different treatment times (a) and concentrations of RSV (b) relative to β-Actin. Values are expressed as mean ± SEM (n = 4).

As shown in Figure 3.21a, the induction of oxidative stress markers was dependent on the duration of treatment with 50 μM RSV. Notably, an increase of gene expression was observed after 12 to 24 hours (Figure 3.21a) of treatment. After 48 hours, expression was strikingly decreased for the majority of marker genes.

Remarkably, the concentration of RSV had only a minor influence on the gene expression (Figure 3.21b). From 5 μM to 100 μM the increases in expression were comparable between the different biomarkers. At higher treatment concentrations, marker genes were either highly down-regulated (150 μM) or not regulated (300 μM).

The expression of marker genes associated with oxidative stress was investigated in additional cellular models, which displayed an expression pattern comparable to that of NHEK cells (Figure S13 and Table S6), suggesting a conserved mode of action.

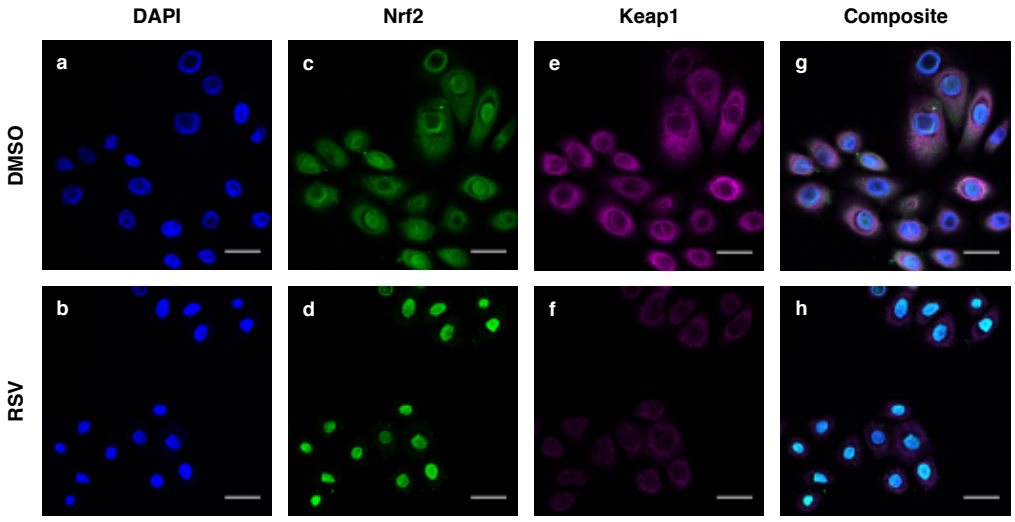

Figure 3.22: Effects of RSV on the translocation of Nrf2. NHEKs were treated with 50 μM RSV and DMSO were subjected to fluorescence staining marking DAPI (blue, **a** and **b**), Nrf2 (green, **c** and **d**) and Keap1 (magenta, **e** and **f**). Scale bar equals 25 μm. Pictures were processed using ImageJ [326, 327].

The increased expression of Nrf2 and corresponding target genes such as NQO1, GCLC and GSR suggests a prominent role of Nrf2 in RSV-induced signaling. To test this hypothesis, NHEK cells were treated for 16 hours with 50 μM RSV to analyze the subcellular localization of fluorescent labeled Nrf2 and KEAP1 (Figure 3.22). Whereas Nrf2 resided in the cytoplasm in DMSO treated cells (Figure 3.22c), it translocated into the nucleus after RSV treatment (Figure 3.22d). Remarkably, Keap1 fluorescence was almost invisible after RSV treatment of NHEKs (Figure 3.22e vs. f).

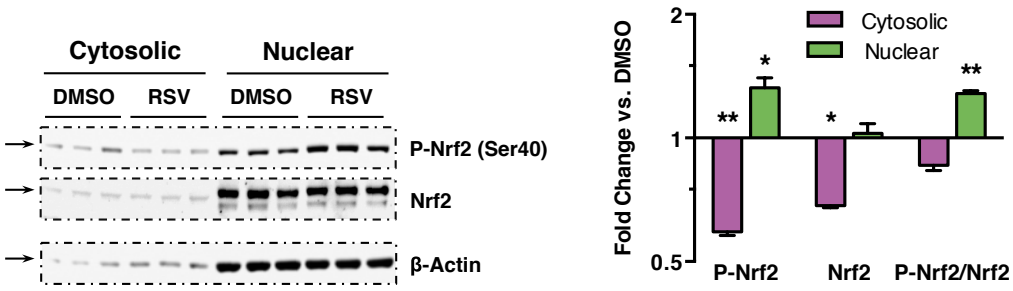

Figure 3.23: Effect of RSV on the translocation and phosphorylation of Nrf2. NHEK cells were treated for 16 hours at 37°C with 50 μM RSV. Nrf2 translocation and phosphorylated at serine 40 was detected by Western blot (left) and analyzed densitometrically (right) relative to β-Actin. Values are expressed as mean $\pm$ SEM (n = 4). Statistical analysis was done using two tailed Student′s t-test: $*p < 0.05$, $**p < 0.01$ versus DMSO.

To induce the transcription of target genes, Nrf2 has i) to translocate into the nucleus and ii) to be phosphorylated (see Section 1.5). Both molecular events were monitored in NHEKs treated for 16 hours with 50 μM RSV (Figure 3.23). Upon treatment with RSV, the cytosolic level of Nrf2 and its phosphorylated form were significantly decreased, whilst the amount of phosphorylated Nrf2 significantly increased in the nuclear fraction (Figure 3.23). In addition, RSV increased the amount of phosphorylated Nrf2 (relative to non-phosphorylated Nrf2) in the nuclear fraction. These findings suggest a RSV-driven translocation and phosphorylation of Nrf2 causing subsequent activation of target genes.

To further investigate the role of Nrf2 in mediating RSV-induced effects, a knockdown of Nrf2 gene was performed prior to RSV treatment. Notably, a knockdown of 80% was achieved for Nrf2 (Figure 3.24a in black). In addition, a SIRT1 knockdown was carried out, resulting in a knockdown efficacy of 70% for SIRT1 and simultaneously 20% for Nrf2 (Figure 3.24a). These finding suggest a link between Nrf2 and SIRT1 in mediating RSV-induced effects.

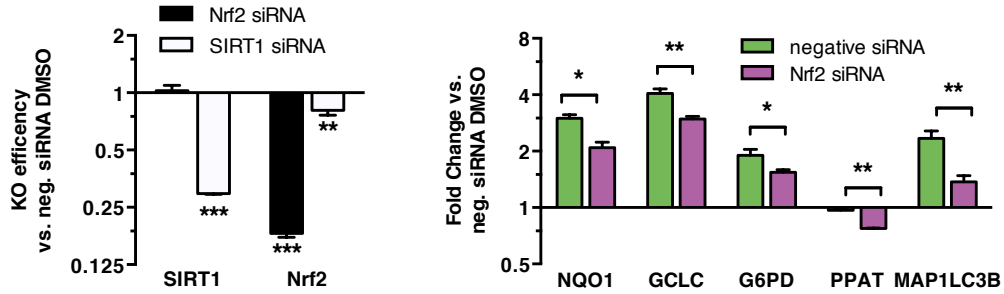

(a) Knockdown efficiency **(b) Nrf2 knockdown: RSV treatment**

Figure 3.24: Effects of RSV in NHEK cells after knockdown of Nrf2 and SIRT1. Expression of marker genes was determined relative to β-Actin. (a) Efficiency of SIRT1 and Nrf2 knockdown. Values are expressed as mean ± SEM (n = 4). Statistical analysis was done using two tailed Student′s t-test: $**p < 0.01$, $***p \leq 0.001$ versus negative siRNA DMSO. (b) Expression of Nrf2 marker genes after Nrf2 knockdown. Values are expressed as mean ± SEM (n = 4). Statistical analysis was done using two tailed Student′s t-test: $*p < 0.05$, $**p < 0.01$ versus negative siRNA DMSO. See also Figure S14.

Knockdown of Nrf2 truncated RSV-induced changes on gene expression, as all Nrf2 target genes were significantly down-regulated. Notably, the effects of Nrf2 knockdown were less distinct (Figure S14). These findings endorse the hypothesis that Nrf2 is a key mediator of the effects observed after RSV treatment in NHEK cells.

Nrf2 is known as the key regulator of oxidative stress response. Induction of Nrf2 signaling could be caused by the RSV-driven generation of ROS. To test this hypothesis, NHEK cells were treated for 16 hours with 50 μM RSV and the expression of selected marker genes was investigated in response to 25 mM GSH, which was directly added to RSV (Figure 3.25).

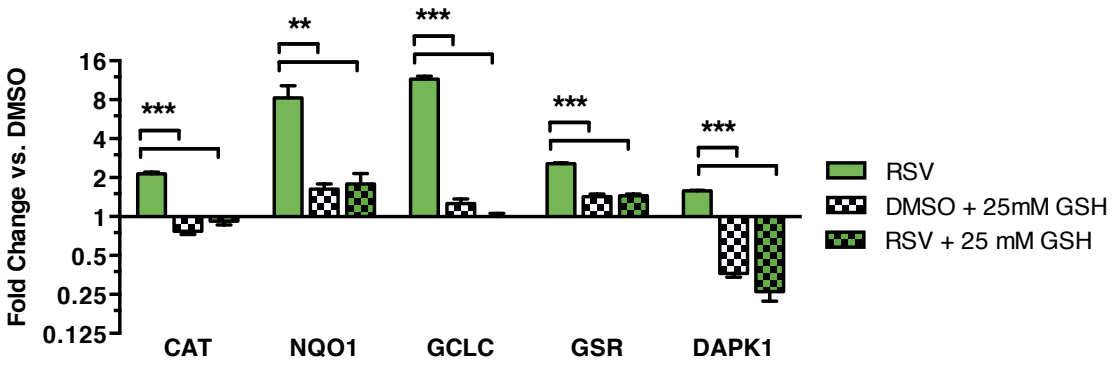

Figure 3.25: GSH quenches effects of RSV on gene expression. NHEKs were treated for 16 hours with 50 μM RSV (green bars) or a combination of RSV/DMSO and 25 mM GSH (patterned bars). Values are expressed as mean $\pm$ SEM (n = 4). Statistical analysis was done using one-way ANOVA with Dunnett′s post test for multiple comparisons: $**p < 0.01$, $***p \leq 0.001$ versus RSV.

The RSV-driven increases in gene expression were significantly quenched in presence of 25 mM GSH, with DAPK1 being the only exception (Figure 3.25). Remarkably, the quenching effect of GSH was also observed for Nrf2 target genes NQO1, GCLC and GSR. These findings endorse the hypothesis that RSV-driven generation of ROS is the major cause for the observed Nrf2 signaling.

3.5.4 Energy metabolism

As revealed by whole-genome gene expression analysis (Figure 3.12) several pathways associated with energy metabolism signaling were significantly up-regulated due to RSV treatment. To further investigate the influence of RSV on the energy metabolism, the expression of several marker genes was monitored. Glucose-6-phosphate dehydrogenase (G6PD) and phosphoribosyl pyrophosphate amidotransferase (PPAT), which seemed regulated by RSV, are both part of the pentose phosphate pathway (PPP). Recently Mitsuishi et al. showed that Nrf2 can promote a metabolic switch by re-routing glucose and glutamine into PPP [261] and that G6PD and PPAT are target genes of Nrf2.

Adenosine triphosphate (ATP) citrate lyase (ACLY) links carbohydrates metabolism to fatty acid biosynthesis, which was also significantly influenced by RSV (Figure 3.12). Moreover, FOXO3 belongs to the family of forkhead box proteins (FOXOs) transcription factors, which are phosphorylated by protein kinase B (PKB) during phosphatidylinositol-4,5-bisphosphate 3-kinase (PI3K) signaling resulting in nuclear exclusion and subsequent

inhibition. In addition, FOXO3 is regulated by post-translational modification and a known target of SIRT1 (see Section 1.3.2).

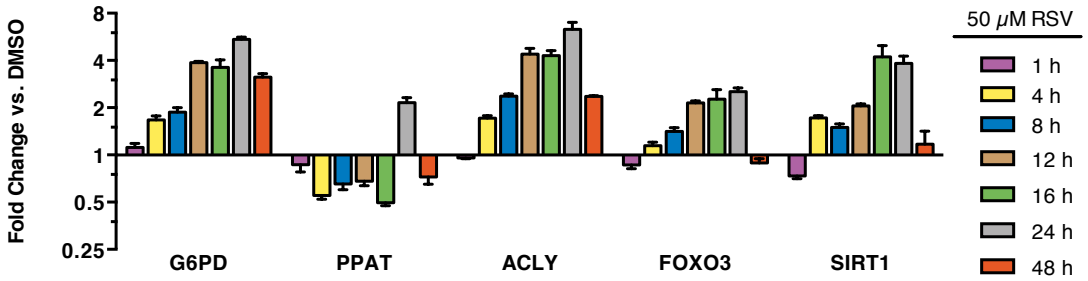

(a) Time-dependent gene expression

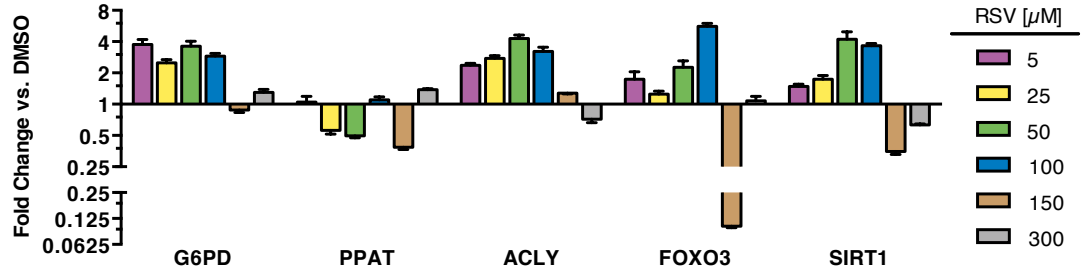

(b) Concentration-dependent gene expression

Figure 3.26: Effects of RSV on expression of energy metabolism marker genes. NHEK cells were treated at 37°C. Expression of marker genes was determined in response to different treatment times (a) and concentrations of RSV (b) relative to β-Actin. Values are expressed as mean ± SEM (n = 4).

As shown in Figure 3.26a the induction of energy metabolism markers was dependent on the duration of treatment with 50 μM RSV. Notably, distinct increases were observed after 4 to 24 hours (Figure 3.21a) of treatment. After 48 hours of treatment, the fold change was decreasing for the majority of marker genes. Remarkably, the concentration of RSV had only a minor influence on the gene expression (Figure 3.26b). Starting from 5 μM the increases in gene expression were comparable between the biomarkers until 100 μM RSV. At higher treatment concentrations, marker genes were either highly down-regulated (150 μM) or not regulated (300 μM).

The expression of marker genes associated with oxidative stress was investigated in additional cellular models, which mostly displayed an expression pattern comparable to that of NHEK cells (Figure S15 and Table S6), suggesting a conserved mode of action.

To further investigate the regulation of SIRT1 by RSV, we analyzed the phosphorylation and subcellular localization of SIRT1 after 16 hours of treatment with 50 μM RSV in NHEK cells (Figure S17). RSV significantly increased the amount of phosphorylated SIRT1 in the nuclear fraction and, compared to SIRT1, in both cytosolic and nuclear fraction. These results suggest that RSV induced phosphorylation and translocation of SIRT1 into the nucleus to promote subsequent signaling [95].

To quantify the redox state and finally the redox environment, a reliable quantitative analysis of intracellular metabolites is mandatory. The glutathione couple (GSH/GSSG) provides by far the largest pool of reducing equivalents and can be used as an indicator for the cellular redox environment [304].

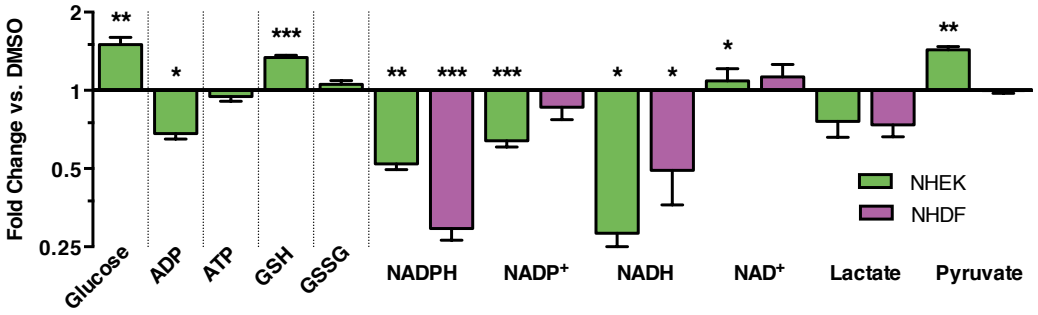

Figure 3.27: Quantification of intracellular metabolites in RSV treated skin cells; NHEKs depicted in green and NHDFs depicted in magenta. Values are expressed as mean ± SEM (NHEK: n = 4; NADPH, $NADP^+$ n = 3; NHDF: n = 4; NADH, NAD^+ n = 3). Statistical analyses were done using two tailed Student′s t-test: $*p < 0.05$, $**p < 0.01$, $***p \leq 0.001$ versus DMSO. See also Figure S19.

The intracellular concentration of several other metabolites (see Section 2.11) was determined in NHEK cells treated for 16 hours with 50 μM RSV (Figure 3.27). While the amount of ATP remained unchanged, glucose was significantly increased and ADP significantly decreased. Remarkably, only concentrations of glucose, GSH and pyruvate were significantly increased. Notably, the strong increase of the GSH level is mirrored by the highly significant regulation of GSH metabolism-associated marker genes (Figure S16). Moreover, RSV increased the phosphorylation of pyruvate dehydrogenase E1-alpha (PDE1α), which inhibited the enzyme and prevented further metabolization of pyruvate (Figure S18).

Concentrations of most of the remaining metabolites were highly significantly decreased including NADPH, $NADP^+$, and NADH. In contrast, the levels of GSSG and

lactate were not influenced by RSV treatment (Figure 3.27). These findings are in line with the results of the whole-genome gene expression analysis, indicating increased glutathione metabolism, pyruvate metabolism, and pentose as well as glucuronate interconversions in NHEKs (Figure 3.12). Notably, NADPH, $NADP^+$, NADH, NAD^+, and lactate were regulated similarly in NHEK and NHDF cells (Figure 3.27 green vs. magenta). In a next step, metabolite ratios of corresponding redox couples were calculated, which are in turn required for the calculation of the redox state and environment (Figure S19 and Section 3.6).

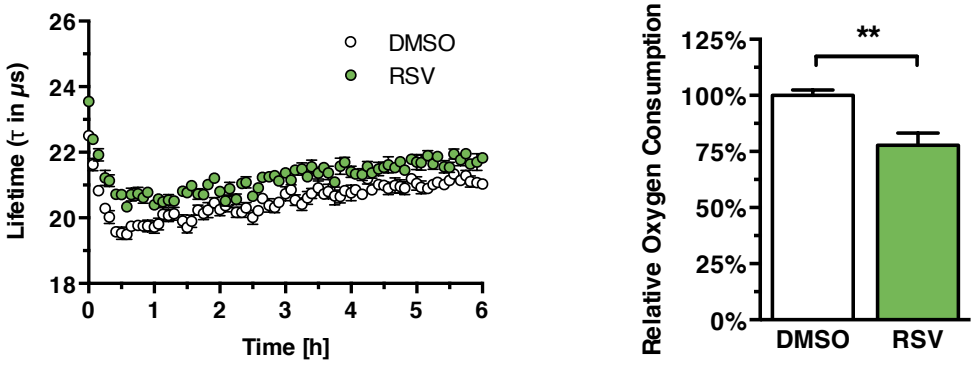

(a) Fluorescence lifetime **(b) Oxygen consumption**

Figure 3.28: Effects of RSV on oxygen consumption. NHEKs were treated for 16 hours with 50 μM RSV. Mitochondrial oxygen consumption was determined by fluorescence quenching. The fluorescence lifetime was kinetically monitored (a) and the rate of fluorescence lifetime change calculated (b). Values are expressed as mean $\pm$ SEM (n = 8). For statistical analysis a two tailed Student's t-test: $***p \leq 0.001$ versus DMSO was applied.

RSV has been linked to mitochondrial biogenesis via the SIRT1-PGC1-α-axis [361–363]. Thus, the mitochondrial oxygen consumption was investigated by fluorescence quenching (Figure 3.28). The increased fluorescence lifetime corresponds to a reduced concentration of extracellular oxygen (Figure 3.28a). The rate of fluorescence lifetime change between 1 and 4 hours after the treatment revealed a significant decrease of relative oxygen consumption (Figure 3.28b). These findings suggest that RSV did not induce mitochondrial biogenesis in treated NHEK cells.

The Nernst equation (Equation (1.3)) provides the basis for calculating redox state and environment. Hence, it is crucial to consider experimental parameters such as temperature (Equation (1.4)) and pH (Equation (1.7)). RSV decreased the lactate concentration though

not significantly (Figure 3.27). To gain more detailed information on lactate fluctuations the extracellular acidification rate (ECAR) was measured in NHEK cells treated with 50 μM RSV for 16 hours (Figure 3.29).

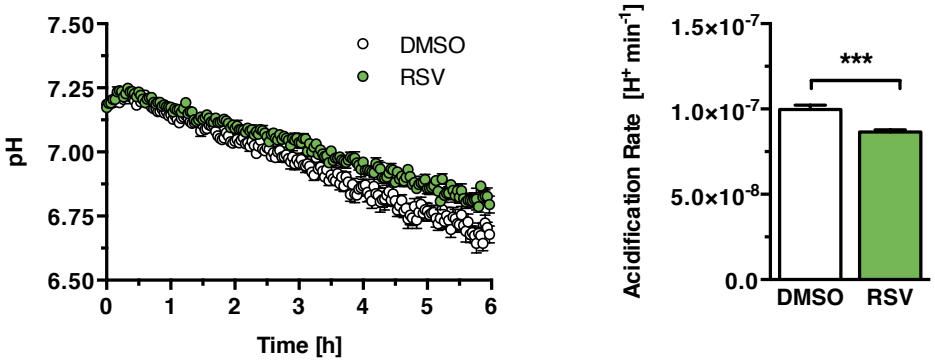

(a) Kinetic pH development **(b) Acidification rate**

Figure 3.29: Effects of RSV on extracellular acidification (ECAR). NHEKs were treated for 16 hours with 50 μM RSV. ECAR was determined and the fluorescence lifetime was transformed to pH values (a) and plotted as hydrogen ion concentration change per minute (b). Values are expressed as mean $\pm$ SEM (n = 8). For statistical analysis a two tailed Student′s t-test: $***p \leq 0.001$ versus DMSO was applied.

RSV treatment resulted in a slightly higher pH compared to DMSO within the first 6 hours after of treatment (Figure 3.29a). Calculating the acidification rate (Figure 3.29a) revealed a significant decrease of pH. As ECAR reflects glycolytic activity [323], these results confirm the slightly reduced lactate concentration (Figure 3.27). In addition, the here determined pH values were considered for the calculation of the redox state according to Equation (1.8).

3.6 Redox environment

The redox state (Equation (1.8)) is defined by the reduction potential ($E^{\circ'}$) of one redox couple and characterized by the concentration of the reduced species. In contrast, the redox environment (Equation (1.9)) takes into account a set of redox couples, thus enabling a more global evaluation of the cellular redox state. The glutathione couple (GSH/GSSG) provides by far the largest pool of reducing equivalents and is a suitable

indicator for the cellular redox state and environment [304, 309].

$$\mathrm{GSSG} + 2H^+ + 2e^- \rightarrow 2\mathrm{GSH} \qquad E^{0'} = -240\ \mathrm{mV} \tag{3.1}$$

$$E_{hc} = -240\ \mathrm{mV} + [(\mathrm{pH} - 7.0) * -61.5\ \mathrm{mV}] - \frac{61.5\ \mathrm{mV}}{2} * \log\frac{[\mathrm{GSH}]^2}{[\mathrm{GSSG}]} \tag{3.2}$$

To further investigate putative protective effects of RSV treatment in NHEK cells, the redox state and the redox environment were calculated according to Equations (1.8), (1.9), (3.1), (3.2) and (S1) to (S6) with the results shown in Tables 3.1, S7 and S8.

Table 3.1: Calculation of redox state and redox environment in RSV-treated NHEK cells. Data presented in Figure 3.27 were normalized to protein content. Quantitative data for $NADP^+$ and NADPH was obtained as relative fluorescence units (RFU), thus could not be used for redox environment calculation. See also Figure 3.27, Tables 3.1, S7 and S8, and Equations (1.8), (3.1), (3.2), (S2) and (S5).

Redox Couple	Redox state [mV]		Δ	Redox environment [mV mmol (g protein)$^{-1}$]		Δ
	DMSO	RSV		DMSO	RSV	
GSH/GSSG	−331.79	−342.55	**−10.77**	−6.87	−9.48	**−2.61**
$NADPH/NADP^+$	−273.21	−277.81	**−4.60**	–	–	–
GSH/GSSG	−331.79	−342.55	**−10.77**			
$NADH/NAD^+$	−286.95	−279.63	**7.32**	−10.81	−13.00	**−2.19**
Lactate/Pyruvate	−204.89	−204.13	**0.76**			

Considering just GSH, both the redox state and the redox environment were markedly decreased after RSV treatment in NHEK cells (Tables 3.1 and S7 indicated in bold font). Although the redox state of $NADPH/NADP^+$ was decreased, the redox state calculated for $NADH/NAD^+$ and lactate/pyruvate was slightly increased. However, the combination of all metabolites resulted in a decreased redox environment (Tables 3.1 and S7). Remarkably, the results were different in NHDF cells treated with 100 μM RSV, as neither the redox state of any redox couple nor the redox environment was decreased but rather increased (Table S8).

According to these calculations (Table 3.1), the reduction of the redox environment should result in a protection against future oxidative stress. To test this hypothesis, NHEK cells were treated for 16 hours with 50 μM RSV or DMSO as vehicle control. Afterwards, the medium was renewed, the cells were exposed to 0.8% ethanol or different

concentrations of HNE, while the generation of ROS was monitored for additional 16 hours (Figure 3.30).

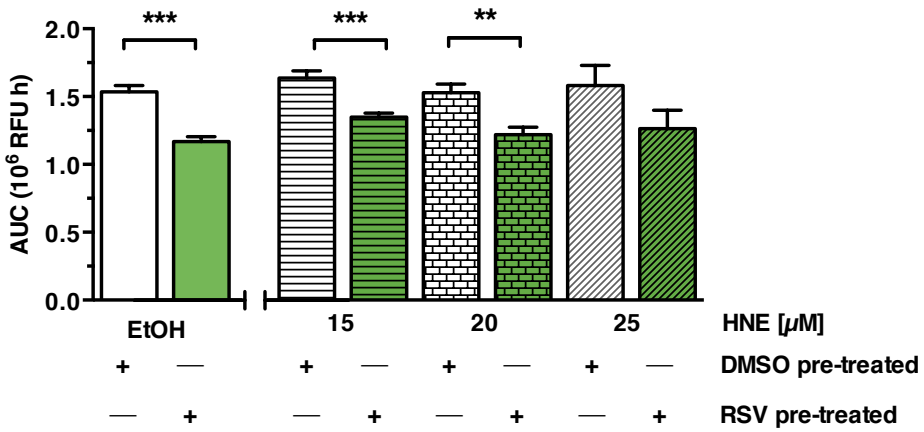

Figure 3.30: Effects of RSV pre-treatment on ethanol-induced intracellular ROS generation. NHEK cells were pre-treated with 50 μM RSV or DMSO for 16 hours. The following day, the medium was changed and cells were treated with ethanol (0.78%) or HNE for 16 hours while the generation of intracellular ROS was monitored. Values are expressed as mean $\pm$ SEM (n = 7). Statistical analysis was done using two tailed Student′s t-test: n.s. not significant, $**p < 0.01$, $***p \leq 0.001$ versus corresponding DMSO control.

The cellular metabolization of ethanol is known to generate ROS [364, 365], correspondingly ethanol (0.8%) induced the generation of ROS in DMSO pre-treated NHEKs. In contrast, RSV pre-treatment resulted in a highly significant reduction of ROS generation (Figure 3.30). We hypothesize that an increased amount of endogenous GSH resulting in an overall reduced redox environment permits RSV-pre-treated NHEKs to tolerate additional oxidative stress such as the biotransformation of ethanol. However, NHEK cells did not tolerate higher doses of ethanol ($> 1\%$) without loss of viability.

NHEKs challenged with HNE did show a reduced ROS generation, when pre-treated with RSV. Notably, the reduction of ROS generation was dependent on the concentration of HNE, as at concentrations above 20 μM the quenching effects of RSV pre-treatment were truncated (Figure 3.30). These results confirm the hypothesis that RSV pre-treatment protects NHEK cells by increasing endogenous amounts of reduced metabolites (such as GSH) leading to a shift of the cellular redox environment which enables cells to tolerate additional oxidative challenges.

4 Discussion

Contents

The phytoalexin resveratrol (RSV) has received a lot of attention from the research community due to its reported health-beneficial effects. However, the underlying mechanism of action remains largely elusive and controversially discussed up to date.

4.1 Oxidation of resveratrol

The majority of studies conducted with RSV presume molecular integrity and a specific RSV-target molecule interaction. In a kinetic wavelength scan the conditions for the decay of RSV were analyzed (Figures 3.1 and S2). The absorbance maximum of RSV was determined at 308 nm [36] and remained stable over almost 16 hours in water (Figures 3.2a and S2). Overall reductions of absorbance observed at longer incubation times were affected by evaporation as the assay was conducted at 37°C (without a lid). Thus, we refrained from using results from incubation times exceeding 16 hours.

In the presence of 44 mM $NaHCO_3$ the absorbance of RSV was truncated in a time-dependent manner (Figures 3.1 and 3.2a), resulting in an almost flat line (Figure 3.1 in green). This behavior confirms analyses of Yang et al. (2010) [42].

As we were targeting physiologically relevant conditions, the stability of RSV was investigated in cell culture media, namely DMEM and KGM (Figure 3.2b). In both media, the absorbance at 308 nm decreased in a time-dependent manner [42] and could be fitted applying a linear regression model (Table S1). In addition, the decay of RSV was equally fast in both media, which was supported by calculated X-intercept values (Table S1).

The difference in curve shape compared to the incubation in water could be attributed to various biomolecules [318, 366–369]; hence RSV and its decay product(s) were likely to interact with components of the media. This might also explain the differences in absorbance after 16 hours of incubation. As cell culture media provide Fenton reaction conditions, an accelerated and complete metabolization of RSV was observed, compared to the incubation in water (Figure 3.2b vs. Figure 3.2a).

In conclusion, we were able to show that RSV remains stable in H_2O at least for 16 hours. However, in presence of 44 mM $NaHCO_3$ the RSV-specific absorbance decreased rapidly in a time-dependent manner, suggesting decomposition of RSV. These findings might explain the reported low bioavailability of RSV as well as the general discrepancy between *in vitro* and *in vivo* studies [26, 54–59].

Next, we were looking for known breakdown products of RSV. Remarkably, the wavelength scan data (Figure 3.1) revealed a time-dependent absorbance increase around 390 nm and 420 nm in presence of 44 mM $NaHCO_3$ (Figure S3). According to Li et al. (2012) the interaction of RSV and $HO^{\bullet}$ results in the formation of intermediate short-lived products [40], with an absorbance maximum at 420 nm, and a long-lived 4′-phenoxyl radical of RSV (absorbance maximum: 390 nm, Figure 3.1).

The abundance and kinetic generation of these oxidation products of RSV was investigated further (Figure S3). For both oxidation products, the absorbance increased in a time-dependent manner and reached a maximum after 7 hours (Figure S3a) and 5 hours (Figure S3b), respectively. Moreover, the increases of absorbance at the specific wavelengths suggest the presence of both oxidation products and consequently $HO^{\bullet}$. To further investigate this hypothesis, we examined the generation of ROS in diverse contexts (see Section 3.2).

In summary, the $NaHCO_3$-driven decomposition of RSV results in the generation of reaction products with characteristic absorbance maxima at 390 and 420 nm. In line with recent a publication [40], these reaction products comprise presumably a hydroxyl radical of RSV and a phenoxyl radical of RSV.

4.1.1 pH-dependent oxidation

As the pH influences the stability of RSV [35–37], we investigated the stability of RSV in water without (Figure 3.3a) and with 44 mM $NaHCO_3$ over a pH range from 1 to 12 (Figure 3.3b). In addition, the generation of oxidation products [40] was monitored. RSV-specific absorbance started to decline at pH above 7 in water and pH 3 in the presence of 44 mM $NaHCO_3$ (Figures 3.3a and 3.3b), corresponding recent literature [35–37]. Notably, the decay of RSV corresponds to the generation of hydroxyl and phenoxyl radical of RSV.

Furthermore, the kinetics of the pH- and time-dependent oxidation of RSV in presence of with 44 mM $NaHCO_3$ were investigated (Figure 3.4). A 3D representation of the influence of $NaHCO_3$, pH and time on the integrity of RSV as well as the generation of putative oxidation products was shown (Figure S4). While RSV remained intact at acid pH (< 3) over at least 16 hours, the decay was accelerated by higher pH levels

and incubation periods (Figures 3.4b to 3.4d and S4). Similarly, the amount of putative oxidation products was increased with higher pH levels and due to elongated incubation times.

In review, the integrity of RSV is strongly influenced by pH. Acid pH levels decelerate the $NaHCO_3$-induced decay of RSV and subsequent generation of oxidation products. Here, the time- and pH-dependent decomposition of RSV has been linked to the time- and pH-dependent formation of corresponding reaction products for the first time.

4.1.2 Oxygen-dependent oxidation

The integrity of RSV can be challenged by various factors. What is sometimes referred to as "cell culture artifact" [41, 47], is the hypothesis that high concentrations of oxygen might trigger the oxidation of RSV [43, 52]. In general cell culture experiments are carried out at 37°C in a humidified environment at 5% CO_2 and 21% oxygen. However, physiological oxygen levels are often lower e.g. for liver, kidney or tumor cells (between 11% and 1% O_2) [50, 53]. We investigated the stability of RSV in a pH-dependent manner not only at atmospheric oxygen level (21%) but at 10% and 1% oxygen (Figures 3.5 and S5).

In the absence of $NaHCO_3$, a reduction to 10% oxygen postponed the starting point of RSV oxidation to pH 10 (Figure S5a) compared to pH 8 at atmospheric conditions (Figure 3.3a). However, a more rigorous limitation of oxygen to 1% (Figure S5b) did not result in an additional shift of the starting point relative to results at 10% (Figure S5a).

The reduction of oxygen partial pressure had comparable effects on the oxidation of RSV even in the presence of 44 mM $NaHCO_3$. While the starting point of oxidation was around pH 3 at atmospheric conditions (Figure 3.3b), it was shifted to pH 6 at 10% oxygen (Figure 3.5a) and almost to pH 7 at 1% oxygen (Figure 3.5b).

In conclusion, we were able to show that oxygen partial pressure indeed influences the oxidation of RSV. A reduction of the oxygen amount shifted of the starting point of oxidation of RSV tremendously. Keeping in mind standard cell culture conditions (5% CO_2, 21% oxygen, pH 7-7.4, 37°C) it seems impossible that RSV remained unimpaired under these conditions. In addition, a reduced oxygen partial pressure would in fact

provide physioxia growth conditions for numerous cell lines used in the laboratory [50, 53].

4.2 Resveratrol and reactive oxygen species

RSV can scavenge ROS and has been attributed antioxidant capabilities. However, during this process, RSV is rapidly oxidized and subsequently generates ROS [38–40]. Moreover, RSV and other polyphenols are known to generate H_2O_2 in various contexts [**?**, 41, 47, 52, 370]. Recently, Li et al (2012) investigated the kinetics of the reaction of RSV with $HO^{\bullet}$ and the generation of subsequent reaction products (Figure 1.6) [40].

4.2.1 Generation of ROS

We investigated the kinetics of RSV-driven generation of ROS in water and KGM (Figures 3.6a and S6) using a fluorescent dye particularly responsive to $HO^{\bullet}$ and $O_2^{\bullet-}$. The incubation of RSV in water did not result in a change of ROS generation (Figures S6a and S6b in green). However, under the same conditions and in presence of 44 mM $NaHCO_3$ the ROS generation was significantly increased after 16 hours (Figures S6a and S6b in magenta). Similar results were observed after the incubation of RSV in KGM, where ROS were generated in a time-dependent manner (Figure 3.6a).

Moreover, we investigated the generation of $O_2^{\bullet-}$ in water and KGM both containing 44 mM $NaHCO_3$ (Figure S7a). In both solvents, the RSV-driven $O_2^{\bullet-}$ generation was increased. The ongoing $O_2^{\bullet-}$ generation in KGM can be accounted to the Fenton conditions provided in cell culture medium in general.

These findings are in accordance with recent publications [**?**, 41, 47, 52, 370]. However, we were able to show that in addition to H_2O_2, also $HO^{\bullet}$ and $O_2^{\bullet-}$ were generated during the decay of RSV. Thus, we can assume that under both conditions, H_2O_2 is converted to $HO^{\bullet}$ e.g. via mechanisms illustrated in Figure 1.10. Subsequently, $HO^{\bullet}$ might interact with RSV to generate the oxidation products suggested by Li et al. (2012) [40].

Next, we investigated the intracellular accumulation of ROS after 16 hours of treatment in NHEK cells (Figure 3.6b). An increased ROS generation was detected at 50 and 150 μM RSV (Figure 3.6b green and blue). In addition, RSV increased the lipid peroxidation in treated NHEK cells (Figure S7b). In conclusion, RSV treatment results in

intracellular accumulation of ROS, which subsequently leads to an increased intracellular lipid peroxidation.

4.2.2 Anti- versus pro-oxidant properties

Despite their ability to generate H_2O_2 in diverse contexts [**?**, 41, 47, 52, 370], RSV and other polyphenols are widely regarded as antioxidants [22, 38–40, 330]. We analyzed the antioxidant properties of RSV and compared it to trolox, a vitamin E analogue (Figures 2.1 and 3.7). In addition, we investigated the influence of 44 mM $NaHCO_3$ on the antioxidant capacity of both compounds (Figures 2.1 and 3.7 magenta and blue).

The antioxidant capacity of RSV turned out to be relatively small compared to trolox (Figure 3.7 and Table S2). Moreover, trolox was not affected by 44 mM $NaHCO_3$ [331], whereas the antioxidant capacity of RSV was truncated even further under the same conditions (Figure 3.7 and Table S2).

In summary, these findings suggest that RSV features a small antioxidant capacity, which is even lower in the presence of 44 mM $NaHCO_3$. As RSV rapidly decomposes in the presence of $NaHCO_3$, it is likely that the subsequent breakdown products have either no or only very limited endogenous antioxidant capacities.

To further investigate the oxidative properties of RSV, the generation of ROS was monitored in presence of potent antioxidants GSH and NAC (Figure 3.8). In a cell-free environment the RSV-driven generation of ROS was efficiently quenched by GSH and NAC (Figure 3.8a).

NAC exhibited potent quenching capabilities in a cell-free setup. However, in a cellular environment, NAC failed to decrease the RSV-driven ROS generation, whereas GSH was able to quench RSV-induced effects (Figure 3.8b). NHEK cells did not tolerate such high NAC concentrations (Figure 3.8a in blue) without increased cytotoxicity (verified by hematoxilin staining, data not shown).

Although the utilized amounts of GSH and NAC seem rather high, lower concentrations ($\leq$ 10 mM) did not result in a decreased ROS generation (data not shown). Notably, the physiological intracellular GSH concentration varies between 0.5 and 15 mM [304, 371, 372] and none of the used GSH concentrations showed adverse effects on NHEK cells (verified by hematoxilin staining, data not shown). The potent quenching

effects of 25 mM GSH were also evident from truncated expression of marker genes (Figure 3.25).

In consequence, we refrained from the use of NAC accounting to its cytotoxic effects on NHEK cells. However, GSH appeared to efficiently reduce the RSV-driven generation of ROS even at high concentrations without adverse effect for NHEK cells. The considerably increased tolerance of NHEK cells against GSH might be accounted to an inherent higher GSH level.

4.3 Hormetic effects of resveratrol caused by oxidation products

Treatment of NHEK cells for 16 hours with 50 μM to 150 μM RSV changed the cellular appearance to a cobble-stone like cell shape (Figure 3.9). However, treatment with higher concentrations ($\geq$ 300 μM) resulted in membrane blebbing and severe membrane damage [328].

To assess effects of RSV treatment in more detail, we investigated the viability of treated NHEK cells. The standard pharmacological model to assess health risks of substances is the linear non-threshold model and the threshold model (Figures 1.8a and 1.8b). Nevertheless, several studies reported a bi-phasic dose-response curve (Figures 1.8c and 1.8d) for RSV [133, 328], with "low" concentrations exhibiting stimulating effects and higher concentrations causing inhibition [117, 119, 120, 127, 373]. Nevertheless, these findings have been widely ignored as the general acknowledgement of applying hormetic concepts remains low and a mechanism exploring this phenomenon has not been proposed so far.

Due to the inhibition of luciferase by RSV [318,319], we used a fluorescent-based cell viability assay to avoid RSV-induced artifacts. We observed a bi-phasic dose-viability curve in NHEK cells treated with RSV (Figure 3.10a and Table S3a). More precisely, the cellular viability was increased up to about 50 μM RSV, whereas higher concentrations inhibited the viability (Figure 3.10a and Table S3a) [127, 133, 328, 373, 374].

The addition of 25 mM GSH, strongly quenched the hormetic dose-viability curve (Figure 3.10a and Table S3b), thus suggesting that an increased viability can be attributed to the generation of ROS and other oxidation products of RSV.

In conclusion, these data endorse the widely ignored bi-phasic response of cells due to RSV treatment [133, 328]. For the first time, we provide evidence that an increased viability induced by treatment with midrange concentrations of RSV can be mainly attributed to the generation of ROS and reaction products of RSV. Hence, we identified for the first time that the induction of mild oxidative stress is a key feature of the mechanism of action of RSV to improve the cellular fitness.

Notably, similar bi-phasic, hormetic dose-viability curves were observed for NHDF (Figure 3.10b and Table S3), HepG2 (Figure S8a and Table S3) and THP-1 cells (Figure S8b and Table S3). Strikingly, THP-1 cells were very susceptible to RSV [328]. The quenching effect of 25 mM GSH was observed in all three cell lines (Figures 3.10b, S8a and S8b and Table S3).

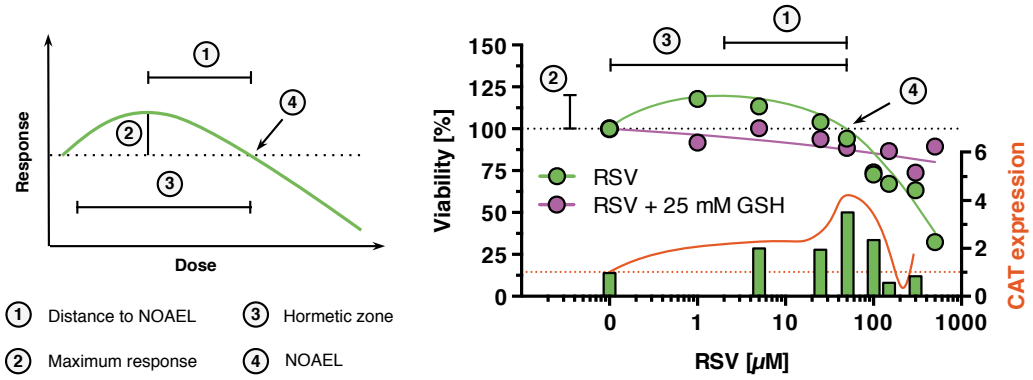

(a) Theoretical features **(b) Observed hormetic effects in NHEKs**

Figure 4.1: Hormesis in theory and experimental data. (a) Quantitative features of hormesis including the hormetic zone (averages 10- to 20-fold concentration), maximum response (averages 130 to 160% of control), no-observed-adverse-effect-level (NOAEL) and distance to NOAEL (averages 5-fold concentration). Control is depicted as dotted line. Adapted from [133]. (b) Observed hormetic effects in NHEK cells after treatment with RSV.

The nature and quantitative features of hormesis are depicted in Figure 4.1a [133]. We combined the bi-phasic dose-viability curve of RSV-treated NHEKs with expression data of the oxidative stress marker catalase (CAT) to distinctly show the hormetic effects of RSV (Figure 4.1b). The hormetic zone, characterized by beneficial treatment effects,

emerged from small RSV amounts up to 50 μM. Notably, our applied treatment concentration (50 μM RSV) is close to the no-observed-adverse-effect-level (NOAEL), which is characterized by a maximum molecular effect (e.g. increased CAT expression) and simultaneously the absence of adverse effects on cellular viability. Strikingly, in presence of 25 mM GSH the hormetic features of the RSV treatment are strongly truncated (Figure 4.1b).

In conclusion, we identified the induction of mild oxidative stress as a common mechanism of action of RSV in diverse cellular models resulting in an improved cellular fitness and a hormetic, bi-phasic cellular response.

4.4 Nrf2 as central mediator

We utilized whole-genome gene expression analysis of RSV-treated NHEK cells and gene set enrichment analysis (GSEA) [316] to identify most enriched pathways (Figure 3.12). In addition, the Connectivity Map tool [317] was used to investigate connections of RSV to other small molecules sharing a common mechanism of action (Table S5). Summarizing, these findings emphasized a rather broad mechanism of action of RSV [60–63]. Accordingly, the reported interaction of RSV with designated target molecules is often only in micromolar range [63–66] corroborating a hormetic, bi-phasic cellular response.

The transcription factor Nrf2 is a key component of the cellular antioxidant defense and enables transcription of diverse defense genes (Figure 1.16). Accounting to the RSV-driven generation of ROS, we hypothesized that Nrf2 might be part of the cellular response to treatment with RSV. Notably, Nrf2 is linked to diverse metabolic pathways including inflammation [334–337], autophagy [286–290], glycolysis and PPP [261, 270, 271], and subsequently central redox metabolites [141, 261, 270, 271, 273].

4.4.1 Inflammatory signaling

Several inflammatory pathways were significantly up-regulated after RSV treatment in NHEK cells as revealed by whole-genome gene expression analysis (Figure 3.12). Thus, the localization of nuclear factor kappa-light-chain-enhancer of activated B cells (NFκB) and the expression of inflammatory markers genes were investigated. RSV

highly significantly increased the amount of NFκB in the nuclear fraction. In contrast, NFκB was significantly decreased in the cytosolic fraction (Figure 3.13). Hence, RSV induced the translocation of NFκB into the nucleus, suggesting activation of downstream signaling. Correspondingly, the expression of inflammatory marker genes was regulated in a time- rather than a concentration-dependent manner (Figure 3.14a). We showed that the observed expression pattern of inflammatory marker genes is a common feature of diverse cell types (Figure S10 and Table S6).

In conclusion, NFκB-mediated inflammatory signaling was slightly increased after treatment with RSV. We suppose that the RSV-driven generation of ROS activates the redox-sensitive transcription factor NFκB [171, 198, 199]. Recently, a relationship between Nrf2 and NFκB has been established [334, 336, 337], hence a transactivation via Nrf2 seems possible [335].

4.4.2 Autophagy versus Senescence

Proliferation associated pathways were significantly down-regulated after RSV treatment in NHEK cells (Figure 3.12). Thus, we analyzed the cell cycle phase distribution and investigated markers of apoptosis, senescence and autophagy [375].

The cell cycle is defined by several highly regulated phases and corresponding checkpoints. In NHEK cells, RSV induced a G_1 phase cell cycle arrest (Figures 3.15 and 3.16) [376–378]. However, other studies reported cell cycle arrests at G_2 and S phase [67, 379, 380]. These findings suggest that the point of RSV-induced cell cycle arrest is context-dependent and as such might be different in each cell line.

Accounting to the close link of cell cycle arrest and apoptosis [349, 350], we investigated whether RSV influenced the proportion of apoptotic cells, the expression of marker genes and the amount of apoptosis marker proteins. The regulation of apoptotic marker gene expression suggests a mild induction of apoptosis by RSV treatment in NHEK cells (Figure 3.17a). To further investigate this matter, we analyzed the externalization of propidium iodide (PI) as a quantitative measure of apoptosis. Notably, even at higher concentrations, RSV seemed to reduce the number of necrotic cells without influencing the amount of apoptotic cells (Figure 3.17b).

In addition, we analyzed the protein content of several components of the apoptotic caspase signaling (Figure 3.18). Although the effector form of caspase 9 was significantly decreased, a significant increase in cleaved caspase 7 suggests apoptotic signaling downstream of caspase 9 [355]. Moreover, RSV-induced cleavage of PARP suggests an efficient activation of the apoptotic cascade in NHEKs (Figure 3.18). In a nutshell, the results suggest a mild induction of apoptosis by RSV treatment [67].

Senescence and autophagy represent two additional possibilities to cope with damaged cellular components or cells in general [277]. In account to reports that senescence is directly linked to an arrest in G_1 cell cycle phase [6, 276], we investigated the expression of senescence marker genes (Figure S11a). Indeed, RSV increased the expression of marker genes, suggesting augmented senescence, which in turn is supposedly attributed to the observed G_1 cell cycle arrest (Figures 3.15 and 3.16).

In contrast to senescence, autophagy describes the regulated disassembly of unnecessary or dysfunctional elements and their subsequent recycling [276, 277, 282]. The influence of RSV on autophagy was investigated by fluorescent labelling of autophagosomal marker protein MAP1LC3 [282, 356, 357, 359] and analysis of marker gene expression. As revealed by fluorescent staining (Figure 3.19), RSV increased the amount of MAP1LC3. The expression of proliferation marker genes was regulated in a time- and to a lesser extent in a concentration-dependent manner (Figure 3.20). Similar results were obtained from marker gene analyses in diverse cellular model systems (Figure S12 and Table S6). These findings suggest at least a mild induction of autophagy by RSV treatment [360].

In conclusion, RSV treatment caused cell cycle arrest with subsequent slight induction of senescence. However, rather than inducing apoptosis RSV treatment resulted in augmented autophagy enabling the cell to facilitate a regulated disassembly of unnecessary or dysfunctional elements and features subsequent recycling [276, 277, 282]. Moreover, recent studies link Nrf2 signaling to autophagy [286–288]. Hence, the RSV-induced activation of Nrf2 and subsequent signaling cascades might actually contribute to increased autophagy as a safeguard mechanism.

4.4.3 Energy metabolism

Energy metabolism associated pathways were significantly up-regulated after RSV treatment in NHEK cells (Figure 3.12). To investigate the influence of RSV on the energy metabolism, the expression of several marker genes was monitored and intracellular concentrations of redox-relevant metabolites were determined for the calculation of redox state and environment.

The expression of energy metabolism marker genes (Figure 3.26) was regulated in a time- rather than a concentration-dependent manner (Figure 3.26). Similar expression patterns of energy metabolism marker genes were obtained in diverse cellular model systems (Figure S15 and Table S6). Pentose phosphate pathway (PPP) associated genes G6PD and PPAT were strongly, though inversely expressed. Notably, both genes are downstream targets of Nrf2 [261]. Accordingly, Nrf2 might promote a metabolic switch resulting in re-routing of glucose and glutamine into the PPP (Figure 1.17) [261].

The two key functionalities of the PPP are i) to generate R5P for nucleotide synthesis and ii) to provide NADPH as reduction equivalent [261]. The down-regulation of PPAT corroborates the findings of whole-genome gene expression analysis (Figure 3.12) and suggests a re-routing of metabolites through PPP, e.g. to increase NADPH generation (Figure 1.17). In contrast, ACLY is connected to the fatty acid synthesis; especially in rapidly growing cancer cells ACLY is increasingly expressed [381]. In light of the observed macroscopical changes of cell shape, ACLY might play a role in restructuring the cell membrane.

As revealed by whole-genome gene expression analysis (Figure 3.12) RSV increased metabolic pathways associated with lipid metabolism. Notably, acetylation increases ACLY stability, whilst SIRT2 has been shown to destabilize ACLY [381]. At first, the histone deacetylase SIRT1 has been identified as direct target of RSV mediating lifespan extension [65]. However, several studies reported fluorescent activation artifacts and that the unlabeled peptide did not activate SIRT1 at all [60, 61, 77]. Although no concrete mechanism of interaction has been established so far, a potential direct enzymatic, allosteric or indirect activation are discussed [60–63].

RSV increased the expression of SIRT1 and its down-stream target FOXO3 (Figure 3.26). In addition, RSV induced phosphorylation and translocation of SIRT1 into

the nucleus (Figure S17). We hypothesize that RSV-driven generation of ROS results in phosphorylation and translocation of SIRT1 [95] and promotion of subsequent SIRT1 signaling [382]. Recently, SIRT2 was linked to PPP via G6PD a known target gene of Nrf2 [271, 272]. Hence, RSV-driven activation of Nrf2 and increased levels of G6PD might also contribute to the observed effects on SIRT1. Remarkably, a knockdown of SIRT1 gene resulted in a 20% decreased expression of Nrf2 (Figure 3.24a), endorsing our hypothesis.

We investigated the intracellular concentration of relevant metabolites to further analyze the influence of RSV on the energy metabolism in NHEK and NHDF cells (Figure 3.27). Notably, similar results were obtained in NHEK and NHDF cells for NADPH, $NADP^+$, NADH, NAD^+ and lactate (Figure 3.27), suggesting a comparable influence of RSV on both skin cell types. However, in NHEK cells the significantly increased amount of glucose and simultaneously decreased amount of NADPH and $NADP^+$, strengthen our hypothesis that RSV-driven activation of Nrf2 results in a metabolic switch towards PPP [261].

Indeed a re-routing of metabolites through PPP would rescue the RSV-induced decrease of NADPH (Figure 1.17). While GSSG was not regulated by RSV, the amount of GSH was highly significantly increased 1.3-fold after treatment (Figure 3.27). In addition, marker genes associated with GSH metabolism were highly significantly up-regulated (Figure S16). As Nrf2 drives the expression of glutamate-cysteine ligase (GCL), glutamine is redirected towards GSH synthesis [141, 146]. In addition, the intracellular GSH level is maintained via Nrf2-dependent regulation of GPX2, GPX4 and GSR (Figure 1.12). Thus, we hypothesize that the observed effects on GSH metabolism and an increased GSH amount are mainly mediated by RSV-driven induction of Nrf2 signaling. In contrast, the slightly increased NAD^+ level in NHEK cells establishes a link to the SIRT1 axis [86, 88, 383].

Moreover, RSV resulted in a slightly reduced intracellular amount of lactate (Figure 3.27). These findings are endorsed by the reduced acidification rate (Figure 3.29). As lactate and pyruvate are interconvertible metabolites, the intracellular amount of pyruvate was increased in NHEK cells, thus corresponding to the results obtained for lactate. In addition, RSV significantly increased the amount of phosphorylated pyruvate dehydrogenase

E1-alpha (PDE1α), which inhibited the enzyme and prevented further metabolization of pyruvate (Figure S18). Notably, Nrf2 has recently been linked to pyruvate metabolism, as Nrf2 facilitates the decarboxylation of malate via malic enzyme 1 (ME1) and causing channeling of pyruvate into the TCA cycle [261] (Figure 1.17). In addition, the relative oxygen consumption was significantly decreased in RSV-treated NHEK cells (Figure 3.28). These findings contradict reports that RSV induces mitochondrial biogenesis via the SIRT1-PGC1-α-axis [361–363].

Summarizing, RSV indues major changes in the cellular energy metabolism and shifts the concentration of key redox metabolites. However, we hypothesize that the majority of these changes can be accounted to the activation of Nrf2. Consequently, we anticipate that Nrf2 is the central mediator of the effects observed after RSV. Moreover, the induced shifts in metabolite concentration might indeed result in a shift of redox environment but certainly the redox state (see Section 4.5).

4.4.4 Oxidative stress signaling

Oxidation of RSV resulted in the generation of oxidation products and ROS (Figures 3.3, 3.6, S3, S6 and S7). Consequently, several oxidative stress pathways were significantly up-regulated after RSV treatment in NHEK cells (Figure 3.12).

Similar to energy metabolism genes, the expression of oxidative stress marker genes was regulated in a time- rather than a concentration-dependent manner (Figure 3.21). We showed that the observed expression pattern of oxidative stress markers is a common feature of primary and cancer cells (Figure S13 and Table S6). Accounting to these findings, we analyzed the subcellular localization of Nrf2 after RSV treatment in NHEK cells (Figures 3.22 and 3.23).

As revealed by fluorescent labeling of Nrf2 (Figure 3.22), RSV induced the translocation of Nrf2. Moreover, the amount of phosphorylated Nrf2 was significantly increased in the nuclear fraction after RSV treatment (Figure 3.23). These findings suggest that RSV-driven generation of ROS results in the translocation of Nrf2 and activation of subsequent signaling. The expression of Nrf2 target genes induces autophagy [286–288], changes in energy metabolism [141, 146, 261] and oxidative stress response [139, 146, 384].

To further evaluate the role of Nrf2 in mediating RSV-induced effects, we performed a knockdown of Nrf2 and SIRT1 in NHEK cells using small interfering RNA (siRNA) (Figures 3.24 and S14). Indeed, knockdown of Nrf2 (efficiency: 80%, Figure 3.24a) significantly truncated the RSV-induced effects on the expression of selected genes (Figure 3.24b); the effects of Nrf2 knockdown were less distinct on protein level (Figure S14). However, these findings corroborate our hypothesis that Nrf2 is the central mediator of RSV-induced effects. Notably, a knockdown of SIRT1 (efficiency: 70%) resulted in a simultaneous decrease of Nrf2 of roughly 20% (Figure 3.24a). These findings suggest an interaction between both factors, which requires further study.

The application of ROS scavengers truncated the RSV-driven generation of ROS (Figure 3.8). Remarkably, 25 mM GSH significantly truncated RSV-induced increases in gene expression. RNA expression analyses corroborate (Figure 3.25) our hypothesis that RSV-driven generation of ROS is primarily responsible for the observed beneficial effects, which were severely quenched by 25 mM GSH.

4.5 Shift of redox state and environment

According to the data presented so far, RSV induces mild oxidative stress resulting in expression of inflammatory, proliferation, energy metabolism, and oxidative stress marker genes. In addition, RSV treatment shifts the intracellular concentration of key metabolites. We hypothesize that changes of redox-relevant metabolites result in a reduced redox state and environment.

To calculate a metabolite-specific redox state and the redox environment, we determined concentration ratios of relevant redox couples in NHEK and NHDF cells (Figure S19). After normalization to protein content, the metabolite concentrations and ratios were used to calculate the individual redox states and the redox environment according to Equations (1.8) and (1.9) (Tables 3.1, S7 and S8).

In NHEK cells the redox state of the NADH/NAD^+ and lactate/pyruvate couples was increased, however, GSH/GSSG and NADPH/$NADP^+$ were highly decreased (Tables 3.1 and S7). Thus, RSV shifts the redox state of selected metabolites to a more reduced status, which is supporting our initial hypothesis. In addition, the GSH/GSSG couple provides by far the largest pool of reducing equivalents and is considered to be the major cellular redox buffer [304]. Consequently, we calculated the cellular redox environment

for NHEKs i) using only GSH/GSSG [304], and ii) using all available metabolite ratios. Notably, in both cases, the redox environment was reduced (Table 3.1). These results suggest that RSV shifts the redox environment to a more reduced status. Moreover, the increased endogenous level of GSH is the driving force for the observed reduction of redox environment.

In NHDF cells, all calculated redox states were increased, thus more oxidative, for each redox couple. Correspondingly, the redox environment was slightly increased after RSV treatment (Table S8). These findings, oppose our hypothesis, as RSV-induced oxidative stress shifted the redox environment to a more oxidized status. In review, we were able to approve our hypothesis in NHEK cells, but not in NHDF cells. Different treatment concentrations might be one explanation for the observed differences. Keeping in mind the hormetic effects of RSV, the treatment concentration of 100 μM RSV for NHDFs is in close vicinity to the NOAEL (Figures 3.10 and 4.1). In contrast to NHEKs, NHDF cells do not face oxidative challenges on a daily basis and have a smaller endogenous amount of Nrf2 [301, 302].

Finally, we anticipate that the reduced redox environment in NHEK cells after RSV treatment would allow for tolerating additional oxidative challenges. Consequently, we analyzed the ethanol-induced intracellular generation of ROS in NHEK cells that were pre-treated and primed by RSV (Figure 3.30). Indeed, the RSV pre-treated cells generated 24% less ROS than DMSO control cells. These effects were depleted by 4-hydroxynonenal (HNE) in a concentration-dependent manner. Notably, HNE acts as strong electrophile and thus depletes cellular sulfhydryl compounds including GSH [385]. In general, these results confirm our hypothesis that RSV pre-treatment protects NHEK cells by increasing endogenous amounts of reduced metabolites (such as GSH); finally leading to a shift of the cellular redox environment, which enables cells to tolerate additional oxidative challenges.

Subsequently, we aimed to quantify, how much more ethanol is tolerated by RSV pre-treated NHEK cells. However, the NHEKs did not tolerate higher doses of ethanol ($> 1\%$) without serious reduction of viability. To further evaluate RSV pre-treatment-related cellular protection against oxidative stress, a gedankenexperiment was conducted (Equations (4.1) to (4.14)). As said, ethanol is known to stimulate the production of

ROS [364,365]. A plethora of data is available for the ethanol/acetaldehyde redox couple, thus it was chosen for the gedankenexperiment (Equation (4.1)).

Eventually, the redox state of DMSO and RSV pre-treated cells shall be calculated based on the ethanol/acetaldehyde redox couple (Equation (4.2)). In addition, determined concentrations for GSH and GSSG (Figure 3.27) were used for the calculation and the pH assumed to be equal to 7 to simplify the calculation (Figure 3.29 and Table S7).

$$\text{Acetaldehyde} + 2H^+ + 2e^- \rightarrow \text{Ethanol} \qquad E^{0'} = -195\ \text{mV} \tag{4.1}$$

$$E_{hc_{\text{pH}}} = -195\ \text{mV} + [(\text{pH} - 7.0) * -61.5\ \text{mV}] - \frac{61.5\ \text{mV}}{2} * \log \frac{[\text{Ethanol}]}{[\text{Acetaldehyde}]} \tag{4.2}$$

The redox state of DMSO pre-treated cells can be calculated by applying physiological conditions (T = 37°C, pH 7). Subsequently, the redox state of RSV pre-treated cells and finally the amount ethanol can be calculated for both pre-treatment conditions (Equations (4.3) and (4.4)).

$$\begin{aligned} E_{\text{Ethanol}_{\text{DMSO}}} &= -195\ \text{mV} - 30.75\ \text{mV} * \log \frac{[\text{Ethanol}]}{[\text{Acetaldehyde}]} \\ &= -195\ \text{mV} - 30.75\ \text{mV} * \log \frac{[\text{Ethanol}]}{[\text{Acetaldehyde}]} \end{aligned} \tag{4.3}$$

$$\begin{aligned} E_{\text{Ethanol}_{\text{RSV}}} &= -195\ \text{mV} - 30.75\ \text{mV} * \log \frac{[\text{Ethanol}]}{[\text{Acetaldehyde}]} \\ &= -195\ \text{mV} - 30.75\ \text{mV} * \log \frac{[\text{Ethanol}]}{[\text{Acetaldehyde}]} \end{aligned} \tag{4.4}$$

The redox state for the ethanol/acetaldehyde redox couple is calculated and the direction of a putative redox state shift ($\Delta E_{\text{Ethanol}}$) RSV-induced can be estimated (Equations (4.5) and (4.6)).

$$\begin{aligned}
\Delta E_{\text{Ethanol}} &= E_{\text{Ethanol}_{\text{RSV}}} - E_{\text{Ethanol}_{\text{DMSO}}} \qquad (4.5)\\
&= -195\ \text{mV} - 30.75\ \text{mV} * \log\frac{[\text{Ethanol}]}{[\text{Acetaldehyde}]}\\
&\quad - (-195\ \text{mV} - 30.75\ \text{mV} * \log\frac{[\text{Ethanol}]}{[\text{Acetaldehyde}]}\\
&= -195\ \text{mV} - 30.75\ \text{mV} * \log\frac{[\text{Ethanol}]}{[\text{Acetaldehyde}]}\\
&\quad + 195\ \text{mV} + 30.75\ \text{mV} * \log\frac{[\text{Ethanol}]}{[\text{Acetaldehyde}]}\\
&= -30.75\ \text{mV} * \log\frac{[\text{Ethanol}]}{[\text{Acetaldehyde}]} + 30.75\ \text{mV} * \log\frac{[\text{Ethanol}]}{[\text{Acetaldehyde}]} \qquad (4.6)
\end{aligned}$$

Sarkola et al. (2002) showed that the formation of acetaldehyde is linearly dependent on the concentration of ethanol. In addition, they were able to determine a mean slope of the reaction Equation (4.7)) [386].

$$\text{Mean slope: } 0.13\ \frac{\mu\text{M Acetaldehyde}}{\text{mM Ethanol}} = \frac{0.13\ \mu\text{M Acetaldehyde}}{1{,}000\ \mu\text{M Ethanol}} \qquad (4.7)$$

Facilitating Equation (4.7), the ethanol/acetaldehyde ratio after pre-treatment with DMSO can be calculated (Equations (4.8) and (4.9)).

$$Q_{\text{DMSO}} = \frac{[\text{Ethanol}]}{[\text{Acetaldehyde}]} = 7{,}692.30769 \qquad (4.8)$$

$$log Q_{\text{DMSO}} = \log\frac{[\text{Ethanol}]}{[\text{Acetaldehyde}]} = 3.88606 \qquad (4.9)$$

Correspondingly, the shift of the redox state based on ethanol/acetaldehyde can be calculated as shown in Equation (4.10).

$$\Delta E_{\text{Ethanol}} = -30.75\ \text{mV} * \log \frac{[\text{Ethanol}]}{[\text{Acetaldehyde}]} + 119.5\ \text{mV} \tag{4.10}$$

As quantitative concentrations of GSH and GSSG have already been determined in NHEK cells (Tables 3.1 and S7) the shift of the redox state can be calculated as shown in Equation (4.11). However, at equilibrium the change of the reduction potentials equals 0 (Equation (4.12)).

$$\Delta E_{\text{GSH}} = E_{\text{GSH}_{\text{RSV}}} - E_{\text{GSH}_{\text{DMSO}}} \tag{4.11}$$

$$\Delta E_{\text{GSH}} = \Delta E_{\text{Ethanol}} = 0 \tag{4.12}$$

Both ($E_{\text{GSH}_{\text{RSV}}}$, $E_{\text{GSH}_{\text{DMSO}}}$) can be calculated according to Equation (1.5) as the pH was set to 7 to simplify the calculation. Thus, the concentration ratio of ethanol/acetaldehyde $\left(\frac{[\text{Ethanol}]}{[\text{Acetaldehyde}]}\right)$ can be calculated accordingly (Equation (4.13)).

$$E_{\text{GSH}_{\text{RSV}}} - E_{\text{GSH}_{\text{DMSO}}} = -30.75\ \text{mV} * \log \frac{[\text{Ethanol}]}{[\text{Acetaldehyde}]} + 119.5\ \text{mV}$$

$$E_{\text{GSH}_{\text{RSV}}} - E_{\text{GSH}_{\text{DMSO}}} - 119.5\ \text{mV} = -30.75\ \text{mV} * \log \frac{[\text{Ethanol}]}{[\text{Acetaldehyde}]}$$

$$Q_{\text{RSV}} = \frac{[\text{Ethanol}]}{[\text{Acetaldehyde}]} = 10^{\frac{E_{\text{GSH}_{\text{RSV}}} - E_{\text{GSH}_{\text{DMSO}}} - 119.5\ \text{mV}}{-30.75\ \text{mV}}}$$

$$= 10^{\frac{-338.67\ \text{mV} - (-331.63\ \text{mV}) - 119.5\ \text{mV}}{-30.75\ \text{mV}}}$$

$$Q_{\text{RSV}} = \frac{[\text{Ethanol}]}{[\text{Acetaldehyde}]} = 9,856.3077 \tag{4.13}$$

Comparing the results for DMSO and RSV pre-treatment (Equations (4.8) and (4.13)), the observed shift of the redox environment was mostly attributed to the increased intracellular GSH levels.

$$Q_{\text{DMSO}} = \frac{[\text{Ethanol}]}{[\text{Acetaldehyde}]} = 7,692.3 = 100\%$$
$$Q_{\text{RSV}} = \frac{[\text{Ethanol}]}{[\text{Acetaldehyde}]} = 9,856.3 = 128.13\% \quad (4.14)$$

According to these calculations (Equations (4.1) to (4.14)) RSV pre-treated NHEK cells are likely to tolerate roughly 28% higher ethanol concentrations compared to DMSO pre-treated cells. Assuming a 1:1 mechanism of ethanol-induced ROS generation, the results of the gedankenexperiment corroborate our experimental data as RSV pre-treated cells generating 24% less ROS than DMSO control cells when exposed to 0.8% ethanol (Figure 3.30). Although these calculations were merely a gedankenexperiment, this is the fist time this mathematical technique is used to quantify the protective effects of RSV.

4.6 Proposed mechanism of action

We propose a hormetic, bi-phasic pharmacological model to understand the mechanism of action of RSV (Figure 4.2). In addition, we expect that our proposed mechanism of action might be applicable to other polyphenols. Our model comprises firstly the oxidation of RSV and concurrent generation of ROS at non-toxic concentrations under physiologically relevant conditions (presence of $NaHCO_3$); secondly, mediation of cellular response to oxidation by the redox-sensitive transcription factor Nrf2 and thirdly, a slight shift of the redox environment resulting in cellular protection from additional oxidative stress (Figure 4.2). The human epidermis represents a prime target for external stressors and thus might particularly benefit from a topical, dermatological application of RSV. Our proposed mechanism provides a new conceptual basis to explain RSV-induced skin resistance against oxidative stress [329].

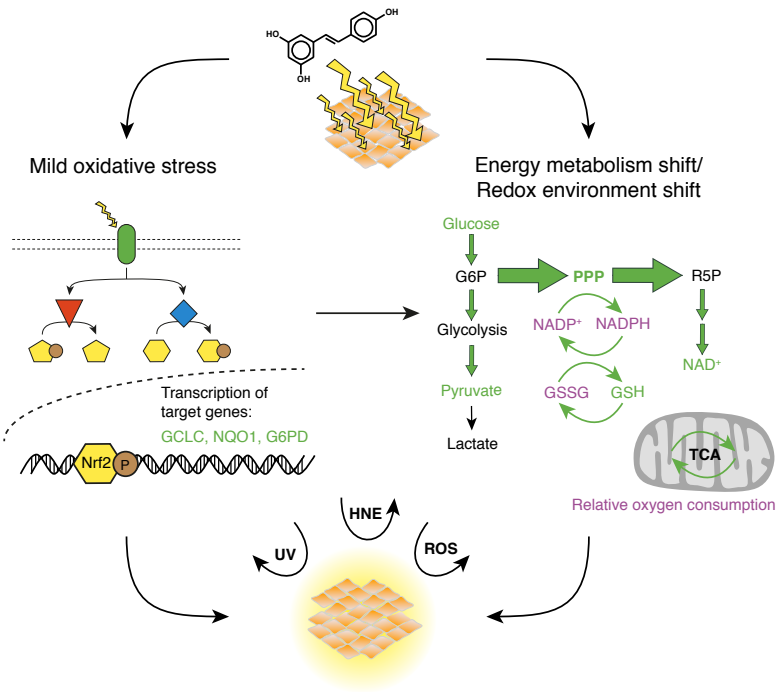

Figure 4.2: Proposed mechanism of action of RSV. Under physiological relevant conditions oxidation of RSV results in the generation of ROS and further reaction products, thus inducing mild oxidative stress. Translocation and phosphorylation of central transcription factor Nrf2 causes expression of target genes. Finally, RSV shifts the energy metabolism towards PPP and an increased generation of redox equivalents, finally resulting in a overall reduced cellular redox environment. Consequently, cells are protected against oxidative challenges. Increased values are depicted in green; decreased values are depicted in magenta. Glucose 6-phosphate (G6P), glucose-6-phosphate dehydrogenase (G6PD), glutamate-cysteine ligase (catalytic subunit) (GCLC), glutathione (GSH), glutathione (GSSG), 4-hydroxynonenal (HNE), nicotinamide adenine dinucleotide phosphate (NAD^+), nicotinamide adenine dinucleotide phosphate ($NADP^+$), nicotinamide adenine dinucleotide phosphate (NADPH), NAD(P)H dehydrogenase (quinone 1) (NQO1), nuclear factor (erythroid-derived 2)-like 2 (Nrf2), Phosphorylation (P), pentose phosphate pathway (PPP), ribose 5-phosphate (R5P), reactive oxygen species (ROS), tricarboxylic acid (TCA), ultraviolet (UV).

Concerning potential nutritional applications of RSV, the previously elaborated influence of pH needs to be considered. Although RSV might endure acid pH conditions, as present in the stomach, immediate oxidation of RSV can be anticipated in the duodenum. The here applied quantitative analysis of redox-relevant metabolites and subsequent determination of the cellular redox environment allow for quantifying the often-reported pleiotropic effects of RSV. Nevertheless, short-lived oxidation products and ROS are difficult to determine quantitatively under *in vitro* and even more under *in vivo* conditions.

4.7 Outlook and future perspectives

This study provides new and comprehensive insights into the mechanism of action of RSV. The calculation of metabolite-specific redox states and the redox environment in general provides a powerful and easyly applicable way to assess the effects of pro-oxidative compounds such as polyphenols. However, new questions have been raised, which require further experimental investigation.

Firstly, the proposed connection of Nrf2 and SIRT1 provides an interesting starting point for further experiments. The knockdown of SIRT1 resulted in a contemporaneous 20% reduction of Nrf2 gene expression. Using chromatin immunoprecipitation (ChIP)-seq technology, the role of SIRT1 in Nrf2 gene regulation could be investigated in detail. Accounting to the data presented in this study, a putative direct or indirect interaction of Nrf2 and SIRT1 could contribute to the further elucidation of the mechanism of action of RSV. Moreover, the "new" clustered regularly-interspaced short palindromic repeats (CRISPR)-Cas technology [387] could be used to edit the genome, as commonly applied knockdown technologies tend to be quite stressful for the cells and thus might induce artifacts.

Secondly, the RSV-induced regulation of lipid metabolism and associated pathways could be of interest, especially in the skin context. The macroscopical changes to a cobble-stone-like cell shape indicate major structural changes of the cellular membrane. Recently, interactions of Nrf2 with the PPARγ promotor [267] as well as a mutual feedback loop of Nrf2 and PPARγ were identified [268].

Thirdly, the translocation of NFκB and subsequent downstream signaling was observed after RSV treatment. However, further experiments are needed to investigate whether RSV-driven generation of ROS activates the redox-sensitive transcription factor NFκB [171, 198, 199]. Recently, a relationship between Nrf2 and NFκB has been established [334, 336, 337], hence a transactivation seems possible [335], which in turn could be investigated using ChIP-seq and CRISPR-Cas technologies [387]. In addition, a putative protection of RSV pre-treated cells against inflammatory challenges (e.g. bacteria, pathogens), due to activation of NFκB signaling, could be investigated.

Fourthly, the oxidation of RSV requires further attention to investigate the generation of oxidation products and ROS in more detail. However, the complex systems used in cell culture applications complicate a quantitive assessment tremendously. Moreover, a

detailed chemical and kinetic analysis of the oxidation products is needed to complete the mechanism of action of RSV.

Fifthly, the RSV-induced reduction of the redox environment requires quantitative data on metabolites and metabolite ratios. To exactly calculate the redox environment, quantitative information are needed for all redox couples. Although GSH is regarded as major cellular redox buffer [304], a combined metabolic-redoxomic approach would enable a more precise calculation of the redox environment. In case of the presented data on NHDF, quantitative knowledge of the redoxome might reveal a reduction of the redox environment after all.

Keeping in mind the small and often pleiotropic changes induced by hormetic compounds, a combined metabolic-redoxomic approach could have an important impact on the research, development, and design of novel polyphenol-inspired drugs.

5 Summary

Polyphenols, historically known as “vegetable tannins”, feature health-beneficial effects [14]. The phytoalexin *trans*-resveratrol (RSV) was originally isolated from *Veratrum grandiflorum O. Loes* [30] and is ascertained to naturally occur in approximately 72 plant species [19]. The “French paradox” [16] and early reports of cancer chemo-preventive properties [19] contributed to the growing popularity of RSV [24, 388, 389].
The human skin is the largest organ of our body [2] and challenged by oxidative and environmental stressors on a daily basis [390–392]. The use of RSV in a skin context is a cutting-edge topic [19, 329] as epidermal keratinocytes are a prime target for RSV-based lotions and emollients. However, the mechanism of action of RSV remains largely elusive and controversially discussed. In this study, neonatal normal human epidermal keratinocyte (NHEK) cells are used as a primary cellular model to investigate the mechanism of action of RSV. We demonstrate that RSV is unstable under physiologically relevant conditions, resulting in the generation of oxidation products and reactive oxygen species (ROS). In addition, RSV increases the cellular viability at “low”, hormetic doses ($\leq$ 50 μM) in representative cell models. The application of ROS scavengers truncates these beneficial effects. Moreover, Nrf2-dependent gene expression is initiated by RSV. A 1.3-fold increase of endogenous glutathione (GSH) is sufficient to cause a quantitative reduction of the cellular redox environment. Consequently, RSV pre-treated cells are more resistant to ethanol-induced oxidative stress and generate 24% less ROS. We propose that the major effect of RSV is to induce a mild oxidative stress resulting in hormetic shifting of cellular metabolism towards a more reductive state.

6 Zusammenfassung

Polyphenole wurden anfänglich als Tannine zur Herstellung von Leder verwendet und sind heutzutage vor allem für ihre gesundheitsfördernden Eigenschaften bekannt [14]. Das Phytoalexin *trans*-Resveratrol (RSV) wurde ursprünglich aus *Veratrum grandiflorum O. Loes* isoliert [30] und wurde bisher in ca. 72 verschiedenen Pflanzen nachgewiesen [19]. Besonders das sogenannte französische Paradoxon [16] sowie Berichte über chemopreventive Eigenschaften [19] rückten RSV in den Fokus der Forschung [24, 388, 389].

Die Haut ist das größte Organ unseres Körpers [2] und tagtäglich verschiedenen oxidativen und umweltbedingten Stressfaktoren ausgesetzt [390–392]. Die Anwendung von RSV im Hautkontext ist ein hochaktueller Themenbereich, insbesondere, da die epidermalen Keratinozyten ein Hauptziel für RSV-basierte Lotionen darstellen. Ungeachtet dessen ist der Reaktionsmechanismus von RSV weitestgehend unbekannt und wird heftig diskutiert. In dieser Arbeit werden vor allem neonatale normale humane epidermale Keratinozyten (NHEK) verwendet, um den Wirkmechanismus von RSV zu untersuchen. Wir zeigen, dass RSV unter physiologischen Bedingungen instabil ist und dass der Zerfall von RSV die Entstehung von Oxidationsprodukten und reaktiven Sauerstoffspezies (ROS) nach sich zieht. Darüber hinaus erhöht die Anwendung von RSV in kleinen, hormetischen Konzentrationen ($\leq$ 50 μM) die zelluläre Viabilität in diversen Zellmodellen. Eine gleichzeitige Anwendung von Radikalfängern beseitigt diese Viabilitätssteigerung vollständig. Zusätzlich initiiert RSV die Expression von Zielgenen über den Transkriptionsfaktor Nrf2. Eine vergleichsweise kleine, 1,3-fache Steigerung des endogenen Glutathiongehalts (GSH) führt zu einer messbaren, quantitativen Verringerung der zellulären Redoxumgebung. Dementsprechend sind mit RSV vorbehandelte

Zellen resistenter gegen bspw. Ethanol-induzierten oxidativen Stress und produzieren 24% weniger ROS. Wir schlagen einen Wirkmechanismus vor, der vor allem auf der Induktion von mildem oxidativen Stress beruht und letzten Endes zu einer hormetischen Verschiebung der zellulären Redoxumgebung führt.

7 Bibliography

[1] R. Milo, P. Jorgensen, U. Moran, G. Weber, and M. Springer. BioNumbers - The database of key numbers in molecular and cell biology. *Nucleic Acids Research*, 38(SUPPL.1):D750–D753, 2009.

[2] A. Oláh, A. G. Szöllosi, and T. Bíró. The channel physiology of the skin. *Reviews of Physiology, Biochemistry and Pharmacology*, 163:65–131, 2012.

[3] M. Stücker, A. Struk, P. Altmeyer, M. Herde, H. Baumgärtl, and D. W. Lübbers. The cutaneous uptake of atmospheric oxygen contributes significantly to the oxygen supply of human dermis and epidermis. *The Journal of Physiology*, 538(Pt 3):985–994, 2002.

[4] E. Bianconi, A. Piovesan, F. Facchin, A. Beraudi, R. Casadei, F. Frabetti, L. Vitale, M. C. Pelleri, S. Tassani, F. Piva, S. Perez-Amodio, P. Strippoli, and S. Canaider. An estimation of the number of cells in the human body. *Annals of Human Biology*, 40(6):463–71, 2013.

[5] Madhero88 and M. Komorniczak. Layers of the skin. https://commons.wikimedia.org/wiki/File:Skin_layers.svg, CC BY-SA 3.0.

[6] G. Jenkins. Molecular mechanisms of skin ageing. *Mechanisms of Ageing and Development*, 123(7):801–810, 2002.

[7] S. Pillai, C. Oresajo, and J. Hayward. Ultraviolet radiation and skin aging: Roles of reactive oxygen species, inflammation and protease activation, and strategies for prevention of inflammation-induced matrix degradation - A review. *International Journal of Cosmetic Science*, 27(1):17–34, 2005.

[8] B. A. Gilchrest. Skin aging and photoaging: An overview. *Journal of the American Academy of Dermatology*, 21(3):610–613, 1989.

[9] L. Rittié and G. J. Fisher. UV-light-induced signal cascades and skin aging. *Ageing Research Reviews*, 1(4):705–720, 2002.

[10] M. Perluigi, F. Di Domenico, C. Blarzino, C. Foppoli, C. Cini, A. Giorgi, C. Grillo, F. De Marco, D. A. Butterfield, M. E. Schininà, and R. Coccia. Effects of UVB-induced oxidative stress on protein expression and specific protein oxidation in normal human epithelial keratinocytes: a proteomic approach. *Proteome Science*, 8:13, 2010.

[11] S. Grether-Beck, A. Marini, T. Jaenicke, and J. Krutmann. Photoprotection of human skin beyond ultraviolet radiation. *Photodermatology Photoimmunology and Photomedicine*, 30(2-3):167–174, 2014.

[12] M. Rinnerthaler, J. Bischof, M. Streubel, A. Trost, and K. Richter. Oxidative Stress in Aging Human Skin. *Biomolecules*, 5(2):545–589, 2015.

[13] A. Kammeyer and R. Luiten. Oxidation events and skin aging. *Ageing Research Reviews*, 21(0):16–29, 2015.

[14] S. Quideau, D. Deffieux, C. Douat-Casassus, and L. Pouységu. Plant polyphenols: chemical properties, biological activities, and synthesis. *Angewandte Chemie (International ed. in English)*, 50(3):586–621, 2011.

[15] E. Haslam and Y. Cai. Plant polyphenols (vegetable tannins): gallic acid metabolism. *Natural Product Reports*, 11(1):41–66, 1994.

[16] S. Renaud and M. De Lorgeril. Wine, alcohol, platelets, and the French paradox for coronary heart disease. *Lancet*, 339(8808):1523–1526, 1992.

[17] E. H. Siemann and L. L. Creasy. Concentration of the Phytoalexin Resveratrol in Wine. *American Journal of Enology and Viticulture*, 43(1):49–52, 1992.

[18] F. Mattivi. Solid phase extraction oftrans-resveratrol from wines for HPLC analysis. *Zeitschrift für Lebensmittel-Untersuchung und Forschung*, 196(6):522–525, 1993.

[19] M. Jang. Cancer Chemopreventive Activity of Resveratrol, a Natural Product Derived from Grapes. *Science*, 275(5297):218–220, 1997.

[20] National Center for Biotechnology Information (NCBI). PubMed. http://www.ncbi.nlm.nih.gov/pubmed.

[21] J. E. Beart, T. H. Lilley, and E. Haslam. Plant polyphenolssecondary metabolism and chemical defence: Some observations. *Phytochemistry*, 24(1):33–38, 1985.

[22] E. Haslam. Natural Polyphenols (Vegetable Tannins) as Drugs: Possible Modes of Action. *Journal of Natural Products*, 59(2):205–215, 1996.

[23] C. S. Yang, X. Wang, G. Lu, and S. C. Picinich. Cancer prevention by tea: animal studies, molecular mechanisms and human relevance. *Nature Reviews Cancer*, 9(6):429–439, 2009.

[24] J. M. Smoliga, J. A. Baur, and H. A. Hausenblas. Resveratrol and health–a comprehensive review of human clinical trials. *Molecular Nutrition and Food Research*, 55(8):1129–1141, 2011.

[25] H.-S. Kim, M. J. Quon, and J.-a. Kim. New insights into the mechanisms of polyphenols beyond antioxidant properties; lessons from the green tea polyphenol, epigallocatechin 3-gallate. *Redox Biology*, 2(0):187–95, 2014.

[26] T. Walle. Bioavailability of resveratrol. *Annals of the New York Academy of Sciences*, 1215(1):9–15, 2011.

[27] M. Asensi, I. Medina, A. Ortega, J. Carretero, M. C. Baño, E. Obrador, and J. M. Estrela. Inhibition of cancer growth by resveratrol is related to its low bioavailability. *Free Radical Biology & Medicine*, 33(3):387–98, 2002.

[28] M. J. Amiot, B. Romier, T. M. Anh Dao, R. Fanciullino, J. Ciccolini, R. Burcelin, L. Pechere, C. Emond, J. F. Savouret, and E. Seree. Optimization of trans-Resveratrol bioavailability for human therapy. *Biochimie*, 95(6):1233–1238, 2013.

[29] M. Sessa, M. L. Balestrieri, G. Ferrari, L. Servillo, D. Castaldo, N. D'Onofrio, F. Donsì, and R. Tsao. Bioavailability of encapsulated resveratrol into nanoemulsion-based delivery systems. *Food Chemistry*, 147:42–50, 2014.

[30] M. Takaoka. Resveratrol, a new phenolic compound from Veratrum grandiflorum. *Nippon Kagaku Kaishi*, 60:1090–1100, 1939.

[31] S. Nonomura, H. Kanagawa, and A. Makimoto. [Chemical Constituents of Polygonaceous Plants. I. Studies on the Components of Ko-J O-Kon. (Polygonum Cuspidatum Sieb. Et Zucc.)]. *Yakugaku zasshi : Journal of the Pharmaceutical Society of Japan*, 83:988–990, 1963.

[32] P. Langcake and R. J. Pryce. Production of Resveratrol by Vitis-Vinifera and Other Members of Vitaceae as a Response to Infection or Injury. *Physiological Plant Pathology*, 9(1):77–86, 1976.

[33] J. Burns, T. Yokota, H. Ashihara, M. E. J. Lean, and A. Crozier. Plant foods and herbal sources of resveratrol. *Journal of Agricultural and Food Chemistry*, 50(11):3337–40, 2002.

[34] M. S. Baliga, S. Meleth, and S. K. Katiyar. Growth inhibitory and antimetastatic effect of green tea polyphenols on metastasis-specific mouse mammary carcinoma 4T1 cells in vitro and in vivo systems. *Clinical Cancer Research*, 11(5):1918–27, 2005.

[35] Š. Zupančič, Z. Lavrič, and J. Kristl. Stability and solubility of trans-resveratrol are strongly influenced by pH and temperature. *European Journal of Pharmaceutics and Biopharmaceutics*, 93(0):196–204, 2015.

[36] B. C. Trela and A. L. Waterhouse. Resveratrol: Isomeric Molar Absorptivities and Stability. *Journal of Agricultural and Food Chemistry*, 44(5):1253–1257, 1996.

[37] J. W. Jhoo, C. Y. Lo, S. Li, S. Sang, C. Y. W. Ang, T. M. Heinze, and C. T. Ho. Stability of black tea polyphenol, theaflavin, and identification of theanaphthoquinone as its major radical reaction product. *Journal of Agricultural and Food Chemistry*, 53(15):6146–6150, 2005.

[38] S. Stojanović and O. Brede. Elementary reactions of the antioxidant action of trans-stilbene derivatives: resveratrol, pinosylvin and 4-hydroxystilbene. *Physical Chemistry Chemical Physics*, 4(5):757–764, 2002.

[39] Y. Bader, R. Quint, and N. Getoff. Resveratrol products resulting by free radical attack. *Radiation Physics and Chemistry*, 77(6):708–712, 2008.

[40] D. D. Li, R. M. Han, R. Liang, C. H. Chen, W. Lai, J. P. Zhang, and L. H. Skibsted. Hydroxyl radical reaction with trans-resveratrol: Initial carbon radical adduct formation followed by rearrangement to phenoxyl radical. *Journal of Physical Chemistry B*, 116(24):7154–7161, 2012.

[41] L. H. Long, M. V. Clement, and B. Halliwell. Artifacts in cell culture: rapid generation of hydrogen peroxide on addition of (-)-epigallocatechin, (-)-epigallocatechin gallate, (+)-catechin, and quercetin to commonly used cell culture media. *Biochemical and Biophysical Research Communications*, 273(1):50–53, 2000.

[42] N.-C. Yang, C.-H. Lee, and T.-Y. Song. Evaluation of resveratrol oxidation in vitro and the crucial role of bicarbonate ions. *Bioscience, Biotechnology, and Biochemistry*, 74(1):63–68, 2010.

[43] Z. Hou, S. Sang, H. You, M.-J. Lee, J. Hong, K.-V. Chin, and C. S. Yang. Mechanism of action of (-)-epigallocatechin-3-gallate: auto-oxidation-dependent inactivation of epidermal growth factor receptor and direct effects on growth inhibition in human esophageal cancer KYSE 150 cells. *Cancer Research*, 65(17):8049–8056, 2005.

[44] L. Camont, C.-H. Cottart, Y. Rhayem, V. Nivet-Antoine, R. Djelidi, F. Collin, J.-L. Beaudeux, and D. Bonnefont-Rousselot. Simple spectrophotometric assessment of the trans-/cis-resveratrol ratio in aqueous solutions. *Analytica chimica acta*, 634(1):121–8, 2009.

[45] F. Orallo. Comparative studies of the antioxidant effects of cis- and trans-resveratrol. *Current Medicinal Chemistry*, 13(1):87–98, 2006.

[46] N. Y. Anisimova, M. V. Kiselevsky, A. V. Sosnov, S. V. Sadovnikov, I. N. Stankov, and A. A. Gakh. Trans-, cis-, and dihydro-resveratrol: a comparative study. *Chemistry Central Journal*, 5(1):88, 2011.

[47] B. Halliwell, M. V. Clement, J. Ramalingam, and L. H. Long. Hydrogen peroxide. Ubiquitous in cell culture and in vivo? *IUBMB life*, 50(4-5):251–7, 2000.

[48] H. Babich, E. J. Liebling, R. F. Burger, H. L. Zuckerbraun, and A. G. Schuck. Choice of DMEM, formulated with or without pyruvate, plays an important role in assessing the in vitro cytotoxicity of oxidants and prooxidant nutraceuticals. *In Vitro Cellular & Developmental Biology. Animal*, 45(5-6):226–33, 2009.

[49] L. H. Long and B. Halliwell. Artefacts in cell culture: pyruvate as a scavenger of hydrogen peroxide generated by ascorbate or epigallocatechin gallate in cell culture media. *Biochemical and Biophysical Research Communications*, 388(4):700–4, 2009.

[50] M. C. Brahimi-Horn and J. Pouysségur. Oxygen, a source of life and stress. *FEBS Letters*, 581(19):3582–3591, 2007.

[51] B. A. Wagner, S. Venkataraman, and G. R. Buettner. The rate of oxygen utilization by cells. *Free Radical Biology & Medicine*, 51(3):700–12, 2011.

[52] B. Halliwell. Cell culture, oxidative stress, and antioxidants: avoiding pitfalls. *Biomedical Journal*, 37(3):99–105, 2014.

[53] A. Carreau, B. El Hafny-Rahbi, A. Matejuk, C. Grillon, and C. Kieda. Why is the partial oxygen pressure of human tissues a crucial parameter? Small molecules and hypoxia. *Journal of Cellular and Molecular Medicine*, 15(6):1239–53, 2011.

[54] T. Walle, F. Hsieh, M. H. DeLegge, J. E. Oatis, and U. K. Walle. High absorption but very low bioavailability of oral resveratrol in humans. *Drug Metabolism and Disposition: the Biological Fate of Chemicals*, 32(12):1377–82, 2004.

[55] E. Wenzel and V. Somoza. Metabolism and bioavailability of trans-resveratrol. *Molecular Nutrition and Food Research*, 49(5):472–481, 2005.

[56] O. Vang, N. Ahmad, C. A. Baile, J. A. Baur, K. Brown, A. Csiszar, D. K. Das, D. Delmas, C. Gottfried, H. Y. Lin, Q. Y. Ma, P. Mukhopadhyay, N. Nalini, J. M. Pezzuto, T. Richard, Y. Shukla, Y. J. Surh, T. Szekeres, T. Szkudelski, T. Walle, and J. M. Wu. What is new for an old molecule? systematic review and recommendations on the use of resveratrol. *PLoS ONE*, 6(6):e19881, 2011.

[57] L. M. Bode, D. Bunzel, M. Huch, G.-S. Cho, D. Ruhland, M. Bunzel, A. Bub, C. M. Franz, and S. E. Kulling. In vivo and in vitro metabolism of trans-resveratrol by human gut microbiota. *The American Journal of Clinical Nutrition*, 97(1):1–15, 2013.

[58] I. Murakami, R. Chaleckis, T. Pluskal, K. Ito, K. Hori, M. Ebe, M. Yanagida, and H. Kondoh. Metabolism of skin-absorbed resveratrol into its glucuronized form in mouse skin. *PLoS ONE*, 9(12):e115359, 2014.

[59] J. Gambini, M. Inglés, G. Olaso, R. Lopez-Grueso, V. Bonet-Costa, L. Gimeno-Mallench, C. Mas-Bargues, K. M. Abdelaziz, M. C. Gomez-Cabrera, J. Vina, and C. Borras. Properties of Resveratrol: In Vitro and In Vivo Studies about Metabolism, Bioavailability, and Biological Effects in Animal Models and Humans. *Oxidative Medicine and Cellular Longevity*, 2015:837042, 2015.

[60] M. Kaeberlein, T. McDonagh, B. Heltweg, J. Hixon, E. A. Westman, S. D. Caldwell, A. Napper, R. Curtis, P. S. DiStefano, S. Fields, A. Bedalov, and B. K. Kennedy. Substrate-specific activation of sirtuins by resveratrol. *The Journal of Biological Chemistry*, 280(17):17038–45, 2005.

[61] S. Holzhauser, A. Freiwald, C. Weise, G. Multhaup, C.-T. Han, and S. Sauer. Discovery and characterization of protein-modifying natural products by MALDI mass spectrometry reveal potent SIRT1 and p300 inhibitors. *Angewandte Chemie (International ed. in English)*, 52(19):5171–4, 2013.

[62] B. P. Hubbard, A. P. Gomes, H. Dai, J. Li, A. W. Case, T. Considine, T. V. Riera, J. E. Lee, S. Y. E, D. W. Lamming, B. L. Pentelute, E. R. Schuman, L. a. Stevens, A. J. Y. Ling, S. M. Armour, S. Michan, H. Zhao, Y. Jiang, S. M. Sweitzer, C. a. Blum, J. S. Disch, P. Y. Ng, K. T. Howitz, A. P. Rolo, Y. Hamuro, J. Moss, R. B. Perni, J. L. Ellis, G. P. Vlasuk, and D. a. Sinclair. Evidence for a common mechanism of SIRT1 regulation by allosteric activators. *Science*, 339(6124):1216–9, 2013.

[63] S.-J. Park, F. Ahmad, A. Philp, K. Baar, T. Williams, H. Luo, H. Ke, H. Rehmann, R. Taussig, A. L. Brown, M. K. Kim, M. A. Beaven, A. B. Burgin, V. Manganiello, and J. H. Chung. Resveratrol ameliorates aging-related metabolic phenotypes by inhibiting cAMP phosphodiesterases. *Cell*, 148(3):421–33, 2012.

[64] B. D. Gehm, J. M. McAndrews, P. Y. Chien, and J. L. Jameson. Resveratrol, a polyphenolic compound found in grapes and wine, is an agonist for the estrogen receptor. *Proceedings of the National Academy of Sciences of the United States of America*, 94(25):14138–14143, 1997.

[65] K. T. Howitz, K. J. Bitterman, H. Y. Cohen, D. W. Lamming, S. Lavu, J. G. Wood, R. E. Zipkin, P. Chung, A. Kisielewski, L.-L. Zhang, B. Scherer, and D. A. Sinclair. Small molecule activators of sirtuins extend Saccharomyces cerevisiae lifespan. *Nature*, 425(6954):191–6, 2003.

[66] B. B. Aggarwal, A. Bhardwaj, R. S. Aggarwal, N. P. Seeram, S. Shishodia, and Y. Takada. Role of resveratrol in prevention and therapy of cancer: Preclinical and clinical studies. *Anticancer Research*, 24(5 A):2783–2840, 2004.

[67] U. Stervbo, O. Vang, and C. Bonnesen. Time- and concentration-dependent effects of resveratrol in HL-60 and HepG2 cells. *Cell Proliferation*, 39(6):479–93, 2006.

[68] L. Pirola and S. Fröjdö. Resveratrol: one molecule, many targets. *IUBMB life*, 60(5):323–32, 2008.

[69] G. Hasko, P. Pacher, G. Haskó, and P. Pacher. Endothelial Nrf2 activation: a new target for resveratrol? *AJP: Heart and Circulatory Physiology*, 299(1):H10–H12, 2010.

[70] R. I. Tennen, E. Michishita-Kioi, and K. F. Chua. Finding a Target for Resveratrol. *Cell*, 148(3):387–389, 2012.

[71] J. L. Bitterman and J. H. Chung. Metabolic effects of resveratrol: addressing the controversies. *Cellular and Molecular Life Sciences*, 72(8):1473–88, 2015.

[72] S. S. Kulkarni and C. Cantó. The molecular targets of resveratrol. *Biochimica et Biophysica Acta*, 1852(6):1114–23, 2015.

[73] G. Han, J. Xia, J. Gao, Y. Inagaki, W. Tang, and N. Kokudo. Anti-tumor effects and cellular mechanisms of resveratrol. *Drug Discoveries & Therapeutics*, 9(1):1–12, 2015.

[74] G. Blander and L. Guarente. The SIR2 Family of Protein Deacetylases. *Annual Review of Biochemistry*, 73(1):417–435, 2004.

[75] R. H. Houtkooper, E. Pirinen, and J. Auwerx. Sirtuins as regulators of metabolism and healthspan. *Nature Reviews. Molecular Cell Biology*, 13(4):225–38, 2012.

[76] H. C. Chang and L. Guarente. SIRT1 and other sirtuins in metabolism. *Trends in Endocrinology and Metabolism*, 25(3):138–145, 2014.

[77] M. T. Borra, B. C. Smith, and J. M. Denu. Mechanism of human SIRT1 activation by resveratrol. *Journal of Biological Chemistry*, 280(17):17187–17195, 2005.

[78] S. J. Lin, P. A. Defossez, and L. Guarente. Requirement of NAD and SIR2 for life-span extension by calorie restriction in Saccharomyces cerevisiae. *Science*, 289(5487):2126–2128, 2000.

[79] S.-J. Lin, M. Kaeberlein, A. A. Andalis, L. A. Sturtz, P.-A. Defossez, V. C. Culotta, G. R. Fink, and L. Guarente. Calorie restriction extends Saccharomyces cerevisiae lifespan by increasing respiration. *Nature*, 418(6895):344–348, 2002.

[80] R. M. Anderson, M. Latorre-Esteves, A. R. Neves, S. Lavu, O. Medvedik, C. Taylor, K. T. Howitz, H. Santos, and D. A. Sinclair. Yeast life-span extension by calorie restriction is independent of NAD fluctuation. *Science*, 302(5653):2124–2126, 2003.

[81] B. Rogina and S. L. Helfand. Sir2 mediates longevity in the fly through a pathway related to calorie restriction. *Proceedings of the National Academy of Sciences of the United States of America*, 101(45):15998–6003, 2004.

[82] F. Flick and B. Lüscher. Regulation of sirtuin function by posttranslational modifications. *Frontiers in Pharmacology*, 3(February):29, 2012.

[83] X. Guo, J. G. Williams, T. T. Schug, and X. Li. DYRK1A and DYRK3 promote cell survival through phosphorylation and activation of SIRT1. *Journal of Biological Chemistry*, 285(17):13223–13232, 2010.

[84] Z. Gerhart-Hines, J. E. Dominy, S. M. Blättler, M. P. Jedrychowski, A. S. Banks, J.-H. Lim, H. Chim, S. P. Gygi, and P. Puigserver. The cAMP/PKA pathway rapidly activates SIRT1 to promote fatty acid oxidation independently of changes in NAD(+). *Molecular Cell*, 44(6):851–63, 2011.

[85] A. Satoh, L. Stein, and S. Imai. The Role of Mammalian Sirtuins in the Regulation of Metabolism, Aging, and Longevity. In T.-P. Yao and E. Seto, editors, *Histone Deacetylases: the Biology and Clinical Implication SE - 7*, volume 206 of *Handbook of Experimental Pharmacology*, pages 125–162. Springer Berlin Heidelberg, 2011.

[86] C. Cantó and J. Auwerx. Targeting sirtuin 1 to improve metabolism: all you need is NAD(+)? *Pharmacological Reviews*, 64(1):166–87, 2012.

[87] L. Zhong and R. Mostoslavsky. Fine Tuning Our Cellular Factories: Sirtuins in Mitochondrial Biology. *Cell Metabolism*, 13(6):621–626, 2011.

[88] S. Imai, C. M. Armstrong, M. Kaeberlein, and L. Guarente. Transcriptional silencing and longevity protein Sir2 is an NAD-dependent histone deacetylase. *Nature*, 403(6771):795–800, 2000.

[89] S. J. Lin, E. Ford, M. Haigis, G. Liszt, and L. Guarente. Calorie restriction extends yeast life span by lowering the level of NADH. *Genes & Development*, 18(1):12–16, 2004.

[90] C. Cantó and J. Auwerx. AMP-activated protein kinase and its downstream transcriptional pathways. *Cellular and Molecular Life Sciences*, 67(20):3407–3423, 2010.

[91] K. J. Bitterman. Inhibition of Silencing and Accelerated Aging by Nicotinamide, a Putative Negative Regulator of Yeast Sir2 and Human SIRT1. *Journal of Biological Chemistry*, 277(47):45099–45107, 2002.

[92] C. Cantó and J. Auwerx. Interference between PARPs and SIRT1: a novel approach to healthy ageing? *Aging*, 3(5):543–547, 2011.

[93] P. Bai, C. Cantó, H. Oudart, A. Brunyánszki, Y. Cen, C. Thomas, H. Yamamoto, A. Huber, B. Kiss, R. H. Houtkooper, K. Schoonjans, V. Schreiber, A. A. Sauve, J. Menissier-de Murcia, and J. Auwerx. PARP-1 inhibition increases mitochondrial metabolism through SIRT1 activation. *Cell Metabolism*, 13(4):461–8, 2011.

[94] A. Luna, M. I. Aladjem, and K. W. Kohn. SIRT1/PARP1 crosstalk: connecting DNA damage and metabolism. *Genome Integrity*, 4(1):6, 2013.

[95] N. Nasrin, V. K. Kaushik, E. Fortier, D. Wall, K. J. Pearson, R. de Cabo, and L. Bordone. JNK1 phosphorylates SIRT1 and promotes its enzymatic activity. *PLoS ONE*, 4(12):e8414, 2009.

[96] S. Chung, H. Yao, S. Caito, J. woong Hwang, G. Arunachalam, and I. Rahman. Regulation of SIRT1 in cellular functions: Role of polyphenols. *Archives of Biochemistry and Biophysics*, 501(1):79–90, 2010.

[97] S. Caito, S. Rajendrasozhan, S. Cook, S. Chung, H. Yao, A. E. Friedman, P. S. Brookes, and I. Rahman. SIRT1 is a redox-sensitive deacetylase that is post-translationally modified by oxidants and carbonyl stress. *The FASEB Journal*, 24(9):3145–3159, 2010.

[98] T. Sasaki, B. Maier, K. D. Koclega, M. Chruszcz, W. Gluba, P. T. Stukenberg, W. Minor, and H. Scrable. Phosphorylation Regulates SIRT1 Function. *PLoS ONE*, 3(12):e4020, 2008.

[99] H.-L. Cheng, R. Mostoslavsky, S. Saito, J. P. Manis, Y. Gu, P. Patel, R. Bronson, E. Appella, F. W. Alt, and K. F. Chua. Developmental defects and p53 hyperacetylation in Sir2 homolog (SIRT1)-deficient mice. *Proceedings of the National Academy of Sciences*, 100(19):10794–10799, 2003.

[100] A. Vaquero, R. Sternglanz, and D. Reinberg. NAD+-dependent deacetylation of H4 lysine 16 by class III HDACs. *Oncogene*, 26(37):5505–20, 2007.

[101] R.-H. Wang, K. Sengupta, C. Li, H.-S. Kim, L. Cao, C. Xiao, S. Kim, X. Xu, Y. Zheng, B. Chilton, R. Jia, Z.-M. Zheng, E. Appella, X. W. Wang, T. Ried, and C.-X. Deng. Impaired DNA damage response, genome instability, and tumorigenesis in SIRT1 mutant mice. *Cancer Cell*, 14(4):312–323, 2008.

[102] A. Vaquero. The conserved role of sirtuins in chromatin regulation. *The International Journal of Developmental Biology*, 53(2-3):303–22, 2009.

[103] L. Bosch-Presegué and A. Vaquero. Sirtuins in stress response: guardians of the genome. *Oncogene*, 33(29):3764–75, 2014.

[104] J. Luo, A. Y. Nikolaev, S.-i. Imai, D. Chen, F. Su, A. Shiloh, L. Guarente, and W. Gu. Negative Control of p53 by Sir2α Promotes Cell Survival under Stress. *Cell*, 107(2):137–148, 2001.

[105] H. Vaziri, S. K. Dessain, E. N. Eaton, S.-I. Imai, R. A. Frye, T. K. Pandita, L. Guarente, and R. A. Weinberg. hSIR2 SIRT1 Functions as an NAD-Dependent p53 Deacetylase. *Cell*, 107(2):149–159, 2001.

[106] T. Bouras, M. Fu, A. A. Sauve, F. Wang, A. A. Quong, N. D. Perkins, R. T. Hay, W. Gu, and R. G. Pestell. SIRT1 deacetylation and repression of p300 involves lysine residues 1020/1024 within the cell cycle regulatory domain 1. *The Journal of Biological Chemistry*, 280(11):10264–76, 2005.

[107] S. C. Kim, R. Sprung, Y. Chen, Y. Xu, H. Ball, J. Pei, T. Cheng, Y. Kho, H. Xiao, L. Xiao, N. V. Grishin, M. White, X.-J. Yang, and Y. Zhao. Substrate and functional diversity of lysine acetylation revealed by a proteomics survey. *Molecular Cell*, 23(4):607–18, 2006.

[108] L. R. Saunders and E. Verdin. Sirtuins: critical regulators at the crossroads between cancer and aging. *Oncogene*, 26(37):5489–504, 2007.

[109] C. L. Brooks and W. Gu. How does SIRT1 affect metabolism, senescence and cancer? *Nature Reviews. Cancer*, 9(2):123–8, 2009.

[110] C.-X. Deng. SIRT1, Is It a Tumor Promoter or Tumor Suppressor? *International Journal of Biological Sciences*, 5(2):147–152, 2009.

[111] S. Zhao, W. Xu, W. Jiang, W. Yu, Y. Lin, T. Zhang, J. Yao, L. Zhou, Y. Zeng, H. Li, Y. Li, J. Shi, W. An, S. M. Hancock, F. He, L. Qin, J. Chin, P. Yang, X. Chen, Q. Lei, Y. Xiong, and K.-L. Guan. Regulation of cellular metabolism by protein lysine acetylation. *Science*, 327(5968):1000–4, 2010.

[112] X. Li. SIRT1 and energy metabolism. *Acta Biochimica et Biophysica Sinica*, 45(1):51–60, 2013.

[113] S. Gonfloni, V. Iannizzotto, E. Maiani, G. Bellusci, S. Ciccone, and M. Diederich. P53 and Sirt1: routes of metabolism and genome stability. *Biochemical Pharmacology*, 92(1):149–56, 2014.

[114] R. van Gent, C. Di Sanza, N. J. F. van den Broek, V. Fleskens, A. Veenstra, G. J. Stout, and A. B. Brenkman. SIRT1 Mediates FOXA2 Breakdown by Deacetylation in a Nutrient-Dependent Manner. *PLoS ONE*, 9(5):e98438, 2014.

[115] S. Rahman and R. Islam. Mammalian Sirt1: insights on its biological functions. *Cell Communication and Signaling*, 9(1):11, 2011.

[116] W. Stünkel and R. M. Campbell. Sirtuin 1 (SIRT1): the misunderstood HDAC. *Journal of Biomolecular Screening*, 16(10):1153–69, 2011.

[117] E. J. Calabrese and L. A. Baldwin. Hormesis: the dose-response revolution. *Annual Review of Pharmacology and Toxicology*, 43:175–197, 2003.

[118] D. Axelrod, K. Burns, D. Davis, and N. Von Larebeke. "Hormesis" - An inappropriate extrapolation from the specific to the universal. *International Journal of Occupational and Environmental Health*, 10(3):335–339, 2004.

[119] E. J. Calabrese, E. J. Stanek, M. A. Nascarella, and G. R. Hoffmann. Hormesis predicts low-dose responses better than threshold models. *International Journal of Toxicology*, 27(5):369–378, 2008.

[120] E. J. Calabrese and L. A. Baldwin. The hormetic dose-response model is more common than the threshold model in toxicology. *Toxicological Sciences*, 71(2):246–250, 2003.

[121] J. V. Rodricks. Hormesis and toxicological risk assessment. *Toxicological Sciences*, 71(2):134–136, 2003.

[122] K. T. Howitz and D. A. Sinclair. Xenohormesis: Sensing the Chemical Cues of Other Species. *Cell*, 133(3):387–391, 2008.

[123] M. P. Mattson and A. Cheng. Neurohormetic phytochemicals: low-dose toxins that induce adaptive neuronal stress responses. *Trends in Neurosciences*, 29(11):632–639, 2006.

[124] M. Ristow and K. Schmeisser. Mitohormesis: Promoting Health and Lifespan by Increased Levels of Reactive Oxygen Species (ROS). *Dose-response*, 12(2):288–341, 2014.

[125] J. Yun and T. Finkel. Mitohormesis. *Cell Metabolism*, 19(5):757–766, 2014.

[126] E. J. Calabrese and L. A. Baldwin. Toxicology rethinks its central belief. *Nature*, 421(6924):691–2, 2003.

[127] E. J. Calabrese. Hormesis: a revolution in toxicology, risk assessment and medicine. *EMBO reports*, 5:S37–S40, 2004.

[128] M. P. Mattson. Hormesis defined. *Ageing Research Reviews*, 7(1):1–7, 2008.

[129] T. G. Son, S. Camandola, and M. P. Mattson. Hormetic dietary phytochemicals. *NeuroMolecular Medicine*, 10(4):236–246, 2008.

[130] J.-S. Lee and Y.-J. Surh. Nrf2 as a novel molecular target for chemoprevention. *Cancer Letters*, 224(2):171–184, 2005.

[131] H. Van Der Woude, A. Gliszczyńska-Świgł;o, K. Struijs, A. Smeets, G. M. Alink, and I. M. C. M. Rietjens. Biphasic modulation of cell proliferation by quercetin at concentrations physiologically relevant in humans. *Cancer Letters*, 200(1):41–47, 2003.

[132] S. Mukherjee, J. I. Dudley, and D. K. Das. Dose-dependency of resveratrol in providing health benefits. *Dose-response*, 8(4):478–500, 2010.

[133] E. J. Calabrese, M. P. Mattson, and V. Calabrese. Resveratrol commonly displays hormesis: occurrence and biomedical significance. *Human and Experimental Toxicology*, 29(12):980–1015, 2010.

[134] V. Calabrese, C. Cornelius, A. T. Dinkova-Kostova, and E. J. Calabrese. Vitagenes, cellular stress response, and acetylcarnitine: Relevance to hormesis. *BioFactors*, 35(2):146–160, 2009.

[135] E. Balogun, M. Hoque, P. Gong, E. Killeen, C. J. Green, R. Foresti, J. Alam, and R. Motterlini. Curcumin activates the haem oxygenase-1 gene via regulation of Nrf2 and the antioxidant-responsive element. *The Biochemical Journal*, 371(Pt 3):887–95, 2003.

[136] M.-C. Kou, S.-Y. Chiou, C.-Y. Weng, L. Wang, C.-T. Ho, and M.-J. Wu. Curcuminoids distinctly exhibit antioxidant activities and regulate expression of scavenger receptors and heme oxygenase-1. *Molecular Nutrition and Food Research*, 57(9):1598–610, 2013.

[137] R. Zhao, B. Yang, L. Wang, P. Xue, B. Deng, G. Zhang, S. Jiang, M. Zhang, M. Liu, J. Pi, and D. Guan. Curcumin protects human keratinocytes against inorganic arsenite-induced acute cytotoxicity through an NRF2-dependent mechanism. *Oxidative Medicine and Cellular Longevity*, 2013:412576, 2013.

[138] Y. Li, Z. Cao, and H. Zhu. Upregulation of endogenous antioxidants and phase 2 enzymes by the red wine polyphenol, resverarol in cultured aortic smooth muscle cells leads to cytoprotection against oxidative and electrophilic stress. *Pharmacological Research*, 53(1):6–15, 2006.

[139] C.-Y. Chen, J.-H. Jang, M.-H. Li, and Y.-J. Surh. Resveratrol upregulates heme oxygenase-1 expression via activation of NF-E2-related factor 2 in PC12 cells. *Biochemical and Biophysical Research Communications*, 331(4):993–1000, 2005.

[140] Y. Zhang, P. Talalay, C. G. Cho, and G. H. Posner. A major inducer of anticarcinogenic protective enzymes from broccoli: isolation and elucidation of structure. *Proceedings of the National Academy of Sciences of the United States of America*, 89(6):2399–2403, 1992.

[141] L. G. Higgins, M. O. Kelleher, I. M. Eggleston, K. Itoh, M. Yamamoto, and J. D. Hayes. Transcription factor Nrf2 mediates an adaptive response to sulforaphane that protects fibroblasts in vitro against the cytotoxic effects of electrophiles, peroxides and redox-cycling agents. *Toxicology and Applied Pharmacology*, 237(3):267–80, 2009.

[142] X. Gao and P. Talalay. Induction of phase 2 genes by sulforaphane protects retinal pigment epithelial cells against photooxidative damage. *Proceedings of the National Academy of Sciences of the United States of America*, 101(28):10446–10451, 2004.

[143] M. Tanito, H. Masutani, Y.-C. Kim, M. Nishikawa, A. Ohira, and J. Yodoi. Sulforaphane Induces Thioredoxin through the Antioxidant-Responsive Element and Attenuates Retinal Light Damage in Mice. *Investigative Ophthalmology & Visual Science*, 46(3):979–987, 2005.

[144] F. Li, H. P. Mao, K. L. Ruchalski, Y. H. Wang, W. Choy, J. H. Schwartz, and S. C. Borkan. Heat stress prevents mitochondrial injury in ATP-depleted renal epithelial cells. *American Journal of Physiology. Cell physiology*, 283(3):C917–C926, 2002.

[145] P. Talalay, J. W. Fahey, Z. R. Healy, S. L. Wehage, A. L. Benedict, C. Min, and A. T. Dinkova-Kostova. Sulforaphane mobilizes cellular defenses that protect skin against damage by UV radiation. *Proceedings of the National Academy of Sciences of the United States of America*, 104(44):17500–5, 2007.

[146] A. Kode, S. Rajendrasozhan, S. Caito, S.-R. Yang, I. L. Megson, and I. Rahman. Resveratrol induces glutathione synthesis by activation of Nrf2 and protects against cigarette smoke-mediated oxidative stress in human lung epithelial cells. *American Journal of Physiology. Lung cellular and molecular physiology*, 294(3):L478–88, 2008.

[147] E. Tapia, V. Soto, K. M. Ortiz-Vega, G. Zarco-Márquez, E. Molina-Jijón, M. Cristóbal-García, J. Santamaría, W. R. García-Niño, F. Correa, C. Zazueta, and J. Pedraza-Chaverri. Curcumin induces Nrf2 nuclear translocation and prevents glomerular hypertension, hyperfiltration, oxidant stress, and the decrease in antioxidant enzymes in 5/6 nephrectomized rats. *Oxidative Medicine and Cellular Longevity*, 2012:269039, 2012.

[148] K. Kleszczyński, I. M. A. Ernst, A. E. Wagner, N. Kruse, D. Zillikens, G. Rimbach, and T. W. Fischer. Sulforaphane and phenylethyl isothiocyanate protect human skin against UVR-induced oxidative stress and apoptosis: role of Nrf2-dependent gene expression and antioxidant enzymes. *Pharmacological Research*, 78:28–40, 2013.

[149] B. Lipinski. Hydroxyl Radical and Its Scavengers in Health and Disease. *Oxidative Medicine and Cellular Longevity*, 2011:1–9, 2011.

[150] S. G. Rhee. Redox signaling: hydrogen peroxide as intracellular messenger. *Experimental & Molecular Medicine*, 31(2):53–9, 1999.

[151] J. Nordberg and E. S. Arnér. Reactive oxygen species, antioxidants, and the mammalian thioredoxin system. *Free Radical Biology & Medicine*, 31(11):1287–312, 2001.

[152] P. D. Ray, B.-W. Huang, and Y. Tsuji. Reactive oxygen species (ROS) homeostasis and redox regulation in cellular signaling. *Cellular Signalling*, 24(5):981–990, 2012.

[153] H. Sies. Role of Metabolic H2O2 Generation: REDOX SIGNALING AND OXIDATIVE STRESS. *Journal of Biological Chemistry*, 289(13):8735–8741, 2014.

[154] D. Trachootham, J. Alexandre, and P. Huang. Targeting cancer cells by ROS-mediated mechanisms: a radical therapeutic approach? *Nature Reviews. Drug Discovery*, 8(7):579–591, 2009.

[155] J. K. Andersen. Oxidative stress in neurodegeneration: cause or consequence? *Nature Medicine*, 10 Suppl:S18–S25, 2004.

[156] T. M. Paravicini and R. M. Touyz. Redox signaling in hypertension. *Cardiovascular Research*, 71(2):247–258, 2006.

[157] M. C. Haigis and B. A. Yankner. The Aging Stress Response. *Molecular Cell*, 40(2):333–344, 2010.

[158] H. J. H. Fenton. LXXIII.-Oxidation of tartaric acid in presence of iron. *Journal of the Chemical Society, Transactions*, 65(0):899–910, 1894.

[159] F. Haber and J. Weiss. The Catalytic Decomposition of Hydrogen Peroxide by Iron Salts. *Proceedings of the Royal Society of London. Series A, Mathematical and Physical Sciences*, 147(861):332–351, 1934.

[160] R. S. Balaban, S. Nemoto, and T. Finkel. Mitochondria, oxidants, and aging. *Cell*, 120(4):483–95, 2005.

[161] M. D. Brand. The sites and topology of mitochondrial superoxide production. *Experimental Gerontology*, 45(78):466–472, 2010.

[162] M. P. Murphy, A. Holmgren, N.-G. Larsson, B. Halliwell, C. J. Chang, B. Kalyanaraman, S. G. Rhee, P. J. Thornalley, L. Partridge, D. Gems, T. Nyström, V. Belousov, P. T. Schumacker, and C. C. Winterbourn. Unraveling the biological roles of reactive oxygen species. *Cell Metabolism*, 13(4):361–6, 2011.

[163] B. Chance, H. Sies, and A. Boveris. Hydroperoxide metabolism in mammalian organs. *Physiological Reviews*, 59(3):527–605, 1979.

[164] W.-L. Lee, J.-Y. Huang, and L.-F. Shyur. Phytoagents for Cancer Management: Regulation of Nucleic Acid Oxidation, ROS, and Related Mechanisms. *Oxidative Medicine and Cellular Longevity*, 2013:925804, 2013.

[165] B. P. Yu. Cellular defenses against damage from reactive oxygen species. *Physiological Reviews*, 74(1):139–62, 1994.

[166] G. R. Buettner. Superoxide dismutase in redox biology: the roles of superoxide and hydrogen peroxide. *Anti-cancer Agents in Medicinal Chemistry*, 11(4):341–6, 2011.

[167] C. C. Winterbourn. Toxicity of iron and hydrogen peroxide: the Fenton reaction. *Toxicology Letters*, 82-83:969–74, 1995.

[168] H. S. Marinho, C. Real, L. Cyrne, H. Soares, and F. Antunes. Hydrogen peroxide sensing, signaling and regulation of transcription factors. *Redox Biology*, 2:535–562, 2014.

[169] S. J. Dixon and B. R. Stockwell. The role of iron and reactive oxygen species in cell death. *Nature Chemical Biolology*, 10(1):9–17, 2014.

[170] E. L. Thomas, R. I. Lehrer, and R. F. Rest. Human Neutrophil Antimicrobial Activity. *Clinical Infectious Diseases*, 10(Supplement 2):S450–S456, 1988.

[171] R. Schreck, K. Albermann, and P. A. Baeuerle. Nuclear factor kappa B: an oxidative stress-responsive transcription factor of eukaryotic cells (a review). *Free Radical Research Communications*, 17(4):221–37, 1992.

[172] Z. Ungvari, Z. Orosz, N. Labinskyy, A. Rivera, Z. Xiangmin, K. Smith, and A. Csiszar. Increased mitochondrial H2O2 production promotes endothelial NF-kappaB activation in aged rat arteries. *American Journal of Physiology. Heart and circulatory physiology*, 293(1):H37–47, 2007.

[173] K. Taguchi, H. Motohashi, and M. Yamamoto. Molecular mechanisms of the Keap1Nrf2 pathway in stress response and cancer evolution. *Genes to Cells*, 16(2):123–40, 2011.

[174] M. Putker, T. Madl, H. R. Vos, H. de Ruiter, M. Visscher, M. C. van den Berg, M. Kaplan, H. C. Korswagen, R. Boelens, M. Vermeulen, B. M. Burgering, and T. B. Dansen. Redox-Dependent Control of FOXO/DAF-16 by Transportin-1. *Molecular Cell*, 49(4):730–742, 2013.

[175] R. Kohen and I. Gati. Skin low molecular weight antioxidants and their role in aging and in oxidative stress. *Toxicology*, 148(2-3):149–157, 2000.

[176] G. R. Buettner. The pecking order of free radicals and antioxidants: lipid peroxidation, alpha-tocopherol, and ascorbate. *Archives of Biochemistry and Biophysics*, 300(2):535–43, 1993.

[177] H. Sies, W. Stahl, and A. R. Sundquist. Antioxidant functions of vitamins. Vitamins E and C, beta-carotene, and other carotenoids. *Annals of the New York Academy of Sciences*, 669(1):7–20, 1992.

[178] N. M. Reddy, S. R. Kleeberger, H.-Y. Cho, M. Yamamoto, T. W. Kensler, S. Biswal, and S. P. Reddy. Deficiency in Nrf2-GSH signaling impairs type II cell growth

and enhances sensitivity to oxidants. *American Journal of Respiratory Cell and Molecular Biology*, 37(1):3–8, 2007.

[179] N. M. Reddy, S. R. Kleeberger, J. H. Bream, P. G. Fallon, T. W. Kensler, M. Yamamoto, and S. P. Reddy. Genetic disruption of the Nrf2 compromises cell-cycle progression by impairing GSH-induced redox signaling. *Oncogene*, 27(44):5821–32, 2008.

[180] I. Fridovich. Superoxide dismutases. *Annual Review of Biochemistry*, 44:147–59, 1975.

[181] G. F. Gaetani, A. M. Ferraris, M. Rolfo, R. Mangerini, S. Arena, and H. N. Kirkman. Predominant role of catalase in the disposal of hydrogen peroxide within human erythrocytes. *Blood*, 87(4):1595–9, 1996.

[182] H. Masaki, Y. Okano, and H. Sakurai. Differential role of catalase and glutathione peroxidase in cultured human fibroblasts under exposure of H2O2 or ultraviolet B light. *Archives of Dermatological Research*, 290(3):113–8, 1998.

[183] H. N. Kirkman, M. Rolfo, A. M. Ferraris, and G. F. Gaetani. Mechanisms of protection of catalase by NADPH. Kinetics and stoichiometry. *The Journal of Biological Chemistry*, 274(20):13908–14, 1999.

[184] S. Li, T. Yan, J. Q. Yang, T. D. Oberley, and L. W. Oberley. The role of cellular glutathione peroxidase redox regulation in the suppression of tumor cell growth by manganese superoxide dismutase. *Cancer Research*, 60(14):3927–3939, 2000.

[185] H. Z. Chae, S. W. Kang, and S. G. Rhee. Isoforms of mammalian peroxiredoxin that reduce peroxides in presence of thioredoxin. *Methods in Enzymology*, 300:219–26, 1999.

[186] H. Z. Chae, H. J. Kim, S. W. Kang, and S. G. Rhee. Characterization of three isoforms of mammalian peroxiredoxin that reduce peroxides in the presence of thioredoxin. *Diabetes Research and Clinical Practice*, 45(2-3):101–112, 1999.

[187] K. Abbas, S. Riquier, and J.-C. Drapier. Peroxiredoxins and Sulfiredoxin at the Crossroads of the NO and H2O2 Signaling Pathways. In *Methods in Enzymology*, volume 527, pages 113–128. 2013.

[188] Y. Shiloh. ATM and related protein kinases: safeguarding genome integrity. *Nature Reviews. Cancer*, 3(3):155–168, 2003.

[189] P. J. Hurley and F. Bunz. ATM and ATR: Components of an integrated circuit. *Cell Cycle*, 6(4):414–417, 2007.

[190] Z. Guo, S. Kozlov, M. F. Lavin, M. D. Person, and T. T. Paull. ATM activation by oxidative stress. *Science*, 330(6003):517–521, 2010.

[191] A. Alexander, S.-L. Cai, J. Kim, A. Nanez, M. Sahin, K. H. MacLean, K. Inoki, K.-L. Guan, J. Shen, M. D. Person, D. Kusewitt, G. B. Mills, M. B. Kastan, and C. L. Walker. ATM signals to TSC2 in the cytoplasm to regulate mTORC1 in response to ROS. *Proceedings of the National Academy of Sciences*, 107(9):4153–4158, 2010.

[192] D. A. Butterfield, T. Koppal, B. Howard, R. Subramaniam, N. Hall, K. Hensley, S. Yatin, K. Allen, M. Aksenov, M. Aksenova, and J. Carney. Structural and functional changes in proteins induced by free radical-mediated oxidative stress and protective action of the antioxidants N-tert-butyl-alpha-phenylnitrone and vitamin E. *Annals of the New York Academy of Sciences*, 854:448–62, 1998.

[193] D. Anastasiou, G. Poulogiannis, J. M. Asara, M. B. Boxer, J.-k. Jiang, M. Shen, G. Bellinger, A. T. Sasaki, J. W. Locasale, D. S. Auld, C. J. Thomas, M. G. Vander Heiden, and L. C. Cantley. Inhibition of pyruvate kinase M2 by reactive oxygen species contributes to cellular antioxidant responses. *Science*, 334(6060):1278–83, 2011.

[194] R. Mathew and E. White. Autophagy, stress, and cancer metabolism: what doesn't kill you makes you stronger. *Cold Spring Harbor Symposia on Quantitative Biology*, 76:389–96, 2011.

[195] A. Vigneron and K. H. Vousden. p53, ROS and senescence in the control of aging. *Aging (Albany NY)*, 2(8):471–474, 2010.

[196] T. M. Johnson, Z. X. Yu, V. J. Ferrans, R. A. Lowenstein, and T. Finkel. Reactive oxygen species are downstream mediators of p53-dependent apoptosis. *Proceedings of the National Academy of Sciences of the United States of America*, 93(21):11848–11852, 1996.

[197] B. D'Autréaux and M. B. Toledano. ROS as signalling molecules: mechanisms that generate specificity in ROS homeostasis. *Nature Reviews. Molecular Cell Biology*, 8(10):813–24, 2007.

[198] G. Gloire, S. Legrand-Poels, and J. Piette. NF-κB activation by reactive oxygen species: Fifteen years later. *Biochemical Pharmacology*, 72(11):1493–1505, 2006.

[199] M. J. Morgan and Z.-g. Liu. Crosstalk of reactive oxygen species and NF-κB signaling. *Cell Research*, 21(1):103–115, 2011.

[200] P. Moi, K. Chan, I. Asunis, A. Cao, and Y. W. Kan. Isolation of NF-E2-related factor 2 (Nrf2), a NF-E2-like basic leucine zipper transcriptional activator that binds to the tandem NF-E2/AP1 repeat of the beta-globin locus control region. *Proceedings of the National Academy of Sciences of the United States of America*, 91(21):9926–30, 1994.

[201] J. D. Hayes, M. McMahon, S. Chowdhry, and A. T. Dinkova-Kostova. Cancer chemoprevention mechanisms mediated through the Keap1-Nrf2 pathway. *Antioxidants & Redox Signaling*, 13(11):1713–48, 2010.

[202] K. Itoh, T. Chiba, S. Takahashi, T. Ishii, K. Igarashi, Y. Katoh, T. Oyake, N. Hayashi, K. Satoh, I. Hatayama, M. Yamamoto, and Y. Nabeshima. An Nrf2/small Maf heterodimer mediates the induction of phase II detoxifying enzyme genes through antioxidant response elements. *Biochemical and Biophysical Research Communications*, 236(2):313–22, 1997.

[203] K. Itoh, N. Wakabayashi, Y. Katoh, T. Ishii, K. Igarashi, J. D. Engel, and M. Yamamoto. Keap1 represses nuclear activation of antioxidant responsive elements by Nrf2 through binding to the amino-terminal Neh2 domain. *Genes & Development*, 13(1):76–86, 1999.

[204] H. Motohashi, F. Katsuoka, J. D. Engel, and M. Yamamoto. Small Maf proteins serve as transcriptional cofactors for keratinocyte differentiation in the Keap1Nrf2 regulatory pathway. *Proceedings of the National Academy of Sciences of the United States of America*, 101(17):6379–6384, 2004.

[205] Y. Hirotsu, F. Katsuoka, R. Funayama, T. Nagashima, Y. Nishida, K. Nakayama, J. D. Engel, and M. Yamamoto. Nrf2-MafG heterodimers contribute globally to antioxidant and metabolic networks. *Nucleic Acids Research*, 40(20):10228–39, 2012.

[206] K. Chan, R. Lu, J. C. Chang, and Y. W. Kan. NRF2, a member of the NFE2 family of transcription factors, is not essential for murine erythropoiesis, growth, and development. *Proceedings of the National Academy of Sciences of the United States of America*, 93(24):13943–13948, 1996.

[207] J. D. Hayes and A. T. Dinkova-Kostova. The Nrf2 regulatory network provides an interface between redox and intermediary metabolism. *Trends in Biochemical Sciences*, 39(4):199–218, 2014.

[208] M.-I. Kang, A. Kobayashi, N. Wakabayashi, S.-G. Kim, and M. Yamamoto. Scaffolding of Keap1 to the actin cytoskeleton controls the function of Nrf2 as key regulator of cytoprotective phase 2 genes. *Proceedings of the National Academy of Sciences of the United States of America*, 101(7):2046–51, 2004.

[209] D. Papp, K. Lenti, D. Módos, D. Fazekas, Z. Dúl, D. Türei, L. Földvári-Nagy, R. Nussinov, P. Csermely, and T. Korcsmáros. The NRF2-related interactome and regulome contain multifunctional proteins and fine-tuned autoregulatory loops. *FEBS Letters*, 586(13):1795–802, 2012.

[210] M.-K. Kwak, K. Itoh, M. Yamamoto, and T. W. Kensler. Enhanced expression of the transcription factor Nrf2 by cancer chemopreventive agents: role of antioxidant response element-like sequences in the nrf2 promoter. *Molecular and Cellular Biochemistry*, 22(9):2883–92, 2002.

[211] T. Nguyen, P. J. Sherratt, and C. B. Pickett. Regulatory mechanisms controlling gene expression mediated by the antioxidant response element. *Annual Review of Pharmacology and Toxicology*, 43(1):233–260, 2003.

[212] T. H. Rushmore and A.-N. Kong. Pharmacogenomics, Regulation and Signaling Pathways of Phase I and II Drug Metabolizing Enzymes. *Current Drug Metabolism*, 3(5):481–490, 2002.

[213] M. Yang, Y. Yao, G. Eades, Y. Zhang, and Q. Zhou. MiR-28 regulates Nrf2 expression through a Keap1-independent mechanism. *Breast Cancer Research and Treatment*, 129(3):983–991, 2011.

[214] X. Cheng, C.-H. Ku, and R. C. M. Siow. Regulation of the Nrf2 antioxidant pathway by microRNAs: New players in micromanaging redox homeostasis. *Free Radical Biology & Medicine*, 64:4–11, 2013.

[215] S. B. Cullinan, D. Zhang, M. Hannink, E. Arvisais, R. J. Kaufman, and J. A. Diehl. Nrf2 is a direct PERK substrate and effector of PERK-dependent cell survival. *Molecular and Cellular Biochemistry*, 23(20):7198–209, 2003.

[216] Y.-S. Keum, S. Yu, P. P.-J. Chang, X. Yuan, J.-H. Kim, C. Xu, J. Han, A. Agarwal, and A.-N. T. Kong. Mechanism of action of sulforaphane: inhibition of p38 mitogen-activated protein kinase isoforms contributing to the induction of antioxidant response element-mediated heme oxygenase-1 in human hepatoma HepG2 cells. *Cancer Research*, 66(17):8804–13, 2006.

[217] X. Yuan, C. Xu, Z. Pan, Y.-S. Keum, J.-H. Kim, G. Shen, S. Yu, K. T. Oo, J. Ma, and A.-N. T. Kong. Butylated hydroxyanisole regulates ARE-mediated gene expression via Nrf2 coupled with ERK and JNK signaling pathway in HepG2 cells. *Molecular Carcinogenesis*, 45(11):841–50, 2006.

[218] Z.-X. Cong, H.-D. Wang, J.-W. Wang, Y. Zhou, H. Pan, D.-D. Zhang, and L. Zhu. ERK and PI3K signaling cascades induce Nrf2 activation and regulate cell viability

partly through Nrf2 in human glioblastoma cells. *Oncology Reports*, 30(2):715–22, 2013.

[219] T. Nguyen, P. J. Sherratt, H.-C. Huang, C. S. Yang, and C. B. Pickett. Increased Protein Stability as a Mechanism That Enhances Nrf2-mediated Transcriptional Activation of the Antioxidant Response Element: DEGRADATION OF Nrf2 BY THE 26 S PROTEASOME. *Journal of Biological Chemistry*, 278(7):4536–4541, 2003.

[220] H.-C. Huang, T. Nguyen, and C. B. Pickett. Phosphorylation of Nrf2 at Ser-40 by protein kinase C regulates antioxidant response element-mediated transcription. *The Journal of Biological Chemistry*, 277(45):42769–74, 2002.

[221] D. A. Bloom and A. K. Jaiswal. Phosphorylation of Nrf2 at Ser40 by protein kinase C in response to antioxidants leads to the release of Nrf2 from INrf2, but is not required for Nrf2 stabilization/accumulation in the nucleus and transcriptional activation of antioxidant response element. *The Journal of Biological Chemistry*, 278(45):44675–82, 2003.

[222] A. K. Jain and A. K. Jaiswal. GSK-3beta acts upstream of Fyn kinase in regulation of nuclear export and degradation of NF-E2 related factor 2. *The Journal of Biological Chemistry*, 282(22):16502–10, 2007.

[223] P. Rada, A. I. Rojo, S. Chowdhry, M. McMahon, J. D. Hayes, and A. Cuadrado. SCF/{beta}-TrCP promotes glycogen synthase kinase 3-dependent degradation of the Nrf2 transcription factor in a Keap1-independent manner. *Molecular and Cellular Biochemistry*, 31(6):1121–33, 2011.

[224] P. Rada, A. I. Rojo, N. Evrard-Todeschi, N. G. Innamorato, A. Cotte, T. Jaworski, J. C. Tobón-Velasco, H. Devijver, M. F. García-Mayoral, F. Van Leuven, J. D. Hayes, G. Bertho, and A. Cuadrado. Structural and functional characterization of Nrf2 degradation by the glycogen synthase kinase 3/β-TrCP axis. *Molecular and Cellular Biochemistry*, 32(17):3486–99, 2012.

[225] S. Chowdhry, Y. Zhang, M. McMahon, C. Sutherland, A. Cuadrado, and J. D. Hayes. Nrf2 is controlled by two distinct β-TrCP recognition motifs in its Neh6 domain, one of which can be modulated by GSK-3 activity. *Oncogene*, 32(32):3765–81, 2013.

[226] Y. Katoh, K. Itoh, E. Yoshida, M. Miyagishi, A. Fukamizu, and M. Yamamoto. Two domains of Nrf2 cooperatively bind CBP, a CREB binding protein, and synergistically activate transcription. *Genes to Cells*, 6(10):857–68, 2001.

[227] Z. Sun, Y. E. Chin, and D. D. Zhang. Acetylation of Nrf2 by p300/CBP augments promoter-specific DNA binding of Nrf2 during the antioxidant response. *Molecular and Cellular Biochemistry*, 29(10):2658–72, 2009.

[228] Y. Kawai, L. Garduño, M. Theodore, J. Yang, and I. J. Arinze. Acetylation-deacetylation of the transcription factor Nrf2 (nuclear factor erythroid 2-related factor 2) regulates its transcriptional activity and nucleocytoplasmic localization. *The Journal of Biological Chemistry*, 286(9):7629–40, 2011.

[229] A. Miseta and P. Csutora. Relationship Between the Occurrence of Cysteine in Proteins and the Complexity of Organisms. *Molecular Biology and Evolution*, 17(8):1232–1239, 2000.

[230] R. Holland and J. C. Fishbein. Chemistry of the Cysteine Sensors in Kelch-Like ECH-Associated Protein 1. *Antioxidants & Redox Signaling*, 13(11):1749–1761, 2010.

[231] S. M. Marino and V. N. Gladyshev. Analysis and Functional Prediction of Reactive Cysteine Residues. *Journal of Biological Chemistry*, 287(7):4419–4425, 2012.

[232] S. B. Cullinan, J. D. Gordan, J. Jin, J. W. Harper, and J. A. Diehl. The Keap1-BTB protein is an adaptor that bridges Nrf2 to a Cul3-based E3 ligase: oxidative stress sensing by a Cul3-Keap1 ligase. *Molecular and Cellular Biochemistry*, 24(19):8477–8486, 2004.

[233] A. Kobayashi, M.-I. Kang, H. Okawa, M. Ohtsuji, Y. Zenke, T. Chiba, K. Igarashi, and M. Yamamoto. Oxidative stress sensor Keap1 functions as an adaptor for Cul3-based E3 ligase to regulate proteasomal degradation of Nrf2. *Molecular and Cellular Biochemistry*, 24(16):7130–7139, 2004.

[234] M. Furukawa and Y. Xiong. BTB protein Keap1 targets antioxidant transcription factor Nrf2 for ubiquitination by the Cullin 3-Roc1 ligase. *Molecular and Cellular Biochemistry*, 25(1):162–171, 2005.

[235] N. F. Villeneuve, A. Lau, and D. D. Zhang. Regulation of the Nrf2-Keap1 antioxidant response by the ubiquitin proteasome system: an insight into cullin-ring ubiquitin ligases. *Antioxidants & Redox Signaling*, 13(11):1699–712, 2010.

[236] A. T. Dinkova-Kostova, W. D. Holtzclaw, R. N. Cole, K. Itoh, N. Wakabayashi, Y. Katoh, M. Yamamoto, and P. Talalay. Direct evidence that sulfhydryl groups of Keap1 are the sensors regulating induction of phase 2 enzymes that protect against carcinogens and oxidants. *Proceedings of the National Academy of Sciences of the United States of America*, 99(18):11908–11913, 2002.

[237] K. I. Tong, Y. Katoh, H. Kusunoki, K. Itoh, T. Tanaka, and M. Yamamoto. Keap1 recruits Neh2 through binding to ETGE and DLG motifs: characterization of the two-site molecular recognition model. *Molecular and Cellular Biochemistry*, 26(8):2887–2900, 2006.

[238] M. McMahon, N. Thomas, K. Itoh, M. Yamamoto, and J. D. Hayes. Dimerization of substrate adaptors can facilitate Cullin-mediated ubiquitylation of proteins by a "tethering" mechanism: A two-site interaction model for the Nrf2-Keap1 complex. *Journal of Biological Chemistry*, 281(34):24756–24768, 2006.

[239] K. Itoh, N. Wakabayashi, Y. Katoh, T. Ishii, T. O'Connor, and M. Yamamoto. Keap1 regulates both cytoplasmic-nuclear shuttling and degradation of Nrf2 in response to electrophiles. *Genes to Cells*, 8(4):379–91, 2003.

[240] J. Alam, E. Killeen, P. Gong, R. Naquin, B. Hu, D. Stewart, J. R. Ingelfinger, and K. A. Nath. Heme activates the heme oxygenase-1 gene in renal epithelial cells by stabilizing Nrf2. *American Journal of Physiology. Renal Physiology*, 284(4):F743–F752, 2003.

[241] D. D. Zhang and M. Hannink. Distinct cysteine residues in Keap1 are required for Keap1-dependent ubiquitination of Nrf2 and for stabilization of Nrf2 by chemopreventive agents and oxidative stress. *Molecular and Cellular Biochemistry*, 23(22):8137–8151, 2003.

[242] T. Nguyen, P. J. Sherratt, P. Nioi, C. S. Yang, and C. B. Pickett. Nrf2 Controls Constitutive and Inducible Expression of ARE-driven Genes through a Dynamic Pathway Involving Nucleocytoplasmic Shuttling by Keap1. *Journal of Biological Chemistry*, 280(37):32485–32492, 2005.

[243] Z. Sun, S. Zhang, J. Y. Chan, and D. D. Zhang. Keap1 controls postinduction repression of the Nrf2-mediated antioxidant response by escorting nuclear export of Nrf2. *Molecular and Cellular Biochemistry*, 27(18):6334–49, 2007.

[244] S. K. Niture, A. K. Jain, and A. K. Jaiswal. Antioxidant-induced modification of INrf2 cysteine 151 and PKC-delta-mediated phosphorylation of Nrf2 serine 40 are both required for stabilization and nuclear translocation of Nrf2 and increased drug resistance. *Journal of Cell Science*, 122(Pt 24):4452–64, 2009.

[245] A. L. Eggler, E. Small, M. Hannink, and A. D. Mesecar. Cul3-mediated Nrf2 ubiquitination and ARE activation are dependent on the partial molar volume at position 151 of Keap1. *The Biochemical Journal*, 422(1):10.1042/BJ20090471, 2009.

[246] T. W. Kensler, T. J. Curphey, Y. Maxiutenko, and B. D. Roebuck. Chemoprotection by organosulfur inducers of phase 2 enzymes: dithiolethiones and dithiins. *Drug Metabolism and Drug Interactions*, 17(1-4):3–22, 2000.

[247] R. Garg, S. Gupta, and G. B. Maru. Dietary curcumin modulates transcriptional regulators of phase I and phase II enzymes in benzo[a]pyrene-treated mice: mechanism of its anti-initiating action. *Carcinogenesis*, 29(5):1022–1032, 2008.

[248] H. Esterbauer, R. J. Schaur, and H. Zollner. Chemistry and Biochemistry of 4-hydroxynonenal, malonaldehyde and related aldehydes. *Free Radical Biology & Medicine*, 11(1):81–128, 1991.

[249] N. Wakabayashi, A. T. Dinkova-Kostova, W. D. Holtzclaw, M.-I. Kang, A. Kobayashi, M. Yamamoto, T. W. Kensler, and P. Talalay. Protection against electrophile and oxidant stress by induction of the phase 2 response: fate of cysteines of the Keap1 sensor modified by inducers. *Proceedings of the National Academy of Sciences of the United States of America*, 101(7):2040–5, 2004.

[250] M. K. Kwak, K. Itoh, M. Yamamoto, T. R. Sutter, and T. W. Kensler. Role of transcription factor Nrf2 in the induction of hepatic phase 2 and antioxidative enzymes in vivo by the cancer chemoprotective agent, 3H-1, 2-dimethiole-3-thione. *Molecular Medicine*, 7(2):135–145, 2001.

[251] M. McMahon, K. Itoh, M. Yamamoto, and J. D. Hayes. Keap1-dependent Proteasomal Degradation of Transcription Factor Nrf2 Contributes to the Negative Regulation of Antioxidant Response Element-driven Gene Expression. *Journal of Biological Chemistry*, 278(24):21592–21600, 2003.

[252] R. Yu, T.-H. Tan, and A.-N. T. Kong. Butylated Hydroxyanisole and Its Metabolitetert-Butylhydroquinone Differentially Regulate Mitogen-activated Protein Kinases: THE ROLE OF OXIDATIVE STRESS IN THE ACTIVATION OF MITOGEN-ACTIVATED PROTEIN KINASES BY PHENOLIC ANTIOXIDANTS. *Journal of Biological Chemistry*, 272(46):28962–28970, 1997.

[253] Y. Huang, W. Li, and A.-N. T. Kong. Anti-oxidative stress regulator NF-E2-related factor 2 mediates the adaptive induction of antioxidant and detoxifying enzymes by lipid peroxidation metabolite 4-hydroxynonenal. *Cell & Bioscience*, 2(1):40, 2012.

[254] G. Covas, H. S. Marinho, L. Cyrne, and F. Antunes. Activation of Nrf2 by H2O2: De Novo Synthesis Versus Nuclear Translocation. *Methods in Enzymology*, 528:157–71, 2013.

[255] J.-M. Lee, M. J. Calkins, K. Chan, Y. W. Kan, and J. A. Johnson. Identification of the NF-E2-related factor-2-dependent genes conferring protection against oxidative stress in primary cortical astrocytes using oligonucleotide microarray analysis. *The Journal of Biological Chemistry*, 278(14):12029–38, 2003.

[256] D. Malhotra, E. Portales-Casamar, A. Singh, S. Srivastava, D. Arenillas, C. Happel, C. Shyr, N. Wakabayashi, T. W. Kensler, W. W. Wasserman, and S. Biswal. Global mapping of binding sites for Nrf2 identifies novel targets in cell survival response through ChIP-Seq profiling and network analysis. *Nucleic Acids Research*, 38(17):5718–34, 2010.

[257] B. N. Chorley, M. R. Campbell, X. Wang, M. Karaca, D. Sambandan, F. Bangura, P. Xue, J. Pi, S. R. Kleeberger, and D. a. Bell. Identification of novel NRF2-regulated genes by ChIP-Seq: influence on retinoid X receptor alpha. *Nucleic Acids Research*, 40(15):7416–29, 2012.

[258] H. K. Bryan, A. Olayanju, C. E. Goldring, and B. K. Park. The Nrf2 cell defence pathway: Keap1-dependent and -independent mechanisms of regulation. *Biochemical Pharmacology*, 85(6):705–717, 2013.

[259] R. K. Thimmulappa, K. H. Mai, S. Srisuma, T. W. Kensler, M. Yamamoto, and S. Biswal. Identification of Nrf2-regulated genes induced by the chemopreventive agent sulforaphane by oligonucleotide microarray. *Cancer Research*, 62(18):5196–5203, 2002.

[260] K. C. Wu, J. Y. Cui, and C. D. Klaassen. Beneficial role of Nrf2 in regulating NADPH generation and consumption. *Toxicological Sciences*, 123(2):590–600, 2011.

[261] Y. Mitsuishi, K. Taguchi, Y. Kawatani, T. Shibata, T. Nukiwa, H. Aburatani, M. Yamamoto, and H. Motohashi. Nrf2 redirects glucose and glutamine into anabolic pathways in metabolic reprogramming. *Cancer Cell*, 22(1):66–79, 2012.

[262] A. Singh, C. Happel, S. K. Manna, G. Acquaah-Mensah, J. Carrerero, S. Kumar, P. Nasipuri, K. W. Krausz, N. Wakabayashi, R. Dewi, L. G. Boros, F. J. Gonzalez, E. Gabrielson, K. K. Wong, G. Girnun, and S. Biswal. Transcription factor NRF2 regulates miR-1 and miR-206 to drive tumorigenesis. *The Journal of Clinical Investigation*, 123(7):2921–34, 2013.

[263] Y. Mitsuishi, H. Motohashi, and M. Yamamoto. The Keap1-Nrf2 system in cancers: stress response and anabolic metabolism. *Frontiers in Oncology*, 2:200, 2012.

[264] J. D. Hayes and M. L. J. Ashford. Nrf2 orchestrates fuel partitioning for cell proliferation. *Cell Metabolism*, 16(2):139–41, 2012.

[265] A. K. MacLeod, M. McMahon, S. M. Plummer, L. G. Higgins, T. M. Penning, K. Igarashi, and J. D. Hayes. Characterization of the cancer chemopreventive NRF2-dependent gene battery in human keratinocytes: demonstration that the KEAP1-NRF2 pathway, and not the BACH1-NRF2 pathway, controls cytoprotection against electrophiles as well as redox-cycling compounds. *Carcinogenesis*, 30(9):1571–80, 2009.

[266] A. S. Agyeman, R. Chaerkady, P. G. Shaw, N. E. Davidson, K. Visvanathan, A. Pandey, and T. W. Kensler. Transcriptomic and proteomic profiling of KEAP1 disrupted and sulforaphane-treated human breast epithelial cells reveals common expression profiles. *Breast Cancer Research and Treatment*, 132(1):175–87, 2012.

[267] J. Pi, L. Leung, P. Xue, W. Wang, Y. Hou, D. Liu, E. Yehuda-Shnaidman, C. Lee, J. Lau, T. W. Kurtz, and J. Y. Chan. Deficiency in the nuclear factor E2-related factor-2 transcription factor results in impaired adipogenesis and protects against diet-induced obesity. *The Journal of Biological Chemistry*, 285(12):9292–300, 2010.

[268] H.-Y. Cho, W. Gladwell, X. Wang, B. Chorley, D. Bell, S. P. Reddy, and S. R. Kleeberger. Nrf2-regulated PPAR{gamma} expression is critical to protection against acute lung injury in mice. *American Journal of Respiratory and Critical Care Medicine*, 182(2):170–82, 2010.

[269] Y. Hou, P. Xue, Y. Bai, D. Liu, C. G. Woods, K. Yarborough, J. Fu, Q. Zhang, G. Sun, S. Collins, J. Y. Chan, M. Yamamoto, M. E. Andersen, and J. Pi. Nuclear factor erythroid-derived factor 2-related factor 2 regulates transcription of CCAAT/enhancer-binding protein β during adipogenesis. *Free Radical Biology & Medicine*, 52(2):462–72, 2012.

[270] S. Pan, C. J. World, C. J. Kovacs, and B. C. Berk. Glucose 6-phosphate dehydrogenase is regulated through c-src-mediated tyrosine phosphorylation in endothelial cells. *Arteriosclerosis, Thrombosis, and Vascular Biology*, 29(6):895–901, 2009.

[271] Y.-P. Wang, L.-S. Zhou, Y.-Z. Zhao, S.-W. Wang, L.-L. Chen, L.-X. Liu, Z.-Q. Ling, F.-J. Hu, Y.-P. Sun, J.-Y. Zhang, C. Yang, Y. Yang, Y. Xiong, K.-L. Guan, and D. Ye. Regulation of G6PD acetylation by SIRT2 and KAT9 modulates NADPH homeostasis and cell survival during oxidative stress. *The EMBO Journal*, 33(12):1304–20, 2014.

[272] L. E. Wu and D. A. Sinclair. SIRT2 controls the pentose phosphate switch. *The EMBO Journal*, 33(12):1287–1288, 2014.

[273] M. M. C. Wamelink, E. A. Struys, and C. Jakobs. The biochemistry, metabolism and inherited defects of the pentose phosphate pathway: A review. *Journal of Inherited Metabolic Disease*, 31(6):703–717, 2008.

[274] L. G. Boros, J. S. Torday, S. Lim, S. Bassilian, M. Cascante, and W. N. P. Lee. Transforming growth factor beta2 promotes glucose carbon incorporation into nucleic acid ribose through the nonoxidative pentose cycle in lung epithelial carcinoma cells. *Cancer Research*, 60(5):1183–1185, 2000.

[275] A. Singh, V. Misra, R. K. Thimmulappa, H. Lee, S. Ames, M. O. Hoque, J. G. Herman, S. B. Baylin, D. Sidransky, E. Gabrielson, M. V. Brock, and S. Biswal. Dysfunctional KEAP1-NRF2 interaction in non-small-cell lung cancer. *PLoS Medicine*, 3(10):1865–1876, 2006.

[276] J. Campisi and F. d'Adda di Fagagna. Cellular senescence: when bad things happen to good cells. *Nature Reviews. Molecular Cell Biology*, 8(9):729–40, 2007.

[277] J. M. Vicencio, L. Galluzzi, N. Tajeddine, C. Ortiz, A. Criollo, E. Tasdemir, E. Morselli, A. Ben Younes, M. C. Maiuri, S. Lavandero, and G. Kroemer. Senescence, apoptosis or autophagy? When a damaged cell must decide its path–a mini-review. *Gerontology*, 54(2):92–9, 2008.

[278] A. B. Maier, R. G. J. Westendorp, and D. VAN Heemst. Beta-galactosidase activity as a biomarker of replicative senescence during the course of human fibroblast cultures. *Annals of the New York Academy of Sciences*, 1100(1):323–32, 2007.

[279] E. J. Moerman, R. Thweatt, A. M. Moerman, R. A. Jones, and S. Goldstein. Special Issue Festschrift in honor of Reubin AndresInsulin-like growth factor binding protein-3 is overexpressed in senescent and quiescent human fibroblasts. *Experimental Gerontology*, 28(4):361–370, 1993.

[280] T. Fujita. Senescence Marker Protein-30 (SMP30): Structure and Biological Function. *Biochemical and Biophysical Research Communications*, 254(1):1–4, 1999.

[281] D.-y. Zhang, H.-j. Wang, and Y.-z. Tan. Wnt/β-Catenin Signaling Induces the Aging of Mesenchymal Stem Cells through the DNA Damage Response and the p53/p21 Pathway. *PLoS ONE*, 6(6):e21397, 2011.

[282] G. Filomeni, D. De Zio, and F. Cecconi. Oxidative stress and autophagy: the clash between damage and metabolic needs. *Cell Death and Cell Growth & Differentiation*, 22(3):377–388, 2015.

[283] Y. Chen, M. B. Azad, and S. B. Gibson. Superoxide is the major reactive oxygen species regulating autophagy. *Cell Death and Cell Growth & Differentiation*, 16(7):1040–52, 2009.

[284] G. Filomeni, E. Desideri, S. Cardaci, G. Rotilio, and M. R. Ciriolo. Under the ROS...thiol network is the principal suspect for autophagy commitment. *Autophagy*, 6(7):999–1005, 2010.

[285] R. Scherz-Shouval, E. Shvets, and Z. Elazar. Oxidation as a post-translational modification that regulates autophagy. *Autophagy*, 3(4):371–3, 2007.

[286] A. Lau, X.-J. Wang, F. Zhao, N. F. Villeneuve, T. Wu, T. Jiang, Z. Sun, E. White, and D. D. Zhang. A noncanonical mechanism of Nrf2 activation by autophagy deficiency: direct interaction between Keap1 and p62. *Molecular and Cellular Biochemistry*, 30(13):3275–85, 2010.

[287] A. Jain, T. Lamark, E. Sjøttem, K. B. Larsen, J. A. Awuh, A. Øvervatn, M. McMahon, J. D. Hayes, and T. Johansen. p62/SQSTM1 is a target gene for transcription factor NRF2 and creates a positive feedback loop by inducing antioxidant response element-driven gene transcription. *The Journal of Biological Chemistry*, 285(29):22576–91, 2010.

[288] Y. Ichimura, S. Waguri, Y.-S. Sou, S. Kageyama, J. Hasegawa, R. Ishimura, T. Saito, Y. Yang, T. Kouno, T. Fukutomi, T. Hoshii, A. Hirao, K. Takagi, T. Mizushima, H. Motohashi, M.-S. Lee, T. Yoshimori, K. Tanaka, M. Yamamoto, and M. Komatsu. Phosphorylation of p62 Activates the Keap1-Nrf2 Pathway during Selective Autophagy. *Molecular Cell*, 51(5):618–31, 2013.

[289] M. Komatsu, H. Kurokawa, S. Waguri, K. Taguchi, A. Kobayashi, Y. Ichimura, Y.-S. Sou, I. Ueno, A. Sakamoto, K. I. Tong, M. Kim, Y. Nishito, S.-i. Iemura, T. Natsume, T. Ueno, E. Kominami, H. Motohashi, K. Tanaka, and M. Yamamoto. The selective autophagy substrate p62 activates the stress responsive transcription factor Nrf2 through inactivation of Keap1. *Nature Cell Biology*, 12(3):213–23, 2010.

[290] K. Taguchi, N. Fujikawa, M. Komatsu, T. Ishii, M. Unno, T. Akaike, H. Motohashi, and M. Yamamoto. Keap1 degradation by autophagy for the maintenance of redox homeostasis. *Proceedings of the National Academy of Sciences of the United States of America*, 109(34):13561–6, 2012.

[291] J. A. Muñoz-Gámez, J. M. Rodríguez-Vargas, R. Quiles-Pérez, R. Aguilar-Quesada, D. Martín-Oliva, G. de Murcia, J. Menissier de Murcia, A. Almendros, M. Ruiz de Almodóvar, and F. J. Oliver. PARP-1 is involved in autophagy induced by DNA damage. *Autophagy*, 5(1):61–74, 2009.

[292] J. M. Rodr\'\iguez-Vargas, M. J. Ruiz-Magaña, C. Ruiz-Ruiz, J. Majuelos-Melguizo, A. Peralta-Leal, M. I. Rodr\'\iguez, J. A. Muñoz-Gámez, M. R. de Almodóvar, E. Siles, A. L. Rivas, M. Jäättela, and F. J. Oliver. ROS-induced DNA damage and PARP-1 are required for optimal induction of starvation-induced autophagy. *Cell Research*, 22(7):1181–1198, 2012.

[293] L. Galluzzi, F. Pietrocola, B. Levine, and G. Kroemer. Metabolic Control of Autophagy. *Cell*, 159(6):1263–1276, 2014.

[294] M. Dodson, M. Redmann, N. S. Rajasekaran, V. Darley-Usmar, and J. Zhang. KEAP1-NRF2 signalling and autophagy in protection against oxidative and reductive proteotoxicity. *The Biochemical Journal*, 469(3):347–55, 2015.

[295] L. Galluzzi, M. C. Maiuri, I. Vitale, H. Zischka, M. Castedo, L. Zitvogel, and G. Kroemer. Cell death modalities: classification and pathophysiological implications. *Cell Death and Cell Growth & Differentiation*, 14(7):1237–43, 2007.

[296] A. Lau, N. F. Villeneuve, Z. Sun, P. K. Wong, and D. D. Zhang. Dual roles of Nrf2 in cancer. *Pharmacological Research*, 58(5-6):262–70, 2008.

[297] X. J. Wang, Z. Sun, N. F. Villeneuve, S. Zhang, F. Zhao, Y. Li, W. Chen, X. Yi, W. Zheng, G. T. Wondrak, P. K. Wong, and D. D. Zhang. Nrf2 enhances resistance of cancer cells to chemotherapeutic drugs, the dark side of Nrf2. *Carcinogenesis*, 29(6):1235–1243, 2008.

[298] A. Singh, M. Bodas, N. Wakabayashi, F. Bunz, and S. Biswal. Gain of Nrf2 function in non-small-cell lung cancer cells confers radioresistance. *Antioxidants & Redox Signaling*, 13(11):1627–1637, 2010.

[299] Y. R. Kim, J. E. Oh, M. S. Kim, M. R. Kang, S. W. Park, J. Y. Han, H. S. Eom, N. J. Yoo, and S. H. Lee. Oncogenic NRF2 mutations in squamous cell carcinomas of oesophagus and skin. *Journal of Pathology*, 220(4):446–451, 2010.

[300] P. Zhang, A. Singh, S. Yegnasubramanian, D. Esopi, P. Kombairaju, M. Bodas, H. Wu, S. G. Bova, and S. Biswal. Loss of Kelch-like ECH-associated protein 1 function in prostate cancer cells causes chemoresistance and radioresistance and promotes tumor growth. *Molecular Cancer Therapeutics*, 9(2):336–346, 2010.

[301] M. Schäfer, S. Dütsch, U. auf dem Keller, and S. Werner. Nrf2: a central regulator of UV protection in the epidermis. *Cell cycle*, 9(15):2917–8, 2010.

[302] Y. Lee, J.-M. Shin, S. Jang, D.-K. Choi, M.-S. Seo, H.-R. Kim, K.-C. Sohn, M. Im, Y.-J. Seo, J.-H. Lee, and C.-D. Kim. Role of nuclear factor E2-related factor 2 (Nrf2) in epidermal differentiation. *Archives of Dermatological Research*, 306(7):677–82, 2014.

[303] M. Schäfer and S. Werner. Nrf2-A regulator of keratinocyte redox signaling. *Free Radical Biology & Medicine*, 88(Pt B):243–52, 2015.

[304] F. Q. Schafer and G. R. Buettner. Redox environment of the cell as viewed through the redox state of the glutathione disulfide/glutathione couple. *Free Radical Biology & Medicine*, 30(11):1191–212, 2001.

[305] F. Q. Schafer and G. R. Buettner. Redox State and Redox Environment in Biology. In H. Forman, J. Fukuto, and M. Torres, editors, *Signal Transduction by Reactive Oxygen and Nitrogen Species: Pathways and Chemical Principles*, pages 1–14. Kluwer Academic Publishers, Dordrecht, 2003.

[306] G. R. Buettner, B. A. Wagner, and V. G. J. Rodgers. Quantitative redox biology: an approach to understand the role of reactive species in defining the cellular redox environment. *Cell Biochemistry and Biophysics*, 67(2):477–83, 2013.

[307] T. Bücher and M. Klingenberg. Wege des Wasserstoffs in der lebendigen Organisation. *Angewandte Chemie*, 70(17-18):552–570, 1958.

[308] G. R. Buettner and F. Q. Schafer. Free radicals, oxidants, and antioxidants. *Teratology*, 62(4):234, 2000.

[309] A. M. Posadino, A. Cossu, R. Giordo, A. Zinellu, S. Sotgia, A. Vardeu, P. T. Hoa, L. H. V. Nguyen, C. Carru, and G. Pintus. Resveratrol alters human endothelial cells redox state and causes mitochondrial-dependent cell death. *Food and Chemical Toxicology*, 78(0):10–16, 2015.

[310] Y. Sun and L. W. Oberley. Redox regulation of transcriptional activators. *Free Radical Biology & Medicine*, 21(3):335–48, 1996.

[311] S. J. Storr, C. M. Woolston, Y. Zhang, and S. G. Martin. Redox environment, free radical, and oxidative DNA damage. *Antioxidants & Redox Signaling*, 18(18):2399–408, 2013.

[312] J. D. Hunter. Matplotlib: A 2D graphics environment. *Computing In Science & Engineering*, 9(3):90–95, 2007.

[313] K. J. Livak and T. D. Schmittgen. Analysis of relative gene expression data using real-time quantitative PCR and the 2(-Delta Delta C(T)) Method. *Methods*, 25(4):402–8, 2001.

[314] S. Rozen and H. Skaletsky. Primer3 on the WWW for general users and for biologist programmers. *Methods in Molecular Biology*, 132:365–386, 2000.

[315] National Center for Biotechnology Information (NCBI). Primer-BLAST.

[316] A. Subramanian, P. Tamayo, V. K. Mootha, S. Mukherjee, B. L. Ebert, M. A. Gillette, A. Paulovich, S. L. Pomeroy, T. R. Golub, E. S. Lander, and J. P. Mesirov. Gene set enrichment analysis: a knowledge-based approach for interpreting genome-wide expression profiles. *Proceedings of the National Academy of Sciences of the United States of America*, 102(43):15545–50, 2005.

[317] J. Lamb, E. D. Crawford, D. Peck, J. W. Modell, I. C. Blat, M. J. Wrobel, J. Lerner, J.-P. Brunet, A. Subramanian, K. N. Ross, M. Reich, H. Hieronymus, G. Wei, S. A. Armstrong, S. J. Haggarty, P. A. Clemons, R. Wei, S. A. Carr, E. S. Lander, and T. R. Golub. The Connectivity Map: using gene-expression signatures to connect small molecules, genes, and disease. *Science*, 313(5795):1929–35, 2006.

[318] A. Bakhtiarova, P. Taslimi, S. J. Elliman, P. A. Kosinski, B. Hubbard, M. Kavana, and D. M. Kemp. Resveratrol inhibits firefly luciferase. *Biochemical and Biophysical Research Communications*, 351(2):481–4, 2006.

[319] A. Braeuning. Firefly luciferase inhibition: a widely neglected problem. *Archives of Toxicology*, 89(1):141–2, 2015.

[320] N. J. Miller, C. Rice-Evans, M. J. Davies, V. Gopinathan, and A. Milner. A novel method for measuring antioxidant capacity and its application to monitoring the antioxidant status in premature neonates. *Clinical Science*, 84(4):407–12, 1993.

[321] N. J. Miller, C. Rice-Evans, and M. J. Davies. A new method for measuring antioxidant activity. *Biochemical Society Transactions*, 21(2):95S, 1993.

[322] N. J. Miller and C. A. Rice-Evans. Factors Influencing the Antioxidant Activity Determined by the ABTS + Radical Cation Assay. *Free Radical Research*, 26(3):195–199, 1997.

[323] J. Hynes, T. C. O'Riordan, A. V. Zhdanov, G. Uray, Y. Will, and D. B. Papkovsky. In vitro analysis of cell metabolism using a long-decay pH-sensitive lanthanide probe and extracellular acidification assay. *Analytical biochemistry*, 390(1):21–8, 2009.

[324] V. A. Fadok, D. L. Bratton, S. C. Frasch, M. L. Warner, and P. M. Henson. The role of phosphatidylserine in recognition of apoptotic cells by phagocytes. *Cell Death and Cell Growth & Differentiation*, 5(7):551–562, 1998.

[325] C. Weidner, M. Rousseau, A. Plauth, S. Wowro, C. Fischer, H. Abdel-Aziz, and S. Sauer. Melissa officinalis extract induces apoptosis and inhibits proliferation in colon cancer cells through formation of reactive oxygen species. *Phytomedicine*, 22(2):262–270, 2015.

[326] W. S. Rasband. ImageJ, U. S. National Institutes of Health, Bethesda, Maryland, USA, http://imagej.nih.gov/ij/, 1997-2016.

[327] C. A. Schneider, W. S. Rasband, and K. W. Eliceiri. NIH Image to ImageJ: 25 years of image analysis. *Nature Methods*, 9(7):671–5, 2012.

[328] V. Radkar, D. Hardej, C. Lau-Cam, and B. Billack. Evaluation of resveratrol and piceatannol cytotoxicity in macrophages, T cells, and skin cells. *Arhiv za higijenu rada i toksikologiju*, 58(3):293–304, 2007.

[329] J. Soeur, J. Eilstein, G. Léreaux, C. Jones, and L. Marrot. Skin resistance to oxidative stress induced by resveratrol: From Nrf2 activation to GSH biosynthesis. *Free Radical Biology & Medicine*, 78:213–223, 2015.

[330] J. Gerszon, A. Rodacka, and M. Puchała. Antioxidant Properties of Resveratrol and its Protective Effects in Neurodegenerative Diseases. *Advances in Cell Biology*, 4(2):97–117, 2014.

[331] M. Whiteman, U. Ketsawatsakul, and B. Halliwell. A reassessment of the peroxynitrite scavenging activity of uric acid. *Annals of the New York Academy of Sciences*, 962:242–59, 2002.

[332] I. M. Verma, J. K. Stevenson, E. M. Schwarz, D. Van Antwerp, and S. Miyamoto. Rel/NF-kappa B/I kappa B family: intimate tales of association and dissociation. *Genes & Development*, 9(22):2723–2735, 1995.

[333] M. D. Jacobs and S. C. Harrison. Structure of an IkappaBalpha/NF-kappaB complex. *Cell*, 95(6):749–58, 1998.

[334] I. Bellezza, A. L. Mierla, and A. Minelli. Nrf2 and NF-κB and Their Concerted Modulation in Cancer Pathogenesis and Progression. *Cancers*, 2(2):483–497, 2010.

[335] S. a. Rushworth, L. Zaitseva, M. Y. Murray, N. M. Shah, K. M. Bowles, and D. J. MacEwan. The high Nrf2 expression in human acute myeloid leukemia is driven by NF-κB and underlies its chemo-resistance. *Blood*, 120(26):5188–98, 2012.

[336] M. Buelna-Chontal and C. Zazueta. Redox activation of Nrf2 & NF-κB: a double end sword? *Cellular Signalling*, 25(12):2548–57, 2013.

[337] J. D. Wardyn, A. H. Ponsford, and C. M. Sanderson. Dissecting molecular cross-talk between Nrf2 and NF-κB response pathways. *Biochemical Society Transactions*, 43(4):621–626, 2015.

[338] C. G. Larsen, A. O. Anderson, J. J. Oppenheim, and K. Matsushima. Production of interleukin-8 by human dermal fibroblasts and keratinocytes in response to interleukin-1 or tumour necrosis factor. *Immunology*, 68(1):31–6, 1989.

[339] R. Venugopal and A. K. Jaiswal. Nrf2 and Nrf1 in association with Jun proteins regulate antioxidant response element-mediated expression and coordinated induction of genes encoding detoxifying enzymes. *Oncogene*, 17(24):3145–56, 1998.

[340] Y. Sano, F. Tokitou, P. Dai, T. Maekawa, T. Yamamoto, and S. Ishii. CBP alleviates the intramolecular inhibition of ATF-2 function. *The Journal of Biological Chemistry*, 273(44):29098–105, 1998.

[341] B. Dérijard, M. Hibi, I. H. Wu, T. Barrett, B. Su, T. Deng, M. Karin, and R. J. Davis. JNK1: a protein kinase stimulated by UV light and Ha-Ras that binds and phosphorylates the c-Jun activation domain. *Cell*, 76(6):1025–37, 1994.

[342] Y.-S. Keum, E. D. Owuor, B.-R. Kim, R. Hu, and a. N. T. Kong. Involvement of Nrf2 and JNK1 in the activation of antioxidant responsive element (ARE) by chemopreventive agent phenethyl isothiocyanate (PEITC). *Pharmacological Research*, 20(9):1351–6, 2003.

[343] S. Pastore, D. Lulli, R. Maurelli, E. Dellambra, C. De Luca, and L. G. Korkina. Resveratrol Induces Long-Lasting IL-8 Expression and Peculiar EGFR Activation/Distribution in Human Keratinocytes: Mechanisms and Implications for Skin Administration. *PLoS ONE*, 8(3):e59632, 2013.

[344] V. Baldin, J. Lukas, M. J. Marcote, M. Pagano, and G. Draetta. Cyclin D1 is a nuclear protein required for cell cycle progression in G1. *Genes & Development*, 7(5):812–21, 1993.

[345] N. Lauper, A. R. Beck, S. Cariou, L. Richman, K. Hofmann, W. Reith, J. M. Slingerland, and B. Amati. Cyclin E2: a novel CDK2 partner in the late G1 and S phases of the mammalian cell cycle. *Oncogene*, 17(20):2637–43, 1998.

[346] M. Pagano, R. Pepperkok, F. Verde, W. Ansorge, and G. Draetta. Cyclin A is required at two points in the human cell cycle. *The EMBO Journal*, 11(3):961–71, 1992.

[347] A. L. Gartel and S. K. Radhakrishnan. Lost in transcription: p21 repression, mechanisms, and consequences. *Cancer Research*, 65(10):3980–5, 2005.

[348] W. Chen, Z. Sun, X.-J. Wang, T. Jiang, Z. Huang, D. Fang, and D. D. Zhang. Direct interaction between Nrf2 and p21(Cip1/WAF1) upregulates the Nrf2-mediated antioxidant response. *Molecular Cell*, 34(6):663–73, 2009.

[349] B. Pucci, M. Kasten, and A. Giordano. Cell Cycle and Apoptosis. *Neoplasia*, 2(4):291–299, 2000.

[350] J. A. Pietenpol and Z. A. Stewart. Cell cycle checkpoint signaling: cell cycle arrest versus apoptosis. *Toxicology*, 181-182:475–81, 2002.

[351] L. Portt, G. Norman, C. Clapp, M. Greenwood, and M. T. Greenwood. Anti-apoptosis and cell survival: A review. *Biochimica et Biophysica Acta. Molecular Cell Research*, 1813(1):238–259, 2011.

[352] P. E. Czabotar, G. Lessene, A. Strasser, and J. M. Adams. Control of apoptosis by the BCL-2 protein family: implications for physiology and therapy. *Nature Reviews Molecular Cell Biology*, 15(1):49–63, 2014.

[353] A. M. Verhagen, E. J. Coulson, and D. L. Vaux. Inhibitor of apoptosis proteins and their relatives: IAPs and other BIRPs. *Genome Biology*, 2(7):REVIEWS3009, 2001.

[354] E. A. Slee, M. T. Harte, R. M. Kluck, B. B. Wolf, C. A. Casiano, D. D. Newmeyer, H. G. Wang, J. C. Reed, D. W. Nicholson, E. S. Alnemri, D. R. Green, and S. J. Martin. Ordering the cytochrome c-initiated caspase cascade: hierarchical activation of caspases-2, -3, -6, -7, -8, and -10 in a caspase-9-dependent manner. *The Journal of Cell Biology*, 144(2):281–92, 1999.

[355] S. Dhandayuthapani, P. Marimuthu, V. Hörmann, J. Kumi-Diaka, and A. Rathinavelu. Induction of apoptosis in HeLa cells via caspase activation by resveratrol and genistein. *Journal of Medicinal Food*, 16(2):139–46, 2013.

[356] S. Pankiv, T. H. Clausen, T. Lamark, A. Brech, J.-A. Bruun, H. Outzen, A. Øvervatn, G. Bjørkøy, and T. Johansen. p62/SQSTM1 Binds Directly to Atg8/LC3 to Facilitate Degradation of Ubiquitinated Protein Aggregates by Autophagy. *Journal of Biological Chemistry*, 282(33):24131–24145, 2007.

[357] H. Bai, J. Inoue, T. Kawano, and J. Inazawa. A transcriptional variant of the LC3A gene is involved in autophagy and frequently inactivated in human cancers. *Oncogene*, 31(40):4397–408, 2012.

[358] V. Prabhu, P. Srivastava, N. Yadav, M. Amadori, A. Schneider, A. Seshadri, J. Pitarresi, R. Scott, H. Zhang, S. Koochekpour, R. Gogada, and D. Chandra. Resveratrol depletes mitochondrial DNA and inhibition of autophagy enhances resveratrol-induced caspase activation. *Mitochondrion*, 13(5):493–9, 2013.

[359] V. Levin-Salomon, S. Bialik, and A. Kimchi. DAP-kinase and autophagy. *Apoptosis: an International Journal on Programmed Cell Death*, 19(2):346–56, 2014.

[360] M. S. Choi, Y. Kim, J.-Y. Jung, S. H. Yang, T. R. Lee, and D. W. Shin. Resveratrol induces autophagy through death-associated protein kinase 1 (DAPK1) in human dermal fibroblasts under normal culture conditions. *Experimental Dermatology*, 22(7):491–4, 2013.

[361] M. Lagouge, C. Argmann, Z. Gerhart-Hines, H. Meziane, C. Lerin, F. Daussin, N. Messadeq, J. Milne, P. Lambert, P. Elliott, B. Geny, M. Laakso, P. Puigserver, and J. Auwerx. Resveratrol improves mitochondrial function and protects against metabolic disease by activating SIRT1 and PGC-1alpha. *Cell*, 127(6):1109–22, 2006.

[362] Z. Ungvari, W. E. Sonntag, R. de Cabo, J. A. Baur, and A. Csiszar. Mitochondrial protection by resveratrol. *Exercise and Sport Sciences Reviews*, 39(3):128–32, 2011.

[363] S.-J. Sheu, N.-C. Liu, C.-C. Ou, Y.-S. Bee, S.-C. Chen, H.-C. Lin, and J. Y. H. Chan. Resveratrol stimulates mitochondrial bioenergetics to protect retinal pigment epithelial cells from oxidative damage. *Investigative Ophthalmology & Visual Science*, 54(9):6426–38, 2013.

[364] S. C. Bondy. Ethanol toxicity and oxidative stress. *Toxicology Letters*, 63:231–241, 1992.

[365] S. M. Bailey, E. C. Pietsch, and C. C. Cunningham. Ethanol stimulates the production of reactive oxygen species at mitochondrial complexes I and III. *Free Radical Biology & Medicine*, 27(7-8):891–900, 1999.

[366] S. Zhang, X. Sun, Z. Jing, and F. Qu. Spectroscopic analysis on the resveratrol-DNA binding interactions at physiological pH. *Spectrochimica Acta. Part A, Molecular and Biomolecular Spectroscopy*, 82(1):213–6, 2011.

[367] M. Salas, P. Obando, L. Ojeda, P. Ojeda, A. Pérez, M. Vargas-Uribe, C. I. Rivas, J. C. Vera, and A. M. Reyes. Resolution of the direct interaction with and inhibition of the human GLUT1 hexose transporter by resveratrol from its effect on glucose accumulation. *American Journal of Physiology. Cell physiology*, 305(1):C90–9, 2013.

[368] M. S. Nair. Spectroscopic study on the interaction of resveratrol and pterostilbene with human serum albumin. *Journal of Photochemistry and Photobiology B: Biology*, 149(0):58–67, 2015.

[369] F. Mohammadi and M. Moeeni. Study on the interactions of trans-resveratrol and curcumin with bovine α-lactalbumin by spectroscopic analysis and molecular docking. *Materials Science & Engineering. C, Materials for Biological Applications*, 50:358–66, 2015.

[370] B. Halliwell and M. Whiteman. Measuring reactive species and oxidative damage in vivo and in cell culture: how should you do it and what do the results mean? *British Journal of Pharmacology*, 142(2):231–55, 2004.

[371] B. Halliwell and J. M. Gutteridge. Lipid peroxidation, oxygen radicals, cell damage, and antioxidant therapy. *Lancet*, 1(8391):1396–7, 1984.

[372] M. Deponte. Glutathione catalysis and the reaction mechanisms of glutathione-dependent enzymes. *Biochimica et Biophysica Acta*, 1830(5):3217–66, 2013.

[373] E. J. Calabrese. Hormesis: from mainstream to therapy. *Journal of Cell Communication and Signaling*, 8(4):289–91, 2014.

[374] D. Gems and L. Partridge. Stress-response hormesis and aging: "that which does not kill us makes us stronger". *Cell Metabolism*, 7(3):200–3, 2008.

[375] E. C. Filippi-Chiela, E. S. Villodre, L. L. Zamin, and G. Lenz. Autophagy interplay with apoptosis and cell cycle regulation in the growth inhibiting effect of resveratrol in glioma cells. *PLoS ONE*, 6(6):e20849, 2011.

[376] N. Ahmad, V. M. Adhami, F. Afaq, D. K. Feyes, and H. Mukhtar. Resveratrol causes WAF-1/p21-mediated G(1)-phase arrest of cell cycle and induction of apoptosis in human epidermoid carcinoma A431 cells. *Clinical Cancer Research*, 7(5):1466–73, 2001.

[377] L. Quoc Trung, J. L. Espinoza, A. Takami, and S. Nakao. Resveratrol induces cell cycle arrest and apoptosis in malignant NK cells via JAK2/STAT3 pathway inhibition. *PLoS ONE*, 8(1):e55183, 2013.

[378] Q. Yang, B. Wang, W. Zang, X. Wang, Z. Liu, W. Li, and J. Jia. Resveratrol inhibits the growth of gastric cancer by inducing g1 phase arrest and senescence in a sirt1-dependent manner. *PLoS ONE*, 8(11):e70627, 2013.

[379] A. K. Joe, H. Liu, M. Suzui, M. E. Vural, D. Xiao, and I. B. Weinstein. Resveratrol induces growth inhibition, S-phase arrest, apoptosis, and changes in biomarker expression in several human cancer cell lines. *Clinical Cancer Research*, 8(3):893–903, 2002.

[380] Y.-C. Liang, S.-H. Tsai, L. Chen, S.-Y. Lin-Shiau, and J.-K. Lin. Resveratrol-induced G2 arrest through the inhibition of CDK7 and p34CDC2 kinases in colon carcinoma HT29 cells. *Biochemical Pharmacology*, 65(7):1053–60, 2003.

[381] R. Lin, R. Tao, X. Gao, T. Li, X. Zhou, K.-L. Guan, Y. Xiong, and Q.-Y. Lei. Acetylation stabilizes ATP-citrate lyase to promote lipid biosynthesis and tumor growth. *Molecular Cell*, 51(4):506–18, 2013.

[382] Y. S. Hori, A. Kuno, R. Hosoda, and Y. Horio. Regulation of FOXOs and p53 by SIRT1 modulators under oxidative stress. *PLoS ONE*, 8(9):e73875, 2013.

[383] C. Cantó, Z. Gerhart-Hines, J. N. Feige, M. Lagouge, L. Noriega, J. C. Milne, P. J. Elliott, P. Puigserver, and J. Auwerx. AMPK regulates energy expenditure by modulating NAD+ metabolism and SIRT1 activity. *Nature*, 458(7241):1056–1060, 2009.

[384] T.-c. Hsieh, X. Lu, Z. Wang, and J. M. Wu. Induction of quinone reductase NQO1 by resveratrol in human K562 cells involves the antioxidant response element ARE and is accompanied by nuclear translocation of transcription factor Nrf2. *Medicinal Chemistry*, 2(3):275–285, 2006.

[385] H. Esterbauer, H. Zollner, and N. Scholz. Reaction of glutathione with conjugated carbonyls. *Zeitschrift fur Naturforschung. Section C: Biosciences*, 30(4):466–73, 1975.

[386] T. Sarkola, M. R. Iles, K. Kohlenberg-Mueller, and C. J. P. Eriksson. Ethanol, acetaldehyde, acetate, and lactate levels after alcohol intake in white men and women: effect of 4-methylpyrazole. *Alcoholism, clinical and experimental research*, 26(2):239–45, 2002.

[387] J. D. Sander and J. K. Joung. CRISPR-Cas systems for editing, regulating and targeting genomes. *Nature Biotechnology*, 32(4):347–55, 2014.

[388] R. A. Baxter. Anti-aging properties of resveratrol: review and report of a potent new antioxidant skin care formulation. *Journal of Cosmetic Dermatology*, 7(1):2–7, 2008.

[389] M. Ndiaye, C. Philippe, H. Mukhtar, and N. Ahmad. The grape antioxidant resveratrol for skin disorders: promise, prospects, and challenges. *Archives of Biochemistry and Biophysics*, 508(2):164–70, 2011.

[390] R. Kohen. Skin antioxidants: Their role in aging and in oxidative stress New approaches for their evaluation. *Biomedicine & Pharmacotherapy*, 53(4):181–192, 1999.

[391] K. J. Trouba, H. K. Hamadeh, R. P. Amin, and D. R. Germolec. Oxidative stress and its role in skin disease. *Antioxidants & Redox Signaling*, 4(4):665–73, 2002.

[392] D. R. Bickers and M. Athar. Oxidative stress in the pathogenesis of skin disease. *The Journal of Investigative Dermatology*, 126(12):2565–75, 2006.

[393] A. Plauth, A. Geikowski, S. Cichon, S. J. Wowro, L. Liedgens, M. Rousseau, C. Weidner, L. Fuhr, M. Kliem, G. Jenkins, S. Lotito, L. J. Wainwright, and S. Sauer. Hormetic shifting of redox environment by pro-oxidative resveratrol protects cells against stress. *Free Radical Biology & Medicine*, 99:608–622, 2016.

[394] A. Plauth, A. Geikowski, S. Cichon, S. J. Wowro, L. Liedgens, M. Rousseau, C. Weidner, L. Fuhr, M. Kliem, G. Jenkins, S. Lotito, L. J. Wainwright, and S. Sauer. Data of oxygen- and pH-dependent oxidation of resveratrol. *Data in Brief*, 9:433–437, 2016.

[395] A. Plauth, A. Geikowski, S. Cichon, S. J. Wowro, L. Liedgens, M. Rousseau, C. Weidner, L. Fuhr, M. Kliem, G. Jenkins, S. Lotito, L. Wainwright, and S. Sauer. Hormetic Shifting of Redox Environment by Pro-Oxidative Resveratrol Protects Cells Against Stress. *bioRxiv*, 2016.

8 Publications

Parts of this dissertation have been published [393–395]:

A. Plauth, A. Geikowski, S. Cichon, S. J. Wowro, L. Liedgens, M. Rousseau, C. Weidner, L. Fuhr, M. Kliem, G. Jenkins, S. Lotito, L. Wainwright, and S. Sauer. Hormetic shifting of redox environment by pro-oxidative resveratrol protects cells against stress. *Free Radical Biology & Medicine*. 2016. http://dx.doi.org/10.1016/j.freeradbiomed.2016.08.006

A. Plauth, A. Geikowski, S. Cichon, S. J. Wowro, L. Liedgens, M. Rousseau, C. Weidner, L. Fuhr, M. Kliem, G. Jenkins, S. Lotito, L. Wainwright, and S. Sauer. Data of oxygen- and pH-dependent oxidation of resveratrol. *Data in Brief*. 2016. http://dx.doi.org/10.1016/j.dib.2016.09.012

A. Plauth, A. Geikowski, S. Cichon, S. J. Wowro, L. Liedgens, M. Rousseau, C. Weidner, L. Fuhr, M. Kliem, G. Jenkins, S. Lotito, L. Wainwright, and S. Sauer. Hormetic Shifting of Redox Environment by Pro-Oxidative Resveratrol Protects Cells Against Stress. *bioRxiv*. 2016. http://dx.doi.org/10.1101/045567

Furthermore, parts of this study were described in the following Master′s theses (Table 8.1):

Table 8.1: Parts of this study were described in the Master′s theses.

Author	Title	University	Year
Sylvia Justina Wowro	Wirkmechanismen der Resveratrol-Behandlung in Fibroblasten	Beuth Hochschule für Technik Berlin (University of Applied Sciences)	2012
Linda Liedgens	Untersuchung regulatorischer Wirkungen von Resveratrol	Johannes Gutenberg Universität Mainz	2014
Anne Geikowski	Effects of Resveratrol treatment on oxidative stress response, metabolism and cell cycle in human primary keratinocytes	Beuth Hochschule für Technik Berlin (University of Applied Sciences)	2014

9 Supplementary Data

Contents

9.1 Supplementary Figures

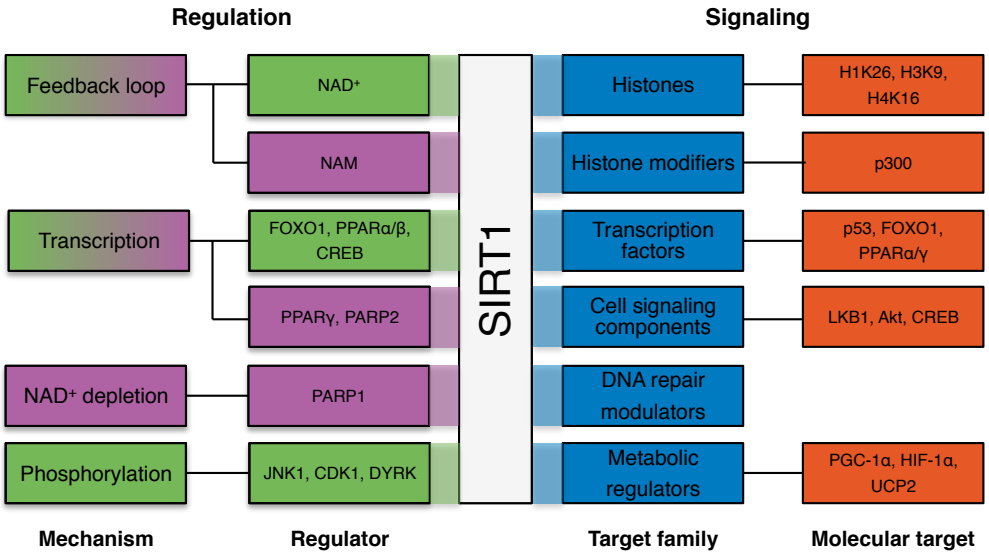

Figure S1: Regulation and signaling of Sirtuin 1 (SIRT1). Protein kinase B (Akt), cyclin-dependent kinases 1 (CDK1), cAMP-response element-binding protein (CREB), dual specificity tyrosine-phosphorylation-regulated kinase (DYRK), forkhead box protein 1 (FOXO1), histone 1 lysine 26 (H1K26), histone 3 lysine 9 (H3K9), histone 4 lysine 16 (H4K16), hypoxia-inducible factor 1-alpha (HIF-1α), c-Jun N-terminal kinase 1 (JNK1), liver kinase B1 (LKB1), nicotinamide adenine dinucleotide phosphate (NAD^+), nicotinamide (NAM), E1A binding protein p300 (p300), tumor protein p53 (p53), poly(ADP-ribose) polymerase 1 (PARP1), PARP2, PPARγ coactivator 1-alpha (PGC1-α), peroxisome proliferator-activated receptor (PPAR) a (PPARα), PPARb (PPARβ), PPAR gamma (PPARγ), mitochondrial uncoupling protein 2 (UCP2), Werner syndrome ATP-dependent helicase (WRN) [75, 76, 99–113, 115, 116].

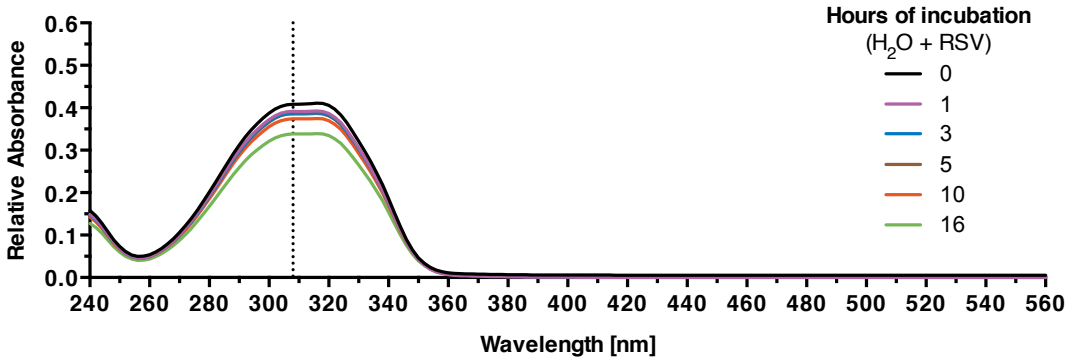

Figure S2: Kinetic wavelength scan of RSV (50 μM) incubated in water. Absorbance was recorded between 240 and 560 nm (Δ 2 nm) and data were smoothed. Dotted line marks RSV absorbance maximum at 308 nm. Data are expressed as mean (n = 3) relative to corresponding DMSO. See also Figure 3.1.

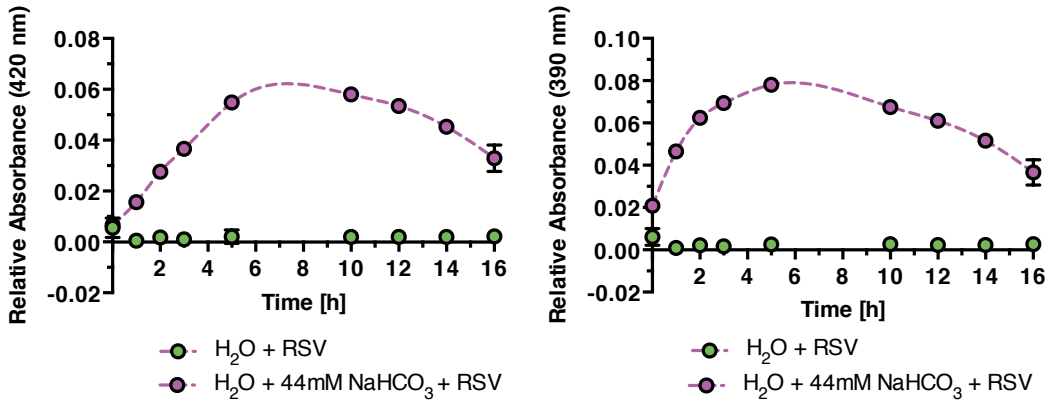

(a) Hydroxyl radical of RSV **(b) Phenoxyl radical of RSV**

Figure S3: Oxidation of 50 μM RSV in water without (in green) and with (in magenta) 44 mM $NaHCO_3$. Oxidation products and corresponding absorbance maxima were recently published by Li et al. (2012) [40]. Values are mean (n = 3) relative to corresponding DMSO control. Data were fitted using cubic spline method with 36 segments. See Figure 3.2a.

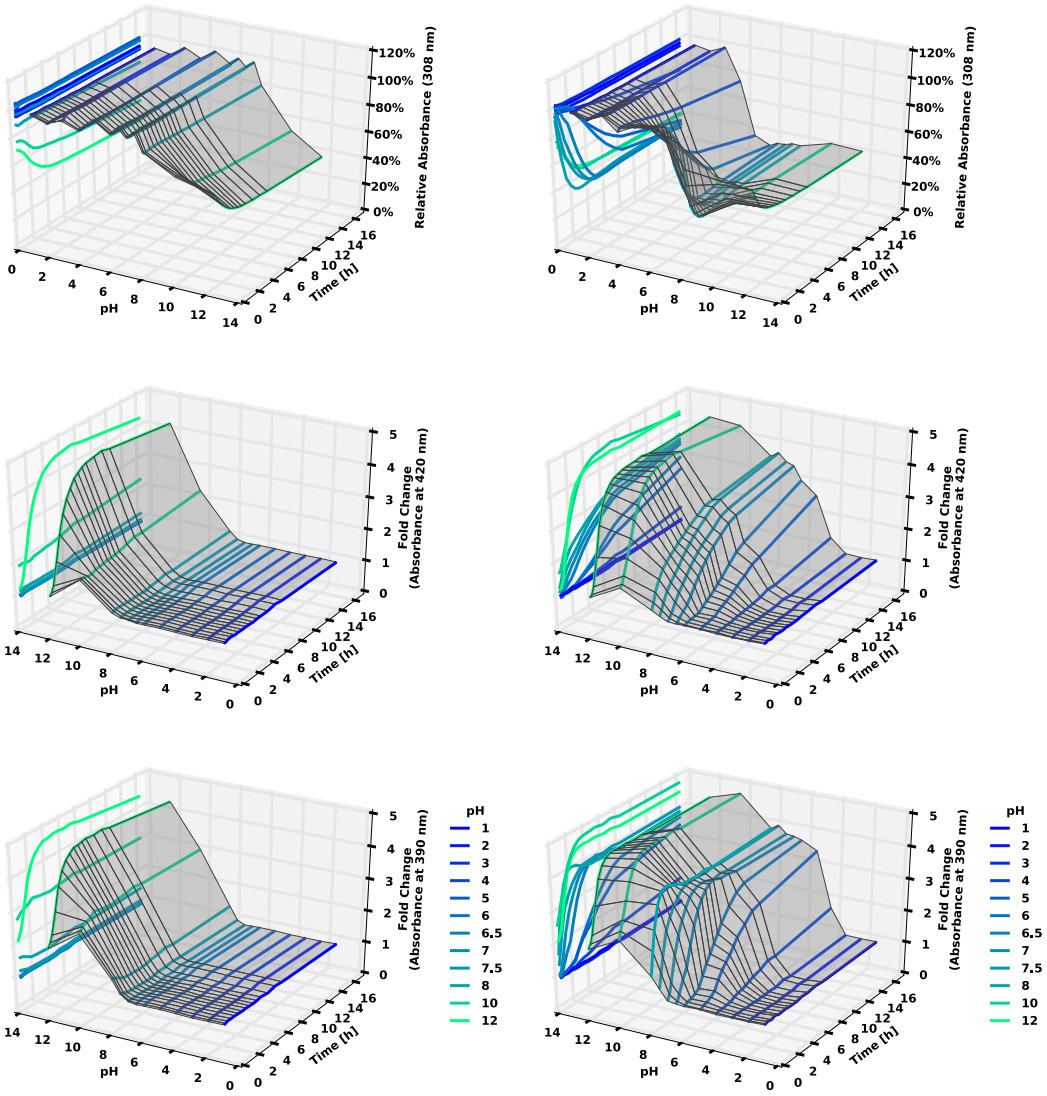

(a) Water **(b) Water + 44mM $NaHCO_3$**

Figure S4: Kinetic effects of pH-dependent oxidation of RSV. Oxidation of 50 μM RSV in pH-adjusted water without (a) or with 44 mM $NaHCO_3$ (b) at 37°C. Absorbance of RSV was recorded at 308 nm, whilst the absorbance of the corresponding oxidation products was measured at 420 nm (hydroxyl radical adduct) and 390 nm (phenoxyl radical adduct), respectively. pH values were adjusted using HCl and NaOH. Values are expressed as mean (n = 6) relative to corresponding DMSO control. See also Figure 3.4. Surface-contour plots were done using Matplotlib [312].

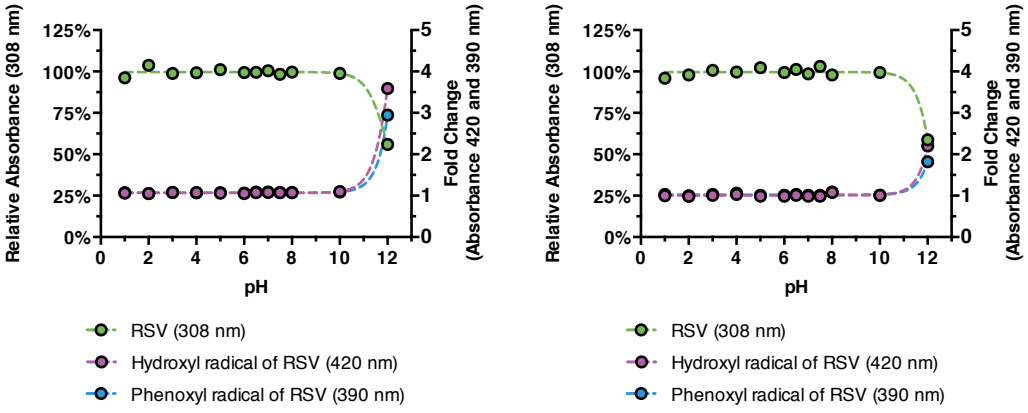

(a) 10% Oxygen **(b) 1% Oxygen**

Figure S5: Effects of oxygen level and pH on the oxidation of RSV. RSV (50 μM) was incubated at 37°C for 16 hours in water and in presence of 10% oxygen (a) and 1% oxygen (b), respectively. Absorbance of RSV was measured at 308 nm, whilst the absorbance of corresponding oxidation products was measured at 420 nm (hydroxyl radical adduct) and 390 nm (phenoxyl radical adduct), respectively. pH values were adjusted using HCl and NaOH. Values are expressed as mean (n = 3) relative to corresponding DMSO controls. Data were fitted (dashed line) according to Equation (2.1). See also Figure 3.5.

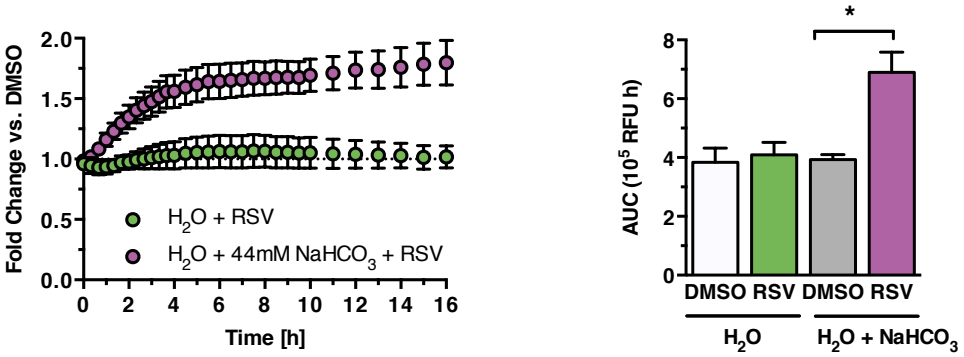

(a) Kinetic ROS generation **(b) Summed ROS generation**

Figure S6: Effects of RSV oxidation on the generation of ROS in water in a cell-free environment. (a) 50 μM RSV were incubated at 37°C for indicated time periods in water without (green) and with 44 mM $NaHCO_3$ (magenta). Values are expressed as mean $\pm$ SEM (n = 4) relative to DMSO. (b) Summed reactive oxygen species (ROS) generation was calculated as area under the curve (AUC) of the data presented in (a). Values are expressed as mean $\pm$ SEM (n = 4) relative to DMSO control. Statistical analysis was done using two tailed Student′s t-test: $*p < 0.05$ versus corresponding DMSO control. See also Figure S7a for $O_2^{\bullet-}$ generation (cell-free environment) as well as Figure 3.6 for intracellular ROS generation and in KGM (cell-free environment).

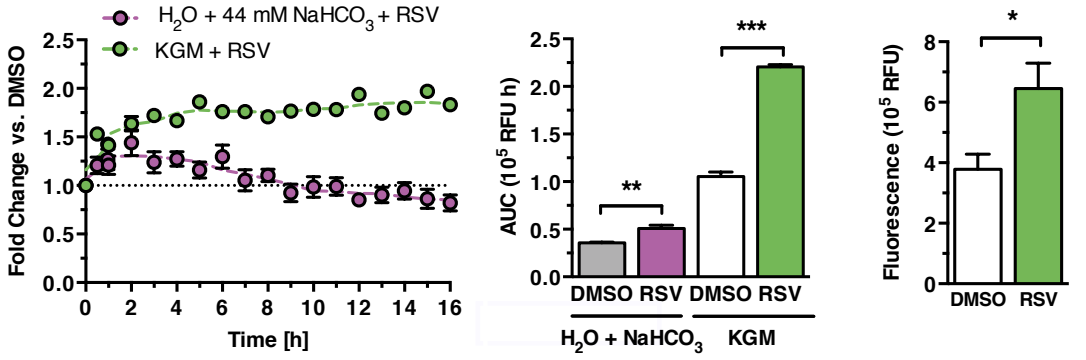

(a) Superoxide generation **(b) Lipid peroxidation**

Figure S7: RSV-driven generation of $O_2^{\bullet-}$ and lipid peroxidation. (a) Kinetic (left) and summed (right) generation of $O_2^{\bullet-}$ after 16 hours of incubation at 37°C. Summed ROS generation was calculated as AUC until 8 (magenta) and 16 (green) hours of incubation. The experiment was done in a cell-free environment. Values are expressed as mean ± SEM (n = 3-4) relative to DMSO. Statistical analyses were done using two tailed Student′s t-test: $**p < 0.01$, $***p \leq 0.001$ versus corresponding DMSO control. (b) neonatal normal human epidermal keratinocyte (NHEK) cells were treated with 50 μM RSV for 16 hours and lipid peroxidation was analyzed. Values are expressed as mean ± SEM (n = 4) relative to DMSO. Statistical analysis was done using two tailed Student′s t-test: $*p < 0.05$ versus DMSO. See also Figure S6 for ROS generation in water (cell-free environment) as well as Figure 3.6 for intracellular ROS generation and in KGM (cell-free environment).

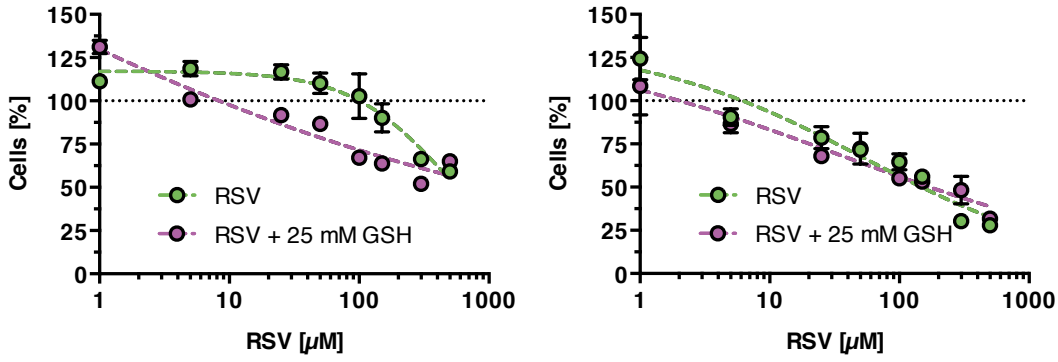

(a) HepG2 cells **(b) THP-1 cells**

Figure S8: Cytotoxicity of RSV in HepG2 (a) and THP-1 cells (b). Cells were treated for 16 hours with either RSV (green) or a combination of RSV and 25 mM GSH (magenta). Data were fitted (dashed line) according to Equation (2.2) using GraphPad 5.0. The concentration required for 50% (IC_{50}) and for 70% (IC_{70}; Equation (2.3)) inhibition were calculated. Values were transformed to relative cell number and expressed as mean ± SEM (n = 6). See also Figure 3.10 for effects on skin cells and Table S3.

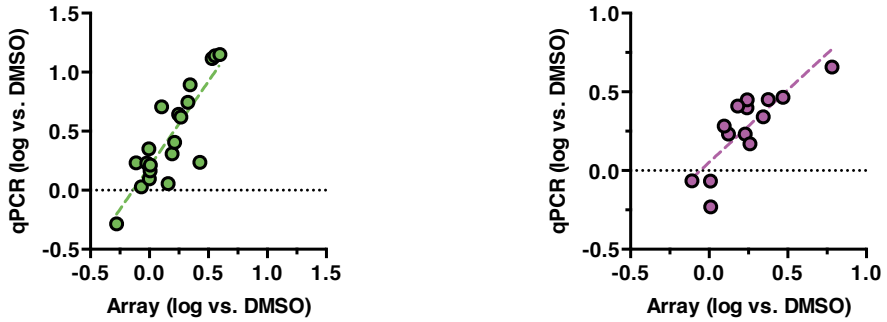

(a) NHEK cells **(b) NHDF cells**

Figure S9: Correlation of array and qPCR data from NHEK cells treated with 50 μM RSV (a) and NHDF cells treated with 100 μM RSV (b) for 16 hours.

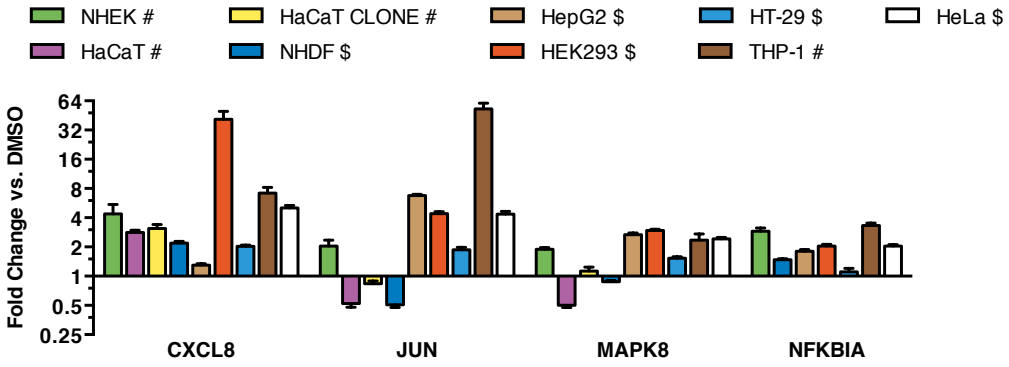

Figure S10: Effects of RSV on expression of inflammatory marker genes in various cells treated with RSV for 16 hours at 37°C. Expression of marker genes was expressed relative to β-Actin. Values are expressed as mean ± SEM (n = 4). See also Table S6.

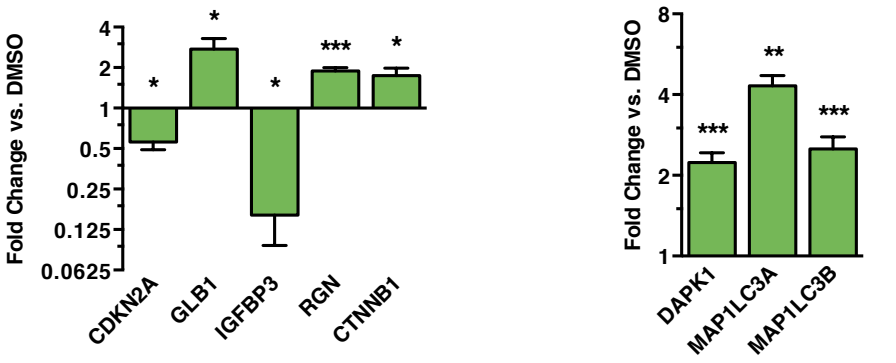

(a) Senescence marker genes **(b) Autophagy marker genes**

Figure S11: Effect of RSV on senescence (a) and autophagy (b) marker gene expression. NHEKs were treated with 50 μM RSV for 16 hours. Values are expressed as mean $\pm$ SEM (n = 4). Statistical analysis was done using two tailed Student′s t-test: $*p < 0.05$, $**p < 0.01$, $***p \leq 0.001$ versus DMSO.

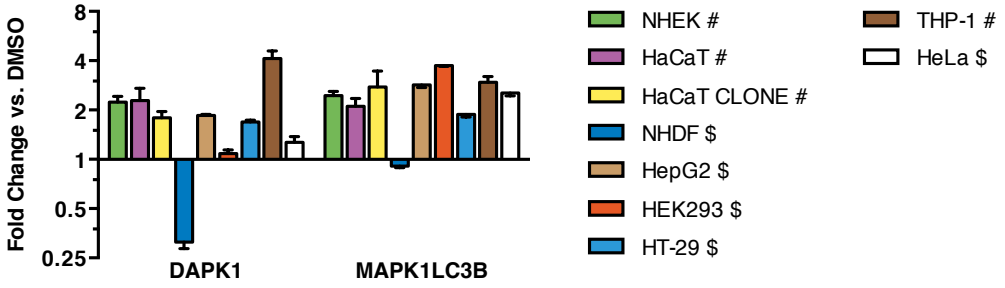

Figure S12: Effects of RSV on expression of proliferation marker genes in various cells treated with RSV for 16 hours at 37°C. Expression of marker genes was expressed relative to β-Actin. Values are expressed as mean $\pm$ SEM (n = 4). See also Table S6.

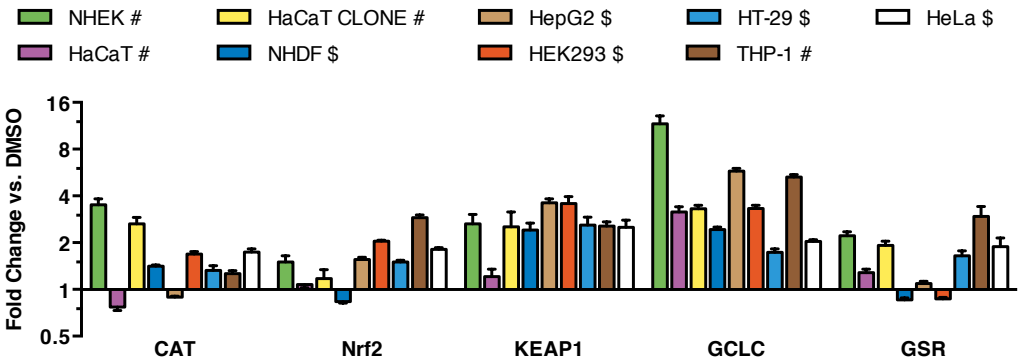

Figure S13: Effects of RSV on expression of oxidative stress marker genes in various cells treated with RSV for 16 hours at 37°C. Expression of marker genes was expressed relative to β-Actin. Values are expressed as mean ± SEM (n = 4). See also Table S6.

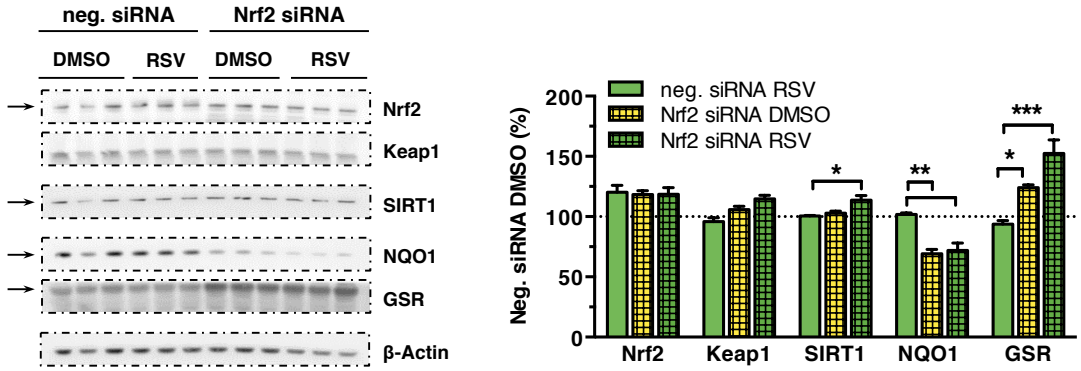

Figure S14: Effects of Nrf2 knockdown on target protein expression in NHEK cells treated for 16 hours at 37°C with 50 μM RSV. Protein expression was detected by Western blot and analyzed densitometrically (right) relative to β-Actin. Values are expressed as mean ± SEM (n = 3). One-way ANOVA with Dunnett′s post test for multiple comparisons: $*p < 0.05$, $**p < 0.01$, $***p \leq 0.001$ versus neg. siRNA RSV. See also Figure 3.24.

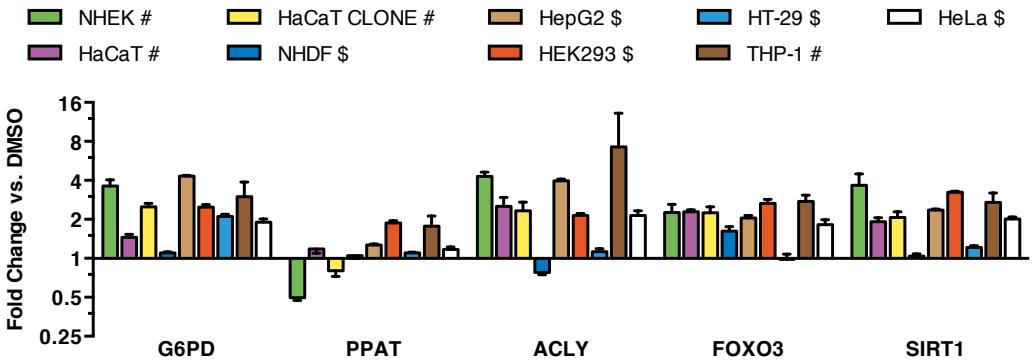

Figure S15: Effects of RSV on expression of energy metabolism marker genes in various cells treated with RSV for 16 hours at 37°C. Expression of marker genes was expressed relative to β-Actin. Values are expressed as mean ± SEM (n = 4). See also Table S6.

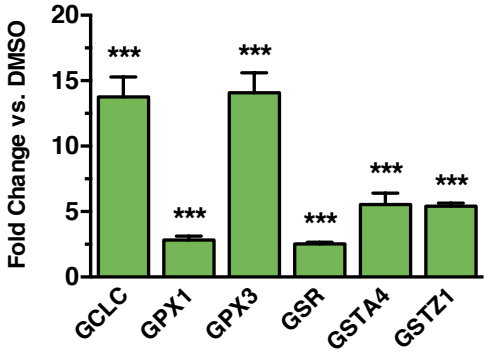

Figure S16: Effect of RSV on the expression of genes associated with GSH metabolism in NHEK cells treated with 50 μM RSV for 16 hours. Values are expressed as mean ± SEM (n = 4). Statistical analysis was done using two tailed Student′s t-test: $***p \leq 0.001$ versus DMSO.

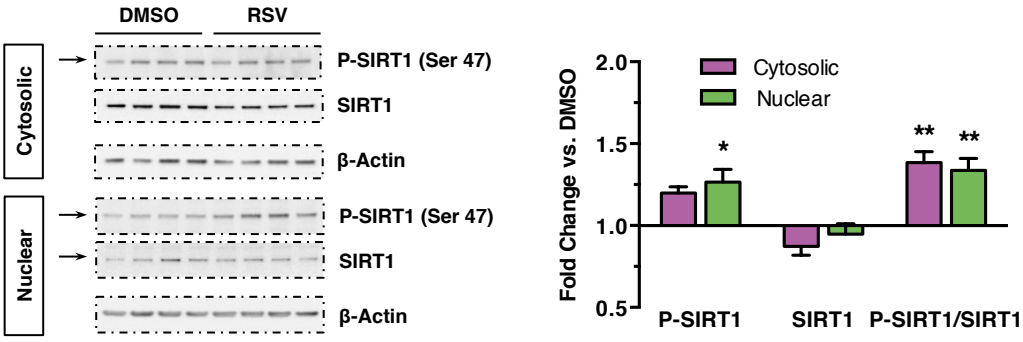

Figure S17: Effects of RSV on SIRT1 phosphorylation and translocation in NHEK cells treated for 16 hours at 37°C with 50 μM RSV. Protein expression was detected by Western blot and analyzed densitometrically (right) relative to β-Actin. Values are expressed as mean ± SEM (n = 4).

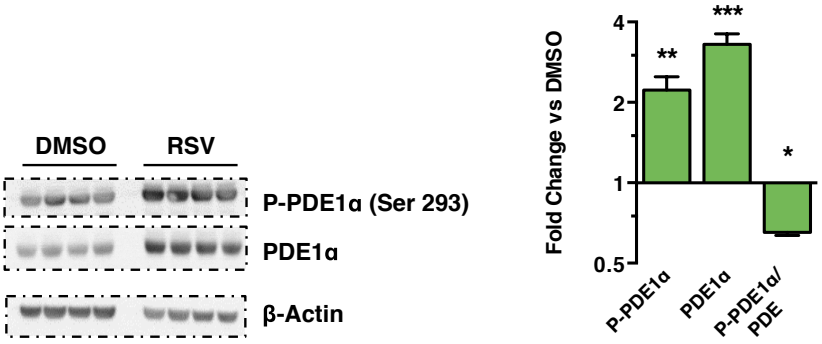

Figure S18: Effects on PDE1α phosphorylation in NHEK cells treated for 16 hours at 37°C with 50 μM RSV. PDE1α phosphorylated at serine 293 (left) was detected by Western blot and analyzed densitometrically (right) relative to β-Actin. Values are expressed as mean ± SEM (n = 4). Statistical analysis was done using two tailed Student′s t-test: $**p < 0.01$ versus DMSO as vehicle control.

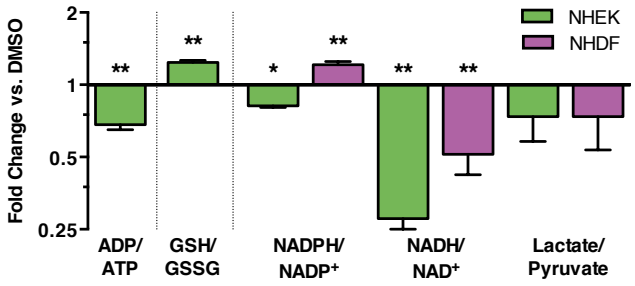

Figure S19: Calculation of metabolite ratios from data presented in Figure 3.27 for NHEK cells (green) and NHDF cells (magenta). Values are expressed as mean ± SEM and statistical analysis was done using two tailed Student′s t-test: $*p < 0.05$, $**p < 0.01$ versus DMSO.

9.2 Supplementary Tables

Table S1: Linear regression fit of the data presented Figure 3.2b. Analysis was done in GraphPad Prism 5.0. Values are expressed as mean ± standard deviation. See also Figure 3.2b.

	KGM (50 μM RSV)	DMEM (100 μM RSV)
Slope	-0.02950 ± 0.001156	-0.05592 ± 0.001542
Y-intercept	0.4642 ± 0.01045	0.8310 ± 0.01394
X-intercept	15.74	14.86
R^2	0.9630	0.9813
***p* value**	< 0.0001	< 0.0001

Table S2: Linear regression fit of the data presented in Figure 3.7a (a) and Figure 3.7b (b). Analysis was done in GraphPad Prism 5.0 and values are expressed as mean ± standard deviation. See also Figure 3.7.

	Trolox	RSV	Trolox + 44 mM $NaHCO_3$	RSV + 44 mM $NaHCO_3$
Slope	-0.001760 ± 0.0001282	$-0.0009624 \pm 6.503*10^5$	$-0.0003878 \pm 3.701*10^5$	$-0.0001649 \pm 1.885*10^5$
Y-intercept	1.210 ± 0.02275	0.5522 ± 0.01154	1.231 ± 0.009829	0.5787 ± 0.005006
X-intercept	687.3	573.7	3175	3510
R^2	0.9084	0.9202	0.8941	0.8547
***p* value**	< 0.0001	< 0.0001	< 0.0001	< 0.0001

(a) Antioxidant Assay: fit

	RSV	RSV + 44 mM $NaHCO_3$
Slope	0.2203 ± 0.02103	0.1713 ± 0.01959
Y-intercept	-12.14 ± 5.584	-27.58 ± 5.202
X-intercept	55.12	161.00
R^2	0.8941	0.8547
***p* value**	< 0.0001	< 0.0001

(b) Trolox equivalents: fit

Table S3: Calculation of the inhibitory concentration required for 50% inhibition (IC_{50}) and 70% (IC_{70}) inhibition of viability. Data are presented in Figures 3.10 and S8. Efficiency (Eff.) is the maximal observed induction of cell death after treatment relative to non-treated cells (set to 0%). Values are expressed as mean ± standard deviation. See also Figures 3.10 and S8.

	IC_{50} [μM]	IC_{70} [μM]	Eff. [%]
NHEK	219.90 ± 1.15	80.60 ± 1.26	67.61 ± 3.98
NHDF	343.50 ± 1.03	274.60 ± 1.05	77.32 ± 0.70
HepG2	445.30 ± 1.15	217.40 ± 1.19	40.88 ± 4.56
THP-1	53.74 ± 1.80	10.08 ± 2.53	72.16 ± 1.34

(a) RSV

	IC_{50} [μM]	IC_{70} [μM]	Eff. [%]
NHEK	247,747 ± 216.27	1,578 ± 11,940	10.65 ± 5.92
NHDF	1,163 ± 1.39	436.90 ± 1.20	28.51 ± 5.86
HepG2	ambiguous	ambiguous	34.90 ± 3.97
THP-1	35.67 ± 8.54	3.18 ± 24.55	68.36 ± 1.84

(b) RSV + 25mM GSH

Table S4: Enriched KEGG pathways (FDR $\leq$ 0.25) in NHEKs treated with RSV for 16 hours subjected to GSEA (DMSO n = 4; RSV n = 3). See also Figure 3.12. False discovery rate (FDR), normalized enrichment score (NES).

Name	NES	FDR q value
Spliceosome	− 2.581	0.000
RNA degradation	− 2.340	0.000
DNA replication	− 2.239	0.000
Cell cycle	− 2.143	0.000
Lysosome	2.160	0.000
Systemic lupus erythematosus	2.110	0.001
Metabolism of xenobiotics by cytochrome p450	1.882	0.015
Steroid hormone biosynthesis	1.898	0.015
Other glycan degradation	1.907	0.017
Adipocytokine signaling pathway	1.847	0.021
Pentose and glucuronate interconversions	1.821	0.025
Pyruvate metabolism	1.777	0.029
PPAR signaling pathway	1.779	0.031
Peroxisome	1.784	0.034
Epithelial cell signaling in helicobacter pylori infection	1.745	0.034
Natural killer cell mediated cytotoxicity	1.732	0.035
Glutathione metabolism	1.750	0.036
Nitrogen metabolism	1.719	0.038
Cytokine cytokine receptor interaction	1.732	0.038
Drug metabolism cytochrome p450	1.691	0.043
Retinol metabolism	1.699	0.044
Proximal tubule bicarbonate reclamation	1.691	0.045
Fatty acid metabolism	1.680	0.045
Purine metabolism	− 1.747	0.055
Arachidonic acid metabolism	1.647	0.060
Pyrimidine metabolism	− 1.721	0.061
Sphingolipid metabolism	1.637	0.062
Toll like receptor signaling pathway	1.626	0.066
Propanoate metabolism	1.620	0.067
Glycine serine and threonine metabolism	1.587	0.087
Valine leucine and isoleucine degradation	1.564	0.094

Table S4: GSEA analysis: KEGG pathways (continued)

Name	NES	FDR q value
Limonene and pinene degradation	1.568	0.095
Glycerolipid metabolism	1.572	0.095
Butanoate metabolism	1.552	0.097
FC epsilon RI signaling pathway	1.557	0.097
Steroid biosynthesis	1.530	0.102
Taste transduction	1.526	0.103
B cell receptor signaling pathway	1.533	0.103
Cell adhesion molecules CAMS	1.538	0.103
RNA polymerase	− 1.633	0.126
NOD like receptor signaling pathway	1.467	0.152
One carbon pool by folate	− 1.595	0.153
Chemokine signaling pathway	1.459	0.157
Glycosaminoglycan biosynthesis keratan sulfate	1.445	0.167
Proteasome	− 1.557	0.168
Oocyte meiosis	− 1.568	0.170
Amino sugar and nucleotide sugar metabolism	1.431	0.174
Tryptophan metabolism	1.426	0.175
Arginine and proline metabolism	1.432	0.177
FC gamma r mediated phagocytosis	1.420	0.178
Inositol phosphate metabolism	1.400	0.193
Glycosaminoglycan biosynthesis chondroitin sulfate	1.401	0.197
Progesterone mediated oocyte maturation	− 1.522	0.199
Citrate cycle TCA cycle	1.382	0.212
Base excision repair	− 1.475	0.218
Nucleotide excision repair	− 1.460	0.224
ECM receptor interaction	− 1.480	0.227
Aminoacyl tRNA biosynthesis	− 1.482	0.243

Table S5: Connectivity of the RSV gene expression profile in NHEKs with other small molecules using the Connectivity Map. The best connection with molecules sharing the same Anatomical Therapeutic Chemical (ATC) classification ($p \leq 0.001$).

Rank	Cmap Name	Mean	n	Enrichment	p	specificity	Percent non-null
1	P02CX	0.653	6	0.88	0	0.0186	100
2	C08EA	0.572	7	0.839	0	0.0052	100
3	N05AG	0.606	8	0.821	0	0.0049	100
4	N05AB	0.597	60	0.703	0	0	95
5	N05AC	0.578	24	0.674	0	0.0046	83
6	L04AA	0.456	51	0.544	0	0.006	88
7	N06AA	0.428	46	0.469	0	0.0096	78
8	P02DA	0.64	5	0.871	0.00008	0.0105	100
9	A07DA	0.641	6	0.809	0.00008	0.0101	100
10	D01AC	0.286	35	0.352	0.00022	0.0353	62
11	P01BC	0.707	5	0.821	0.00038	0.0539	100
12	R02AD	0.228	13	0.548	0.0004	0.0065	61
13	G04BX	0.608	4	0.865	0.00044	0.026	100
14	C01AA	0.357	10	0.583	0.00084	0.2917	90
15	C03CA	−0.28	16	−0.468	0.00094	0.0118	50
16	R06AX	0.337	36	0.317	0.00102	0.0809	69

Table S6: Calculation of Pearson correlation coefficient r (a) and p (b) value from the data presented in Figures S12, S13 and S15.

	NHEK #	NHEK $	HaCaT #	HaCaT # CLONE #	NHDF $	HepG2 #	HepG2 $	HEK #	HEK $	HT29 #	HT29 $	THP $	THP #	HeLA $	HeLa #
NHEK #	–	0.716	0.654	0.799	0.373	0.515	0.525	0.428	0.430	−0.011	0.432	0.047	0.041	0.406	0.439
NHEK $	0.716	–	0.704	0.414	0.159	0.512	0.502	0.676	0.689	−0.258	0.277	0.415	0.394	0.659	0.680
HaCaT #	0.654	0.704	–	0.523	0.261	0.538	0.612	0.301	0.333	−0.176	0.103	0.278	0.291	0.346	0.386
HaCaT CLONE #	0.799	0.415	0.523	–	0.692	0.412	0.483	0.109	0.110	0.119	0.407	−0.073	−0.106	0.107	0.117
NHDF $	0.373	0.159	0.261	0.691	–	0.236	0.373	−0.164	−0.141	0.136	0.338	−0.123	−0.179	−0.232	−0.253
HepG2 #	0.515	0.512	0.538	0.412	0.233	–	0.959	0.443	0.486	0.498	0.677	0.512	0.490	0.593	0.573
HepG2 $	0.525	0.502	0.612	0.483	0.373	0.959	–	0.279	0.336	0.397	0.562	0.484	0.469	0.419	0.401
HEK293 #	0.428	0.676	0.301	0.109	−0.164	0.443	0.279	–	0.986	0.124	0.544	0.307	0.298	0.910	0.913
HEK293 $	0.430	0.689	0.333	0.110	−0.141	0.486	0.336	0.986	–	0.110	0.501	0.269	0.253	0.876	0.876
HT-29 #	−0.011	−0.258	−0.176	0.119	0.136	0.498	0.397	0.125	0.110	–	0.601	0.157	0.130	0.190	0.200
HT-29 $	0.432	0.277	0.103	0.407	0.338	0.677	0.562	0.544	0.501	0.601	–	0.273	0.245	0.586	0.558
THP-1 $	0.0468	0.415	0.277	−0.073	−0.123	0.512	0.484	0.307	0.269	0.157	0.273	–	0.990	0.598	0.568
THP-1 #	0.041	0.394	0.291	−0.106	−0.179	0.490	0.469	0.298	0.253	0.130	0.245	0.990	–	0.597	0.570
HeLa $	0.406	0.659	0.346	0.107	−0.232	0.593	0.419	0.910	0.876	0.190	0.586	0.598	0.597	–	0.983
HeLa #	0.439	0.680	0.386	0.117	−0.253	0.573	0.401	0.913	0.876	0.200	0.558	0.569	0.570	0.983	–

with **#**: Treatment with 50 μM RSV
$: Treatment with 100 μM RSV

(a) Pearson correlation coefficient r

Table S6: Calculation of Pearson correlation coefficient r (a) and p (b) value (continued).

	NHEK #	NHEK $	HaCaT #	HaCaT # CLONE #	NHDF $	HepG2 #	HepG2 $	HEK #	HEK $	HT29 #	HT29 $	THP $	THP #	HeLA $	HeLa #
NHEK #	–	0.001	0.004	0.000	0.128	0.034	0.030	0.076	0.075	0.965	0.074	0.854	0.871	0.094	0.069
NHEK $	0.001	–	0.002	0.110	0.542	0.043	0.047	0.003	0.002	0.317	0.282	0.098	0.118	0.004	0.003
HaCaT #	0.004	0.002	–	0.031	0.311	0.032	0.012	0.240	0.191	0.500	0.695	0.282	0.258	0.174	0.126
HaCaT CLONE #	0.000	0.110	0.031	–	0.002	0.113	0.058	0.677	0.674	0.648	0.105	0.779	0.686	0.684	0.654
NHDF $	0.128	0.542	0.311	0.002	–	0.369	0.140	0.516	0.576	0.590	0.170	0.627	0.477	0.355	0.312
HepG2 #	0.034	0.043	0.032	0.113	0.370	–	0.000	0.075	0.048	0.042	0.002	0.036	0.046	0.012	0.016
HepG2 $	0.030	0.047	0.012	0.058	0.140	0.000	–	0.279	0.188	0.115	0.019	0.049	0.058	0.094	0.111
HEK293 #	0.077	0.003	0.240	0.677	0.516	0.075	0.279	–	0.000	0.623	0.020	0.215	0.230	0.000	0.000
HEK293 $	0.075	0.002	0.191	0.674	0.576	0.048	0.188	0.000	–	0.664	0.034	0.280	0.312	0.000	0.000
HT-29 #	0.965	0.317	0.500	0.648	0.590	0.042	0.115	0.623	0.664	–	0.008	0.533	0.608	0.450	0.427
HT-29 $	0.074	0.282	0.695	0.105	0.170	0.003	0.019	0.020	0.034	0.008	–	0.273	0.326	0.011	0.016
THP-1 $	0.854	0.098	0.282	0.779	0.627	0.036	0.049	0.215	0.280	0.533	0.273	–	0.000	0.009	0.0138
THP-1 #	0.871	0.118	0.258	0.686	0.477	0.046	0.058	0.230	0.312	0.608	0.326	0.000	–	0.009	0.0134
HeLa $	0.094	0.004	0.174	0.684	0.355	0.012	0.094	0.000	0.000	0.450	0.011	0.009	0.009	–	0.000
HeLa #	0.069	0.003	0.126	0.654	0.312	0.016	0.111	0.000	0.000	0.427	0.016	0.014	0.013	0.000	–

with **#**: Treatment with 50 μM RSV
$: Treatment with 100 μM RSV

(b) Pearson correlation p value

Table S7: Calculation of the pH-dependent half-cell potential (E_{pH}) (a) and the redox state (b) for each redox couple in NHEK cells treated with 50 μM RSV for 16 hours. Data presented in Figure 3.27 were normalized to protein content. Values are expressed as mean, while relative fluorescence units are depicted in in italic font. See also Figure 3.27, Tables 3.1 and S8, and Equations (1.8), (3.1), (3.2) and (S1) to (S6).

Redox Couple	$\mathbf{E_0}$	e^-	H^+	$\frac{\Delta E}{\Delta \mathbf{pH}}$	**pH** DMSO	**pH** RSV	$E_{\mathbf{pH}}$ DMSO	$E_{\mathbf{pH}}$ RSV
GSH/GSSG	−240	2	2	−61.50	7.0026	7.0632	−240.16	−243.89
NADPH/NADP$^+$	−315	2	1	−30.75			−315.08	−316.94
NADH/NAD$^+$	−316	2	1	−30.75			−316.08	−317.94
Lactate/Pyruvate	−183	2	2	−61.50			−183.89	−1186.89

(a) Consideration of pH

Redox Couple	**Reduced species** [μmol per g protein] DMSO	**Reduced species** [μmol per g protein] RSV	**Oxidized species** [μmol per g protein] DMSO	**Oxidized species** [μmol per g protein] RSV	**n**	$E_{\mathbf{hc,\,pH}}$ DMSO	$E_{\mathbf{hc,\,pH}}$ RSV
GSH/GSSG	20.71	27.68	0.45	0.47	2	−331.79	−342.55
NADPH/NADP$^+$	*14,349.64*	*9,043.69*	*329,983.45*	*169,419.42*	2	−273.21	−277.81
NADH/NAD$^+$	0.37	0.21	3.25	3.71	2	−286.95	−279.63
Lactate/Pyruvate	18.09	17.72	3.56	4.87	2	−204.89	−204.13

(b) Calculation of redox state

Table S8: Calculation of redox state and redox environment in NHDF treated with 100 μM RSV for 16 hours. Data presented in Figure 3.27 were normalized to protein content and pH values were assumed equal to NHEK cells (Table S7a). See also Figure 3.27, Tables 3.1 and S7, and Equations (1.8), (3.1), (3.2), (S2) and (S5).

Redox Couple	**Reduced species** [μmol per g protein]		**Oxidized species** [μmol per g protein]		**n**	$E_{\mathrm{hc,\,pH}}$	
	DMSO	RSV	DMSO	RSV		DMSO	RSV
NADPH/NADP$^+$	0.26	0.05	0.46	0.46	2	−307.41	−288.58
NADH/NAD$^+$	2.29	1.25	3.65	4.59	2	−309.89	−300.58
Lactate/Pyruvate	0.64	0.56	0.10	0.12	2	−208.30	−207.79

(a) Calculation of the redox state

Redox Couple	**Redox state** [mV]		Δ	**Redox environment** [mV mmol (g protein)$^{-1}$]		Δ
	DMSO	**RSV**		**DMSO**	**RSV**	
NADPH/NADP$^+$	−307.41	−288.58	**18.83**			
NADH/NAD$^+$	−309.89	−300.58	**9.32**	−0.94	−0.52	**0.42**
Lactate/Pyruvate	−208.30	−207.79	**0.51**			

(b) Redox state vs. redox environment.

9.3 Supplementary Equations

$$\mathrm{NADP^+} + H^+ + 2e^- \rightarrow \mathrm{NADPH} \qquad E^{0'} = -320\ \mathrm{mV} \tag{S1}$$

$$E_{\mathrm{hc,\,pH}} = -320\ \mathrm{mV} + [(\mathrm{pH} - 7.0) * -30.75\ \mathrm{mV}] - \frac{61.5\ \mathrm{mV}}{2} * \log \frac{[\mathrm{NADPH}]}{[\mathrm{NADP^+}]} \tag{S2}$$

$$\mathrm{NAD^+} + H^+ + 2e^- \rightarrow \mathrm{NADH} \qquad E^{0'} = -320\ \mathrm{mV} \tag{S3}$$

$$E_{\mathrm{hc,\,pH}} = -320\ \mathrm{mV} + [(\mathrm{pH} - 7.0) * -30.75\ \mathrm{mV}] - \frac{61.5\ \mathrm{mV}}{2} * \log \frac{[\mathrm{NADH}]}{[\mathrm{NAD^+}]} \tag{S4}$$

$$\mathrm{Pyruvate} + 2H^+ + 2e^- \rightarrow \mathrm{Lactate} \qquad E^{0'} = -190\ \mathrm{mV} \tag{S5}$$

$$E_{\mathrm{hc,\,pH}} = -190\ \mathrm{mV} + [(\mathrm{pH} - 7.0) * -61.5\ \mathrm{mV}] - \frac{61.5\ \mathrm{mV}}{2} * \log \frac{[\mathrm{Lactate}]}{[\mathrm{Pyruvate}]} \tag{S6}$$

Abbreviations

Notation	Description
ABTS	2,2′-azino-di-[3-ethylbenzthiazoline sulphonate]
ACLY	Adenosine triphosphate (ATP) citrate lyase
ADP	Adenosine diphosphate
AhR	Aryl hydrocarbon receptor
Akt	Protein kinase B (also known as PKB)
AMP	Adenosine monophosphate
AMPK	5′AMP-activated protein kinase
ANOVA	Analysis of variance
AP-1	Activating protein 1
ARE	Antioxidant response element
ATM	Ataxia telangiectasia mutated
ATP	Adenosine triphosphate
ATR	Ataxia telangiectasia and Rad3-related protein
AUC	Area under the curve
BAD	BCL2-associated death promoter (protein symbol Bad)
BAK	BCL2-antagonist/killer (protein symbol Bak)
BAX	BCL2-associated X protein (protein symbol Bax)
BCL2	B-cell lymphoma 2 (protein symbol Bcl-2)
BIRC5	Baculoviral inhibitor of apoptosis repeat-containing 5 (protein symbol Survivin)
BNID	BioNumbers ID [1]
BSA	Bovine serum albumin
c-Jun	c-Jun (gene symbol JUN)
C/EBPβ	CCAAT/enhancer-binding protein beta (gene symbol CEBPB)

Notation	Description
cAMP	Cyclic adenosine monophosphate
CAT	Catalase
CBP	CREB binding protein protein (gene symbol CREBBP)
CDK	Cyclin-dependent kinase
CDKN2A	CDK inhibitor 2A
CEBPB	CCAAT/enhancer-binding protein beta (protein symbol C/EBPβ)
ChIP	Chromatin immunoprecipitation
CM-H_2DCFDA	5-(and-6)-chloromethyl-2′,7′-dichlorodihydrofluorescein diacetate, acetyl ester
COX	Cyclooxygenase
CR	Calorie restriction
CREB	cAMP-response element-binding protein
CRISPR	Clustered regularly-interspaced short palindromic repeats
CTNNB1	β-Catenin
Cul3	Cullin 3-based ubiquitin E3 ligase
CXCL8	Interleukin 8 (protein symbol IL-8)
CYP	Cytochrome p450 monooxygenase
DAPI	4',6-diamidino-2-phenylindole
DAPK1	Death associated protein kinase 1
DDR	DNA damage repair
DIABLO	Direct IAP binding protein with low pI
DMEM	Dulbecco′s modified Eagle′s medium
DMEM/F-12	DMEM Nutrient Mixture F-12
DMSO	Dimethyl sulfoxide
DNA	Deoxyribonucleic acid
DTAB	Dodecyltrimethylammonium bromide
DTT	Dithiothreitol
DYRK	Dual specificity tyrosine-phosphorylation-regulated kinase
E1A	Adenovirus early region 1A
ECAR	Extracellular acidification rate
ECM	Extracellular matrix
EDTA	Ethylenediaminetetraacetic acid
EpRE	Electrophile response element
ER	Endoplasmatic reticulum
F6P	Fructose 6-phosphate
FACS	Fluorescence-activated cell sorting
FBS	Fetal bovine serum
FDR	False discovery rate
FOXO	Forkhead box protein

Notation	Description
G6P	Glucose 6-phosphate
G6PD	Glucose-6-phosphate dehydrogenase
GAP	Glyceraldehyde 3-phosphate
GCL	Glutamate-cysteine ligase
GCLC	Glutamate-cysteine ligase (catalytic subunit)
GCLM	Glutamate-cysteine ligase (modifier subunit)
GLB1	Galactosidase β 1
GPX	Glutathione peroxidase
GSEA	Gene set enrichment analysis
GSH	Glutathione (reduced form)
GSK3β	Glycogen synthase kinase 3 beta
GSR	Glutathione reductase
GSS	Glutathione synthase
GSSG	Glutathione (oxidized form)
GST	Glutathione *S*-transferase
GSTA1	Glutathione *S*-transferase alpha 1
H_2O_2	Hydrogen peroxide
H1K26	Histone 1 lysine 26
H3K9	Histone 3 lysine 9
H4K16	Histone 4 lysine 16
HaCaT	Human adult low calcium high temperature keratinocyte
HDAC	Histone deacetylase
HEK293	Human embryonic kidney cell
HeLa	Human cervical cancer cell
HepG2	Human liver carcinoma cell
HIF-1α	Hypoxia-inducible factor 1-alpha
HMOX1	Heme oxygenase 1
HNE	4-Hydroxynonenal
HSP	Heat shock protein
HT-29	Human colon cancer cell
$HO^{\bullet}$	Hydroxyl radical
IκB	Nuclear factor of kappa light polypeptide gene enhancer in B-cells inhibitor
IκB α	Nuclear factor of kappa light polypeptide gene enhancer in B-cells inhibitor alpha (gene symbol NFκBIA)
IAP	Inhibitor of apoptosis protein
IDCR	Ionic detergent compatibility reagent
IDH1	Isocitrate dehydrogenase 1
IGFBP3	Insulin-like growth factor-binding protein 3

Notation	Description
IL	Interleucin
IL-8	Interleukin 8 (gene symbol CXCL8)
JNK	c-Jun N-terminal kinase
JNK1	c-Jun N-terminal kinase 1 (gene symbol MAPK8)
JUN	c-Jun (protein symbol c-Jun)
KBM	Keratinocyte basal medium
KEAP1	Kelch-like ECH-associated protein 1 (protein symbol Keap1)
Keap1	Kelch-like ECH-associated protein 1 (gene symbol KEAP1)
KGM	Keratinocyte growth medium
KRT14	Keratin 14
LAA	Linoleamide alkyne
LC3	Microtubule-associated protein 1 light chain 3
LKB1	Liver kinase B1
LOX	Lipoxygenase
LXRα	Liver X receptor alpha
Maf	Small musculoaponeurotic fibrosarcoma
MAP1LC3	Microtubule-associated protein 1 light chain 3 (protein symbol LC3)
MAPK	Mitogen-activated protein kinase
MAPK8	Mitogen-activated protein kinase 8 (protein symbol JNK)
MCP-1	Monocyte chemoattractant protein 1
ME1	Malic enzyme 1
miRNA	Micro RNA
MMP	Matrix metalloproteinase
mRNA	Messenger RNA
NAC	N-acetyl-cysteine
NAD^+	Nicotinamide adenine dinucleotide (oxidized form)
NADH	Nicotinamide adenine dinucleotide (reduced form)
$NADP^+$	Nicotinamide adenine dinucleotide phosphate (oxidized form)
NADPH	Nicotinamide adenine dinucleotide phosphate (reduced form)
NAM	Nicotinamide
Neh	Nuclear factor (erythroid-derived 2)-like 2 (Nrf2)-ECH homology
NES	Normalized enrichment score
NFκB	nuclear factor kappa-light-chain-enhancer of activated B cells
NFκBIA	Nuclear factor of kappa light polypeptide gene enhancer in B-cells inhibitor alpha (protein symbol IκB α)
NHDF	Neonatal normal human dermal fibroblast
NHEK	Neonatal normal human epidermal keratinocyte

Notation	Description
NO	Nitric oxide
NOAEL	No-observed-adverse-effect-level
NOX	NADPH oxidase
NQO1	NAD(P)H dehydrogenase (quinone 1)
Nrf2	Nuclear factor (erythroid-derived 2)-like 2
$O_2^{\bullet -}$	Superoxide
p21	CDK inhibitor 1A
p300	E1A binding protein p300
p53	Tumor protein p53
p62	Sequestosome-1 (also known as SQSTM1)
PARP	Poly(ADP-ribose) polymerase
PBS	Phosphate buffered saline
PCR	Polymerase chain reaction
PDE1α	Pyruvate dehydrogenase E1-alpha
PDE4	cAMP-specific 3′,5′-cyclic phosphodiesterase 4
PGC1-α	PPARγ coactivator 1-alpha
PGC1-β	PPARγ coactivator 1-beta (gene symbol)
6PGD	Phosphogluconate dehydrogenase (protein symbol PGD)
PGD	Phosphogluconate dehydrogenase (gene symbol 6PGD)
PI	Propidium iodide
PI3K	Phosphatidylinositol-4,5-bisphosphate 3-kinase
PKB	Protein kinase B (also known as Akt)
PKC	Protein kinase C
PKM	Pyruvate kinase
PPAR	Peroxisome proliferator-activated receptor
PPARG	PPAR gamma (protein symbol PPARγ)
PPARγ	PPAR gamma (gene symbol PPARG)
PPARGC1B	PPARγ coactivator 1-beta (protein symbol PGC1-β)
PPAT	Phosphoribosyl pyrophosphate amidotransferase
PPP	Pentose phosphate pathway
PRX	Peroxiredoxin
qPCR	Quantitative PCR
R5P	Ribose 5-phosphate
RFU	Relative fluorescence units
RGN	Regucalcin
RNA	Ribonucleic acid
ROS	Reactive oxygen species
RPMI	Roswell Park Memorial Institute medium

Notation	Description
RSV	*Trans*-resveratrol
RXRA	Retinoid X receptor alpha (protein symbol RXRα)
RXRα	Retinoid X receptor alpha (gene symbol RXRA)
SDS	Sodium dodecyl sulfate
SFN	1-Isothiocyanato-4-methylsulfinylbutane (Sulforaphane)
SIR2	Silent information regulator 2
siRNA	Small interfering RNA
SIRT	Sirtuin
SIRT1	Sirtuin 1
SOD	Superoxide dismutase
TALDO1	Transaldolase 1
tBHQ	*tert*-Butylhydroquinone
TBS	Tris-buffered saline
TCA	Tricarboxylic acid
THP-1	Human monocytic cell
TKT	Transketolase
TNFα	Tumor necrosis factor α
TR	Thioredoxin reductase (gene symbol)
Tris	Tris(hydroxymethyl)aminomethane
TXN	Thioredoxin
UCP2	Mitochondrial uncoupling protein 2
UV	Ultraviolet
WBSSH	White-Bate-Smith-Swain-Haslam
WRN	Werner syndrome ATP-dependent helicase
XRE	Xenobiotic response element

List of Figures

List of Tables

List of Equations